Fall 2009

Effects of waves and the free surface on a surface-piercing flat-plate turbulent boundary layer and wake

Matthew William Marquardt
University of Iowa

EFFECTS OF WAVES AND THE FREE SURFACE ON A SURFACE-PIERCING FLAT-PLATE TURBULENT BOUNDARY LAYER AND WAKE

by

Matthew William Marquardt

A thesis submitted in partial fulfillment
of the requirements for the Master of
Science degree in Mechanical Engineering
in the Graduate College of
The University of Iowa

December 2009

Thesis Supervisors: Professor Frederick Stern
Research Engineer Joseph Longo

Graduate College
The University of Iowa
Iowa City, Iowa

CERTIFICATE OF APPROVAL

_____

MASTER'S THESIS

_____

This is to certify that the Master's thesis of

Matthew William Marquardt

has been approved by the Examining Committee
for the thesis requirement for the Master of Science
degree in Mechanical Engineering at the December 2009 graduation.

Thesis Committee: _____
Frederick Stern, Thesis Supervisor

_____
Joseph Longo, Thesis Supervisor

_____
Pablo Carrica

To my parents

ACKNOWLEDGMENTS

I wish to acknowledge all of those who have lent their time, labor, and expertise in order to complete the experiments and this thesis. This study reflects not only my work but that of a collaborative effort.

I thank my advisor Dr. Fredrick Stern for the opportunity to pursue higher education and his assistance along the way. I am equally grateful for the help and advice I received from Dr. Joseph Longo, without whom, much of this work would not have been completed. My appreciation for these gentlemen surpasses all others-for the lessons they have taught me extend beyond fluid mechanics. I would also like to express my appreciation to Dr. Pablo Carrica for serving on my thesis committee.

Hyunse Yoon and Dong Hoon Kang graciously provided the necessary tools to process data. Without their assistance, various calculations and plots would have been rough at best. Several students have assisted acquiring data and maintaining the laboratory in ship shape fashion, they include Chelsea Cross, Brian Jaffe, Adam Keen, Andrew Porter, and Michael Skrypczak. Their help aside, they have made the time spent in the laboratory far more enjoyable. The IT support personnel and the Model Annex personnel have to be commended for their prompt response servicing computerized controls and equipment.

Finally, I like to thank any other person who contributed to the completion of this thesis and is not specifically mentioned.

ABSTRACT

Results are presented for towing tank experiments of a surface-piercing flat plate with superimposed Stokes wave in order to examine free surface and wave effects on the boundary layer and wake. Measurements with servo wave gauges are made to characterize the Stokes-wave wave field in terms of its two-dimensionality, amplitude, and wavelength. Flow field measurements using stereo particle image velocimetry are used to identify the boundary layer and wake velocities. Particular attention is drawn to the juncture region to resolve the complex and poorly understood secondary flow patterns. Four test cases are presented (1) flat free surface without plate, (2) Stokes-wave without plate, (3) flat free surface with plate, and (4) Stokes-wave with plate; the cases were chosen in order to isolate and identify the performance of the velocimeter system, Stokes-wave flow field, free-surface effects, and combined Stokes-wave and free surface effects, respectively. All cases are conducted at Froude numbers of $Fn = 0.4$, length-based Reynolds number of $Re = 1.64\times10^6$, and momentum thickness-based Reynolds number of about $Re_\theta = 4000$. Results show, as expected, that the free surface effects penetrate to a depth slightly greater than the boundary layer thickness and wave effects diminish at roughly one half the wavelength. The juncture region flow was resolved to levels that far exceed previous towing tank experiments, but leave more to be desired. The data and analysis are important, not only from a scientific perspective, but have a practical application with regard to development of turbulence models for computational fluid dynamic techniques.

TABLE OF CONTENTS

LIST OF TABLES

LIST OF FIGURES

LIST OF SYMBOLS

Alphabetical symbols

Ak	wave steepness
b	wake half width, systematic error
c	cord length of foil
d	submergence depth of foil
C_f	wall friction coefficient
G	shape parameter
H	shape factor
k	wave number
L	length of plate
P	precision limit
R	result in an experiment
Re	Reynolds number
s	random error
U_c	carriage speed
U_e, W_e	edge velocities
U, V, W	mean velocities
uu, vv, ww uv, uw, vw	turbulent fluctuations
$u_i u_j$	Reynolds stress tensor
u^*	wall-friction velocity
w_o	wake deficit
x, y, z	Cartesian coordinates
y^+, z^+	wall coordinates

Greek symbols

δ	boundary layer thickness
δ^*	displacement thickness
λ	wavelength
υ	kinematic viscosity
θ	momentum thickness
ρ	fluid density
τ_w	wall shear stress
ζ	wave elevation
υ	degree of freedom
ω_x	axial vorticity

LIST OF ACRONYMS

AD	analog-to-digital
AIAA	The American Institute of Aeronautics and Astronautics
ASME	The American Society of Mechanical Engineers
CFD	computational fluid dynamics
DA	digital-to-analog
EFD	experimental fluid dynamics
ISO	The International Organization for Standardization
IIHR	IIHR Hydrosciene and Engineering
ITTC	The International Towing Tank Committee
RMS	root mean square
RSS	root sum square
SEE	standard error of estimate
SPIV	stereo particle image velocimetry
PC	personal computer

CHAPTER 1

INTRODUCTION

The dynamics of flows bounded by a wall and a free-surface are decidedly different than those constrained by a wall alone. Turbulent flows bordered by a wall exhibit the canonical two-dimensional boundary layer. With the introduction of a free surface boundary, and possibly waves, the flow characteristics vary up to a depth of the boundary layer thickness or the wave amplitude, whichever is greater. The conditions imposed by the free surface and waves causes the flow to be highly three dimensional and complex. Generally speaking, boundary layers have been studied at great lengths, but little insight has been given to this unique influence of waves and the free surface. Its lack of attention should by no means overshadow its importance in several engineering applications, notably ship boundary layers. Other examples include open channel flows, off shore oil rigs, and manufacturing processes such as paper-making.

The current experiment examines the boundary layer and wake flows of a surface-piercing flat plate with imposed Stokes-wave. Of particular interest, are free surface and wave induced effects on the flow. Attention is drawn to the solid surface and free surface juncture region, a small region bound by a wall, water, and air know to have a complex flow pattern. The study follows a theme of research within a group of the IIHR Hydroscience and Engineering, investigating unique flow phenomenon occurring in ship boundary layers and wakes. The related research topics include documenting breaking wakes, wave-induced separation, free surface damped turbulence, and bubble entrainment. This assembly of research emerged from the desire to understand the flow physics and the continuing need for benchmark data for computational fluids dynamics, CFD, validation. The research and discussions of this flat plate boundary layer and wake flows rely upon and complement previous studies using both experimental fluid dynamics, EFD, and CFD techniques. Earlier EFD and CFD analysis, using the same

model and conditions focused on wave effects on the boundary layer. Modern measurement techniques and sophisticated free surface models have only recently been able to observe and simulate free surface effects and the juncture flows. The current experiment confirms what is already known about wave effects on boundary layers and wakes, but more importantly expands the current knowledge base of free surface effects and the juncture flows.

The motivation for this work is for reasons both of scientific interest and practical application. The physics of juncture flow are weakly understood. Researchers refute, as much as they confirm, the behavior of the juncture flows. Until further documentation, juncture flows shall be considered unresolved and by shear curiosity should garner attention. The practical importance of the study is for validation of CFD codes.

Hopefully upon the completion of this study, several objectives are met. First, a comprehensive review of similar boundary layer and wake studies is discussed. The author aims at not only documenting other researchers finding and results, but to form connections between the past and present work. A "compare and contrast" technique is employed when appropriate. Second, inclusive measurements of the boundary layer and wake flow field, along with the wave field, are presented. Previous flow field techniques relied on point-by-point measurements to capture the flow, the current study employees a state of the art system that performs palm of hand-sized flow field measurements. This comprehensive data set will leave less to interpretation and provides a more global picture of the flow. The dimensionless boundary layer, wake parameters, and turbulence characteristics will be indentified along with the important flow features associated with wave effects, free-surface effects, and the juncture flow. The results will be compared to benchmark data and related studies. Third, perform rigorous uncertainty assessments for all measurements following the most up to date procedures. Finally, document the flow features in sufficient detail for validation of CFD codes.

The test apparatus chosen for the study is one that is simple, but inventive, and allows a researcher to break down the flow conditions. Any generic ship model will not do, as it would impart a pressure and wake field that would otherwise complicate measurements and its effect would be dependent on the hull form. The requisite for such a fundamental study, applicable to a variety of ship flows as well as those not nautical, is a model of basic geometry. The chosen test model is a surface-piercing thin flat plate. In order to examine wave effects, a Stokes wave is superimposed on the plate. A submerged foil is placed upstream of the flat plate and generates this harmonic wave pattern in its wake. The plate and foil are fixed to the underside of a carriage and are towed. The plate, foil, and wave move as one, with the celerity of the wave train equal to the towing speed. The wave is intended to be as two-dimensional as possible. The carriage speed and depth of the foil are controlled to create a wave pattern of wavelength equal to the plate length.

The topography of the wave field, the wave-driven flow, boundary layer, and wake are of importance here. The wave field and flow are inspected qualitatively using video and photograph. Wave gauges are used to measure the wave elevations surrounding the starboard side of the plate. Wave elevations are gathered across a coarse grid to identify the global wave pattern and are accompanied by multiple sets of finely spaced measurements along several transverse outlines. Stereo particle image velocimetry (SPIV) is used to measure the flow velocities. SPIV measurements are taken at several locations along the plate and wake in order to analyze wave effects at all sections of the wave; the peaks, troughs, and inflection points of a wave have their unique effect on the flow.

To better understand juncture flows, a basic description of the of near-plate flow field must be discussed. Figure 1 shows a definition sketch of the region of interest. The region can be divided into five regions:

I. Stokes wave/outer flow

II. Deep boundary layer

III. Intermediate boundary layer

IV. Juncture region boundary layer

V. Free surface boundary layer

VI. Meniscus boundary layer region

In Region I, the viscous effects are negligible, and in the absence of waves, the flow is uniform. With waves, the flow dynamics oscillate. The wave will cause the streamwise velocity component to oscillate about the wave speed, and the vertical velocity component will fluctuate about zero; the piezometric pressure gradients fluctuate in much the same behavior. Wave effects are more pronounced near the free surface. Region II exists at a sufficient depth where free surface and wave effects are negligible. The deep boundary layer is canonical and can be estimated using any thin-boundary layer equations. The intermediate boundary layer region is the connection between the deep boundary layer and the juncture boundary layer. Region IV is the area where the wall, air, and water meet. This spot is also called the mixed-boundary region or corner region, but herein will be labeled the juncture region. The juncture region is of primary importance because the flow is rather complex. The juncture region is subject to the external-flow pressure field and the boundary conditions of the free surface and the wall. Similar to corner flows of other kinds, i.e. solid wall to sold wall and solid wall to shear free boundaries, these geometric configurations initiate a small degree of streamwise vorticity. The size, strength, and rotational direction of the vortex pattern of solid wall to free surface flows have been the topic of common debate. Also disputed, are the trends of turbulence in and surrounding the region. It is generally agreed that the free surface has a damping effect on turbulence, but the direction that turbulence is redirected and the levels it is reduced are not well established.

CHAPTER 2

BACKGROUND

2.1 Overview of literature review

Limited amount of literature is available on wave-effects on boundary layers and wakes. Much of what is known about this situation was studied at the IIHR Hydroscience and Engineering. In the past quarter of a century, the institute has performed several tests of the same basic model, both computationally and experimentally, yet the focus has changed each time. This chapter reviews previous literature from the institute, and to provide an outside perspective, discusses similar work performed elsewhere. In view of the fact that the present work is intended for CFD validation, numerical studies are also cited. A review of the most influential study is discussed first: the direct numerical simulation of a surface piercing flat plate with and without waves by Stern (1986). Afterwards, the literature review is divided in experimental and numerical sections, each section is organized chronographically.

The study that prompted this experiment was that of Stern (1986). Stern performed direct numerical simulation of a surface-piercing plate with and without waves for laminar and turbulent conditions. Stern's proceedure was to start with a basic geometry, a thin flat plate, and modeling the flow with proven thin-boundary-layer equations. Then, in a progressive manner, complexities were added to the simulation such as wave equations and turbulence models. The technique made it possible to isolate and identify the contributing features of the flow. Stern's laminar flow solutions, at a Reynolds number of Re = 20,000, examined four wave steepnesses, Ak = 0.01, 0.1, 0.2, and 0.3. Laminar solutions show the boundary layer thickness, ζ, was largely influenced by the pressure gradients induced by the external flow. Favorable streamwise piezometric pressure gradients accelerated the streamwise flow across the plate, thus thinning the boundary layer. Similarly, favorable vertical piezometric pressure gradients

would drive the flow down along the plate, also thinning the boundary layer. At greater wave steepnesses, the pressure gradients are larger in magnitude, lending to greater effects on the boundary layer thickness. Along the plate and downstream of a wave trough, wave-induced separation was observed for all but the smallest wave steepness. Separation appeared to be a requisite for a grossly thickening boundary layer but also coincided with a region of adverse streamwise and vertical piezometric pressure gradients. Stern noted that a better indication of separation occurs when the streamwise shear stress component becomes $\tau_w \leq 0$. In examining the streamwise velocity profile, for all wave steepnesses, a Blasius profile exists for much of the plate.

Stern also presented turbulent flow solutions at a Reynolds number of 5×10^6. Turbulent flow results are consistence with those of laminar solutions. The most noticeable difference is the lessened three-dimensionality of the flow, as the turbulence dampened cross flow. The reduction in cross flow inhibits wave-induced separation for all but the largest wave steepness condition. Stern concluded that waves have a pronounced effect on the boundary layer, largely attributed to external flow pressure gradients. The external flow pressure gradients have an influence up to a depth of about one-half the wavelength.

2.2 Experimental work

Stern's simulation prompted a similar experimental study documented by Stern et al. (1987 and 1989). The aim of the experiment was not only to verify the computational results, but based on the general lack of experimental data on the issue, to obtain physical measurements on the flow. The boundary layer was examined on a 2.5 m-long towed surface-piercing flat plate in a towing tank. Waves were generated from a horizontal submerged foil, upstream of the flat plate. The depth of submergence of the symmetric foil was controlled to generate waves of various steepnesses. The foil was placed near the free surface for large wave steepnesses and at its lowest position where it had no

observed effect on the free surface. Both the flat plate and the foil are towed on the underside of a drive carriage. The wave train generated by the foil travels at the same speed as the plate. The foil geometry and mounting assembly were based on experiments of Salvesen (1969) who investigated high-order wave perturbation theory.

Tests were conducted at a carriage velocity of U_c = 1.37 m/s, resulting in a Reynolds number, based on wavelength, of $Re = 1.64\times10^6$. Measurements were performed with a three-hole pitot probe that provided velocity information in the streamwise and vertical directions. Three wave steepnesses were measured Ak = 0, 0.11, and 0.21. For the larger of two wave steepness conditions, the waves were aperiodic, dampening in amplitude downstream of the foil. Dampening was attributed to the flat plate. An unsteady and turbulent free surface region along the plate, with proximity to a wave inflection point, indicated wave induced separation. The region was wedge shaped with a 20° angle relative to the flat plate. The separation was characterized by flow reversal and free surface vorticity. Stern's earlier turbulent flow calculations did not forecast separation, as separation was not expected until a wave steepness of $Ak \geq 0.035$. Note, Stern's previous laminar solutions predicted separation for wave steepnesses as small as $Ak = 0.10$. Separation is largely dependent on wave steepness since greater wave steepness produces regions of greater adverse pressure gradients. It was noted that Stratfords laminar flow separation criterion was not indicative of the separation point for the turbulent flow tests, having predicted separation far upstream of the true location.

Unfortunately, free surface effects were not examined as the depth of submergence of the pitot probe was no less than $2\cdot\zeta$ relative to the calm free surface. It was believed that the free surface effects penetrate to a depth of $\sim \zeta$ although no such effects were observed. In summary, Stern was able to illustrate the effects of waves on the boundary layer. He also documented wave-induced separation and provided notable insight on a poorly understood phenomenon.

The flat plate foil experiment was revisited four years later and was reported by Stern et al. (1993). The experiment was improved upon by use of a five-hole pitot probe allowing for three-component velocity information. Unlike before, the wake of the flat plate was examined. The flat plate was shortened to 1.2 m and featured a tapered trailing edge for a more streamlined profile. The flat plate boundary layer and Stokes wave results were much like the findings that preceded it, with some subtle differences. One observation was that the tapered trailing edge resulted in a region of slightly adverse pressure giving rise to larger displacement thickness.

Where this research gained ground was on the wake flow findings. Stern observed an inner wake with growth and decay rates noticeably higher than expected. The wake showed a rapid recovery of the streamwise velocity component. High wall-normal velocities were noticed at the trailing edge where the flow tried to fill the void left by the flat plate. The displacement thickness in the wake was far different that the accompanied computational values. The displacement thins in the wake monotonically, comparatively, the simulation values under-shot ζ^* in a non-linear fashion. Along the plate and away from the free surface, the displacement thickness is uniform across all depths. However, in the wake the displacement thickness varies noticeably by depth. In general, the minimum ζ^* was observed at greater depths. In all, this study concluded that wave effects can be more pronounced in the wake than along the body. Wake flows were distinctly more responsive to favorable, as compared to adverse pressure gradients.

Longo et al. (1998) examined the model roughly five years later. This time the focus was drawn to free surface effects and the flow physics of the juncture boundary layer and wake. Tests were performed at slower carriage speeds, $U_c = 0.46$ m/s, without waves, $Ak = 0$. The Reynolds number, based on plate length was $Re = 2.41\times10^5$, and based on momentum thickness, was $Re_\theta = 1.16\times10^3$. The experiment employed a two component laser Doppler velocimeter, LDV. The LDV system was unaffected by the air-water interface moving through the measurement region, a condition that plagued use of

pitot probes in years past. Measurements were made at the flat plate midsection and the near wake. Longo observed free surface effects penetrating to a depth of $1.25 \cdot \delta$. At a depth of $\delta/2$, the boundary layer was thin and then rapidly thickened just below the free surface.

Analysis of the streamwise vorticity illustrated two regions of vorticity of opposite sign in the juncture region. The vorticity region was not unlike the vorticity observed in the corner of a duct where two orthogonal walls meet. In which case, two contra rotating regions form in the corner, separated by the corner bisector. Unlike the combined solid wall juncture, Longo noticed at the juncture the vorticity near the wall is of greater dominance, occupying a more of corner; albeit at a lesser intensity when compared to the vorticity near the free surface. As a means of describing the rotational direction of the vorticity and the turbulence behavior, Longo stated that vorticity near the wall rotates counterclockwise when viewed downstream, transporting high mean-velocity low-turbulence from the outer to inner reaches of the boundary layer. However, the clockwise vorticity near the free surface transports low velocity, high-turbulence fluids from the inner to outer portions of the boundary layer. The two regions of vorticity were identified in the wake of the plate, but of much smaller intensity and size.

The Reynolds-averaged streamwise vorticity equation was utilized to determine the physical mechanism for the streamwise vorticity. The results indicate that production and damping are the most dominate terms, but being opposite in sign effectively canceling out. Anisotropy of the cross plane normal Reynolds stresses was identified at the source of the vorticity

Experimental studies of juncture flow by Grega et al. used flow visualization and one-dimensional LDA techniques (1995) and later progressed using a two-dimensional DPIV technique (2002). In both cases, Grega examined the flow on a vertically orientated plate model semi-emerged in a water tunnel. In his earlier work, measurements were made at a free stream velocity of 0.206 m/s, corresponding to a

Reynolds number based on momentum thickness of $Re_\theta = 1150$. He observed that the near free surface boundary layer was twice as thick as the deep boundary layer. The reported streamwise turbulence intensities near the free surface were less than those in the deep region, noting that the free surface has a damping effect on streamwise turbulence. Grega could not ascertain at what depth free surface effects were negligible but speculated that canonical, two dimensional, boundary layer existed at distances greater than 1000 viscous units below the free surface. In Grega's later study, the experimental setup was similar, except the free stream velocity was reduced to 0.12 m/s, resulting in a Reynolds number of $Re_\theta = 670$. PIV measurements were made in the cross plane to better resolve the non-axial velocity components. Grega noted a vortex pair in the juncture region consisting of a circular vortex ring ~ 60 viscous units in diameter and an elliptical ring having a major axis dimension of ~100 viscous units. The centers of each vortex extend a radial distance 50 viscous units from corner, with a circular vortex located closer to the wall and the elliptical vortex near the free surface. A noticeable peak in the cross-stream Reynolds stresses is seen where the boundaries of the two vortexes meet. Grega noted that highly three dimensional boundary layers exhibited strong cross stream Reynolds stresses, and lack of which is indicative of a two-dimensional boundary layer. Grega then distinguished the rotational flow into vorticity production, transport, advection, mean, and turbulence terms by means of Tennekes and Lumley equation for mean turbulent vorticity. The juncture region was dominated by advection driven vorticity.

The work of Hsu et al. (2000) complements the work of Grega by examining the same water channel based flow, but using a combined PIV and LDV measurement techniques. Hsu observed a reduction in the streamwise and free-surface-normal turbulent fluctuations near the wall and the free surface. Hsu believed that this caused an increase in the streamwise and wall-normal turbulent fluctuations far from the wall.

2.3 Computational work

Stern (1986) was not the first to examine wave effects on a surface-piercing flat plate; the earliest known studies appear to be those by Sachdeva and Preston (1978). The direct numerical simulations of Sachdeva and Preston tested several boundary layer equations, each displaying a wide variety of results. Although their findings lack continuity some conclusions can be made. They illustrated that at a depth of one wavelength from the calm free surface waterline, the wave effects were non-existent and the boundary layer solution was identical to the Blasius solution. Closer to the free surface, all but one boundary layer equation predicts strong wave-induced effects on the boundary layer. The results showed that the boundary layer behavior near the free surface is dominated by pressure gradients caused by waves. Interestingly, the calculations using hodographic techniques captured the increasing shape factor and decreasing skin friction coefficient that exists in a region of adverse pressure gradients at the wave inflection point; while it does not illustrate separation which is known to occur, the results are similar to current experimental and computational observations.

Grega performed a numerical simulation modeling the same water tunnel experiment (1995). The domain was simplified by examining only a section of the wall and the free stream velocity was lower, such that $Re_\theta = 220$. Grega's results show a small, ~100 viscous units in diameter but relatively strong vortex formation in the juncture region. Circumferential maximum velocities were on the order of 1% of the free stream velocity. The vortex was centered roughly ~50 viscous units from the wall and the free surface. Grega defined this vortex as the inner secondary cell. This inner secondary cell was accompanied by a counter rotating vortex that was weaker in terms of is circumferential velocities, but larger in area; this vortex was called the outer secondary cell. This larger vortex was located further away from the juncture, centered ~100 viscous units below the inner secondary cell. Reynolds shear stress distributions showed greater intensity in the regions of the vortex pair, illustrating turbulent transfer of

streamwise momentum in the free-surface normal direction. Grega observed a thickening of the boundary layer at the free surface and attributed it to the outer secondary cell. The outer secondary cell is believed to transport low momentum fluid along the wall, around the inner secondary cell and along the free surface; thus enlarging the boundary layer. The secondary cells were caused by an imbalance of gradients of the wall-normal and free-surface normal turbulent fluctuations. Mean pressure distribution plots showed a mean pressure maxima at the juncture and hypothesized that the high pressure area is the sight of a stagnation point arising from the inner secondary cell.

Stern et al (1993) presented Reynolds-averaged Navier-Stokes calculations alongside their experimental data. Compared to their previous work, (Stern, 1986 and Stern et al 1989) this study included wake flows. The wake flow solutions show good agreement with experimental results and benchmark data everywhere from the near wake to asymptotic region. The similitude is surprising since wake flows generally pose a challenge for simulations, even from seemingly simple flat plate flows. The rapid changes in boundary conditions, velocities, and turbulent production processes test the quality of turbulence models. The simulations showed the characteristic growth of the half width, proportional to $x^{1/2}$ and the centerline velocity defect decay proportional to $x^{-1/2}$.

2.4 Summary of findings

Wave induced pressure gradients have a pronounced influence on the boundary layer and the wake. Wave effects are proportional to the wave steepness and penetrate to depths of about one-half the wavelength. Waves can induce separation at a sufficient wave steepness. The mechanism for separation is the adverse streamwise piezometric pressure gradient and strong upward-driven cross flow.

The documentation and analysis of free surface effect and juncture flows is growing and evolving, the following discusses what has been addressed. Free surface

effects penetrate to depth roughly equal to the boundary layer thickness. Free surface effects cause the boundary layer to thin at a depth below the free surface of about one-half the boundary layer thickness and rapidly swell just below the free surface; but results vary. Of the results that show thinning boundary layers, it is generally agreed that it is caused by streamwise vorticity driven by anisotropic Reynolds stresses. Typically, two contra-rotating vortices are detected, one that transports low energy fluid away from the free surface down along the wall, while directing high momentum fluid along the corner bisector to the wall. The other vortex moves high momentum fluid closer to the wall and then across the free surface. The strength and size of the vortices vary, but in general, tangential velocities are on the order of < 5% of the streamwise velocity and vortex core diameter is about one-third the boundary layer thickness. The vortices are asymmetric, relative to the corner bisector, illustrating the different boundary conditions of the free surface and those of the wall.

There are challenges preventing a more complete understanding of the juncture region physics. EFD researchers are faced with the difficultly of resolving the small turbulence and vorticity levels, especially right below the free surface. CFD turbulence models cannot accurately predict the mechanism for redistributing free-surface normal turbulence. From a computational modeling perspective, it is critical to know the location and intensity of the anisotropic flow-herein lies the collaboration required between the EFD and CFD fields.

CHAPTER 3

TEST DESIGN

3.1 Facility and coordinate system

Tests are conducted at the IIHR Hydroscience and Engineering towing tank facility. The tank is 100 m long, 3.05 m wide, and 3.05 m deep. As shown in Figure 2, the tank is equipped with automated wave dampeners and drive carriage. The wave dampeners consist of a string of floating plastic disks placed longitudinally along the walls of the tank. The drive carriage chassis suspends the test model below and carries the operator cabin above. The drive carriage is instrumented with two data acquisition computers, speed circuit, SPIV system, and servo wave gauges.

A fixed, right-handed Cartesian coordinate system is established at the intersection of the flat plate leading edge and the waterplane. The *x*-, *y*-, and *z*-axis extend in the downstream, transversely to starboard, and upward as shown in Figure 3. The axes of the coordinate system are normalized with the flat plate length L and are denoted (x, y, z). The following equations are the normalized location quantities.

$$x = \frac{X}{L} \tag{1}$$

$$y = \frac{Y}{L} \tag{2}$$

$$z = \frac{Z}{L} \tag{3}$$

3.2 Model

The experimental model and drive carriage are shown in Figure 4. The model consists of a vertically-oriented surface-piercing flat plate and horizontal submerged foil towed underneath the drive carriage. The top edge of the flat plate is sandwiched between two angled sections of aluminum, each 1 m in length, that bolt to a U-channel beam connected to the drive carriage. Elongated holes in the beam allow the longitudinal

position of the plate to be adjusted. The flat plate is aligned along the centerline of the drive carriage, which coincides to the tank centerline. The flat plate is made of Acrylic and has thickness, length, and height dimensions of 12.7 mm, 1200 mm, and 800 mm respectively. The leading edge is rounded to a radius of 6.35 mm and the trailing edge is tapered to a 2 mm thickness; the taper is 210 mm long. The draft of the plate is 520 mm. A row of turbulent-stimulating cylindrical studs are placed 60 mm aft of the leading edge; the studs are 3.2 mm in diameter, 1.6 mm in height, with a 9.5 mm spacing. The stud specifications are in accordance with the recommendations by the 23rd ITTC (ITTC, 2002). The flat plate is braced to prevent vibration. The brace is constructed of 50.8 mm square aluminum tubes bolted to the carriage and connected to the flat plate via four rod ends. The brace is situated 100 mm above the waterline.

The fiberglass foil nearly spans the width of the tank. The foil is symmetric with a chord of c = 332 mm and 114 mm maximum thickness. The foil is supported by aluminum endplates which control the depth of submergence. The endplates slide vertically within a grove formed within two sidewall plates. The sidewall plates measure 3m in length, 1.5 m in height, and 12 mm in thickness. The sidewall plates have an aluminum fore section, with a tapered leading edge, and an Acrylic mid and aft section. The foil and sidewall plate configuration is designed to generate waves that are two-dimensional, with as few disturbances as possible. A horizontal distance of 770 mm is maintained between the leading edge of the flat plate and the trailing edge of the foil.

3.3 Test Conditions

The conditions for the experiments are based on Stern et al. (1989 and 1993) along with Kang et al. (2008). A summary of the test conditions, measurements, and measurement locations are documented in Table 1 and Table 2. Tests are conducted at one carriage speed, U_c = 1.372 m/s, and two wave steepnesses, Ak = 0 and 0.21. The Froude number and Reynolds number are Fn = 0.4 and $Re = 1.64 \times 10^6$, respectively.

The term Ak represents the product of the wave amplitude, A, and the wave number, k. The wave amplitude reflects the average wave amplitude at wave crests (x = 0 and 1.0) and troughs (x = 0.5 and 1.5). The wave number is equal to $k = 2\pi / \lambda$, where λ is the wavelength. The depth of submergence of the foil is adjusted to control the wave steepness. The foil is submerged to a depth of d = 0.77 m (or non-dimensionally expressed as the ratio of depth and chord length, d/c = 1.39) to generate the medium steepness wave, Ak = 0.21. The medium steepness wave condition has a wave length of λ = 1.2 m, equal to the plate length. The plate is positioned longitudinally such that the leading and trailing edges coincide with the second and third wave crests, the first wave crest appears directly above the foil. The foil is lowered further to d = 0.92 m (d/c = 2.77) to create a zero steepness wave. The foil is not removed from the test setup for Ak = 0 since free surface disturbances are lessened for the foil deeply submerged, than for the foil removed (noted by Stern et al 1989 and 1993, Longo 1998). Additionally, the difficulty in handling the foil discourages frequent disassembly.

3.4 Data acquisition and reduction methodology

This section provides a general overview of the measurements performed and equations of the resultant quantities. The three main measurements are the carriage speed, wave field, and the flow field.

3.4.1 Carriage speed

The carriage speed indicates the flat plate's velocity relative to the calm water. However, the coordinate system and frame of reference are relative to the flat plate. Relatively speaking, the flat plate's velocity is then zero and the fluid upstream of the model travels at the carriage speed. The carriage speed is recorded for all tests, for those involving flow field measurements the carriage speed is used to nondimsionalize velocity information.

3.4.2 Wave field

Wave field data is taken in the horizontal *x*-*y*-plane. Wave elevations, made in the z-direction, are measured relative to the calm free surface. Wave elevations are normalized with the plate length L, and are represented as ζ.

$$\zeta(x,y) = \frac{z\,(x,y)}{L} \tag{4}$$

3.4.3 Flow field

For the flow field tests, instantaneous three-dimensional vector fields are collected from a series of two-dimensional planes. At the same time, the carriage speed is acquired. Raw instantaneous velocity vectors (u_{ri}, v_{ri}, and w_{ri}) are normalized with the instantaneous carriage speed U_{ci}, resulting in normalized velocity components (u_i, v_i, and w_i).

$$u_i = \frac{u_{ri}}{U_{ci}} \tag{5}$$

$$v_i = \frac{v_{ri}}{U_{ci}} \tag{6}$$

$$w_i = \frac{w_{ri}}{U_{ci}} \tag{7}$$

In the following discussion, the angular brackets ⟨ ⟩ denote an average over time and a prime denotes fluctuations with respect to the mean resolved quantity. The time average of u_i, v_i, and w_i are expressed as

$$\langle U \rangle = \frac{1}{N}\sum_{i=1}^{N} u_i \tag{8}$$

$$\langle V \rangle = \frac{1}{N}\sum_{i=1}^{N} v_i \tag{9}$$

$$\langle W \rangle = \frac{1}{N}\sum_{i=1}^{N} w_i \tag{10}$$

where N represents the number of samples; the maximum number of samples is 1500 or 375 (depending on the test condition), but due to dropouts of spurious vectors, the estimated average number of samples per grid point is round 1350 and 325, respectively.

The fluctuations in a velocity is equal to the difference between the average and instantaneous velocity components

$$u' = u_i - \langle U \rangle \tag{11}$$

$$v' = v_i - \langle V \rangle \tag{12}$$

$$w' = w_i - \langle W \rangle \tag{13}$$

The average fluctuations of *u*', *v*', and *w*' are equal to zero, to better characterize average fluctuations, the mean–square value is calculated by

$$\langle uu \rangle = \frac{1}{N}\sum_{i=1}^{N}[u_i - \langle U \rangle]^2 \tag{14}$$

$$\langle vv \rangle = \frac{1}{N}\sum_{i=1}^{N}[v_i - \langle V \rangle]^2 \tag{15}$$

$$\langle ww \rangle = \frac{1}{N}\sum_{i=1}^{N}[w_i - \langle W \rangle]^2 \tag{16}$$

These quantities are often referred to as Reynolds normal stresses. The turbulent kinetic energy is half of the sum of the Reynolds stress and is shown as

$$\langle TKE \rangle = \frac{1}{2}(\langle uu \rangle + \langle vv \rangle + \langle ww \rangle) \tag{17}$$

The covariance of the Reynolds stress, known as the Reynolds shear stresses are given by

$$\langle uv \rangle = \frac{1}{N}\sum_{i=1}^{N}[u_i - \langle U \rangle]\,[v_i - \langle V \rangle] \tag{18}$$

$$\langle uw \rangle = \frac{1}{N}\sum_{i=1}^{N}[u_i - \langle U \rangle][w_i - \langle W \rangle] \tag{19}$$

$$\langle vw \rangle = \frac{1}{N}\sum_{i=1}^{N}[v_i - \langle V \rangle][w_i - \langle W \rangle] \tag{20}$$

The term, $\langle uv \rangle$, is commonly referred as the turbulent shear. The axial vorticity is a quantity of interest and is calculated by

$$\langle \omega_x \rangle = \frac{\partial \langle W \rangle}{\partial y} - \frac{\partial \langle V \rangle}{\partial Z} \tag{21}$$

Note that the ⟨ ⟩ symbol is omitted hereafter for simplicity.

A boundary layer is defined by the slow moving fluid adjacent to a solid surface. The location where the local velocity is 99% of the freestream velocity defines the

boundary layer thickness. Measuring the small velocity differences poses a challenge to experimentalists so the momentum, θ, and displacement, δ^+, thickness are used, where

$$\theta = \int_0^{y_{max}} \frac{\bar{u}}{U_e}\left(1 - \frac{\bar{u}}{U_e}\right) dy \tag{22}$$

$$\delta^* = \int_0^{y_{max}} \left(1 - \frac{\bar{u}}{U_e}\right) dy \tag{23}$$

$$H = \frac{\delta^*}{\theta} \tag{24}$$

The term U_e denotes the edge velocity and H is called the shape factor. Equalities 22, 23, and 24 come from the momentum-integral relation of Karman.

In turbulent boundary layers, the majority of the boundary layer is turbulent, yet a very thin laminar sublayer, called the viscous sublayer, exists next to the wall. An overlap layer is the region that bridges the inner viscous sublayer to the outer turbulent layer. The logarithmic law of the wall, or simply log law, is used to plot the dimensionless velocity profile of the overlap layer. The log law is defined as

$$\frac{U}{u^*} = \frac{1}{\kappa}\ln\frac{yu^*}{\nu} + B \tag{25}$$

where

$$u^* = \left(\frac{\tau_w}{\rho}\right)^{1/2} \tag{26}$$

$$\tau_w = \rho\upsilon\left(\frac{\partial \mathrm{U}}{\partial \mathrm{y}}\right)_{\mathrm{y}=0} \tag{27}$$

$$\kappa \approx 0.4$$

$$B \approx 5.5$$

The inner law variables are then,

$$u^+ = \frac{U}{u^*} \tag{27}$$

and

$$y^+ = \frac{yu^*}{\upsilon} \tag{28}$$

The new terms introduced in Equations 25-28, notably u^*, u^+, and y^+ characterize the viscous scales of the boundary layer. The term y^+, is the distance from the wall in viscous lengths, also called the wall units. The term u^*, is the wall-friction velocity and reflects the shear stress in units of velocity. The wall-shear stress magnitude, C_f, is calculated using the friction velocity, u^*, where

$$C_f = \frac{2u^{*2}}{U_c^2} \tag{29}$$

The exact y^+ location of the data set and precise shear stress at the wall, τ_w, is difficult to measure. An error in calculating τ_w, has large implications on the friction velocity, u^* and the wall-shear stress magnitude, C_f. The method for determining the precise y^+ and u^* values is adopted from Kendall and Koochesfahni (2008). The method compares the measured data to the benchmark Musker profile in the region of $35 < y^+ < 350$. The results of the method are correctional values of y^+ and u^* that best fit the benchmark profile. The former correctional value is used to better align the y-location of the data set and the latter correctional value is used to adjust u^*, then used to calculate C_f. The log law values of Musker are compared to the measured data using a residual function. This function is used to determine appropriate u^* and y^+ correctional values. The residual function is

$$\Phi = \frac{1}{N}\sum_{i=0}^{N} \frac{|u_{i\,data}^{+} - u_{i\,Musker}^{+}|}{u_{i\,Musker}^{+}} \tag{30}$$

where $u_i^{+}{}_{data}$ corresponds to the inner law variable values located at y_i^+, obtained from the measurements using estimated values for u^* and y_i^+. The expression $u_i^{+}{}_{Musker}$ corresponds to the inner variable values documented by Musker (1979). The derivate of the residual function is set to zero and is then used in a two-parameter set of optimization equations. An iterative FORTRAN routine determines the set of u^* and y^+ values that minimize the residual function.

The advantage of inner law analysis is that boundary layer velocity profiles of various pressure gradients can be compared on the same plot. Effects of the pressure gradient appear in inner law variable plots when $y^+ > 350$.

At the flat plate trailing edge, the starboard and port side boundary layers coalesce and form the wake. The flow transitions from wall shear to free shear. The fluid in the immediate vicinity of the plate has zero velocity but later assumes some finite value along the wake centerline. The relatively slower moving fluid entrained by the flat plate is known as the wake depression. The difference in velocity between the outer flow and the wake flow is denoted the velocity defect. Further downstream, the width of the wake depression increases as slow moving wake flow moves away from the wake centerline, mixing with the faster outer flow. The interaction decreases the velocity defect.

The wake is characterized by the wake half width, b, which is measured from the point of the maximum velocity defect, w_o, at the wake centerline, to a distance where the velocity is ½· w_o. For zero external pressure gradient flows and constant free stream velocity, the wake behaves asymptotically, with an increase in the half width and decrease in the maximum velocity moving further downstream of the flat plate. This well-known behavior is approximated by the following relations

$$b \propto x^{1/2} \text{ and } w_o \propto x^{-1/2} \tag{31}$$

These half-power growth and delay estimates are used to measure the wake's asymptotic approach to mean flow conditions. The similarity variables that define the wake are $(b/\theta)^2$, $(w_o/U_c)^2$, and (x/θ), and the relationship is expressed by the equations of Sclichting (1968).

$$(b/\theta)^2 = 16\left(\frac{\nu_T}{U_\infty \theta}\right)\left(\frac{x}{\theta}\right)\ln 2 \tag{32}$$

$$(U_c/w_o)^2 = 4\pi\left(\frac{\nu_T}{U_\infty \theta}\right)\left(\frac{x}{\theta}\right) \tag{33}$$

where υ_T is the turbulent eddy viscosity. The value of $\frac{\nu_T}{U_\infty \theta}$ is assumed to be 0.032 based on the work of Ramaprian et al. (1982) and Pot (1979). Figure 9 illustrates boundary layer and wake parameters are shown in a definition sketch.

3.5 Measurement systems and calibration procedures

3.4.1 Carriage speed

Carriage speed is measured by tracking the angular velocity of one of the drive carriage wheels. The carriage speed is indicated by the product of the angular velocity and the wheel circumference. A belt and pulley system connects an optical encoder to the wheel axis. Rotation of the carriage wheel causes a disk within the encoder to rotate. The gear reduction is 1:1. The disk has 8000 equally spaced perforations around its peripheral, and a pulse counter senses the perforations that pass in a 100 ms time base. A precision vernier caliper is used annually to measure the diameter of the wheel, which is taken at several locations around its perimeter and averaged. The diameter of the wheel D = 0.318 m. The carriage speed is calculated using the equation

$$U_c = \frac{c}{8000\,\Delta t}\pi D \tag{34}$$

where c is the number of perforations the pulse counter detects in the time base Δt.

The carriage speed is monitored using the encoder, digital panel meter, and digital-to-analog card. The digital panel meter provides instantaneous velocity readouts of the carriage speed. The operator adjusts a speed-control dial on the carriage until the correct speed is reached. The panel meter produces an analog voltage output proportional to the carriage speed. This voltage is recorded by one of two computers, each with an analog-to-digital card, as a means of logging carriage speed.

Calibration of the speed circuit is periodically conducted in the IIHR electronics shop. A precision frequency generator, replicating the output of the encoder, sends

square wave voltage signals at prescribed frequencies to the panel meter. The system is then adjusted such that the indicated speed and output voltages reflect the simulated speed produced by the frequency generator.

3.4.2 Wave gauge

Wave elevations are measured with Kenek servo-type wave gauge(s). Each wave gauge has a thin needle-tipped electrode that remains in constant contact with the water surface. The electrode is driven by a servo-motor as to attain a constant electrical resistance between the needle tip and the ground electrode. The resistance is affected by the depth of submergence of the needle; the desired resistance occurs when the needle just breaks the surface of the water. Fluctuations of this resistance, caused by waves or ripples striking the needle, offset the voltage across a bridge circuit. A servo amplifier forces this voltage to zero by driving the servo motor up or down until the needle is at the proper elevation. Mechanically connected to the servo-motor and needle drivetrain is a rotational potentiometer that tracks the relative displacement of the needle. The potentiometer's signal is amplified to give a voltage output linearly dependent on the needle displacement. The hardware consists of two model SWT-10 sensors, two model SWT-30 sensors, four model SW-101 amplifiers, four earth ground wires, and 14-bit analog-to-digital card, and laptop computer. Figure 5 shows the wave gauges and related hardware. The sensor has a range of ± 50 mm, 0.1 mm resolution, and 700mm/s maximum linear needle speed. The sensor has a 2.2 Hz frequency response for 50 mm amplitude waves, but is capable of 100 Hz measurements for amplitudes up to 1 mm. Table 3 lists wave gauge specifications.

The wave gauges are calibrated statically end-to-end by moving the probe incrementally on a linear, vertical traverse. The probes move a total distance of 100 mm in increments of 5 mm. Voltage and displacement measurements are recorded for each step. A linear regression voltage-displacement relationship is established after each

calibration; the slope of this calibration curve is used as a scale factor for wave elevation measurements.

3.4.3 SPIV

A stereo particle image velocimetry system is used to measure the velocity field along the starboard side of the flat plate. The system captures a three-dimensional flow field in a two dimensional space. The measurement area is normal to both the plate and free stream direction. The SPIV technique measures the velocity field by tracking the time-variant displacement of particles. Particles are dispersed into the tank water prior to each run. Silver-coated hollow glass spheres, with an average diameter of 14 μm, are chosen as the particle material based on its neutral buoyancy and strong light scattering behavior. A double pulsed underwater laser generates a sheet of light which illuminates the particles in suspension. A dual-headed Big Sky Nd:Yag laser generates light of 532 ηm wavelength and a pulse energy of 80 mJ. Each laser head operates at a 5 Hz repetition rate with a pulse delay of 150 μs. The pulse delay is carefully chosen based on the light sheet thickness and the mean flow velocity. The beam is steered underwater through a tube into an enclose containing a cylindrical lens that manipulate the beam into a diverging light sheet; the light sheet thickness and the divergence angle can be adjusted. Two cameras contained in submersible enclosures record images of light scatter from particles illuminated by the light sheet. Each camera is a Redlake MegaPlus II charge coupled device, CCD, having 1200 by 1600 pixel resolution, mated to single-axis Shiempflug adaptor and a Canon EOS 100 mm f/2 lens; Shiempflug angles, focus, and aperture are controlled remotely via computer. The laser and cameras are controlled using DaVis v.7.1 software. A photograph of the camera and laser equipment is shown in Figure 6 (a) and (b) respectively; table 4 lists SPIV specifications.

Calibration of the SPIV requires information of the camera positions in space relative to the light sheet, the optical axis location, focal length, Scheimpglug angle, and

relationship between the dimension of the image plane and object space. The calibration is performed with a two-tier calibration plate. The target face of the calibration plate measures 100 mm square with a tier-to-tier distance of 2 mm. This face is placed coincident to the light sheet and the measurement region of interest. An image of the calibration plate, showing about 140 dot markers, is obtained from each camera. A user then identifies a series of three identical dot markers on each image. The selected dots locate the local origin of measurement and the direction of the transverse, y-axis, and vertical, z-axis. A camera pinhole model is used to obtain two mapping functions, one for each camera. The mapping function is used to relate the two-dimensional image (camera) plane to the three-dimensional measurement space (calibration plate). Mapping function matrix for camera 1, $\boldsymbol{M_1}$, is used to relate world coordinates $\boldsymbol{X_W} = (X_w, Y_w, Z_w)$ (analogous to (x, y, z)) to camera pixel coordinates $\boldsymbol{x_1} = (x_1, y_1)$ where

$$(x_1, y_1) = \boldsymbol{M_1}(X_W, Y_W, Z_W) \tag{35}$$

similarly for camera 2,

$$(x_2, y_2) = \boldsymbol{M_2}(X_W, Y_W, Z_W) \tag{36}$$

Herein subscript 1 and 2 denote the parameters relating to camera 1 and camera 2 respectively; to eliminate redundancy only parameters relating to camera 1 are discussed. The SPIV data acquisition software is programmed to indentify the calibration plate, in doing so, it can then determine the location of all the dot markers in world coordinates. Additional information must be obtained to identify each camera's perspective of the measurement region and to determine the local magnification factor. The position of the camera must be identified to extract the intrinsic parameters (focal length and optical center) and extrinsic parameters (rotation and translation of the camera). The camera coordinates $\boldsymbol{X_{C1}}$ are related to the world coordinates $\boldsymbol{X_W}$ by

$$\boldsymbol{X_{C1}} = \boldsymbol{R_1 X_W} + \boldsymbol{T_1} \tag{37}$$

where $\boldsymbol{R}$ is a 3×3 rotation matrix and $\boldsymbol{T}$ is the translation vector. The focal length is then

$$x_{u1} = f_1 \frac{X_C}{Z_C} \tag{38}$$

$$y_{u1} = f_1 \frac{Y_C}{Z_C} \tag{39}$$

where x_u and y_u come from the undistorted camera pixel coordinates $\boldsymbol{x_u} = (x_u, y_u)$. Omitted is the discussion of the radial distortion terms. Another calibration option is the third-order polynomial model, which has the advantage of being less susceptible to optical distortions. Subtle distortions are known to exist for the current setup as astigmatism effects are common in arrangements where the optical path travels through various media, each with different indices of refraction. While the third-order polynomial model may initially be appealing to remove such effects, it provides no feedback of the camera position, focal length, and other camera parameters important to researchers.

An additional calibration step is performed to enhance the calibration accuracy by accounting for errors in aligning the calibration plate relative to the light sheet. This step may also negate effects caused by the buffeting and deflection of the enclosures as they move through water. This calibration refinement uses test images, not those of the calibration plate, and dewarps the images using the mapping function. Next, a cross-correlation is performed of camera 1 and 2 images jointly. Meaning images from camera 1 and 2 taken at the same time are correlated, compared to the typical correlation process performed on images from the same camera separated in time. Particle pairs are identified in relatively large interrogation windows and are assigned global coordinates from each camera. The coordinates will be identical if the calibration plate is exactly aligned with the light sheet and if the relative location of the light sheet and the cameras does not change. Such a situation is highly unlikely. Discrepancies of the coordinates are used to triangulate the distance between the plane were the calibration was performed and the light sheet plane. The collection of these distances is used to identify a plane which is precisely aligned to the light sheet plane. The mapping function is adjusted to

reflect this new plane and a new origin is created. The process is performed three times iteratively, until the average disparity between the coordinates converges to sub-pixel levels, a distance of roughly 0.07 mm.

3.6 Data acquisition and reduction procedures

3.6.1 Data acquisition setup

The wave gauge(s) is suspended above water, starboard of the plate. A rail system on the underside of the drive carriage allows the gauge to be manually traversed in the x-direction; two automated traverses control movement in the *y*- and *z*- directions. The traverse aligned in the *z*-direction is primarily used for calibrating. Figure 7 is a diagram of the wave gauge setup for wave field measurements. The wave gauge(s) and its amplifier(s) are connected to a remote 16 channel, 14 bit analog-to-digital card and data acquisition computer aboard the drive carriage.

Wave elevations can be classified into three groupings consisting of 1) global wave field measurements, 2) local wave field measurements, and 3) precision test measurements. The global wave measurements describe a grid-like distribution of measurements surrounding the entire starboard side of the plate, for the $Ak = 0$ and $Ak = 0.21$ condition. The purpose of this data is to obtain a large-scale survey of the wave field caused by Stokes-wave and the plate. These measurements are made using 3 or 4 wave gauges simultaneously. Measurements are made at 27 *x*-positions and 30 *y*-positions, resulting in a total of 810 equally spaced points. The grid domain is a slightly irregular shape for the $Ak = 0.21$ case, where a probe was removed from service amid testing allowing for only 24 *y*-positions to be measured; the total number of grid points amounted to 726.

Local wave field measurements are made up of readings taken near the plate at six *x*-positions, at $x = 0.25, 0.50, 0.75, 1.00, 1.25$, and 1.50. At each *x*-position, 27 measurements were made, extending transversely from the plate, from $y = 0.00167$ to

0.075. The locations of these measurements correspond to those made by the SPIV system. Often times the SPIV system photographs water and air regions and cannot decipher between the two. These local wave field measurements are used to delineate the air-water interface and mask out the SPIV data in the air region.

Precision test measurements are used to estimate the repeatability of wave gauge data. These measurements were conducted at a wave steepness of $Ak = 0.21$. A series of 10 measurements, at a single point, are used to make a single repeatability estimate. Precision tests are conducted at 12 locations, corresponding to two y-locations per station.

For both zero and medium steepness conditions, with and without the foil, SPIV measurements are performed along the starboard side of the flat plate at six axial positions, x= 0.25, 0.50, 0.75, 1.00, 1.25, and 1.50. Figure 8 is a diagram of the SPIV setup for flow field measurements. The SPIV data is required to encompass a cross sectional area of the flow extending roughly $0.6 \cdot L$ (72 mm), in the transverse direction and to a depth of $0.125 \cdot L$ (150 mm), relative to the calm free surface.

The modular SPIV system is arranged on both sides of the plate. The dual headed laser and a camera are placed on the starboard side. These pieces are mounted on an automated two-axis (y, z) traverse and a manual traverse (x-axis). The laser is located above the free surface, and light generated from the heads is steered underwater to a small lens enclosure. The enclosure is placed transverse of the measurement region, about 500 mm from the plate. The camera 1, mounted near the laser, is downstream of the measurement area. Camera 1 is offset from the measurement area 678 mm in the x-direction and 728 mm in the y-direction, resulting in a 995 mm standoff distance. The camera is contained is a vertically orientated, semi-submerged cylindrical enclosure. The camera, Schiemphlug adapter, and lens are kept above the free surface elevation. The camera's initial optical path is directed downward to the bottom of the enclosure to an adjustable mirror and reflected through an underwater window. The mirror is angled 41.5° relative to horizontal allowing the cameras to look upward at an angle of 3.5°. This

upward looking perspective allows an undisturbed viewing of measurement region, free from obstacles in the optical path posed by wave troughs. The mirror is then angled to 38.5° for measurements at station x = 1.00, enabling a more upward looking perspective. On the port side of the plate is camera 2. The camera is mounted on an automated traverse (z-axis) and manual traverse (x-axis). The location of camera 2 is symmetrical to camera 1, relative to the plate's longitudinal centerline. For measurements at axial positions x = 0.25, 0.50, and 0.75 the optical path of camera 2 is through the flat plate. The optical path of the cameras 43° offset from the flat plate centerline, with an included angle of 86°. The Schiempflug angle for cameras 1 and 2 is -6° and 6° respectively. Specifics regarding SPIV recording parameters are shown in Table 5.

The measurement region was aligned normal to the flat plate and stream-wise direction since it can measure the velocity profile in just one test and it also better resolves the vertical and transverse velocity components. A challenge for such a setup is that that pulse delay and laser sheet thickness have to be properly chosen. A balance must be reached from reducing the pulse delay too much such that the signal-to-noise ratio diminishes, but not so long that particle enter and leave the light sheet. The pulse delay for this experiment was 150 μs. Thick light sheets can account for out-of-plane motion but can be associated with somewhat larger uncertainty of the in-plane velocity components and poor resolution of in plane velocity gradients. The light sheet has a 2 mm thickness.

The camera lenses were carefully chosen for this experiment. Past researchers found that short focal length lenses required the camera to be placed too close to the measurement area and disrupting the flow. While long focal length lenses seemed to degrade image quality and may be sensitive to vibrations. A discussion of camera lenses for this type of measurement can be found in Kang et al (2008). To prevent the lens and camera enclosures from buffeting during a test, five stainless steel tie rods were attached to the enclosures. The ends of the tie rods were fixed to under-carriage truss members.

3.6.2 Data acquisition procedures

Much consideration is given to the carriage operation to ensure that steady state conditions exist and data is acquired for an appropriate duration of time. Although the towing tank is 100 m long, only 60 m of the tank may be traversed by the drive carriage. The remaining 40 m. are covered and or obstructed by various equipment. Of the 60 m. available, for precautionary reasons, 10 m at each end of the tank are set aside as a safety buffer. About 2.3 m are used to accelerate the carriage. Once the carriage is up to speed, the carriage travels an additional 14.4 m allowing the drive carriage to hone in on a speed of U_c = 1.372 m/s and enable a steady flow pattern. Only then does data acquisition begin. Wave elevations and SPIV measurements require 15 seconds of time, covering a distance of 20.6 m or 17.2 L. After the completion of data acquisition, roughly 1.6 m are used to decelerate the drive carriage. As a point of reference, if the time a fluid particle spends near the plate is estimated by L/U_c, roughly 16 time scales pass in the course of a single data acquisition cycle. Furthermore, if the time needed for viscous effect to diffuse across the streamlines is of the order $\sqrt{\upsilon L/U_c}$, then approximately 1000 of these time scales go by in a given data acquisition cycle. Carriage runs are made every 12 minutes, allowing wave motion from the previous run to be sufficiently damped. The time interval is determined based on visual inspection and wave gauge readings of the calm free surface.

For wave field measurements, a calm free surface recording is made prior to each run to establish a reference voltage and elevation. Once the carriage is up to speed, data acquisition occurs at 200 Hz for global wave field measurements and 1000 Hz for local wave field and precision tests measurements, carriage speed is recorded at the same time and frequency as those for wave elevation measurements. Point by point measurements are recorded as time histories. The wave gauge probe tips are cleaned periodically to prevent fouling.

For each SPIV carriage run, data acquisition lasts for 15 seconds and operates at 5 Hz, resulting in 75 recordings. A recoding is defined as two pairs of images taken at the same time interval, one pair from each camera. When the plate is installed, twenty carriage runs are made to produce a single boundary layer or wake zone measurement. Either 2, 3, or 4 zones are measured per x-station per condition. A flow field region of interest is illustrated by patching the zones one on top of the other. Each zone is roughly 84 mm ($0.06 \cdot L$) square. The number of zones and the height of the flow field measurement is based on the ability to capture the maximum height of the free surface and reach a depth of $0.125 \cdot L$ (150 mm) below the calm free surface. This allows for measurement of the outer flow and to a depth where comparisons to benchmark data can be made. The carriage speed is sampled all the while. The carriage speed is not recorded continuously, rather it is sampled at the discrete time intervals corresponding to each image acquisition. The carriage speed is sampled at 10,000 Hz for a 0.01 second window of time. The carriage speed is later averaged within each interval and is used to nondimensionalize the flow field vectors measured at the same instant. Blockage caused by the model or measurement equipment are believed to have a negligible effect on the flow, therefore no blockage correction is performed.

3.6.3 Data reduction procedures

A MATLab software program on a Windows PC is used to process global wave field results, and an EXCEL software program is used to process local and precision wave results. Each calm free surface recording is averaged, and this average is subtracted from the subsequent averaged wave elevation recording. The resulting value is scaled from voltage units into metric units using the calibration curve information. Next, the wave elevation is normalized as per Equation 4.

LaVision DaVis v7.1 software is used to process the SPIV recordings. The total number of recordings per zone reflects the product of the number of carriage runs and the

number of recordings per run. For every carriage run, 75 recordings are acquired. For cases with the plate installed, 20 runs are performed (therefore totaling 75·20 = 1500 recordings), without the plate only 5 runs are performed (375 recordings). The collection of 1500 or 375 recordings are processed together. First, each image is rotated and mirrored. Second, images from each camera are dewarped via the mapping functions and the global coordinates are established. This method allows the global size and shape of the interrogation windows to be nearly identical between cameras, thereby corresponding vectors from each camera are positioned at identical global coordinates. Next, a two-dimensional, two component, vector field computation is performed on each pair of images using a 64 by 64 pixel interrogation window, with 75% overlap in the vertical and horizontal direction. Velocity information is obtained by tracking patterns of particles. Similar particle patterns identified in two sequential images from the same camera are called particle pairs. The displacement of a particle pair is measured on a dewarped image whose spatial dimensions are those of measured plane, not of the image plane. The velocity of a particle pair is found by simply dividing the displacement by the pulse delay. A Fast Fourier transform space correlation function, with no zero-padding, is the mathematical means of identifying particle pairs. The amount of overlap of the interrogation window improves accuracy, but subsequently results in a spatially averaged vector field. Vector field computations are performed five additional times with the final three passes using a 32 by 32 pixel interrogation window. Each pass enhances the quality of the correlations because corresponding interrogation windows were displaced by an amount prescribed by the previous correlation. Typically, with each pass there is a decrease in the number of erroneous vectors. As the images are deformed, correlations must be made at non-integer locations where the light intensity is interpolated. While a basic bilinear interpolation scheme is sufficient to estimate this light intensity, a 10 pixel Whittaker reconstruction method is used as a high order, high accuracy means of interpolating.

A peak ratio, range, and median filter are applied to the collection of velocity fields. The peak ratio filter deletes a vector if the likelihood of a given correlated particle pair displacement is weak, i.e. the correlation level of a given displacement estimate must be 30% greater than other displacement estimates. The range filter rejects a vector if either u_{ri}, v_{ri}, and w_{ri} component lie outside the range of 0.75 ± 1.0, 0.0 ± 0.5, and 0.0 ± 0.5 respectively. A median filter rejects remaining vectors if the magnitude of the vector is greater than two times the root mean square value of its neighboring vectors. Deleted vectors are not replaced and blank spots are not filled. Text files of the instantaneous veclocity fields and analog voltage recordings of carriage speed are exported from DaVis.

Four FORTRAN codes are used to process the velocity fields. The first code compiles the pathnames of the velocity fields and carriage speed text files. The second code performs the following tasks. The first task is to assign new nondimensional coordinates to the velocity field data sets. A prescribed x-coordinate is given depending on the station (x = 0.25, 0.50, 0.75, 1.00, 1.25, or 1.50), and the spatial coordinates of the velocity vectors are appointed y and z coordinates nondimensioalized by L. With the velocity field roughly aligned to the specified coordinate system, the next task is to nondimensionalize all instantaneous velocity components by the corresponding instantaneous carriage speed. Next, the mean quantities U, V, W, and ω_x are calculated, followed by the turbulence quantities uu, vv, ww, uv, uw, vw, and TKE. Then, the convergence errors of the mean and turbulent quantities are calculated. The final step of the code is to create four output data files containing all these quantities.

Before further FORTRAN processing, the mean and turbulence data files are inspected using TECPLOT. TECPLOT is used to extract three slices of data taken at constant z locations, z = -0.04, -0.08, and -0.125, a data file is created for each slice. These data files are then processed using the third FORTRAN code. Slice data of the U versus y profiles are transformed into the log law profiles consisting of the inner law variables of u^+ and y^+. Musker fit method is used to find the y^+ offset; see section 3.4.3.

The y^+ value is converted into units, nondimensionalized by L, to offset the y values of the data set; this represents the best known way of aligning the data set with respect to the plate surface. From there, u^* and C_f are determined. The corrected U versus y profile is used to calculate the integral relations δ^* and θ, via the Simpson's Rule. The terms δ^* and θ are used to calculate H and Re_θ. If the profile was retrieved from a wake station, then w_o, b, x/θ, $b/2\theta$, and y/b are determined as well. The code not only generates this parameters, but outputs profiles of 1) U, V, and W versus y, 2) u^+ versus y^+, and 3) uu/u^*, vv/u^*, ww/u^*, and uv/u^* versus y^+.

The final FORTRAN code is used to make adjustments to the contour plots. The contour plots are divided by station, and each station is made up of 2, 3, or 4 data sets, also called zones. Zones are overlaid on another providing a seamless representation of the flow at each station; the overlap of the zones is not averaged. The previously calculated y^+ value from the slice at z = -0.125 is used to translate the corresponding zone in the y-direction. All other zones are manually translated via TECPLOT so that good continuity is observed in the contour levels. All zones are slightly rotated to correct for any misalignment of the data set. SPIV images taken while the drive carriage is stationary, and are used to identify landmarks on the vertical plate edge and the horizontal waterline; the coordinates of the data set are made orthogonal to these landmarks.

CHAPTER 4

UNCERTAINTY ASSESSMENT

Detailed uncertainty assessments are provided for carriage speed, wave field, and flow field measurements, following the ASME PTC 19.1-2005 standards and guidelines (ASME 2005). Initially, an experimental uncertainty analysis methodology is presented, which outlines the procedures and highlights the important terms. The uncertainty for carriage speed, wave field, and flow field will be presented separately.

The ASME 2005 guidelines differ from past guidelines (ASME 1998 and counterpart AIAA 1999) to parallel the ISO Guide (1995). Errors are now classified as either 'systematic' or 'random'; these terms replace the more common definitions 'bias' and 'precision' respectively. Furthermore, the concept of 'standard' uncertainty is introduced and term 'total' uncertainty is superseded by the terms 'combined standard' uncertainty and 'expanded' uncertainty. The uncertainty assessment procedures are based on assumptions of large sample sizes, normal distributions, and a 95% level of confidence.

4.1 Uncertainty assessment methods and procedure overview

A measurement error is the difference between the measured value and the true value. This error consists of two components: random error and systematic error. Random error accounts for the repeatability of the measurements and systematic error reflects a consistent deviation from the true value. Measurement uncertainty is then the combination of the random standard uncertainty due to the random error, and systematic standard uncertainty, due to the systematic error.

If a resultant measurement R, is made of several independent parameters, M_i, such that $R = f(M_1, M_2, \ldots, M_i)$, the uncertainty of each parameter must be factored into the resultant uncertainty. Each parameter's uncertainty is weighted based on its sensitivity on the resultant, the sensitivity is expressed by

$$\theta_i = \frac{\partial R}{\partial M_i} \tag{40}$$

where θ_i is the sensitivity coefficient and represents the partial derivative of M_i with respect to R. The systematic standard uncertainty, b_R, is then shown by

$$b_R = \left[\sum_{i=1}^{M}\left(\theta_i b_{M_i}\right)^2\right]^{1/2} \tag{41}$$

where b_{Mi} is the error or uncertainty of a given parameter. At times, an error or uncertainty that exists for a parameter can be decomposed into a subset of elemental errors, b_{mi}, these are combined in the following manner

$$b_{M_i} = \left[\sum_{i=1}^{m}\left(b_{m_i}\right)^2\right]^{1/2} \tag{42}$$

Random standard uncertainty is calculated using either the single test equation or the multiple test equation. In multiple tests situations, the result is calculated from several sets of measurements, in which case the random standard uncertainty is

$$s_R = \frac{t_{95} s_{\bar{i}}}{\sqrt{M}} \tag{43}$$

where t_{95} represents the coverage factor, $s_{\bar{i}}$ is the standard deviation across the collection of sets, and M is the number of sets. In some instances, multiple sets of measurements are not obtained and the result is based on a single test. The single test precision is then calculated by

$$s_R = t_{95} s_i \tag{44}$$

where s_i is the standard deviation of the set. In most cases, where the sample size is large, M <30, the coverage factor t_{95} = 2. In other situations, the sample size maybe small and an appropriate degree of freedom must be determined based on the Welch-Satterthwaite formula (Nonmandatory Appendix B of ASME 2005)

$$\upsilon_{\mathrm{R}} = \frac{\left[\sum_{i=1}^{I}\left[(\theta_i b_i)^2 + (\theta_i s_i)^2\right]\right]^2}{\sum_{i=1}^{I}\left[\frac{(\theta_i s_i)^4}{\upsilon_{s_i}} + \sum_{i=1}^{m}\frac{\left(\theta_i b_{i_k}\right)^4}{\upsilon_{b_{i_k}}}\right]} \tag{45}$$

where $\upsilon_{si} = N_i - 1$ is the degree of freedom of the random standard uncertainty s_i. The term υ_{bik} is the degree of freedom of the kth elemental uncertainty of the systematic standard uncertainty b_i is approximated by

$$\upsilon_{b_{i_k}} = \frac{1}{2}\left(\frac{\Delta b_{i_k}}{b_{i_k}}\right)^{-2} \tag{46}$$

the quotient is an estimate of the relative variability of the estimate b_{ik} (ISO 1995).

The combined standard uncertainty of a resultant is the combination of the systematic and random standard uncertainties, shown as

$$u_R = [b_R^2 + s_R^2]^{1/2} \tag{47}$$

Lastly, the expanded uncertainty is the combined standard uncertainty extrapolated to the 95% confidence level by

$$U_{R\,95} = t_{95} \cdot u_R \tag{48}$$

4.2 Carriage speed

Uncertainty estimates for the carriage speed are not performed for the current study, but are rather adopted from the work of Yoon (2009) which was conducted at the same facility with identical equipment. Yoon measured the travel time of the carriage using a series of photogates placed a known distance apart. The average velocity calculated with the photogates was compared to the panel meter output; the difference between the two values is the error of the digital panel meter. The systematic standard uncertainty, as ascertained by Yoon, is $b_{Uc} = 0.01$ m/s, or about 0.7% of the carriage speed.

4.3 Wave field

Wave elevation uncertainties are examined for the local and global wave elevation measurements which are accompanied by the precision test wave elevation measurements. Note that the precision test measurements are used solely to calculate the

random error. Equation 4 gives the wave elevation data reduction equation consisting of ζ and normalized positions x and y. In functional form, $\zeta(x, y) = f(x, y, z, L)$. Since ζ is a collection of free surface measurements, directly dependent on z, naturally errors in this direction are most prevalent. Errors in the x- and y-direction are also accounted for. The systematic and random standard uncertainties and combined standard uncertainty of ζ are summarized in Table 6.

The systematic standard uncertainty equation for wave elevation measurements is taken from Equation 41 and is given by

$$b_\zeta = \left[b_x^2\theta_x^2 + b_y^2\theta_y^2 + b_z^2\theta_z^2 + b_L^2\theta_L^2\right]^{1/2} \tag{49}$$

where b_x, b_y, b_z, and b_L are the systematic error in the x-, y-, and z-direction and the plate length respectively. A misalignment of the wave gauge in the horizontal plane is known as a position error. The inaccuracies of the spatial coordinates of the data are of little importance, but the effect of these errors on the final result must be analyzed. Meaning, an error in aligning the gauge in the x- and or y-directions can translate to an error in the wave elevation measurement in the z-direction due to the spatial gradients of the wave field. The wave gauge is positioned in the x-direction using a manual traverse, and y-direction using an automated traverse. The manual traverse has a dial indicator that points to a steel metric tape measure on the underside of the drive carriage, whereas the automated traverse is controlled via a computer and monitored with a digital panel meter. The initial x-position of the wave gauge(s) is determined by placing a carpenter's square against the flat plate. The square identifies a line normal to the plate's centerline at the leading edge, coinciding to the y-axis of the coordinate system. The wave gauge is moved with the manual traverse until the probe tip barely touches the square. The dial reading from the traverse is recorded and all subsequent movements are done via the dial and tape measure. The initial y-position is identified by moving the wave gauge needle inboard, until it is next to the plate. With the gauge located at $y = 0$, the digital readout

display is zeroed. The offset probe tip of the gauge rotates slightly about its axis giving rise to a small movement in the *x*- and *y*-directions. When the wave gauge is installed, it is checked for plum, yet a small systematic error exists for the off vertical alignment. The estimated combined effect of these error sources is estimated at $b_x = 3$ mm and $b_y = 2$ mm, representing the errors in the *x*- and *y*- directions respectively.

The error b_x, is combined with one of two sensitivity coefficients θ_x. For the $Ak = 0$ condition, $\theta_x = 0$ because there are no significant elevation gradients in the *x*-direction. For $Ak = 0.21$, the sensitivity coefficients is determined by taking the partial derivative of second-order Stokes wave equation (Equation 58) with respect to the variable *x*; this determines the gradients of the wave field in the *x*-direction. The product of the b_x and θ_x indicates an error in a wave elevation measurement as a result of an *x*-direction position error. The systematic error b_y, is combined with sensitivity coefficients that are unique for each data point. To determine the wave elevation gradients in the y-direction that account for this small, Kelvin-like wave made by the plate, a central difference scheme is used to define the change of the wave field in the *y*-direction. The result is multiplied by b_y, and reflects an error in the wave elevation caused by this position error. Random errors related to repeated movements of the probe are deemed as negligible, and are omitted from the uncertainty analysis.

The *z*-direction error is made up of several elemental error sources occurring in the calibration and data acquisition steps of the experimental process. The wave gauge is calibrated using an automated traverse aligned in the vertical *z*-direction. A Velmex Bi-Slide traverse uses a lead screw to drive a threaded carriage. An optical encoder tracks the rotation of the lead screw, scales the angular displacement by the pitch of the screw, and displays the displacement of the carriage on a digital panel meter. The encoder has a resolution of 200 counts per revolution and the pitch of the lead screw is 2 mm; the resulting accuracy is ½ (2 mm / 200) = 0.005 mm. The traverse makes 19 moves, in 5

mm increments, to establish a calibration relation. The cumulative error from the accuracy of the traverse and the calibration procedure results in a systematic error of

$$b_{z1} = 5\,mm\sqrt{19 \cdot 0.005\,mm} = 0.1090\,mm \quad (50)$$

The vertical orientation of the traverse is measured with a spirit level. Any errors in this alignment relative to vertical will manifest in the calibration. Since no angular measurement are made, other than the level, the error is estimated at ± 1.00 degrees, and will affect the measured wave elevation as

$$b_{z2} = 48.5\text{ mm} - (48.5 \cos 1.00°) = 0.0070\text{ mm} \quad (51)$$

The wave amplitude of 48.5 mm is the amplitude for a wave of steepmess, $Ak = 0.21$, and therefore is chosen as the scalar for which to analyze this error.

To convert the analog output voltages to elevations, the wave gauge is moved statically end-to-end by moving the probe on a traverse. The data is fit using a linear regression curve. The systematic error that results from the linear approximation takes the form of a standard error estimate (SEE) and is written from Coleman and Steele (1999) as

$$\text{SEE} = \sqrt{\frac{\sum_{i=1}^{N}(Y_i - (a\,X_i + b))^2}{N-2}} \quad (52)$$

A ±2·SEE band about the regression line will contain approximately 95% of the data points and is the confidence interval of the curve fit. The representative systematic error from the curve fit is $b_{z3} = 0.2362$ mm.

Wave elevation data is acquired by an analog-to-digital converter which normally has an error of 1 bit out of an accuracy of 14 bits. The error associated with this conversion is expressed as the quotient of the error in bit and voltage range by the conversion accuracy. This voltage is translated into millimeters using the slope of the calibration.

$$b_{z4} = \frac{1 \cdot 20}{2^{14}} \cdot 9.99 = 0.0122\text{ mm} \quad (53)$$

Wave elevations are reduced to wave field data by normalizing the elevation with the plate length. The plate length is taken as 1200 mm, no uncertainty is implied. Without an error of the plate length, there is no data reduction related elemental error source. The root sum square of the elemental errors gives the z-direction bias, shown by

$$b_z=\sqrt{b_{z1}^2 + b_{z2}^2 + b_{z3}^2 + b_{z4}^2} \quad (54)$$

The bias b_z is combined with the sensitivity coefficient $\theta_L = 1/L$. As stated above, there is no uncertainty associated with L therefore $B_L = 0$ and the term θ_L can be neglected. The systematic standard uncertainty associated with the wave field measurements is $b_\zeta =$ 0.00029, equating to about 0.7% of the dynamic range $D_\zeta = 0.04$.

Random standard uncertainty for the wave field determined from the precision test results. Precision test measurements were made with the plate installed, $Ak = 0.21$, for locations $y = 0.0033$ and 0.05, at each x-station. A total of 10 measurements are made per location. The random standard uncertainty is calculated using Equation 42, where M = 10. The average random standard uncertainty across all locations and stations is $s_\zeta =$ 0.00099, which is about three times more than the systematic standard uncertainty and corresponds to roughly 2.4% of the dynamic range. The combined standard uncertainty for the wave field measurements (Equation 47) is $u_\zeta = 0.00104$, and expanded uncertainty (Equation 48) is $U_\zeta = 0.00207$; the expanded uncertainty is about 2.6% of the dynamic range.

4.4 Flow field

The uncertainty analysis for the SPIV measurements employs the same methodology, but slightly different procedure. The uncertainty of the flow field is determined relative to the uncertainty of the carriage speed. Select SPIV results from the uniform test are compared to their corresponding carriage speed recordings, the comparison allows the systematic standard uncertainty to be estimated. The random

standard uncertainty is inferred by examining the randomness of SPIV results from a sample of Stokes-wave with plate results. The test cases used for the uncertainty assessment are presented in Table 7. This uncertainty assessment technique is per Yoon (2009).

Systematic standard uncertainty is estimated for all velocity components (*U*, *V*, *W*), the Reynolds stress tenor (*uu*, *vv*, *ww*, *uv*, *uw*, *vw*), turbulent kinetic energy (*TKE*), and axial vorticity (ω_x). The systematic errors are determined by evaluating the difference between the SPIV results for the uniform flow test and the corresponding carriage speed recording. If the SPIV measurement domain is aligned precisely orthogonal to the coordinate system and calibrated correctly, the streamwise velocity component will be identical to the carriage speed and the vertical and spanwise velocity components will be zero. Further, the flow should show no turbulence or vorticity. Any deviation from the expected results is a systematic error. The SPIV systematic error results are compiled from three uniform flow test cases. There are five runs per case and 75 recordings per run. Each case represents a repeat test, meaning the SPIV system was disassembled and reassembled between cases, and measurements were acquired across a several month time span.

Let *R* represent either *U*, *V*, *W*, *uu*, *vv*, *ww*, *uv*, *uw*, *vw*, *TKE*, and ω_x, obtained from a SPIV measurement and R_{Ref} is the corresponding reference data. The reference data is either the carriage speed, for the case of *U*, or is taken as 0 for *V*, *W*, *uu*, *vv*, *ww*, *uv*, *uw*, *vw*, *TKE*, and ω_x. The systematic error, δ, is then written as

$$\delta = R - R_{Ref} \tag{55}$$

Herein, *R* will represent the mean variable data from each repeat test. The systematic error, b_R, is then expressed as

$$b_R = \left[\bar{\delta}^2 + \left(2\frac{s_\delta}{\sqrt{M}}\right)^2\right]^{1/2} \tag{56}$$

where $\bar{\delta}$ and s_δ are the mean and standard deviation of δ values collected from a number of M repeat measurements. A factor of 2 is shown on the right hand side of Equation 56, which is the bias limit of δ at the 95% confidence level, assuming a normal distribution of δ with a large degree of freedom ($M > 30$). Since the reference value has an associated error, b_{Ref}, then Equation (56) is modified and takes the form

$$b_R = \left[\left(\bar{\delta}^2 + \left(2\frac{s_\delta}{\sqrt{M}}\right)^2\right) + b_{Ref}^2\right]^{1/2} \quad (57)$$

The term b_{Ref} is equal to the carriage speed systematic standard error. Results from the uniform flow tests are shown in Table 8, while the systematic standard uncertainties are shown in Table 9. Results indicate that b_U, b_V, and b_W are within 1.8%, 0.14%, 0.66% of U_c, respectively, and Reynolds stress and vorticity b_X's are 5-10% dynamic range of Stokes-wave juncture boundary layer and wake measurements.

The random standard uncertainty of R is established from a different set of SPIV measurements, those of the Stokes-wave, $Ak = 0.21$, and plate. The uniform flow results are not used since random standard uncertainties of the Reynolds stresses are best estimated in flows that are turbulent. Three test cases at $x = 0.50$, are used, each containing twenty carriage runs. An average across all twenty runs represents R for each case, and standard deviation denoted s_R. The random standard uncertainty is calculated from Equation 43where $M = 3$. The random standard uncertainty is calculated in two regions, the boundary layer and the outer inviscid flow; the criteria for delineating each region is based on the TKE, $TKE > 0.001$ is the boundary layer and $TKE < 0.001$ is the outer flow. Table 10 and 11 present the uncertainty results for the boundary layer and inviscid flow regions, respectively. The results presented in these tables are preliminary, as some of the values are greater in magnitude than expected. Further analysis will be conducted in order to obtain levels of uncertainty that are deemed more reasonable. In the outer flow, systematic uncertainties are dominant, accounting for 81.9 % to 99.7% of the expanded uncertainties. The expanded uncertainties, U_{95u}, U_{95v}, and U_{95w} are

0.04406, 0.00362, and 0.01629, respectively, corresponding to 4.4%, 0.3%, and 1.6% of U_c respectively. However in the boundary layer, the random standard uncertainties were higher than the systematic uncertainty, representing 61.4% to 94.3% of the expanded uncertainties. Here, the expanded uncertainties, U_{95u}, U_{95v}, and U_{95w} are 0.17918, 0.01380, and 0.02503, respectively, corresponding to 17.9%, 1.4%, and 2.5% of U_c respectively.

CHAPTER 5

RESULTS AND DISCUSSION

This chapter discusses the wave field and flow field results. The wave and flow field results are presented separately and are sub-divided by condition. Table 2 lists all the measurements and test conditions. The wave field measurements are performed with the plate installed and the results are divided into the flat free surface, $Ak = 0$, and Stokes-wave, $Ak = 0.21$, conditions. Flow field measurements are made with the plate removed and installed. Flow field results, without the plate, are divided into the uniform flow, $Ak = 0$, and Stokes-wave, $Ak = 0.21$, condition. Similarly, flow field results with the plate installed, are sectioned into boundary layer and wake, $Ak = 0$, and boundary layer and wake, $Ak = 0.21$. Theoretical estimates and results from other researchers are presented intermittently throughout.

5.1 Wave field

The wave field is qualitatively examined using photographs and measured with servo wave gauges. Wave field measurements are sampled across a global and local grid. An outline of the global grid is shown in Figure 7, the local grid corresponds to the locations where flow field measurements are obtained. Global wave field results are presented on contour plots and line plots, and local wave field results are shown in line plots.

5.1.1 Flat free surface, $Ak = 0$

Wave field measurements are made with the plate installed, without invoking the Stokes wave, in order to document the wave created by the plate. Photographs of the test conditions and free surface appearance are shown in Figure 10. The photographs show a small bow wave at the leading edge of the plate. At the turbulence stimulators, a small Kelvin wave becomes apparent. The small diverging wave pattern radiates at an angle of

roughly 20° from the plate and has an amplitude of roughly 5 mm. The plate wave pattern is only vaguely captured by the global wave elevation measurements shown in Figure 11 and Figure 12. Wave field measurements at six *x*-stations are averaged across all *y*-values, the results are presented in Table 12. Free surface disturbances from the stern wave, though poorly captured, can be identified. The dominating wave field pattern stems from the sidewall. This wave pattern radiates ever closer to the plate and intercepts the plate wave pattern at $x = 1.25$. Wave elevations surrounding the plate, for the most part, have a dimensionless amplitude in the neighborhood of 0.005, or about 10% of the Stokes wave amplitude. Although, the bow and stern wave measure about 0.01, or about 25% of the Stokes wave amplitude. Comparatively, the unwanted disturbance from the sidewall has an amplitude on the order of 0.02, twice as great as the plate's wave pattern.

Figure 13 is a longitudinal wave field cut featuring local and global measurements at about the same transverse distance from the plate, $y \approx 0.05$; this distance is just outside of the boundary layer. Also illustrated are the results from Stern et al (1993). The wave elevation data are in close agreement. Local wave elevation measurements, with single test uncertainty bands, are shown in Figure 14; the results are plotted alongside those of Stern et al. (1993).

5.1.2 Stokes wave, $Ak = 0.21$

The Stokes-wave wave field is measured to examine the plate's effect on the imposed wave train. The wave field for $Ak = 0.21$ consists of a wave train beginning upstream of the flat plate that is intended to be two-dimensional with little variation in the spanwise direction. The wave train may be estimated using the theoretical second-order Stokes-wave equation

$$\zeta(\mathrm{x}) = \frac{1}{2}kA^2 + A\cos kx + \frac{1}{2}kA^2\cos 2kx \tag{58}$$

where *x* is the streamwise coordinate, with origin at the leading edge of the flat plate.

Photographs of the test conditions and free surface appearance are shown in Figure 15. The same free surface features identified in the former condition exist here, plus the superposition of the Stokes wave. Global wave field measurements of the Stokes-wave are shown in Figure 16 and Figure 17 (a). Wave field measurements at six x-stations are averaged across all y-values, the results are presented in Table 12. Shown in Figure 17 (b) is the theoretical wave profile. The Stokes wave had an average estimated amplitude at the second and third wave crests of $0.042 \cdot L$ and $0.040 \cdot L$; and an amplitude at the second and third wave trough of $-0.034 \cdot L$ and $-0.031 \cdot L$, respectively. The decreasing amplitude of the wave is due to viscous dampening and interactions with the plate. The average amplitude measured at the wave crests is greater than the wave troughs; which is consistent with second- and third-order theory and experimental data (Salvesen 1969, and Kang et al. 2008). The average measured wave amplitude, at crests and troughs, is roughly $0.037 \cdot L$, or about 44 mm; the designed wave amplitude is $0.04 \cdot L$ or 48.5 mm. The observed wavelength is $\lambda = 0.95 \cdot L$, resulting in a wavelength that is 5%, or 60 mm shorter than predicted. Other researchers have noticed that second–order wave theory often over-predicts the observed wavelength (Kang et al 2008); Salvesen (1969) commonly observed this discrepancy on the order of 10%. Salvesen argues that third-order effects must be included to accurately predict the wavelength. In his third-order equations, the wave length is predicted by

$$\lambda = \frac{2\pi}{g} U_c^2 \left(1 - \left(\frac{Ag}{U_c}\right)^2\right) \tag{59}$$

The term g, is the gravitational acceleration term, equal to 9.81 m/s^2. Equation 60 indicates a wavelength of $0.947 \cdot L$.

Figure 17 (c) shows a full comparison of the measured wave to the ideal second-order Stokes wave. The average wave elevations at constant x-locations are compared to the theoretical values and tabulated in Table 12. Large discrepancies, in the order of 50% A, occur in the region of $x = 1.20$, caused by slight differences in wavelengths and the

strong wave elevation gradients. The average difference over the entire measurement grid is 19.4% A.

Figure 18 (a) illustrates the benchmark wave elevation data of Kang et al. (2008). This data set is less dense, totaling 170 datum points, measured from $x = 0$ to 2; for illustration purposes only data up to $x = 1.5$ is shown. Figure 18 (b) shows the difference between the measured wave field and the benchmark data. The data sets are in close agreement. Overall, the average difference over the measurement grid is 9.0% A.

A longitudinal cut of global and local wave measurements are shown in Figure 19, alongside theoretical and benchmark results. There is strong similitude amongst all data sets until $x = 0.50$; thereafter noticeable discrepancies are observed. The results of Stern et al. (1993) are in best agreement with the theoretical results; the current results and those of Kang et al. (2008) tend to over predict the wave amplitude. The disparity in results at $x > 0.50$ can be attributed to the various y-positions of the data. Transverse cuts of the local wave measurements, benchmark, and theoretical data are shown in Figure 20.

5.2 Flow field

Flow field measurements are preformed under four conditions that vary based on plate installation and free surface condition. The first two conditions presented are those without the plate, and consist of uniform flow, $Ak = 0$, and Stokes flow, $Ak = 0.21$, results. The other conditions are those with the plate installed, boundary layer and wake, $Ak = 0$, and boundary layer and wake, $Ak = 0.21$. The flow field is examined at six stations that vary in the x-direction, denoted $x = 0.25$, 0.50, 0.75, 1.00, 1.25, and 1.50. The results are summarized by table (uniform flow only), contour plots, and line plots.

5.2.1 Without plate

5.2.1.1 Uniform Flow, $Ak = 0$

Measurements were made of the uniform flow, $Ak = 0$, in order to baseline the SPIV system's performance; the results are also used to identify systematic errors in the velocimeter system discussed in the uncertainty assessment, section 4.4. The flow field is measured at all six stations requiring sixteen separate zones. Table 13 presents the uniform flow results, divided by x-station and averaged across all y and z locations. The results from one representative zone, $x = 0.75$, are shown in Figure 21 showing all velocity components, turbulence quantities, and vorticity. The streamwise velocity component is roughly equal to the carriage speed, $U = 1.016$, and all other flow quantities are near zero, $V \approx W \approx \omega_x \approx 0$ and uu, vv, ww, uv, uw, $vw \approx 0$.

5.2.1.2 Stokes wave flow, $Ak = 0.21$

Stokes wave flow field measurements for $Ak = 0.21$, are performed with the plate removed in order to examine the wave-driven flow without interference of the plate. The results are compared to theoretical Stokes-wave solutions.

Wave-driven flow is discernible by streamwise and vertical velocity components that vary in magnitude based on depth and location on the wave. The transverse velocity component remains zero. Wave effects are most prevalent near the free surface and diminish exponentially with increasing depth. The Stokes-wave equations for the flow are

$$U = 1 - Ake^{-kz} \cos kx \tag{60}$$

$$W = Ake^{-kz} \sin kx \tag{61}$$

where x and z are the streamwise and vertical coordinates. These equations are discussed in detail by (Stokes (1847), Salvesen (1966 and 1969), Giesing and Smith (1967), and Sachdeva and Preston (1978)). The streamwise and vertical velocity components

oscillate about dimensionless velocities of $U \approx 1$ and $W \approx 0$. The streamwise velocity component is greater than the carriage speed at a wave trough, less than the carriage speed at a wave crest, and equal to the carriage speed at an inflection point. The vertical velocity component is comparatively out-of-phase by $\pi/2$ radians or 90 degrees, having a positive value at inflection points following a wave trough, negative value at inflection points following wave crests, and zero value at crests and troughs.

Figure 22 shows the experimental Stokes-wave flow pattern. The average differences, across all y and z locations, between the measured and theoretical flow fields are presented by x-station in Table 13. The plots highlight the wave-induced oscillations of U and W; all other velocity, turbulence, and vorticity quantities are omitted since they deviate little from the expected value of zero. The plots vary by x-location, shown in ascending order in terms of distance from the plate leading edge. The stations $x = 0.25$, 0.50, 0.75, 1.00, 1.25, and 1.50, correspond to a wave inflection point, trough, inflection point, crest, inflection point, and trough, respectively. The theoretical Stokes-wave flow field is shown in Figure 23. Figure 24 shows the percent difference between the theoretical and measured Stokes-wave flow. The differences are tabulated in Table 12. The differences between the measured and theoretical Stokes-wave flow are small, indicating a 0.50% to 4.88 % difference in U and 0.03% to 4.54% difference in W. The largest discrepancy in W occurs at x =0.25 for the lower zone, located at $-0.06 < y < -0.125$; which could be related to an error in SPIV calibration. Otherwise, the measured data conforms to the theoretical values from $0.25 < x < 1.00$; poorer agreement is observed in the wake, $1 < x < 1.5$, which can be correlated to the large differences between the measured and theoretical wave field.

5.2.2. With plate

5.2.2.1 Boundary layer and wake, $Ak = 0$

Flow field measurements are made with the plate installed for the flat free surface condition as a basis of comparison with the Stokes wave case (discussed later) and to identify free surface effects. The mean flow quantities U, V, W, and ω_x, for the full measurement domain are shown in Figures 25, 26, 27, and 28; the boundary layer and wake is highlighted in Figures 36, 37, 38, and 40. Figures 72, 73, 74, 75, 76, 77, and 78 are close-up views of the juncture region U, V, W, and ω_x contours. The plots are annotated with boxes, lines, and dots to highlight important locations and flow regions. For the boundary layer stations, a gray box represents a cross section of the starboard half of the plate; while in the wake stations, a box with "dash-dot" lines outlines the upstream location of the plate. Horizontal dashed lines at $z = 0.04$, 0.08, and 0.125, indicate cuts where data is extracted and used to examine velocity profiles and boundary layer and wake parameters. Symbols represent local wave elevation measurements which indentify the free surface; each symbol is accompanied by a single test uncertainty band.

The U contours in Figure 25 and 36 are discussed first. Moving in ascending x-position, the boundary layer grows in thickness. At $x = 1.00$, the boundary layers on the starboard and port side of the plate coalesce and form the wake. The plots show that the free surface effects penetrate to a depth of roughly $z = -0.04$, and for greater depths the boundary layer appears both two-dimensional and canonical. Examining V contours (Figure 26 and 37) and W contours (Figures 27 and 38), these velocity components rarely fluctuate more than ± 1.5% of the free stream velocity. Under closer inspection, at $x = 0.25$, somewhat higher transverse velocities are found near the plate, on the order of $V = 0.05$. The behavior may be attributed to the blunt leading edge and turbulence stimulators. The highest V velocity components are found at the trailing edge, $x = 1.00$, where the flow rapidly converges toward the wake centerline. For W, the most prevalent

features are the downward velocities, $W \approx -0.1$, near the free surface at stations $x = 0.25$ and 1.50. These locations correspond to regions downstream of localized high spots in the wave field, as seen in Figure 12.

The turbulent quantities *TKE*, *uu*, *vv*, *ww*, *uv*, *uw*, and *vw* for the full domain are shown in Figures 29, 30, 31, 32, 33, 34, and 35. These same quantities are isolated in the boundary layer and wake regions for Figures 54, 55, 56, 57, 58, 59, and 60. Figures 76, 77, 78, 79, 80, 81, and 82 are close-up views of the juncture region turbulent contours. Strong turbulence is observed at the trailing edge where the flow abruptly transitions into free shear. Examining Figures 30, 31, 32, 41, 42, and 43, the streamwise normal Reynolds stress magnitude, *uu*, is dominate in comparison to *vv* and *ww*. However, in the wake the Reynolds normal stresses demonstrate an isotropic distribution. Contours of the Reynolds shear stress tensor, *uv*, at $x = 0.25$ have an irregular pattern caused by leading edge effects.

Figure 58 (a) show mean velocity profiles for U at z-elevations of $z = -0.04$, -0.08, and -0.125; similarly, Figures 59 (a) and 60 (a) document velocity profiles V and W. For clarity, the profiles of the current results show every third data point. Two distinct profiles are observed, one for the boundary layer and the other for the wake. From the U profiles one can notice the boundary layers becoming thicker with increasing x-position. In the wake, the flow recovers rapidly as the wake centerline velocity increases from $U = 0$ at the trailing edge to $U = 0.7$ at $x = 1.25$, and $U = 0.83$ at $x = 1.50$. The relatively large negative velocities for V at station $x = 1.00$, are caused by the inflow at the trailing edge mentioned previously.

To identify the outer flow velocities, the edge velocities U_e and W_e are plotted in Figure 61 (a) and (b) respectively. In general, both U_e and W_e fall near the expected value of 1 and 0, respectively, with some subtle differences. The trends in the edge velocity plots mirror those of the wave field. The benchmark data of Stern displays good agreement with the current results.

The log law is plotted alongside the experimental data in Figures 63. The precise y^+ location of the current data set is discussed in section 3.4.3. The characteristic log law profile for flat plate flow is observed by the slight rise in U^* in the outer layer, i.e. $y^+ = 1000$. The log law profiles closely follow the logarithmic overlap line given by Equation 25, which indicates that the velocity profile in the boundary layer is similar to the canonical turbulent boundary layer.

Figure 64 shows select Reynolds stress profiles versus y^+, where the Reynolds normal stresses are nondimensionalized by u^*. At $x = 0.25$, the peak measured value of $uu/u^* = 2$ at $y^+ = 20$; further on the plate at $x = 1.00$, the maximum is $uu/u^* = 3$ at $y^+ = 70$. The difference in the Reynolds stress magnitudes illustrates a Reynolds number dependence. For all stations, uu, is about three to four times greater than vv or ww, in the viscous wall region, i.e. $y^+ < 50$. Contrary to expectations vv is always greater than ww, as turbulent fluctuations typically dampen in the wall-normal direction. This small, albeit noticeable, abnormality may be caused by vibrations in the plate. The measurements show no dependence on depth, nor for that matter, free surface effects. The vv term shows elevated levels at $x = 1.00$ due to trailing edge effects. All Reynolds normal stress plots show non-zero values in the outer flow, $y^+ > 10^3$; ideally the magnitude of the Reynolds stresses would be zero since the flow in known to be turbulent-free. One should not interpret this disparity as a bias over all y^+ values. The discrepancy may be attributed to the short pulse delay of the SPIV system. As the SPIV system resolves particle movements across very small time intervals, even for the best sub-pixel correlation schemes, velocity fluctuations will exist at levels inversely proportional to the pulse delay. Meaning, short pulse delays will result in larger velocity fluctuations, whereas a longer duration pulse delay would have the opposite effect (Wieneke and Anderson, 2008). Figure 65 shows wake turbulence. The magnitude of uu, vv, and ww, is more uniform in the wake. The Reynolds normal stresses and turbulent kinetic energy

profiles display an overshoot at roughly $y/b = 0.4$. The uv terms is roughly 5 times greater in the wake than along the plate.

5.2.2.1.1 Underlying flow, $Ak = 0$

Figure 66 (a) shows a comparison of the wall-shear stress magnitude C_f for the current results and those of Stern et al. (1993). Compared to previous experiments that use the Clauser and Bradshaw methods to find C_f, the current approach is adopted by Kendall and Koochesfahni (2008) and is mentioned in section 3.4.3. Schoenherr (presented in Granville (1977)) demonstrated that for relatively constant shape factors, H, C_f will vary almost linearly with Re_θ, when plotted on a logarithmic scale. Schoenherr's relation is expressed by

$$C_f = \frac{0.02932}{log_{10}(2Re_\theta)\left[\frac{1}{2}log_{10}(2Re_\theta)+0.4343\right]} \tag{61}$$

The relation dictates, as do the results, that C_f and H decrease with increasing Re_θ, see Figure 67 and 68. The displacement thickness is shown in Figure 69 (a), for the current data and the benchmark data of Stern et al (1993). The plot shows a sharp increase in δ^* at the trailing edge, $x = 1.00$. The displacement thickness is over predicted due to separation at the trailing edge. The displacement thickness then drops off in the wake region. Similar trends are observed for the momentum thickness plotted in Figure 70 (a).

Figure 71 shows the wake half-width, wake centerline defect, and shape factor. The results show that the wake half-width increases with distance from the trailing edge. As the wake radiates outward from the wake centerline and mixes with the faster-moving outer flow, the wake centerline defect decreases rather rapidly. The exponential decrease in the wake centerline defect is very similar to the decrease in the shape factor.

5.2.2.1.2 Juncture flow, $Ak = 0$

Contour plots of U, V, W, and ω_x in the juncture region are found in Figures 72, 73, 74, and 75. Moving to the free surface from a constant y-position, the boundary thins

and then thickens rapidly right below the free surface. It is believed that the thinning of the boundary layer is caused by streamwise vorticity, in the form of two counter rotating vortices. One vortex is located near the free surface and draws high momentum fluid towards the inner boundary layer and low momentum fluid away from the wall, along the free surface. The other vortex is lower and it transports high momentum fluid toward the corner bisector and then down along the wall. Where the boundary layer is the thinnest, at about z = -0.01 and $y = \delta/2$, is where the two vortices converge; the high momentum flow that is drawn toward the wall accelerates the flow, thus thinning the boundary layer. These vortices continue in the wake but at reduced strength. Contour plots of the turbulence *uu*, *vv*, *ww*, *uv*, *uw*, and *vw* are shown in Figures 76 through 82.

5.2.2.2 Boundary layer and wake, $Ak = 0.21$

The Stokes wave, Ak =0.21, is invoked to test wave effects on the boundary layer and wake. The wave effects on the boundary layer may be inferred by analyzing order-of-magnitude estimates of the pressure field. The boundary layer thickens where the piezometric pressure gradient is adverse, or the piezometric-pressure gradient coefficient is negative. Conversely, the boundary layer thins where the piezometric pressure gradient is favorable. The second-order piezometric pressure coefficient C_p is given by

$$C_{pe}(x,z) = Ake^{-kz}\cos kx - (Ak)^2 e^{-2kz} \tag{66}$$

where

$$C_{pe} = \frac{P_e}{\frac{1}{2}\rho U_c^2} \tag{67}$$

and P_e is the piezometric pressure and ρ is the fluid density. The piezometric-pressure-gradient coefficients are given by

$$P_x(x,z) = \frac{\partial\left(\frac{P_e}{\rho U_c^2}\right)}{\partial z} = -Ak^2 e^{-kz}\sin kx \tag{68}$$

$$P_z(x,z) = \frac{\partial\left(\frac{P_e}{\rho U_c^2}\right)}{\partial z} = -Ak^2 e^{-kz}\cos kx + k(Ak)^2 e^{-2kz} \tag{69}$$

Between the wave crest and inflection point, at $x = 0$ and 0.25, U and W are accelerating and both P_x and P_z are negative and favorable. From $x = 0.25$ to 0.50, P_x is favorable and P_z is adverse. As the flow approaches the wave inflection point, between $x = 0.50$ and 0.75, both P_x and P_z are adverse. Near the wave crest, $x = 1.00$, P_x is adverse and P_z is favorable. The trend repeats, and each region has a unique influence on the flow.

The full domain of mean flow quantities U, V, W, and ω_x are shown in Figures 25, 26, 27, and 28 respectively; similar plots showing just the boundary layer and wake are shown in Figure 47, 48, 49 and 50. The data displays the expected wave-induced effects. The orbital velocities of U and W are observed as well as the thinning δ at $x = 0.25$, 0.50, 1.25, and 1.50, and thickening δ at $x = 0.75$ and 1.00. Like the flat free surface condition, thinning of the boundary layer, followed by rapid thickening, is observed just below the free surface. Wave induced vorticity can be identified along the plate. At x =0.25, the down flow, $W < 0$, causes negative streamwise vorticity. The region of vorticity is roughly uniform in thickness with depth; the thickness of this region is roughly $\delta/4$. The vorticity changes sign at $x = 0.50$ as the vertical velocity component transitions to up flow. Strong positive streamwise vorticity is apparent at $x = 0.75$. Full domain contours of turbulence are shown in Figures 29, 30, 31, 32, 33, 34, and 35, and the boundary layer and wake contour of turbulence are shown in Figures 51, 52, 53, 54, 55, 56, and 57.

Figures 58 (b), 59 (b), and 60 (b) show detailed velocity profiles. The orbital velocities of U and W can be more easily identified in these plots. The thinning and thickening of δ is apparent in the U profiles. In regions of accelerating flow and favorable pressure gradients (for example, $x = 0.25$ and 0.50), the boundary layer profile becomes fuller, with large wall-shear-stress angles. Under the opposite conditions, the boundary layer thickness widens and the profile appears less full; consequently the wall-shear-stress angle is smaller. The W profiles reveal that the inner part of the boundary layer seemingly responds faster to changes in the cross flow, compared to the slight lag in

the outer boundary layer. Figures 62 (a) and (b) show the U_e and W_e edge velocities versus x.

Figure 63 shows a plot of the inner variables. At $x = 0.50$, the strong favorable pressure gradients cause an undershoot in u^+ for $y^+ > 1500$, when compared to the Musker profile. At the same distance from the wall, adverse pressure gradients cause an overshoot in u^+ (see the profile for $x = 0.75$).

5.2.2.2.1 Underlying flow, $Ak = 0.21$

The wall-shear-stress magnitude is illustrated in Figure 66 (b). Compared to the flat free surface case, where C_f decreases monotonically with x, here C_f displays an oscillatory behavior, evidence of the fluctuating pressure gradients. Figure 69 (b) displays the displacement thickness versus x. Along the plate, δ^* is relatively uniform with depth. However at the trailing edge and in the wake, δ^*, varies significantly. At $x = 1.00$, greater δ^* are observed nearer the free surface, but the trend reverses at $x = 1.25$. The momentum thickness shows similar patterns (see Figure 70 (b)).

5.2.2.2.1 Juncture flow, $Ak = 0.21$

Contour plots of U, V, W, and ω_x in the juncture region are found in Figures 83, 84, 85, and 86 respectively. The secondary flow pattern caused by vorticity found in the juncture region for the flat free surface condition is also observed here. Comparing these two conditions, $Ak = 0$ and 0.21, it is difficult to determine if wave-effects have an influence on this secondary flow phenomena. Contour plots of the turbulence uu, vv, ww, uv, uw, and vw are shown in Figures 87 through 93.

CONCLUSION

Boundary layer and wake results are presented for a towed, surface-piercing flat plate with superimposed Stokes-wave. The wave field is measured with servo wave gauges in order to document the wave and to make estimates of wave induced velocities. The flow field is measured with SPIV equipment to examine velocity profiles and turbulence levels. The SPIV is focused on the juncture region in order to analyze energy transfer, namely the anisotropic Reynolds stresses which induce a small secondary flow. The conclusions from the four test cases are presented below.

The uniform flow results are consistent with expectations, illustrating that the SPIV system can accurately measure velocity and does not over predict turbulence. The Stokes wave results illustrated the wave driven flow without interference from the plate. The flat free surface with plate condition showed a three dimensional boundary layer and wake near the free surface and two-dimensional canonical profiles at greater depths. The results are consistent with benchmark data. The juncture region is better resolved than before. The boundary layer thinning and thickening trends are consistent with other researchers. A pair of streamwise vortices is identified, but not in absolute clarity. Stokes-wave with plate results are in agreement with benchmark data. The wave-induced oscillations of U and W along with the piezometric pressure gradients have pronounced effect on the boundary layer and wake. In favorable pressure gradients, the boundary layer thins, and thickens where gradients are adverse and the flow decelerates; in relatively strong adverse pressure regions weak separation occurs. It is believed that the wake is more responsive to wave-effects than the boundary layer. Newly documented results are shown on the streamwise vorticity in the boundary layer caused by wave-effects.

Table 1: Summary of previous IIHR Hydroscience and Engineering solid/free-surface juncture boundary layer and wake experiments

Study	Data	Equip-ment	*Ak*	*d/c*	*L* (m)	U_c (m/s)	*Fr*	*Re*† (10^6)	*x*	*y*	*z*
Stern et al., 1989	Wave elevations	Photo	0 0.11 0.21	2.75 1.39 1.12	2.5	1.37	0.28	3.43	0-1.0	0	
	Boundary layer*	3-hole probe	0 0.11 0.21	2.75 1.39 1.12	2.5	1.37	0.28	3.43	0.125-1.0	0-0.05	-0.041 - -0.125
Stern et al., 1993	Wave elevations	Servo	0 0.21	2.75 1.12	1.2	1.37	0.4	1.64	0.25-1.88	0.02-0.1	
	Boundary layer*	5-hole probe	0 0.11 0.21	2.75, 1.39, 1.12	1.2	1.37	0.4	1.64	0.25 - 1.0	0-0.05	-0.041-0.125
	Wake*	5-hole probe	0 0.11 0.21	2.75, 1.39, 1.12	1.2	1.37	0.4	1.64	1.04 - 2.0	0-0.05	-0.041 - -0.125
Longo et al., 1998	Boundary layer*	LDV	0	2.75	1.2	0.46	0.13	0.55	0.5	0-0.03	-0.125-0
	Wake*	LDV	0	2.75	1.2	0.46	0.13	0.55	1.25	0-0.06	-0.125-0
Kang et al., 2008	Wave elevations	Servo	0.24	2.75	1.2	1.37	0.4	1.64	0-2.0	0.03-0.78	
	Boundary layer	SPIV	0 0.24	2.75 1.39	1.2	1.37	0.4	1.64	0.25 - 1.5	0-0.1	-0.125-0
	Wake	SPIV	0 0.24	2.75 1.39	1.2	1.37	0.4	1.64	1.0 - 1.5	0-0.1	-0.125-0

†: Reynolds number based on plate length, *, juncture region not measured

Table 2: Summary of current IIHR Hydroscience and Engineering solid/free-surface juncture boundary layer and wake experiment

Data	Subset	Equip-ment	*Ak*	*d/c*	*L* (m)	U_c (m/s)	*Fr*	*Re*† (10^6)	*x*	*y*	*z*
Wave elevations	Global wave field	Servo	0 0.21	2.75 1.39	1.2	1.37	0.4	1.64	-0.13-1.5	0.042-0.73	
	Local wave field	Servo	0 0.21	2.75 1.39	1.2	1.37	0.4	1.64	0.25-1.5	0.002-0.075	
	Precision	Servo	0.21	1.39	1.2	1.37	0.4	1.64	0.25-1.5	0.003-0.05	
Boundary layer		SPIV	0 0.21	2.75 1.39	1.2	1.37	0.4	1.64	0.25 1.5	0-0.07	-0.125 - 0
Wake		SPIV	0 0.21	2.75 1.39	1.2	1.37	0.4	1.64	0.25 1.5	-0.01-0.07	-0.125 - 0

†, Reynolds number based on plate length

Table 3: Wave gauge specifications

Brand	Kenek
Power Source	
Model	SW-101
Power Supply	120 ± 10 VAC
Output Voltage	± 5 VDC
Probe	
Model	SWT-10
Measurement Range	100 mm
Resolution	0.1 mm
Maximum linear needle speed	700 mm/s
Full-scale amplitude response	2.2 Hz
Response for ±1 mm amplitudes	100 Hz
Linearity error	0.1 %
Drift	0.1 %

Table 4: Three dimensional stereo particle image, SPIV, camera, lens, and laser specifications

Camera setup	stereo, symmetric, submerged cameras are placed downstream of measurement area
Cameras	2 × Redlake MegaPlus II; resolution = 1600 × 1200 pixels
Lenses	2 × Canon EOS; f = 100 mm $f_{\#}$ = 2.0, with automatic Shiempflug and aperture control
Recording method	single frame / double exposure
Pulse delay	Δt = 150 μs
Operation frequency	5 Hz
Lasers	Big Sky, water-cooled, dual-headed Nd:YAG laser 190 mJ / pulse, frequency doubled

Table 5: Three dimensional stereo particle image velocimetry, SPIV, recording parameters for boundary layer measurement

Flow geometry	Light sheet aligned normal to stream-wise direction
Maximum in-plane velocity	$V_{max} \approx 0.5$ m/s
Maximum out-of-plane velocity	$U_{max} \approx 1.5$ m/s
Field of view	95 × 70 mm^2
Interrogation volume	2.1 × 2.1 × 3.0 mm^3 ($H \times W \times D$)
Dynamic spatial range	DSR ≈ 110 : 1
Dynamic velocity range	DVR ≈ 125 : 1
Observation distance and angle	$z_o \approx 0.99$ m, ±40°
Seeding material	silver hollows ($d_p \approx 14$ μm)

Table 6: Wave field uncertainties determined from the precision test results

	x = 0.25	0.50	0.75	1.00	1.25	1.50
b_x	3.0000	3.0000	3.0000	3.0000	3.0000	3.0000
b_y	2.0000	2.0000	2.0000	2.0000	2.0000	2.0000
b_{z1}	0.1090	0.1090	0.1090	0.1090	0.1090	0.1090
b_{z2}	0.0070	0.0070	0.0070	0.0070	0.0070	0.0070
b_{z3}	0.2362	0.2362	0.2362	0.2362	0.2362	0.2362
b_{z4}	0.0122	0.0122	0.0122	0.0122	0.0122	0.0122
b_z	0.2605	0.2605	0.2605	0.2605	0.2605	0.2605
b_L	0	0	0	0	0	0
$d\zeta/dx$	0	0	0	0	0	0
$d\zeta/dy$	0.0001	0.0001	0.0001	0.0001	0.0001	0.0001
$d\zeta/dz$	0.0008	0.0008	0.0008	0.0008	0.0008	0.0008
$d\zeta/dL$	0.00003	0.00003	0.00003	0.00003	0.00003	0.00003
$b_x^2(d\zeta/dx)^2$	0	0	0	0	0	0
$b_y^2(d\zeta/dy)^2$	4.000E-08	4.000E-08	4.000E-08	4.000E-08	4.000E-08	4.000E-08
$b_z^2(d\zeta/dz)^2$	4.714E-08	4.714E-08	4.714E-08	4.714E-08	4.714E-08	4.714E-08
$b_L^2(d\zeta/dL)^2$	0	0	0	0	0	0
b_ζ	2.952E-04	2.952E-04	2.952E-04	2.952E-04	2.952E-04	2.952E-04
% of $U_{\zeta,\, y = 0.0033}$	9.1%	8.6%	15.6%	14.1%	2.3%	14.9%
% of $U_{\zeta,\, y = 0.05}$	4.8%	13.9%	10.0%	17.9%	16.7%	6.4%
$s_{\zeta(S),\, y = 0.0033}$	9.327E-04	9.643E-04	6.864E-04	7.273E-04	1.929E-03	7.044E-04
% of $U_{\zeta,\, y = 0.0033}$	90.9%	91.4%	84.4%	85.9%	97.7%	85.1%
$s_{\zeta(S),\, y = 0.05}$	1.319E-03	7.341E-04	8.848E-04	6.314E-04	6.592E-04	1.133E-03
% of $U_{\zeta,\, y = 0.05}$	95.2%	29.5%	42.9%	21.8%	23.8%	70.3%
$U_{\zeta,\, y = 0.0033}$	9.783E-04	1.008E-03	7.472E-04	7.849E-04	1.951E-03	7.638E-04
% of D_ζ = 0.033 (40 mm)	2.9%	3.0%	2.2%	2.4%	5.9%	2.3%
$U_{\zeta,\, y = 0.05}$	1.352E-03	7.913E-04	9.328E-04	6.970E-04	7.223E-04	1.171E-03
% of D_ζ = 0.033 (40 mm)	4.1%	2.4%	2.8%	2.1%	2.2%	3.5%

Table 7: Test conditions for SPIV UA

Description	U_c (m/s)	x	y	y	No. of recodings per run	No. of runs per test	No. of repeat tests
Uniform flow	1.372	0.50, 0.75	0-0.05	0.05-0.1	75	5	3
Stokes wave boundary layer and wake	1.372	0.50	0-0.05	0.05-0.1	75	20	3

Table 8: Results from the uniform test cases used in the uncertainty assessment, results are shown in dimensionless form

Result variable	Reference data	Average SPIV data per case		
R	R_{Ref}	$\bar{R}$, Case 1	$\bar{R}$, Case 2	$\bar{R}$, Case 3
U	1.0	1.03258	1.039219	1.035076
V	0.0	-0.00374	-0.002003	-0.000569
W	0.0	-0.00804	-0.014235	0.006112
uu	0.0	0.00083	0.000791	0.001056
vv	0.0	0.00065	0.000611	0.000804
ww	0.0	0.00040	0.000346	0.000412
uv	0.0	-0.00017	-0.000098	0.000012
uw	0.0	0.00003	0.000010	0.000033
vw	0.0	-0.00006	-0.000044	-0.000074
TKE	0.0	0.00094	0.000874	0.001136
ω_x	0.0	-0.00812	-0.054665	-0.006958

Table 9: Systematic uncertainties of SPIV uniform flow measurement results are shown in dimensionless form

Result variable	Average SPIV data	Reference data	Average difference	Standard deviation of difference	Systematic standard uncertainty of difference	Systematic standard uncertainty of reference	Systematic standard uncertainty of Result
R	$\bar{R}$	R_{Ref}	$\bar{\delta}$	s_δ	b_δ	$b_{R_{Ref}}$	b_R
U	1.03562	1.0	0.035626	0.003352	0.017918	0.005154	0.018644
V	-0.00210	0.0	-0.002104	0.001587	0.001395	0.0	0.001395
W	-0.00538	0.0	-0.005388	0.010430	0.006597	0.0	0.006597
uu	0.00089	0.0	0.000892	0.000144	0.000454	0.0	0.000454
vv	0.00068	0.0	0.000688	0.000102	0.000349	0.0	0.000349
ww	0.00038	0.0	0.000387	0.000036	0.000195	0.0	0.000195
uv	-0.00008	0.0	-0.000085	0.000091	0.000068	0.0	0.000068
uw	0.00002	0.0	0.000024	0.000013	0.000014	0.0	0.000014
vw	-0.00005	0.0	-0.000059	0.000015	0.000031	0.0	0.000031
TKE	0.00098	0.0	0.000984	0.000136	0.000498	0.0	0.000498
ω_x	-0.02324	0.0	-0.023247	0.027215	0.019545	0.0	0.019545

Table 10: Random and systematic outer flow results, $TKE < 0.001$

Result variable	Average SPIV data	Systematic standard uncertainty	Random standard uncertainty	Combined standard uncertainty	Relative systematic uncertainty contribution	Relative random uncertainty contribution	Expanded uncertainty	Relative expanded uncertainty
R	$\bar{R}$	b_R	s_R	u_R	b_R^2/u_R^2(%)	s_R^2/u_R^2(%)	U_{95R}	U_{95R}/R (%)[a]
U	1.17435	0.01864	0.00107	0.01867	99.7	0.3	0.04406	3.7
V	0.00866	0.00139	0.00065	0.00154	81.9	18.1	0.00362	41.9
W	0.03695	0.00659	0.00205	0.00690	91.2	8.8	0.01629	44.1
uu	0.00061	0.00045	0.00002	0.00045	99.8	0.2	0.00106	173.9
vv	0.00044	0.00034	0.00001	0.00034	99.8	0.2	0.00080	181.7
ww	0.00059	0.00019	0.00003	0.00019	98.2	1.8	0.00045	76.7
uv	-0.00002	0.00006	0.00001	0.00006	95.1	4.9	0.00015	852.0
uw	-0.00013	0.00003	0.00001	0.00003	86.6	13.4	0.00008	59.2
vw	0.00002	0.00001	0.00001	0.00001	59.1	40.9	0.00003	172.7
TKE	0.00082	0.00049	0.00002	0.00049	99.8	0.2	0.00116	140.8
ω_x	-0.03580	0.01954	0.44526	0.44569	0.2	99.8	1.05183	-2937.7

[a]: Results are preliminary

Table 11: Random and systematic inner flow results, $TKE > 0.001$

Result variable	Average SPIV data	Systematic standard uncertainty	Random standard uncertainty	Combined standard uncertainty	Relative systematic uncertainty contribution	Relative random uncertainty contribution	Expanded uncertainty	Relative expanded uncertainty
R	$\bar{R}$	b_R	s_R	u_R	b_R^2/u_R^2(%)	s_R^2/u_R^2(%)	U_{95R}	U_{95R}/R(%)[a]
U	1.04311	0.01864	0.07360	0.07592	6.0	94.0	0.17918	17.2
V	0.00145	0.00139	0.00568	0.00585	5.7	94.3	0.01380	954.3
W	0.04698	0.00659	0.00831	0.01061	38.6	61.4	0.02503	53.3
uu	0.00587	0.00045	0.00424	0.00426	1.1	98.9	0.01006	171.3
vv	0.00164	0.00034	0.00049	0.00060	32.5	67.5	0.00141	85.8
ww	0.00165	0.00019	0.00043	0.00047	16.6	83.4	0.00110	66.8
uv	-0.00028	0.00006	0.00018	0.00019	10.3	89.7	0.00044	157.7
uw	-0.00030	0.00003	0.00039	0.00039	0.6	99.4	0.00092	306.7
vw	-0.00005	0.00001	0.00003	0.00004	7.8	92.2	0.00008	172.5
TKE	0.00458	0.00049	0.00250	0.00255	3.7	96.3	0.00601	131.3
ω_x	-3.43248	0.01954	4.07438	4.07442	0.0	100.0	9.61564	280.1

[a]: Results are preliminary

Table 12: Wave field, flat free surface and Stokes-wave results

			x - station			
Variable	0.25	0.50	0.75	1.00	1.25	1.50
			Wave field, flat free surface, $Ak = 0$			
ζ_{Global} [#]	0.0006	-0.0106	-0.0027	0.0078	0.0014	-0.0088
ζ_{Local}	-0.0040	-0.0062	-0.0025	-0.0007	0.0084	-0.0046
			Wave field, Stokes-wave, $Ak = 0.21$			
ζ_{Global}	-0.0058	-0.0343	0.0038	0.0374	-0.0180	-0.0297
ζ-$\zeta_{Theoretical}(\%A)^{+}$	14.5	14.3	9.5	6.5	45.0	25.8

[+]: $A = 0.04$ (nondimensionalized by plate length), [#]: average ζ over all y-values

Table 13: Flow field, uniform and Stokes-wave flow results

			Flow field, without plate, uniform flow, $Ak = 0$			
U	1.0091	1.0296	1.0402	1.0000	0.9858	1.0326
V	-0.0033	-0.0049	0.0005	-0.0019	-0.0059	-0.0019
W	-0.0211	-0.0109	0.0091	0.0193	-0.0073	-0.0431
uu	0.0008	0.0007	0.0008	0.0010	0.0009	0.0009
vv	0.0006	0.0005	0.0006	0.0008	0.0006	0.0007
ww	0.0002	0.0003	0.0002	0.0004	0.0003	0.0003
uv	0.0000	-0.0002	0.0000	-0.0002	-0.0002	-0.0001
uw	0.0000	0.0000	0.0000	0.0000	0.0000	0.0000
vw	0.0000	0.0000	0.0000	0.0000	0.0000	0.0000
TKE	0.0008	0.0007	0.0009	0.0011	0.0009	0.0010
ω_x	0.0410	0.0392	0.0828	0.0761	0.0399	0.0069
			Flow field, without plate, Stokes-wave, $Ak = 0.21$			
U-$U_{Theoretical}(\%U_c)^{*}$	1.20	0.50	1.57	0.72	3.54	4.88
W-$W_{Theoretical}(\%U_c)^{*}$	4.54	0.28	0.03	3.21	1.54	0.44

[*]: average difference in velocity over all measured y and z values

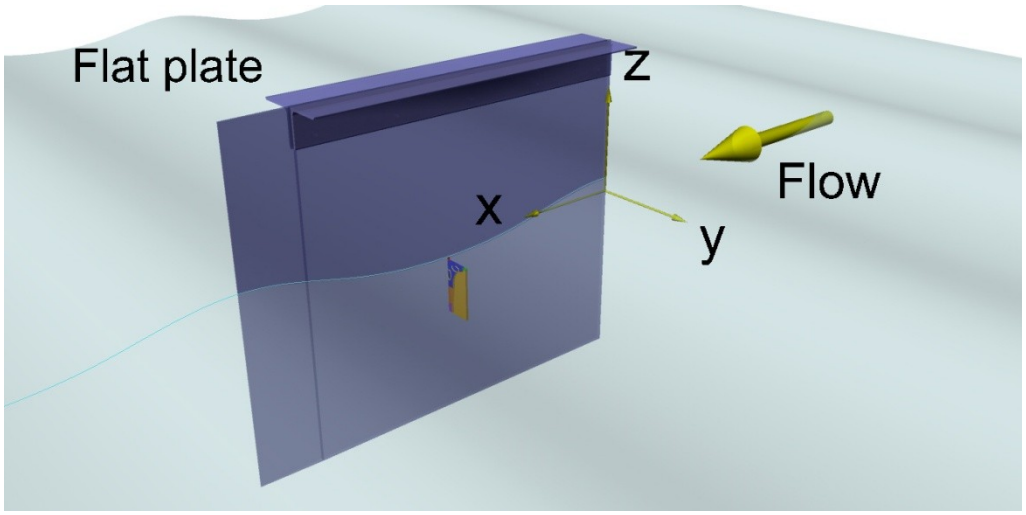

(a)

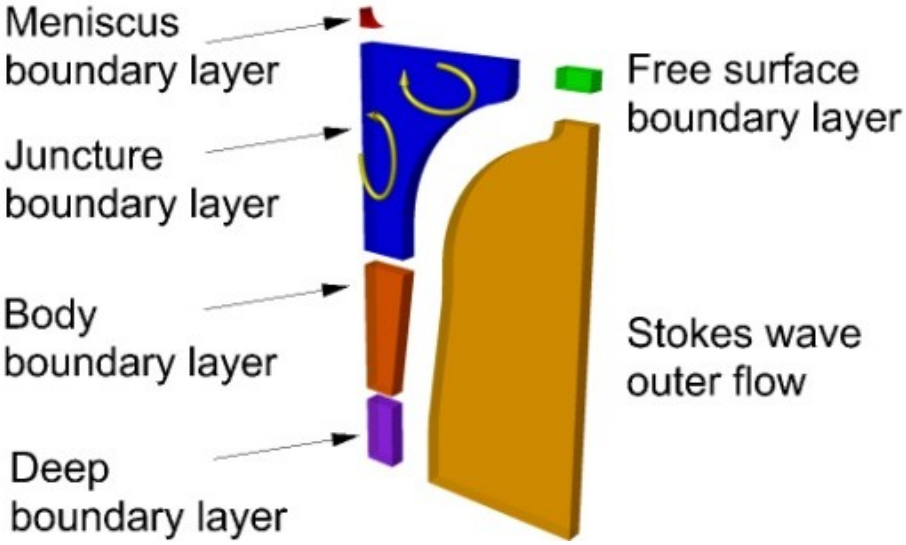

(b)

Figure 1: Illustration of the experimental model and measurement showing (a) the flat plate, Stokes wave, and juncture region. The juncture region (b) is divided into regions of interest and shows the vorticity direction

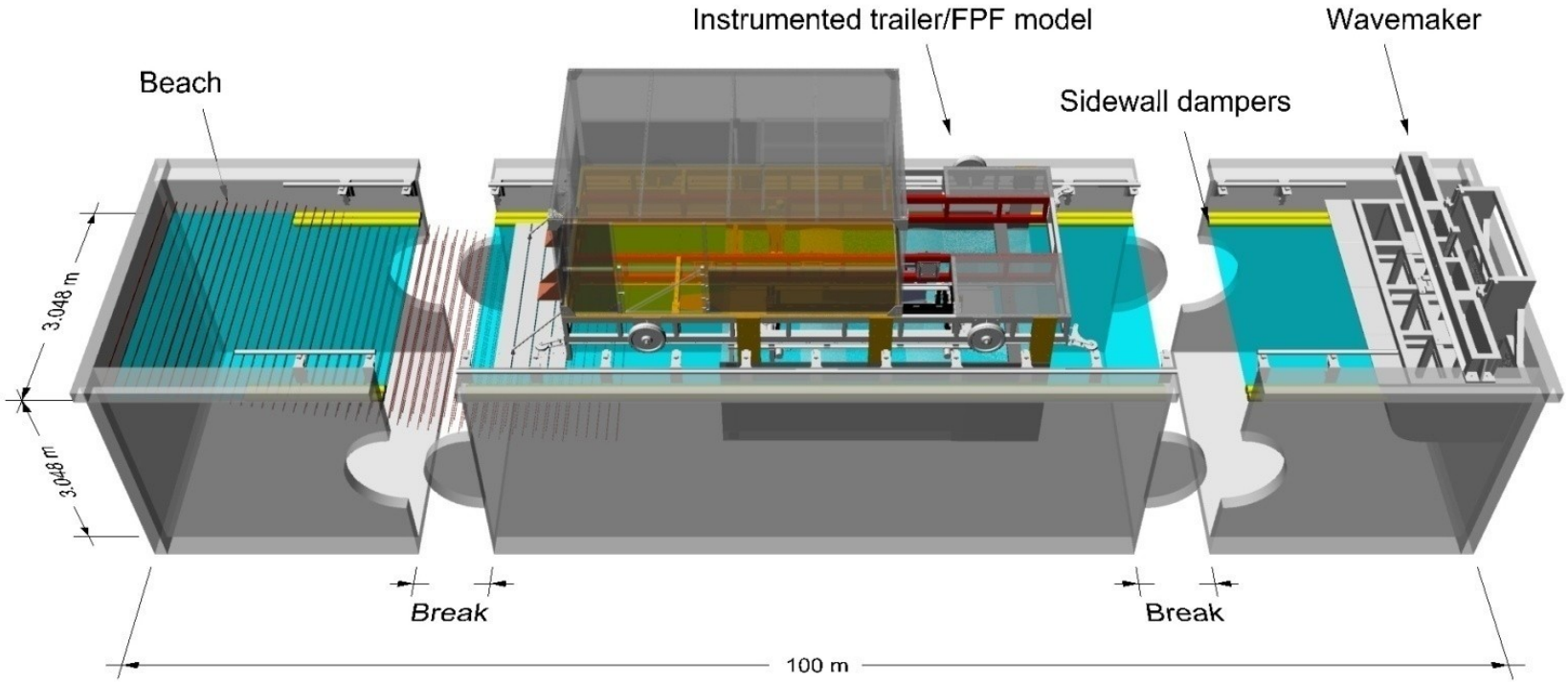

Figure 2: IIHR Hydroscience and Engineering Towing Tank Facility

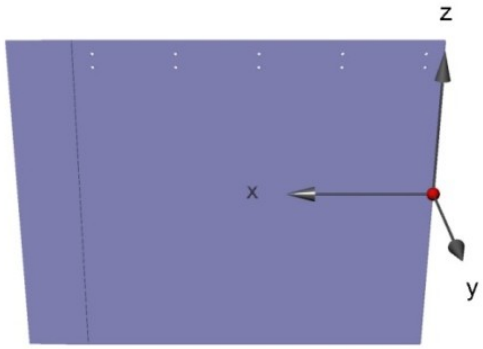

Figure 3: Flat plate and coordinate system

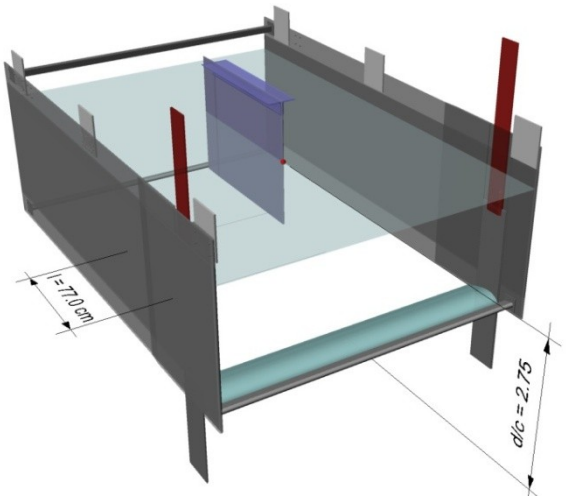

(a)

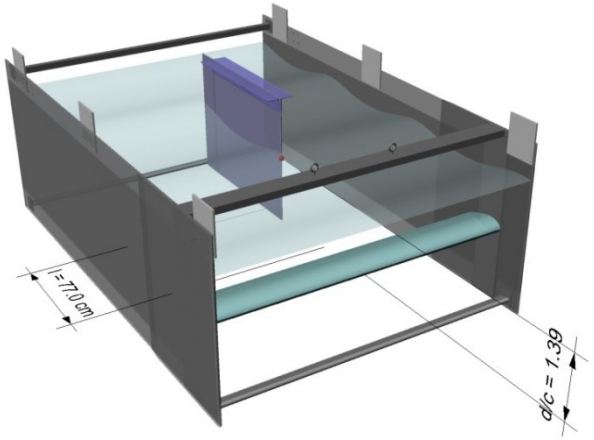

(b)

Figure 4: Flat plate foil model arrangement for (a) $Ak = 0$ tests where $d/c = 2.75$, and (b) $Ak = 0.21$ tests where $d/c = 1.39$.

Figure 5: Wave gauges, amplifiers, AD card and PC for wave elevation

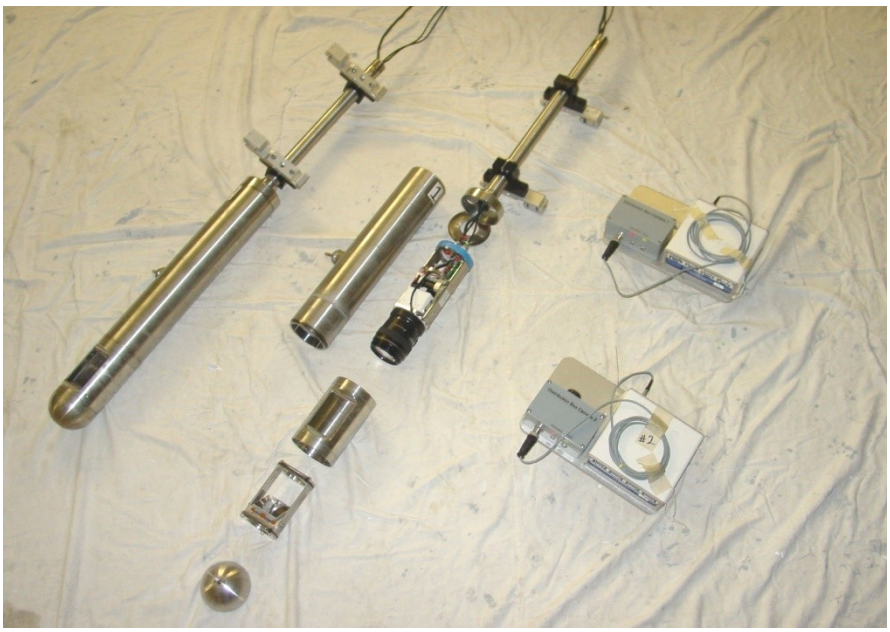

(a)

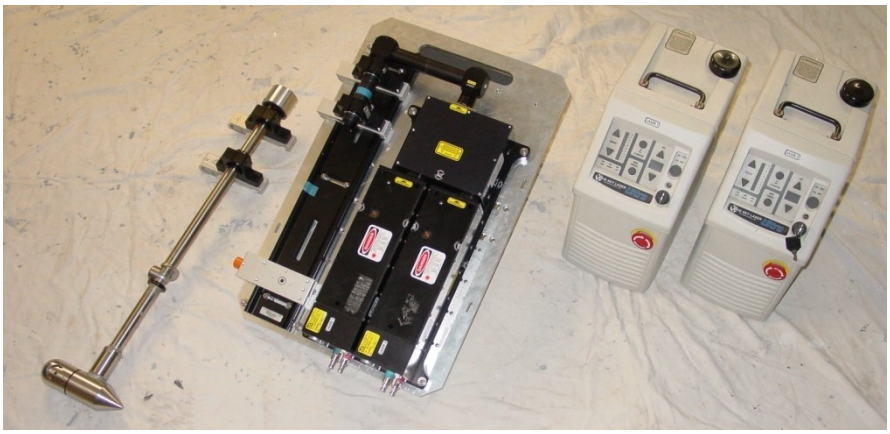

(b)

Figure 6: SPIV equipment showing (a) cameras and (b) laser assemblies

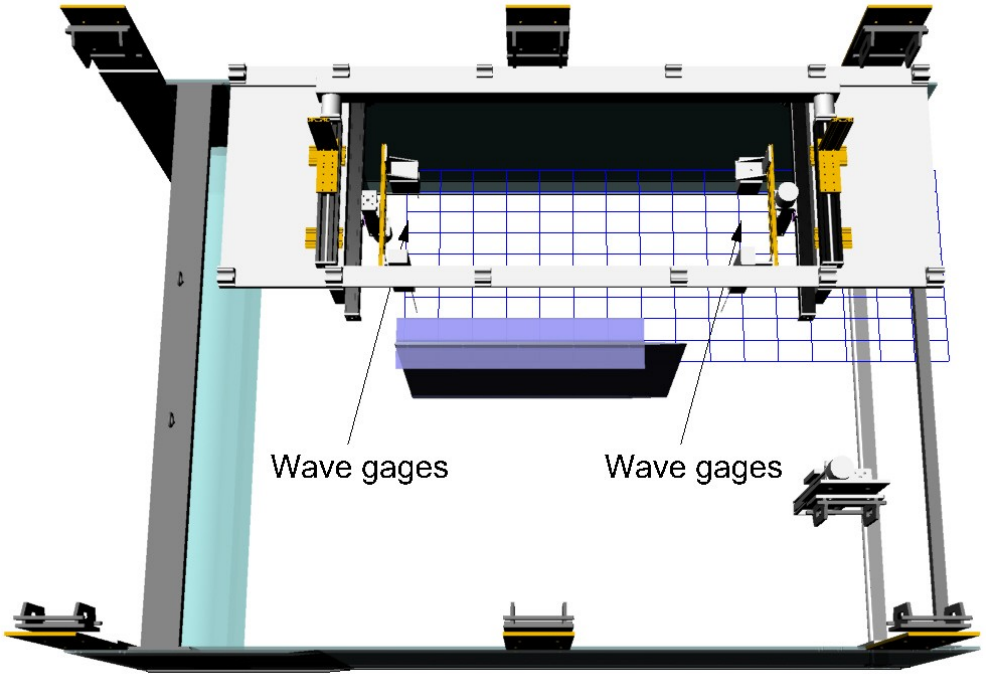

Figure 7: Overhead view of experimental setup for wave field measurements

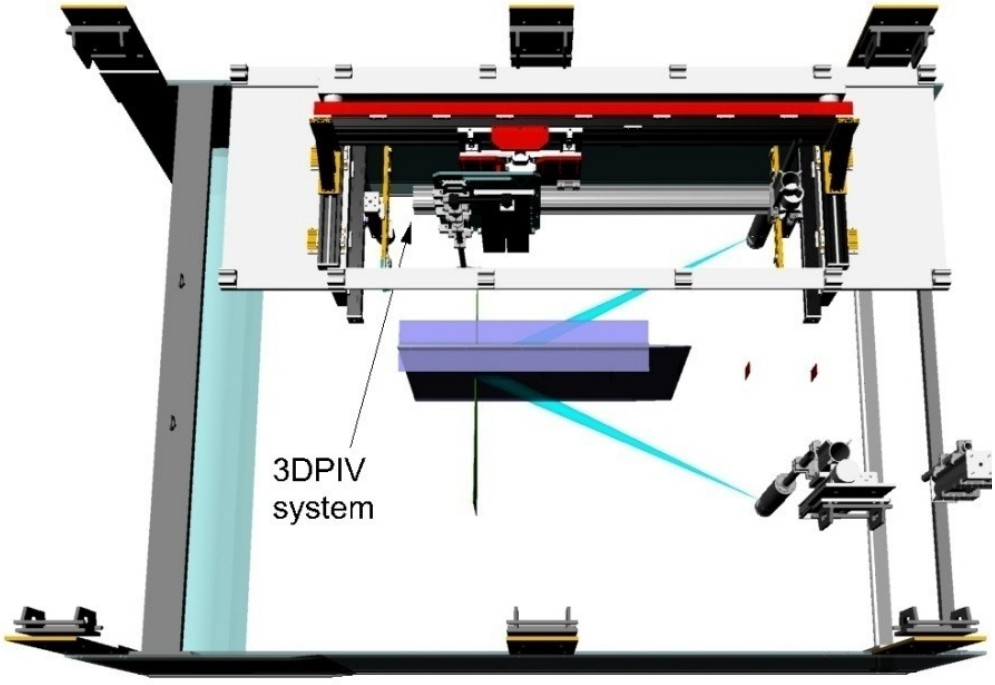

Figure 8: Overhead view of experimental setup for flow field measurements

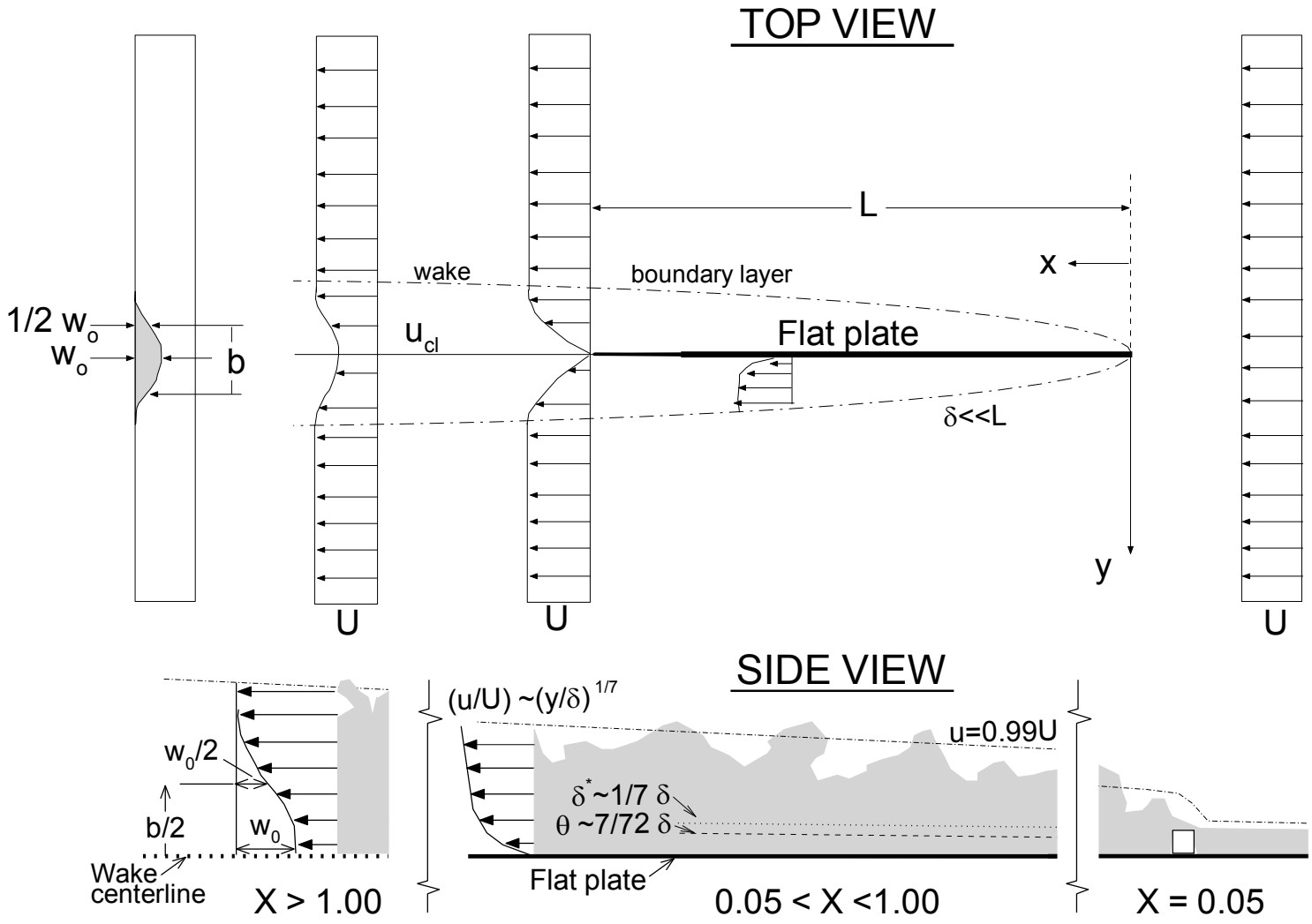

Figure 9: Growth of boundary layer on a flat plate, also showing the wake

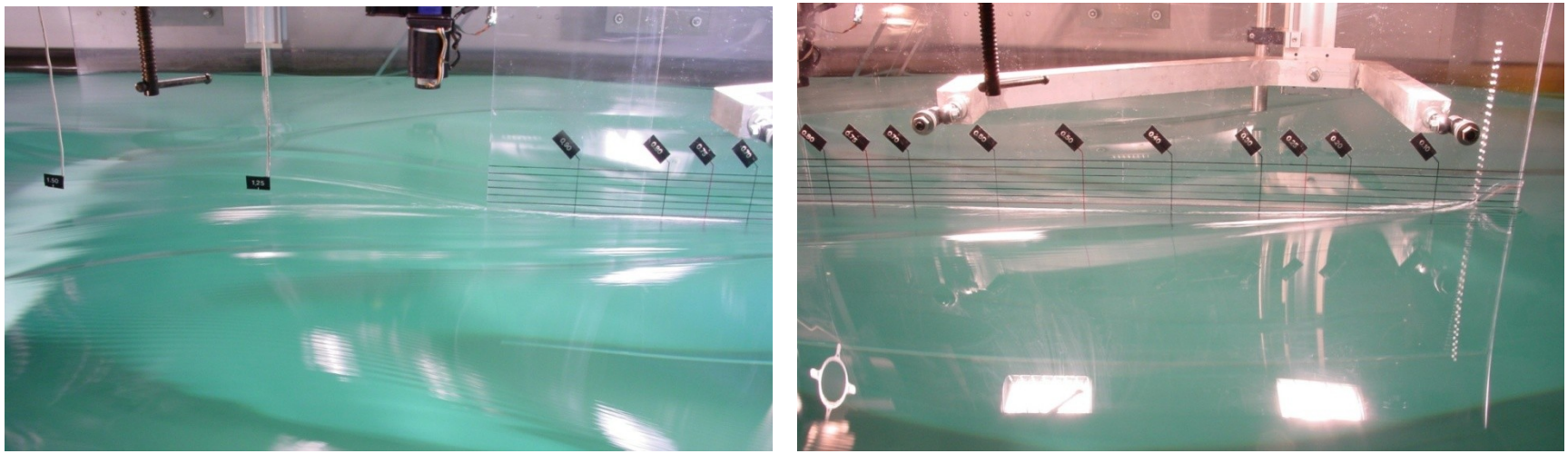

Figure 10: Downward looking perspective of the starboard side of the flat plate showing the fore (right) and aft (left) section, $Ak = 0$

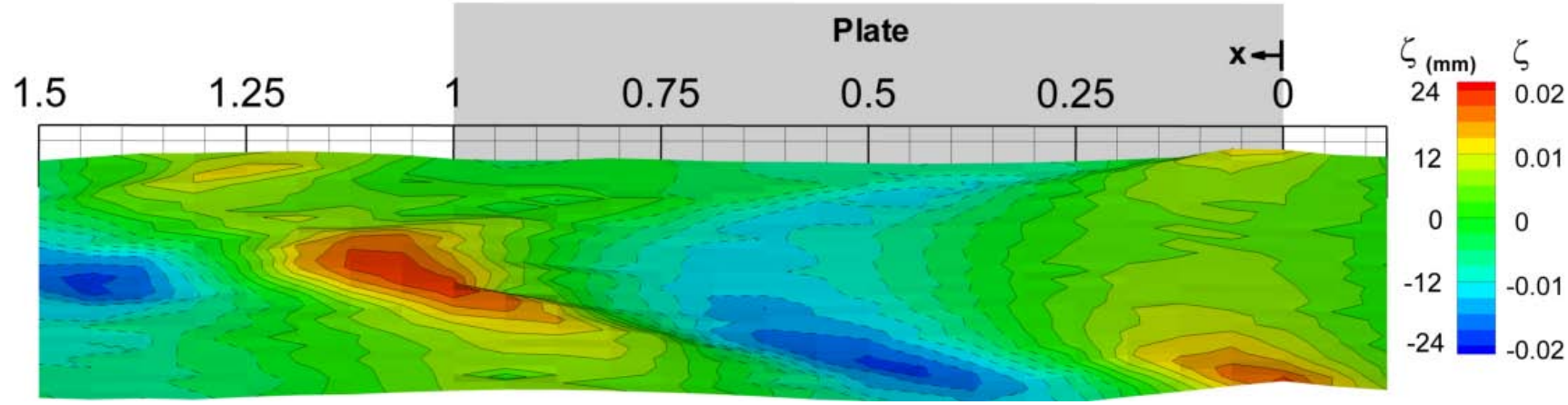

Figure 11: Global wave elevation measurements on starboard side of plate, $Ak = 0$

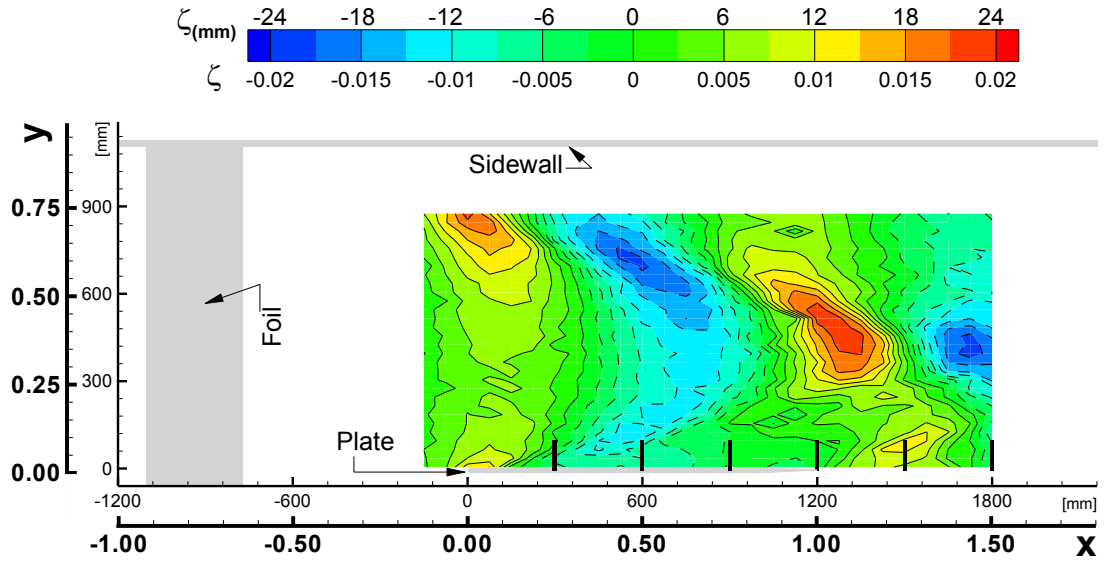

Figure 12: Contour plot of global wave elevations, $Ak = 0$

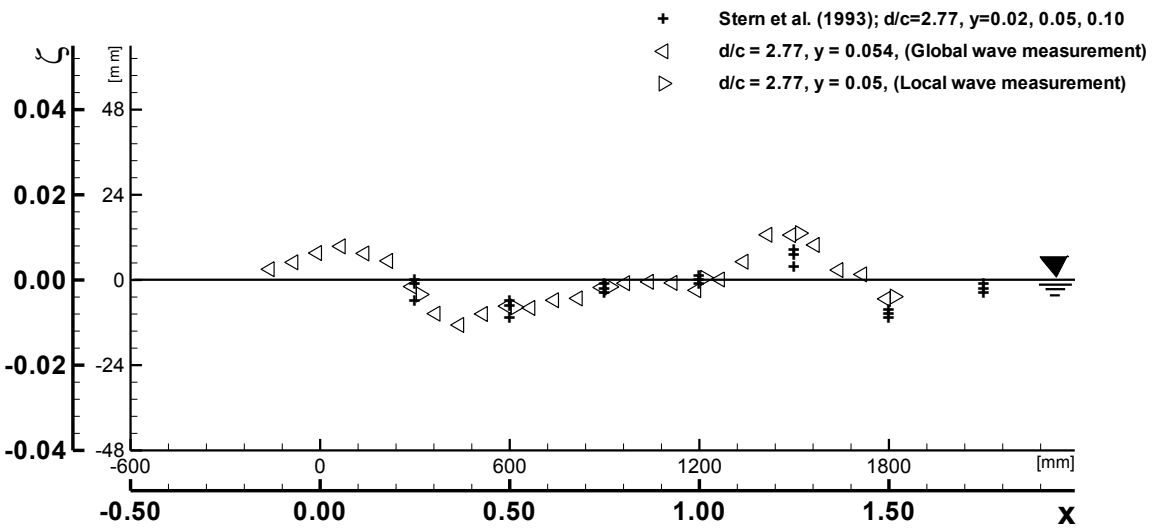

Figure 13: Longitudinal wave cut showing benchmark data and global and local wave elevation measurements, $Ak = 0$

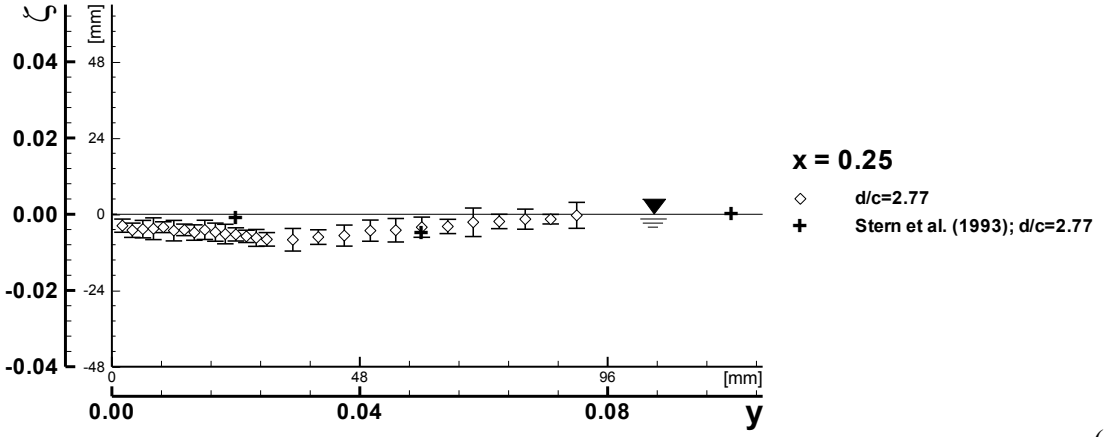

(a)

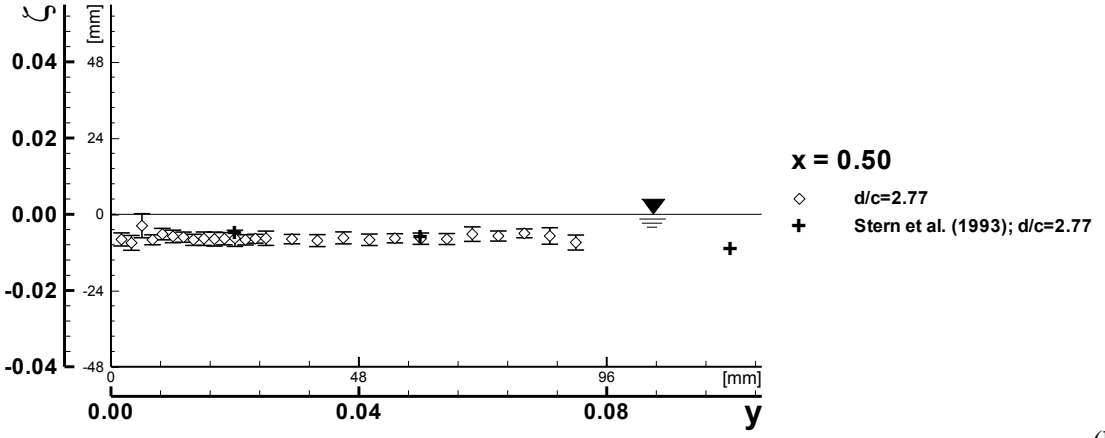

(b)

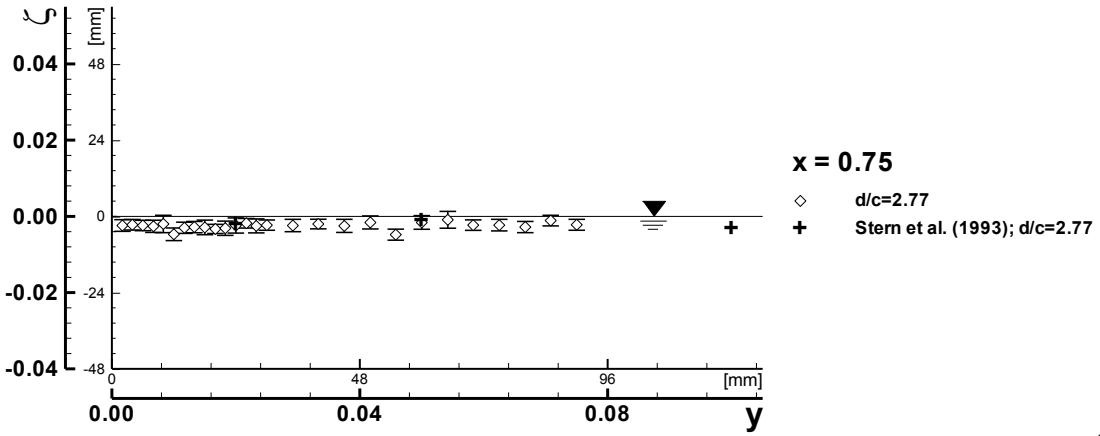

(c)

Figure 14: Local wave elevations at x = (a) 0.25, (b) 0.50, and (c) 0.75, Ak = 0

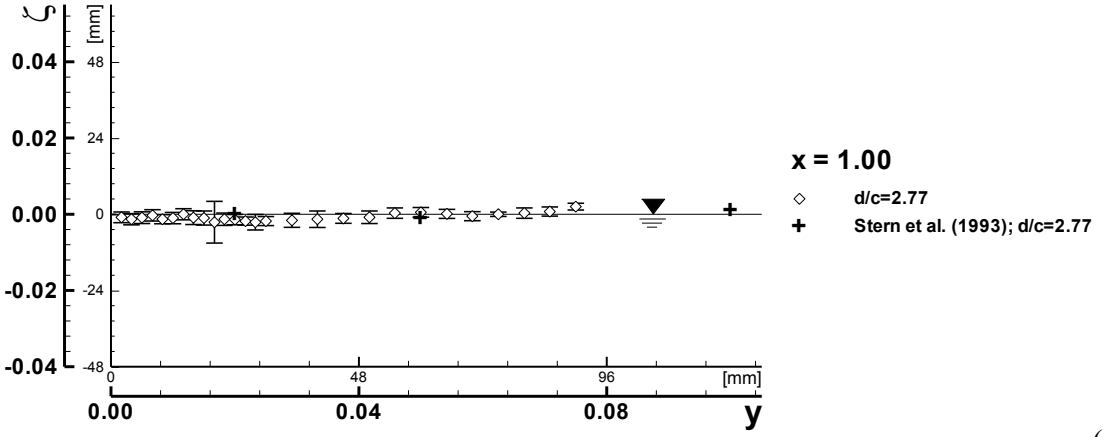

(d)

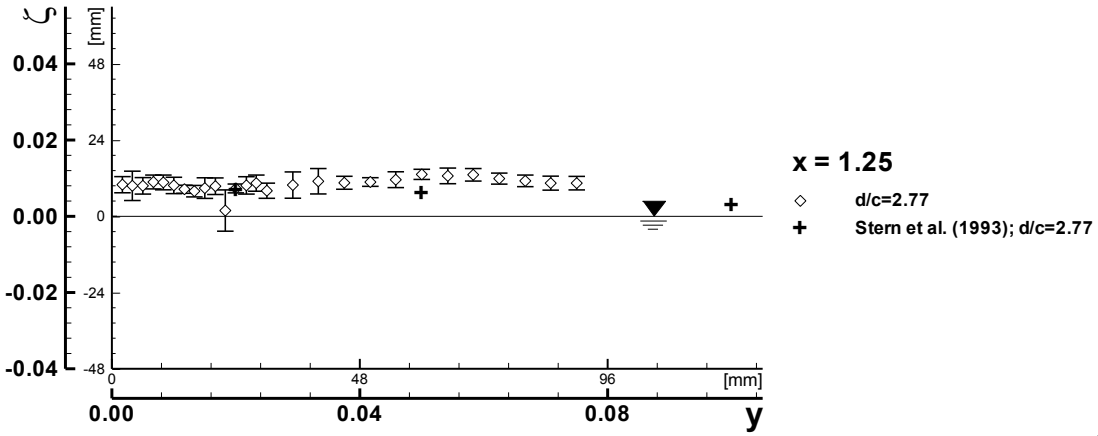

(e)

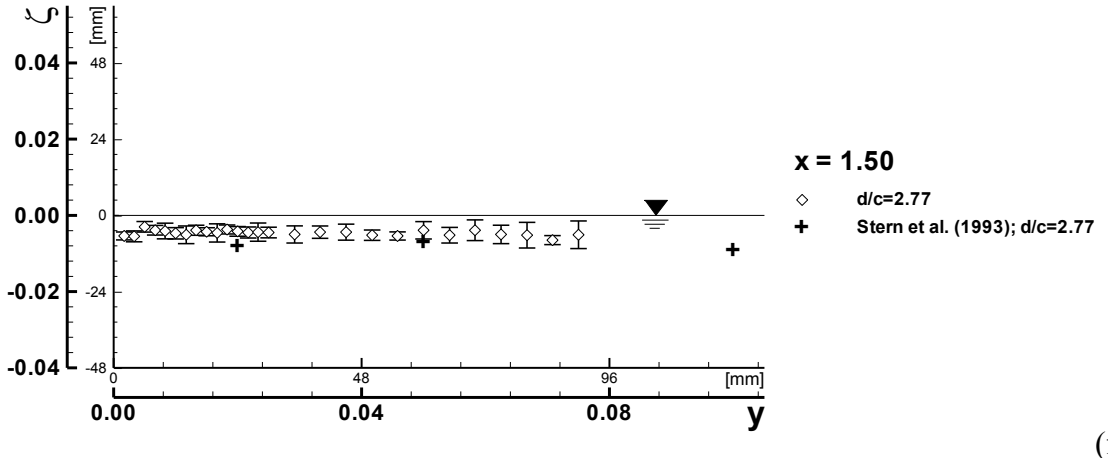

(f)

Figure 14 continued: Local wave elevations at x = (d) 1.00, (e) 1.25, and (f) 1.50, $Ak = 0$

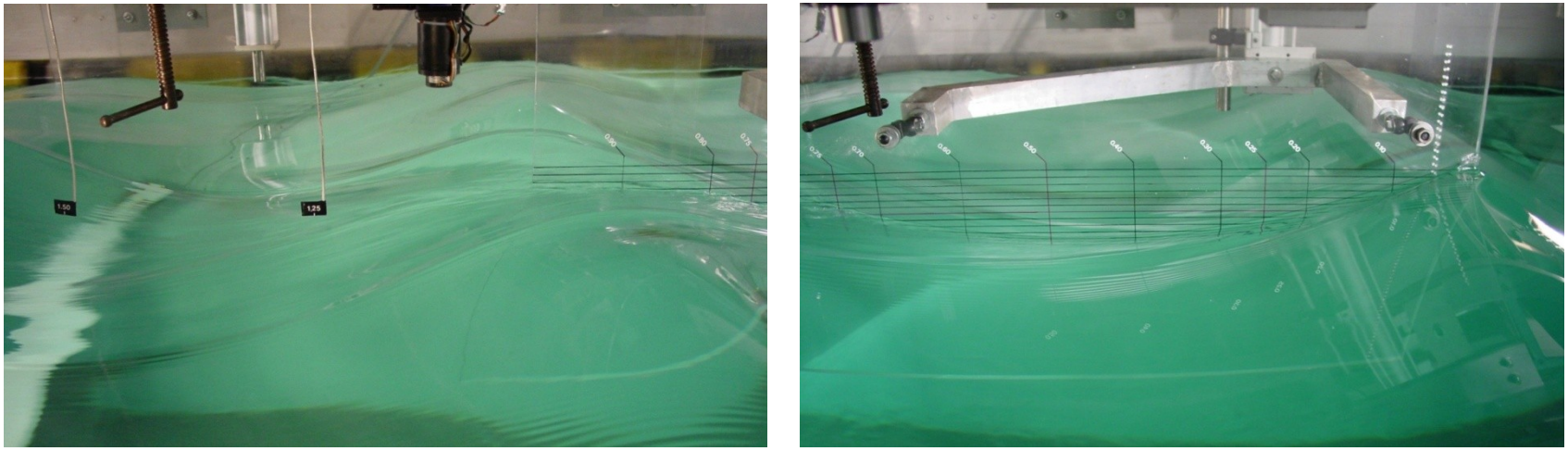

Figure 15: Downward looking perspective of the starboard side of the flat plate showing the fore (right) and aft (left) section, $Ak = 0.21$

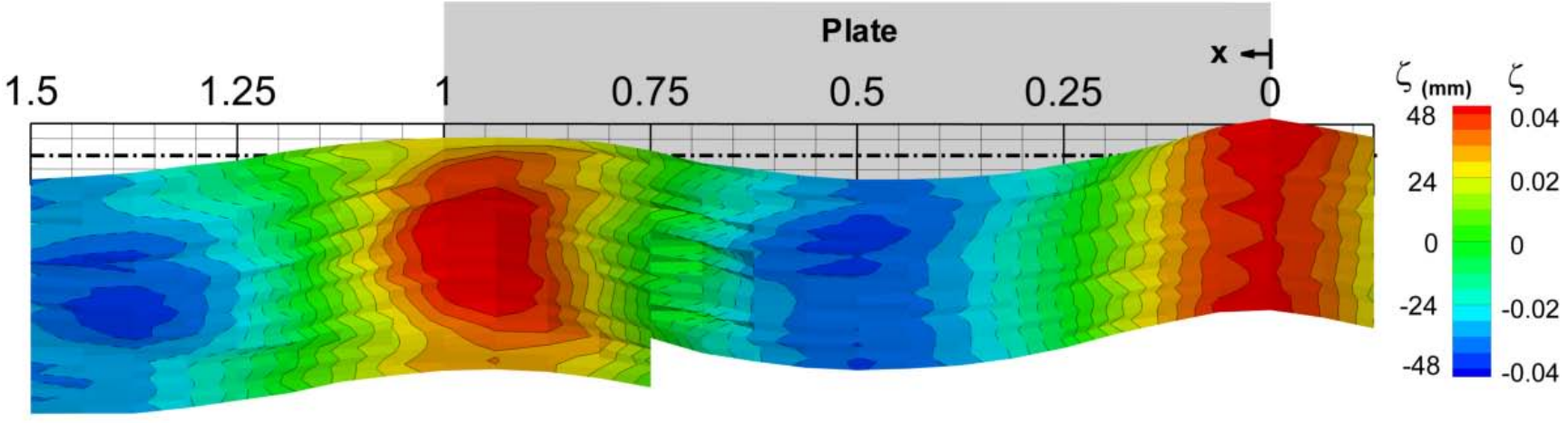

Figure 16: Global wave elevation measurements on starboard side of plate, $Ak = 0.21$

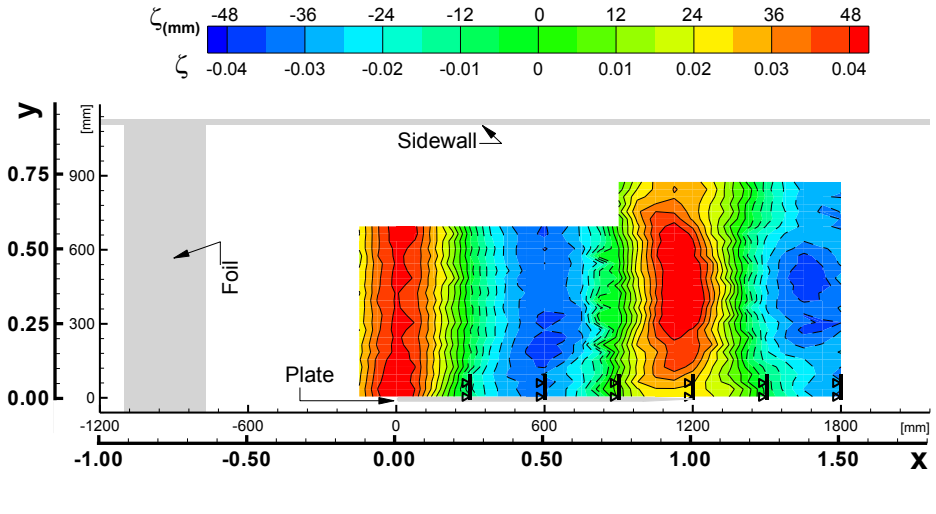

(a)

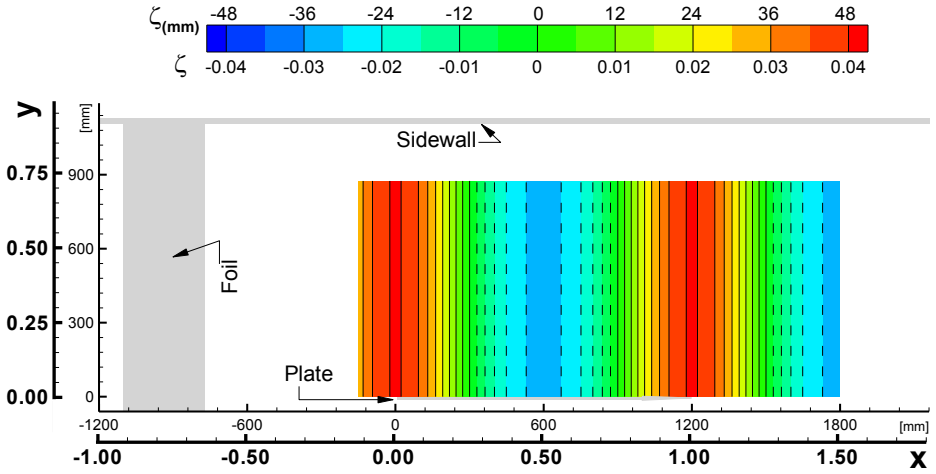

(b)

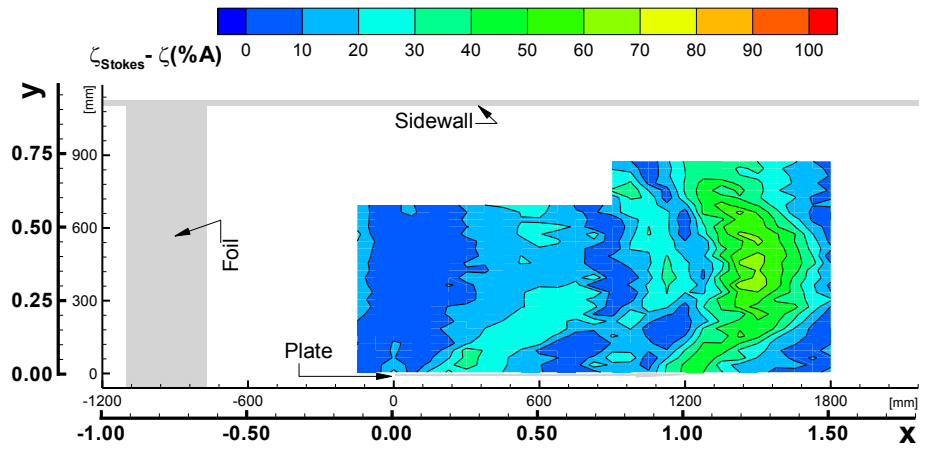

(c)

Figure 17: Contour plots of global wave elevations, showing (a) measured values for Ak = 0.21, (b) theoretical second-order Stokes wave, Ak = 0.21, and (c) difference (shown in % A) between theoretical Stokes wave and measured wave for Ak = 0.21

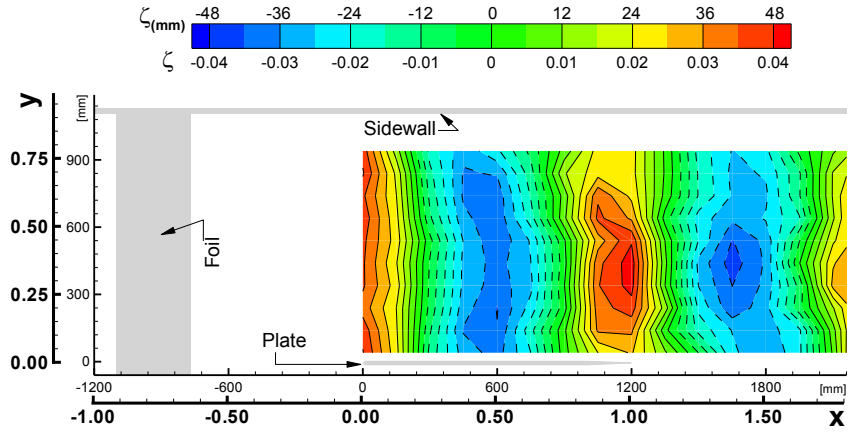

(a)

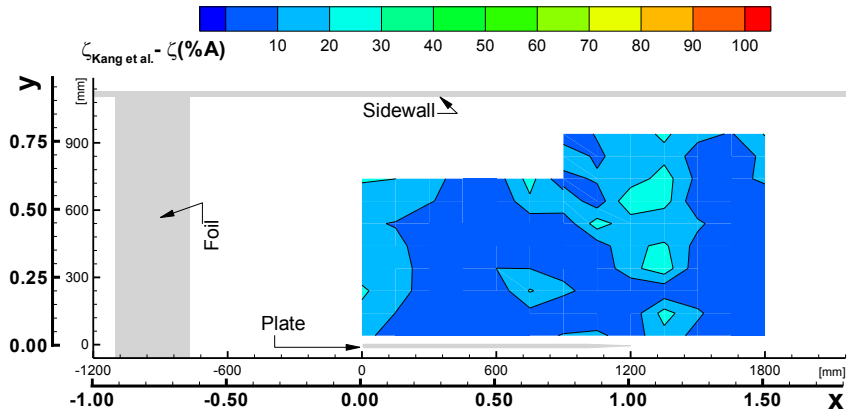

(b)

Figure 18: Contour plots of global wave elevations, showing (a) wave elevations of Kang et al. (2008) and (b) difference (shown in % A) between the benchmark wave of Kang et al. (2008) and measured wave for $Ak = 0.21$

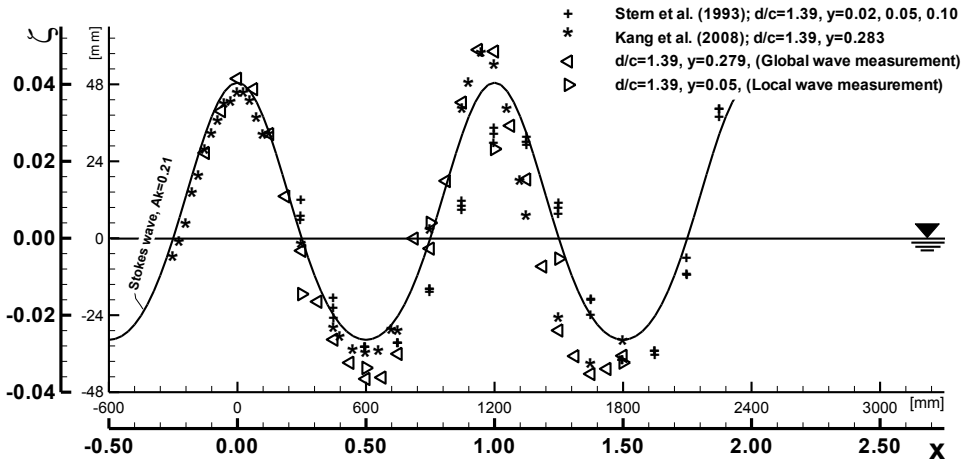

Figure 19: Longitudinal wave cut showing benchmark data and global and local wave elevation measurements, $Ak = 0.21$

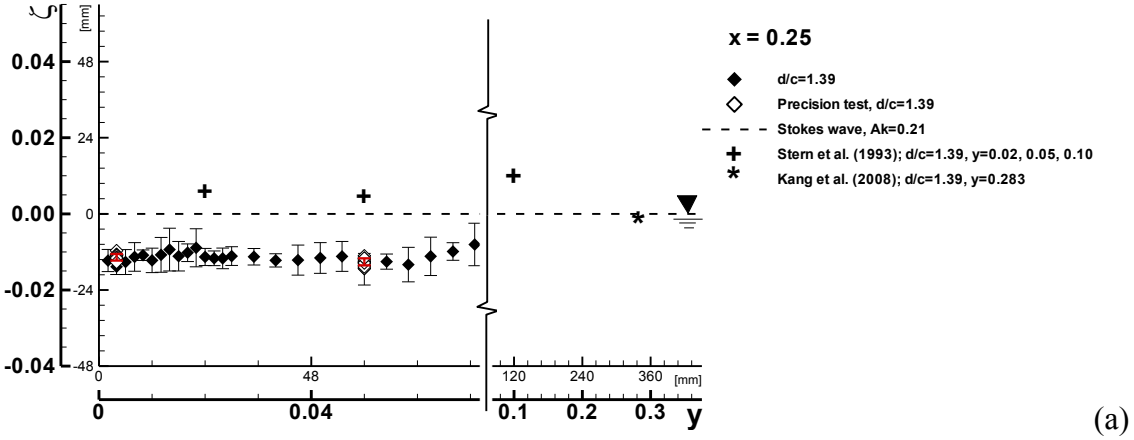

(a)

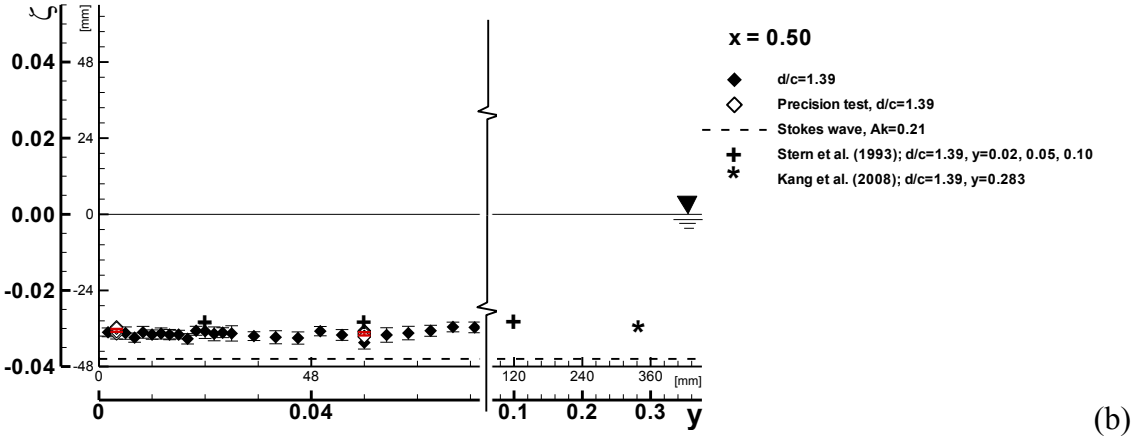

(b)

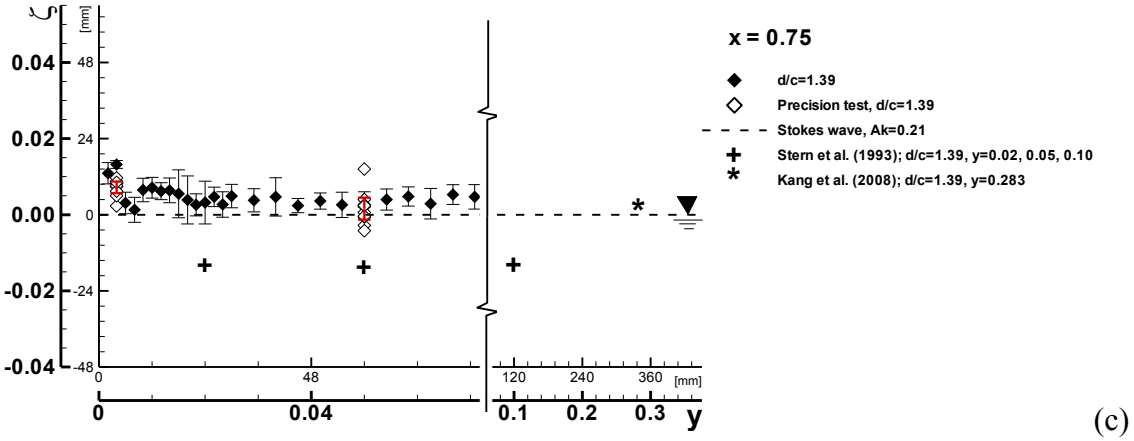

(c)

Figure 20: Local wave elevations at x = (a) 0.25, (b) 0.50, and (c) 0.75, Ak = 0.21

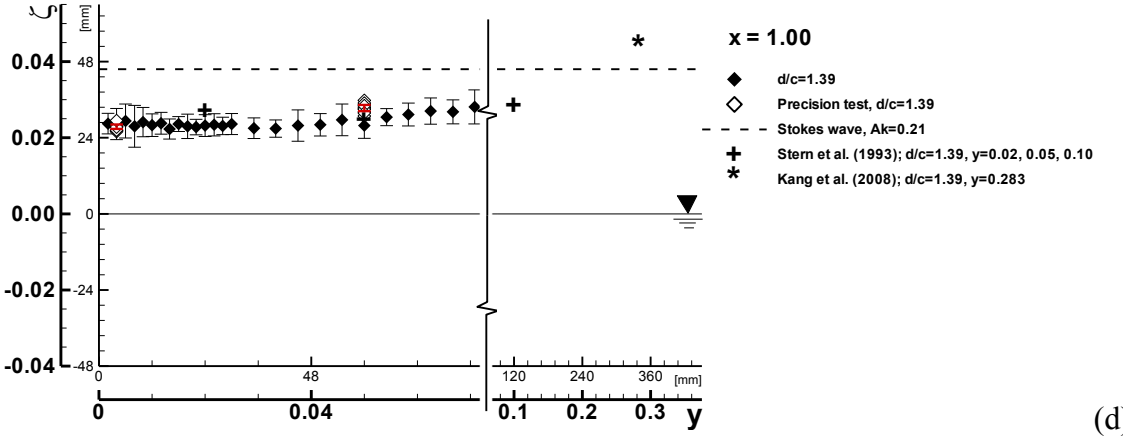

(d)

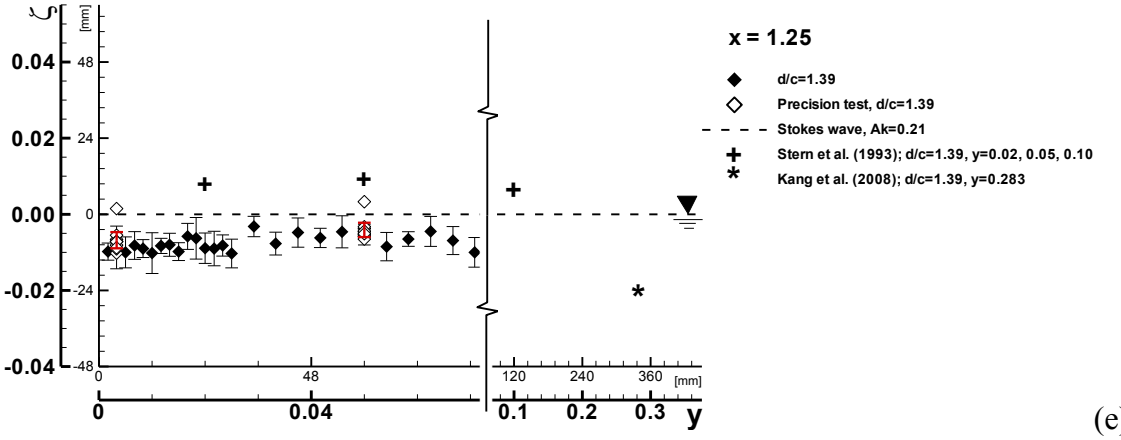

(e)

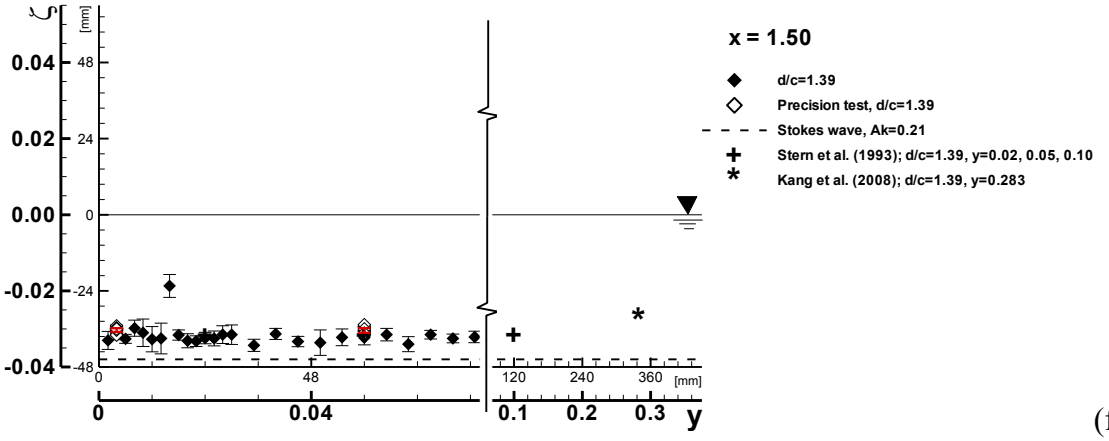

(f)

Figure 20 continued: Local wave elevations at x = (d) 1.00, (e) 1.25, and (f) 1.50, Ak = 0.21

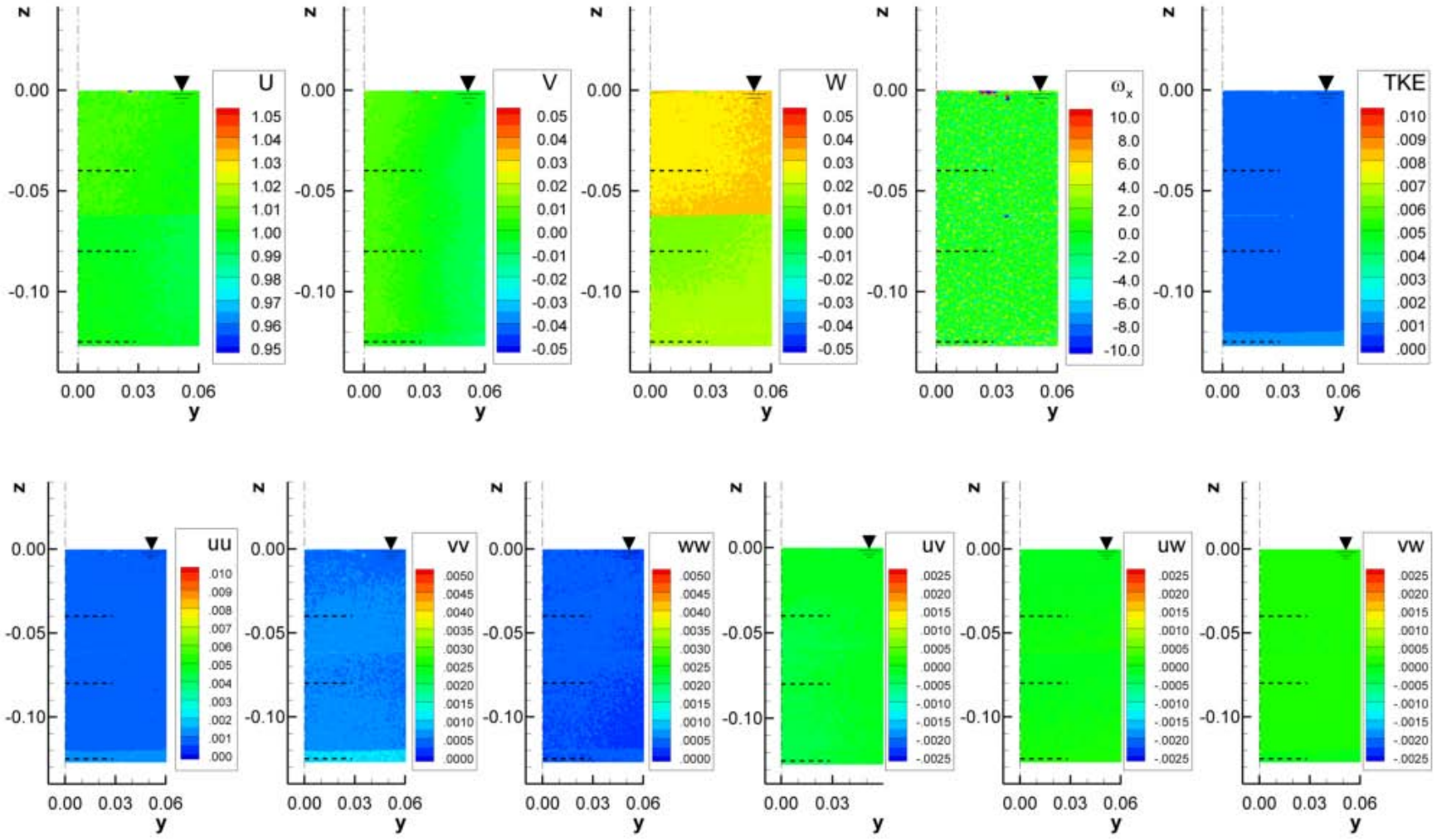

Figure 21: Uniform flow field results showing mean and turbulent quantities, $Ak = 0$

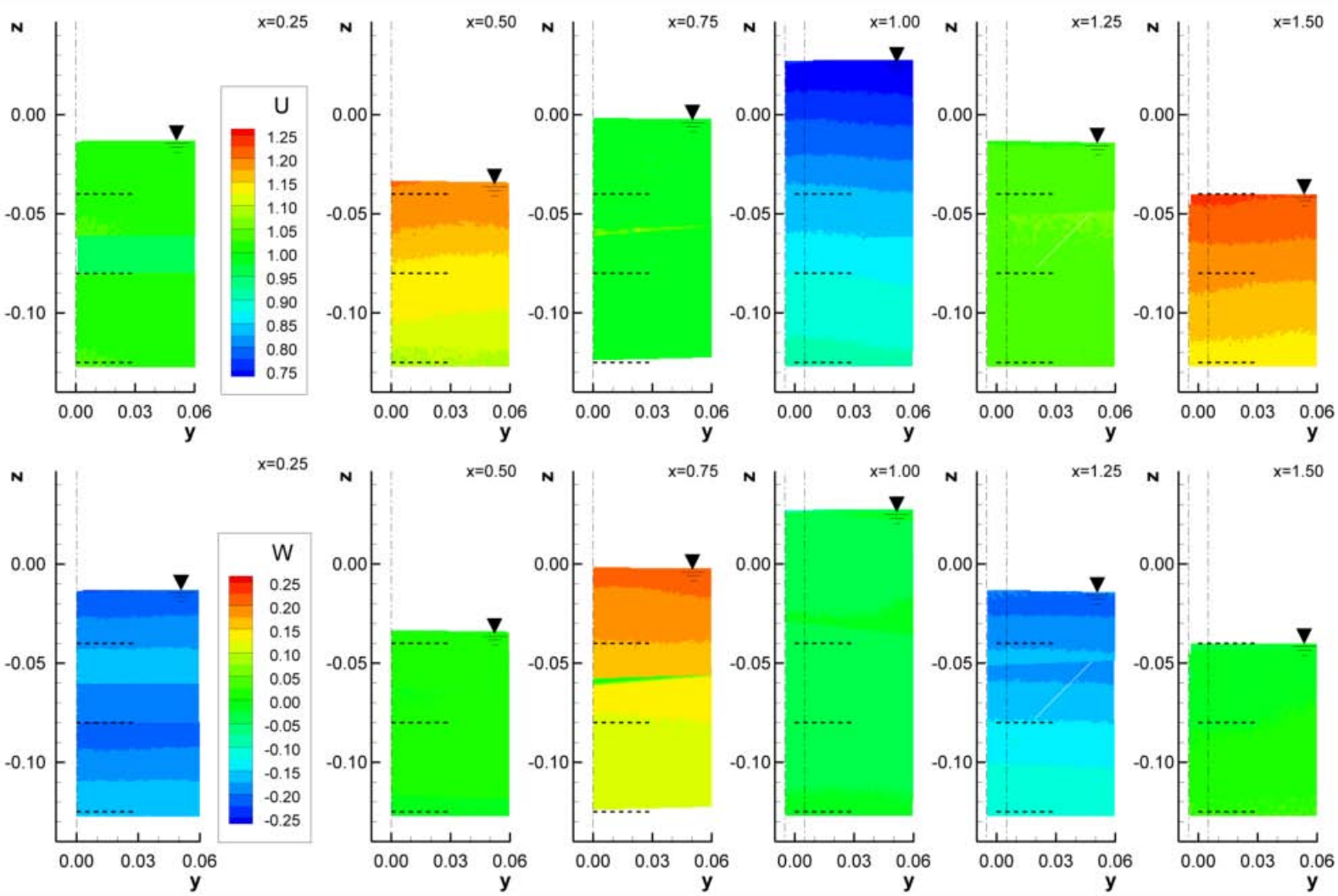

Figure 22: Stokes-wave flow field results highlighting U (top row) and W (bottom row) velocity components, $Ak = 0.21$

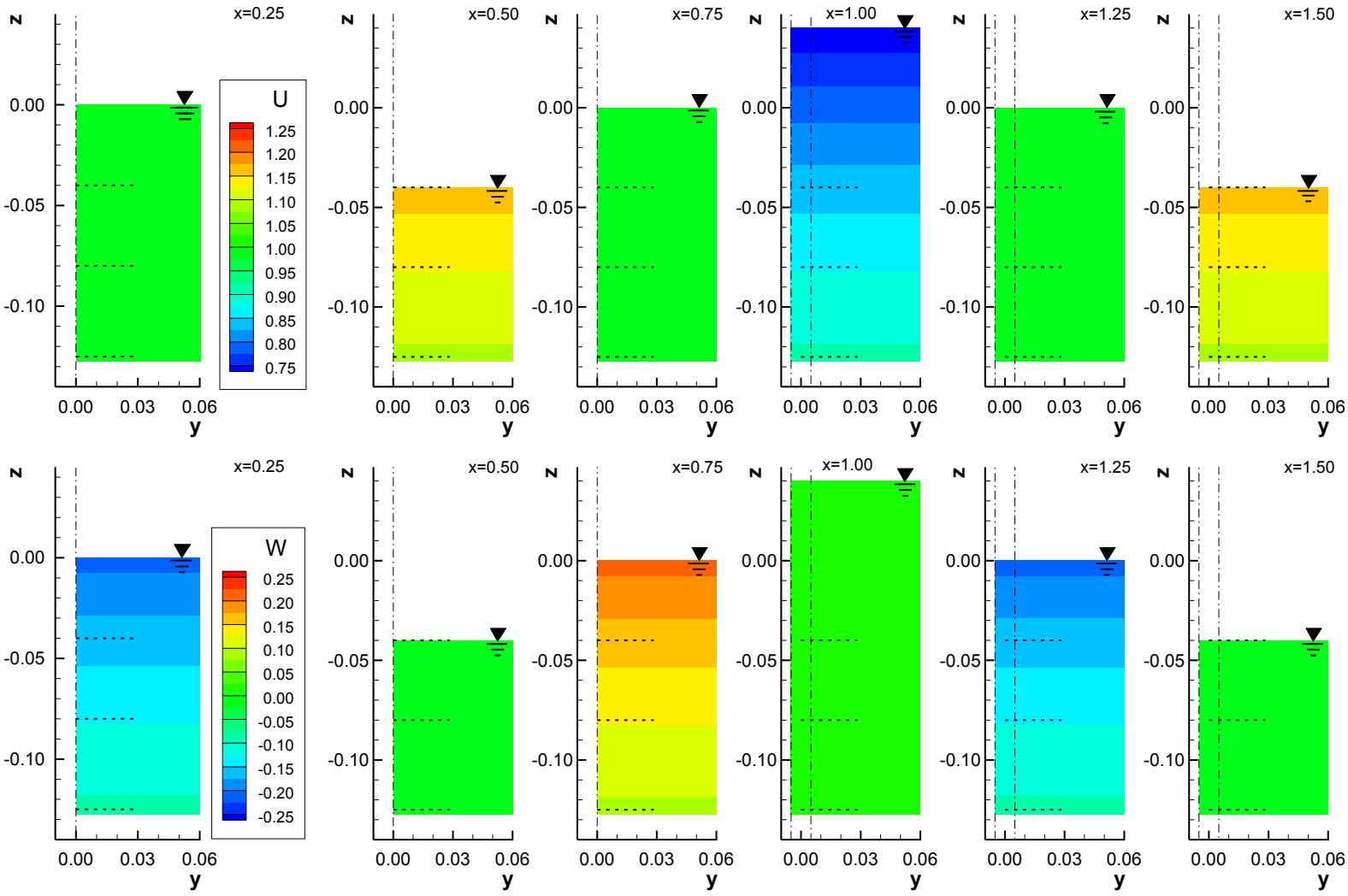

Figure 23: Theoretical Stokes-wave flow field showing the U (top row) and W (bottom row) velocity components, $Ak = 0.21$

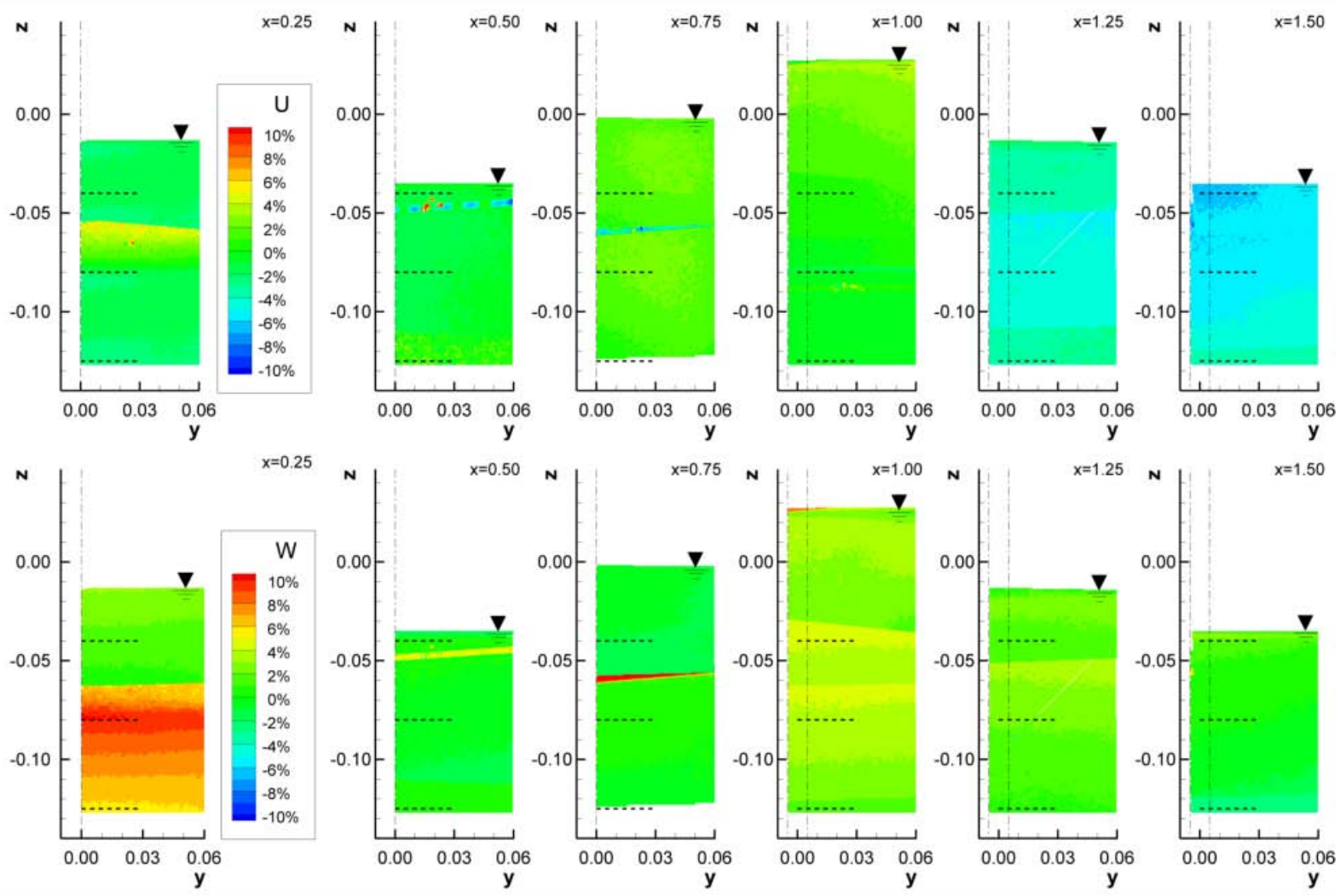

Figure 24: Percent difference between theoretical and measured Stokes-wave flow of the U (top row) and W (bottom row) velocity components, $Ak = 0.21$

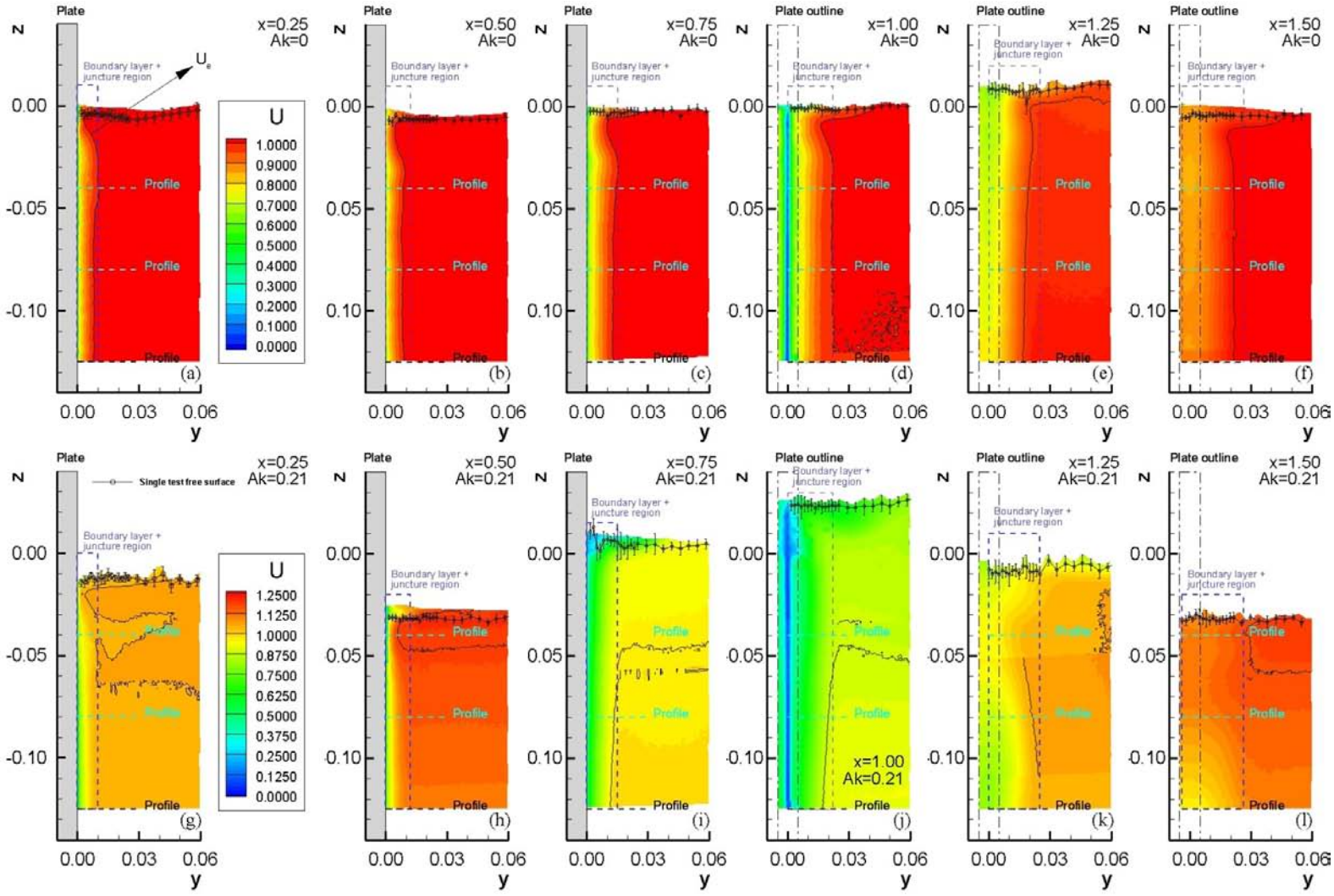

Figure 25: Full-domain U contours for all x and $Ak = 0$ (top: a-f) and $Ak = 0.21$ (bottom; g-l). Wave field data is overlaid on contours

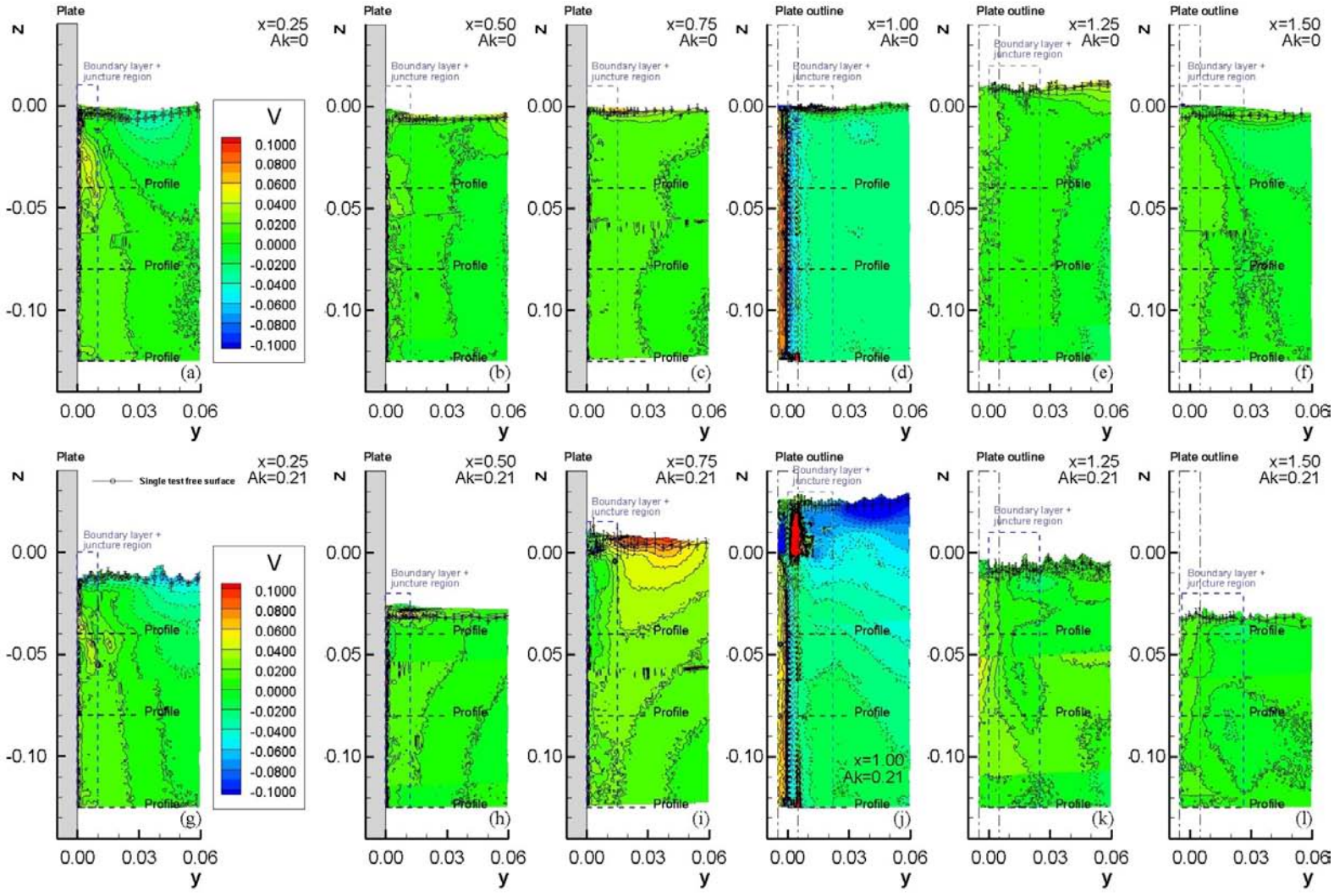

Figure 26: Full-domain V contours for all x and $Ak = 0$ (top: a-f) and $Ak = 0.21$ (bottom: g-l). Wave field data is overlaid on contours

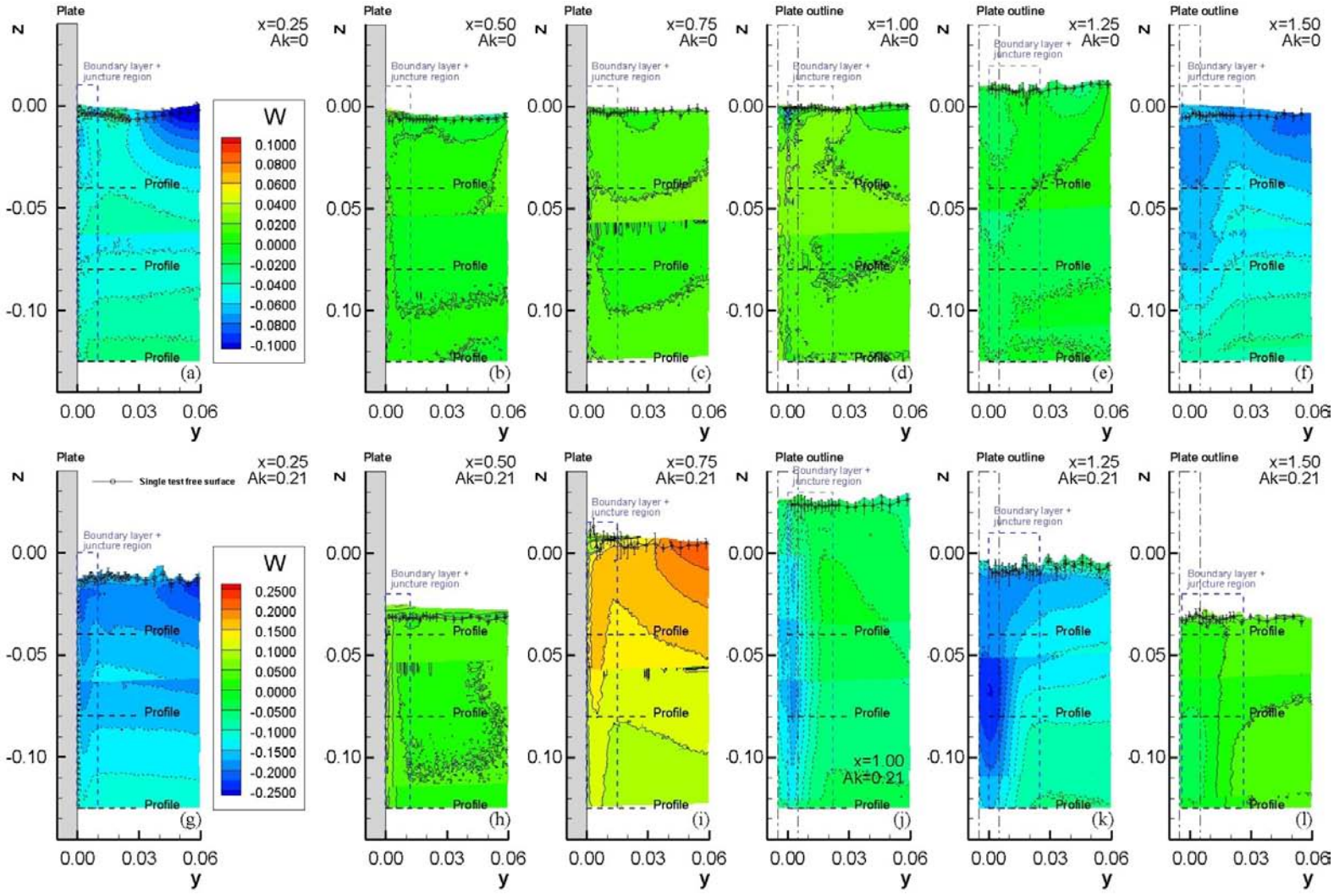

Figure 27: Full-domain W contours for all x and $Ak = 0$ (top: a-f) and $Ak = 0.21$ (bottom: g-l). Wave field data is overlaid on contours

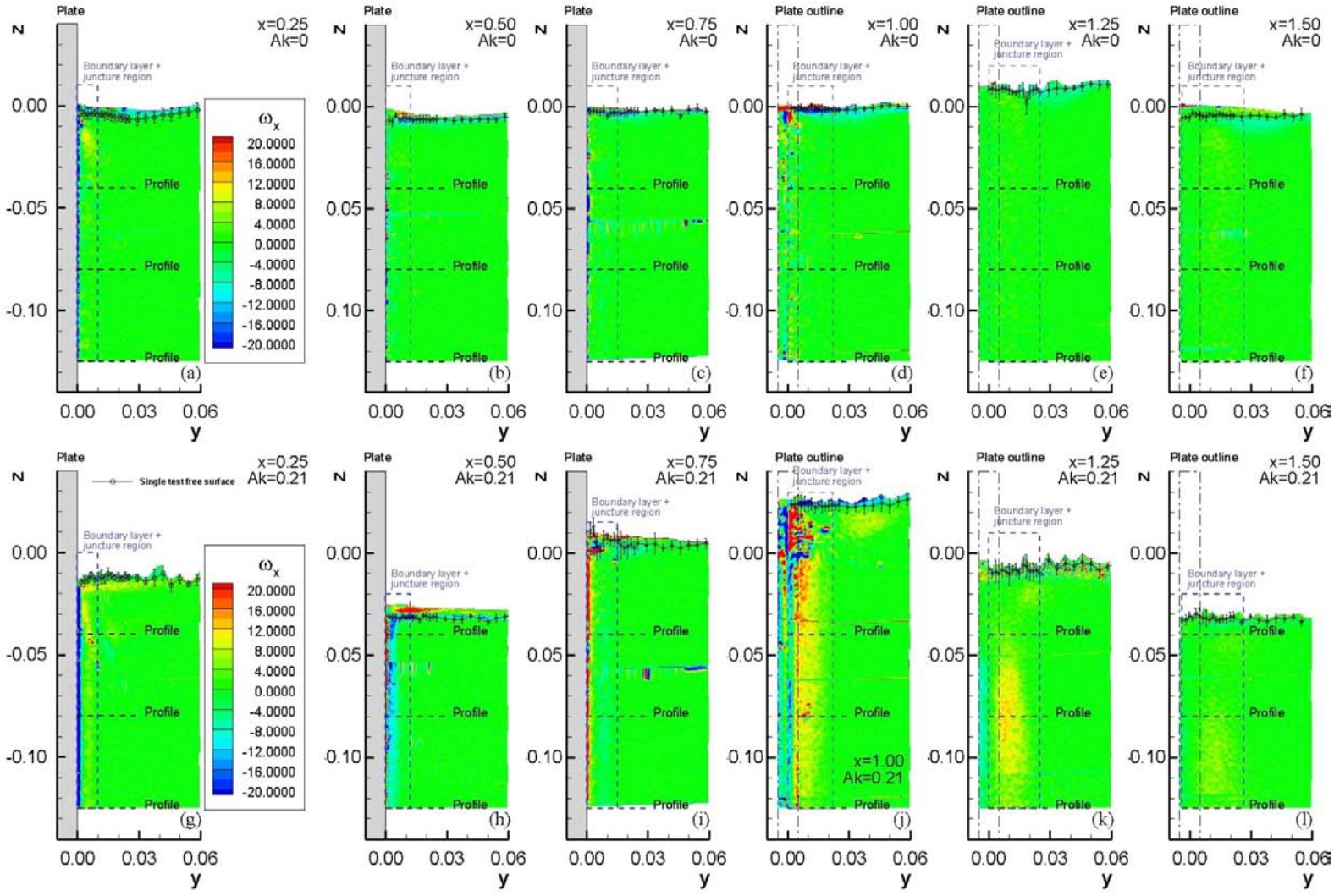

Figure 28: Full-domain ω_x contours for all x and $Ak = 0$ (top: a-f) and $Ak = 0.21$ (bottom: g-l). Wave field data is overlaid on contours

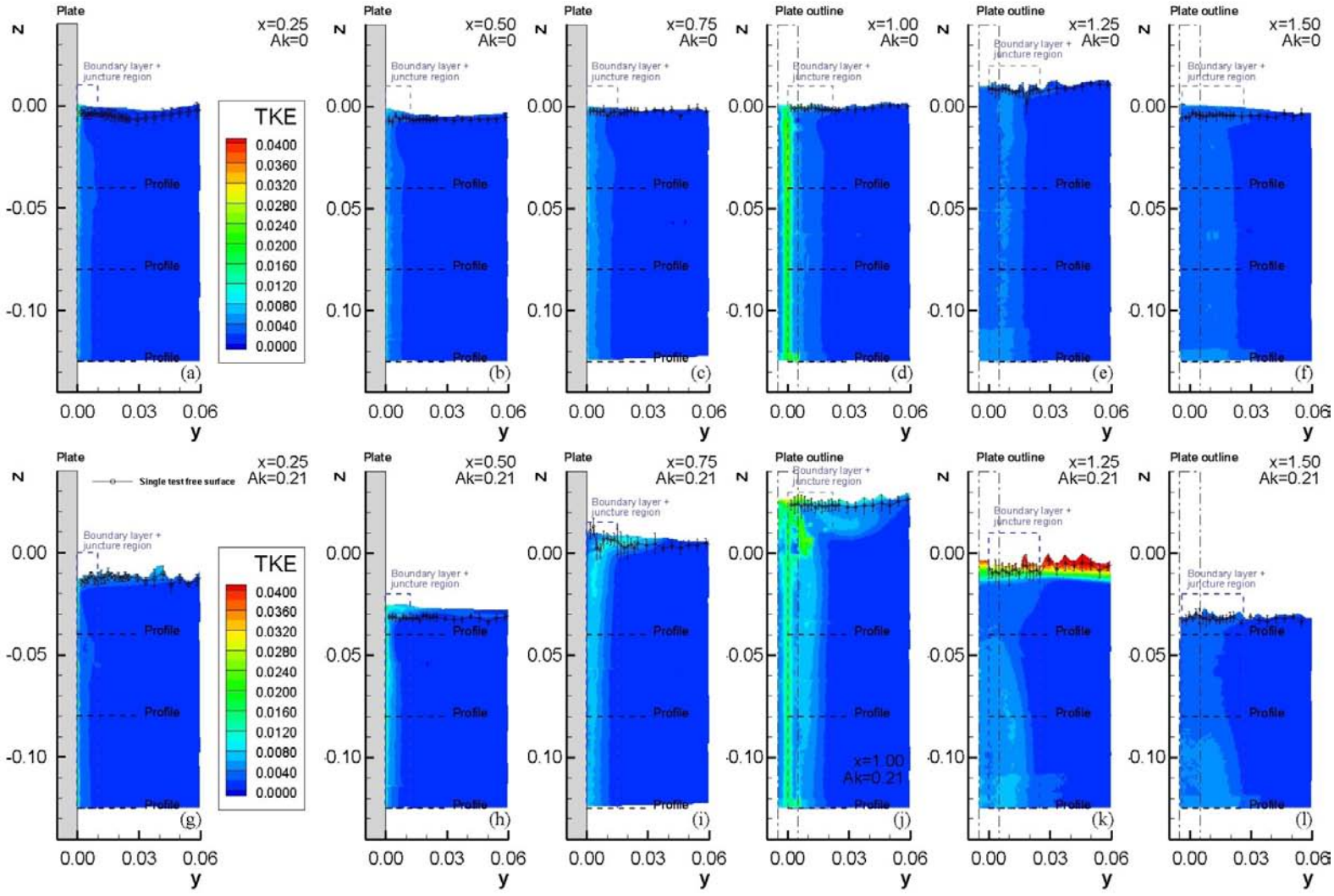

Figure 29: Full-domain *TKE* contours for all *x* and *Ak* = 0 (top: a-f) and *Ak* = 0.21 (bottom: g-l). Wave field data is overlaid on contours

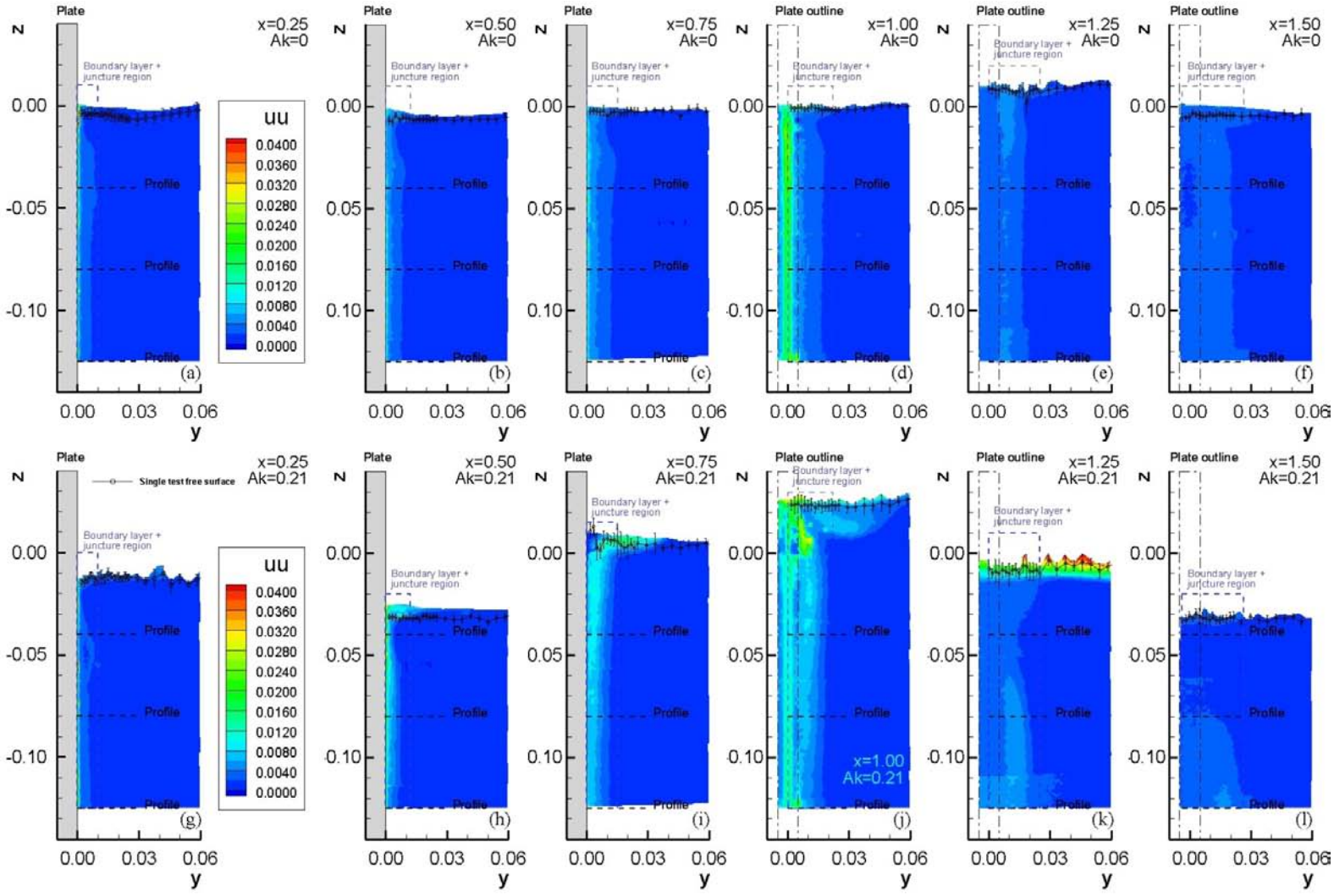

Figure 30: Full-domain *uu* contours for all *x* and *Ak* = 0 (top: a-f) and *Ak* = 0.21 (bottom: g-l). Wave field data is overlaid on contours

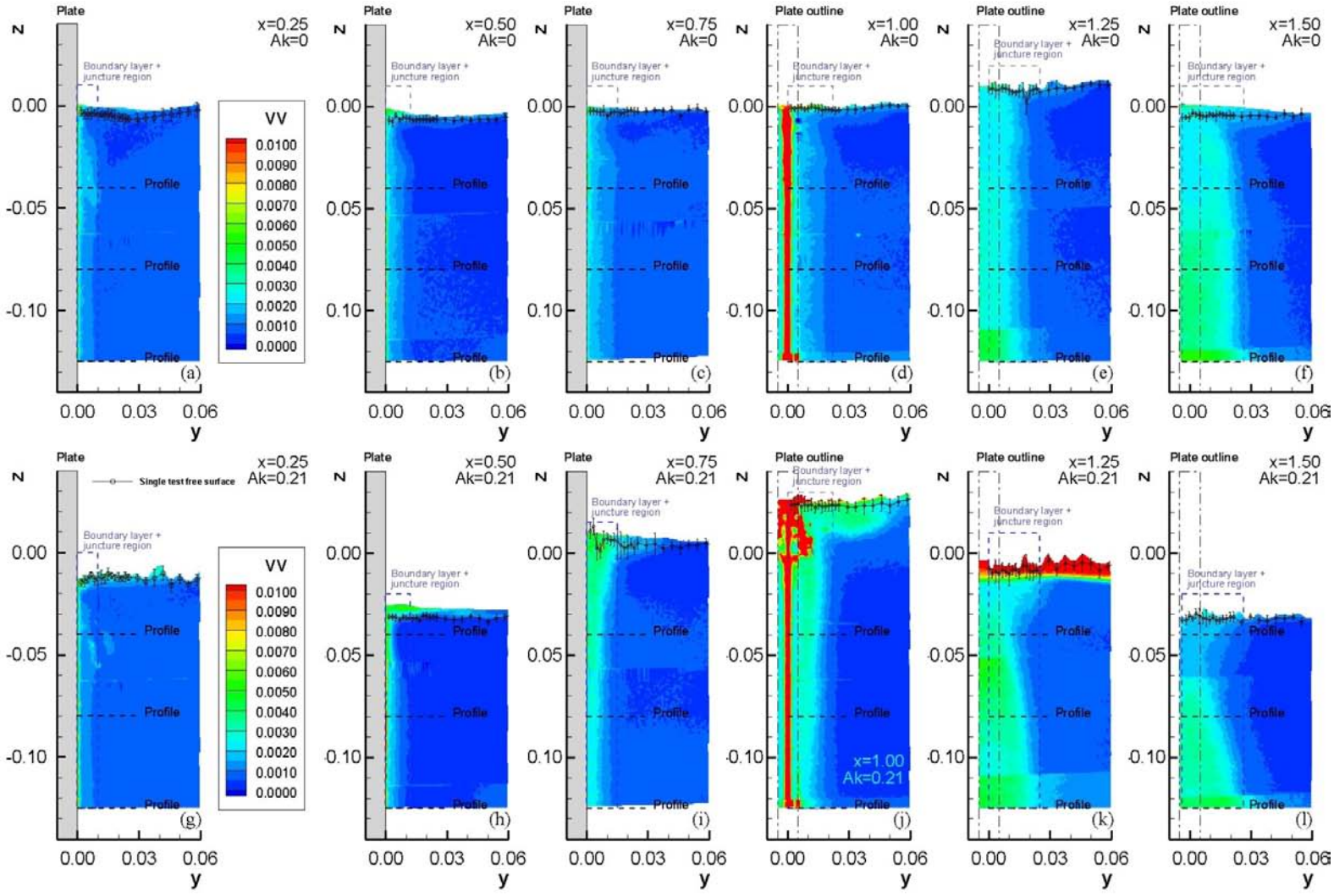

Figure 31: Full-domain *vv* contours for all *x* and *Ak* = 0 (top: a-f) and *Ak* = 0.21 (bottom: g-l). Wave field data is overlaid on contours

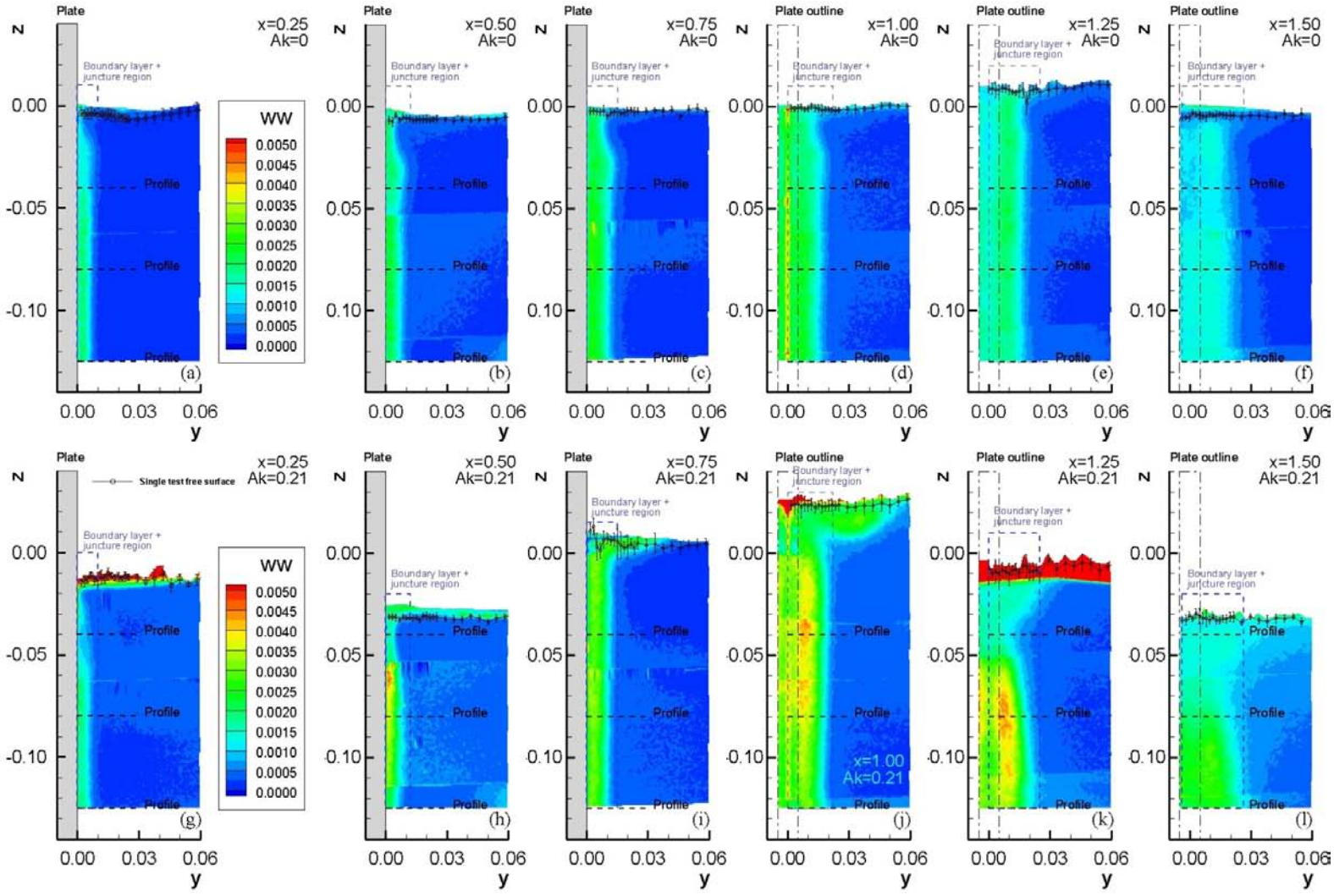

Figure 32: Full-domain *ww* contours for all *x* and *Ak* = 0 (top: a-f) and *Ak* = 0.21 (bottom: g-l). Wave field data is overlaid on contours

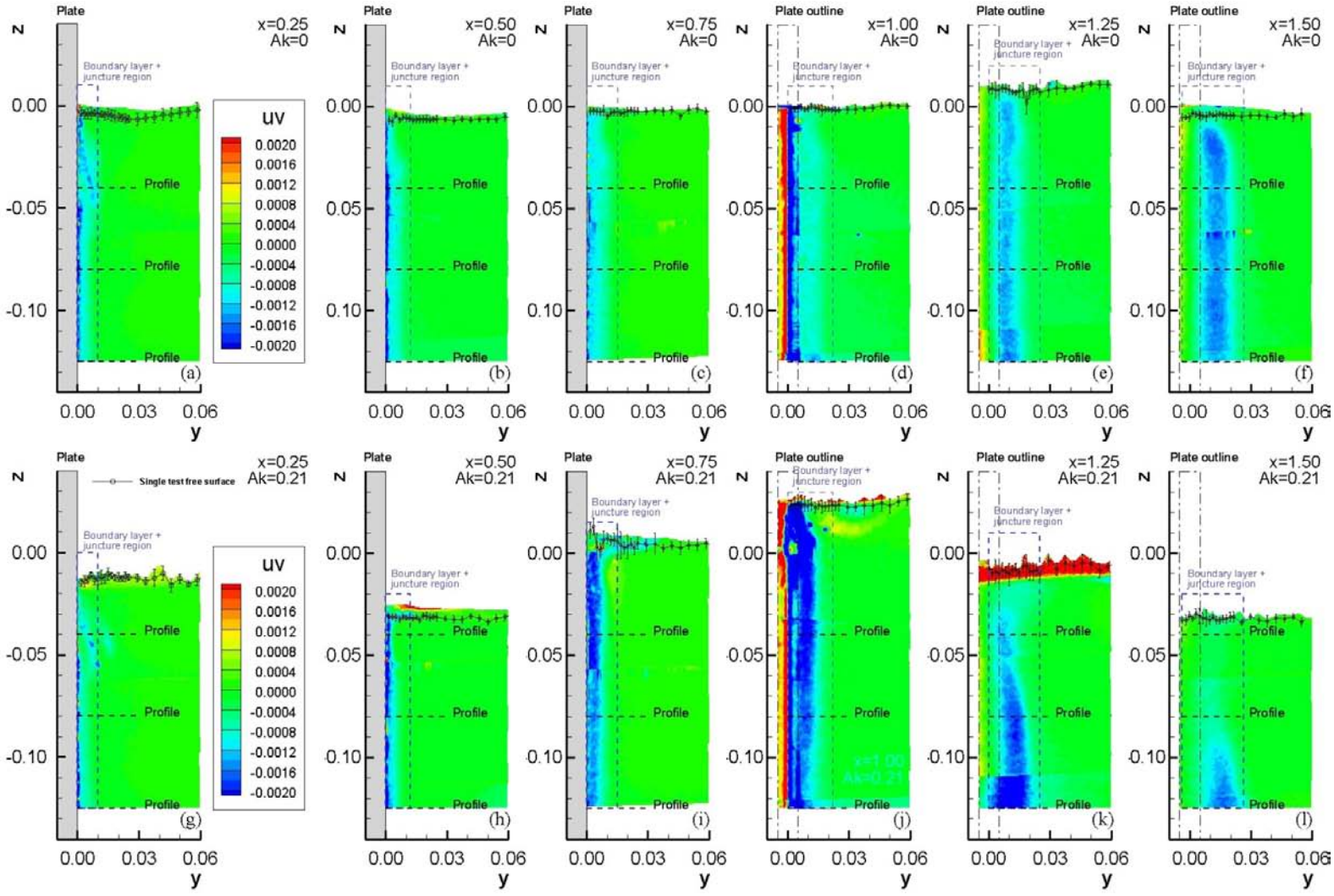

Figure 33: Full-domain *uv* contours for all *x* and *Ak* = 0 (top: a-f) and *Ak* = 0.21 (bottom: g-l). Wave field data is overlaid on contours

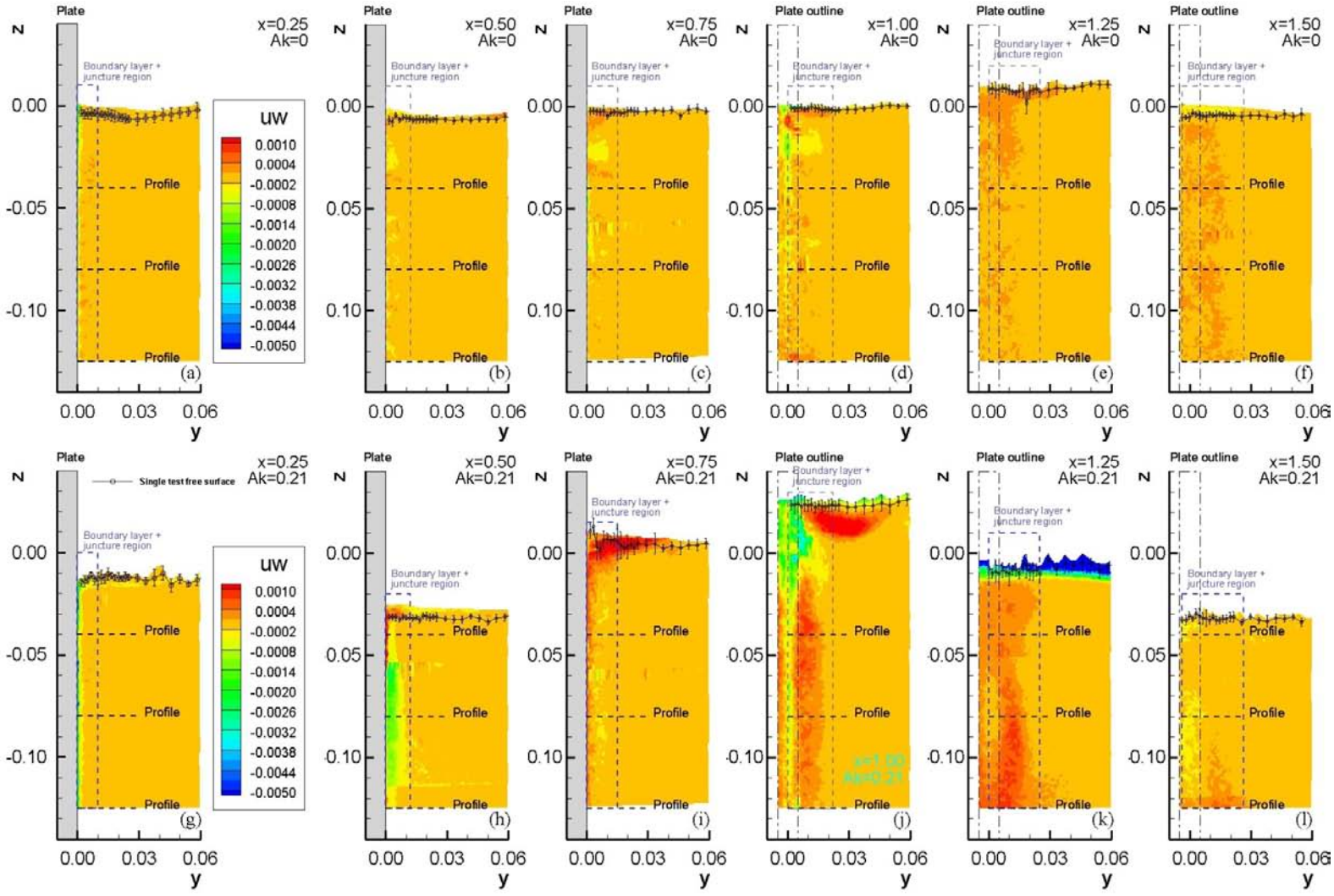

Figure 34: Full-domain *uw* contours for all *x* and *Ak* = 0 (top: a-f) and *Ak* = 0.21 (bottom: g-l). Wave field data is overlaid on contours

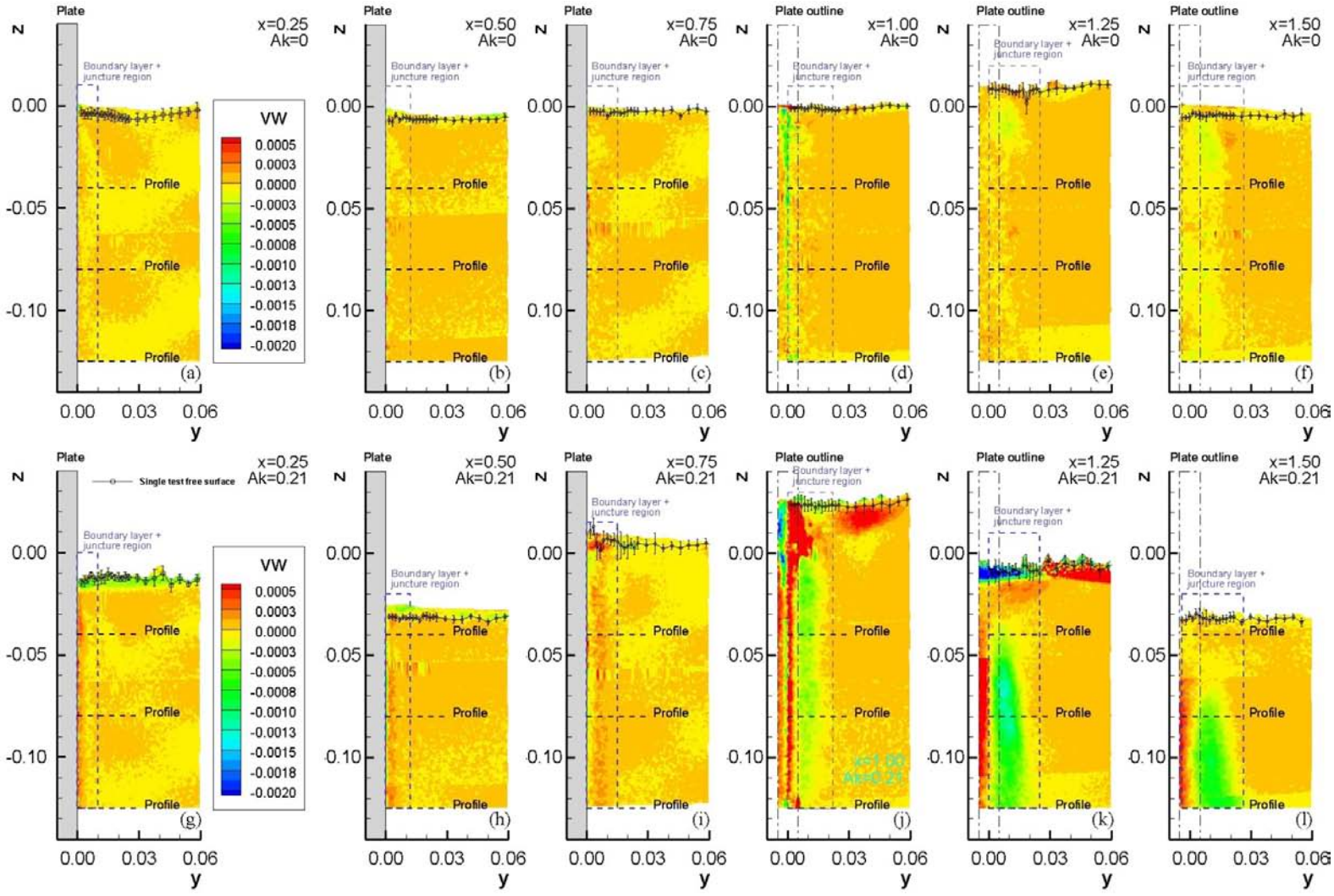

Figure 35: Full-domain *vw* contours for all *x* and *Ak* = 0 (top: a-f) and *Ak* = 0.21 (bottom: g-l). Wave field data is overlaid on contours

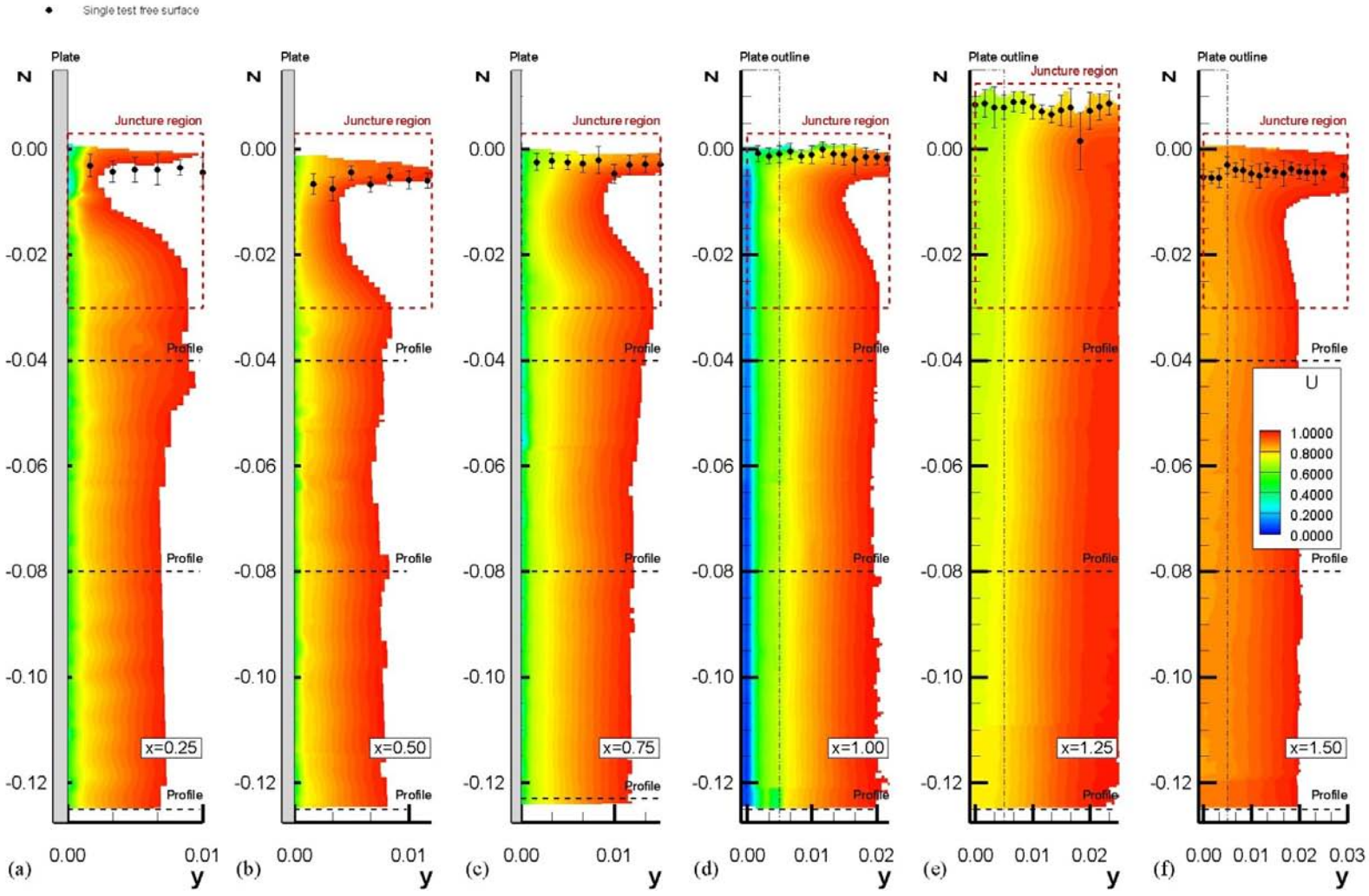

Figure 36: Boundary layer and wake U contours for $Ak = 0$

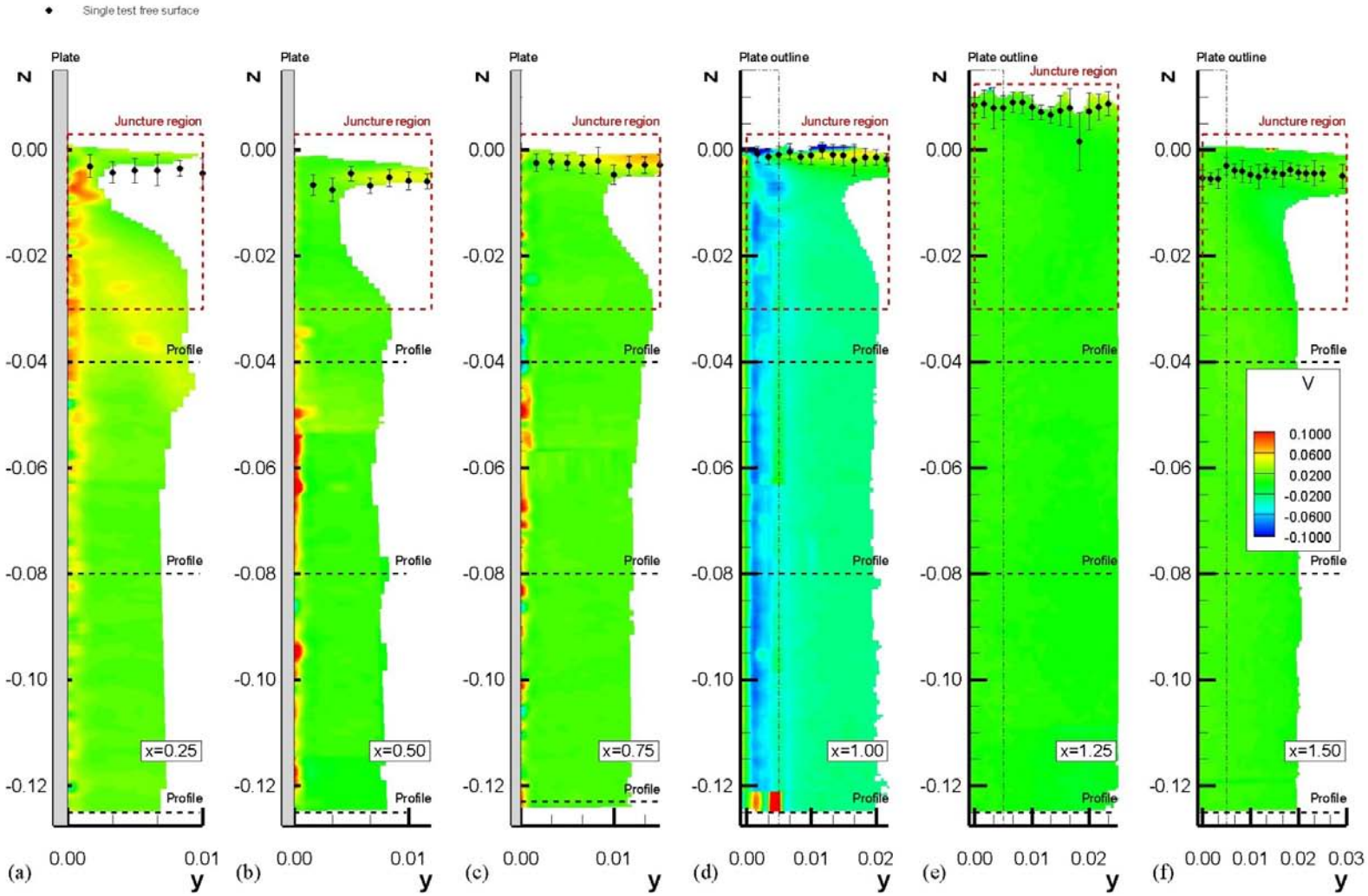

Figure 37: Boundary layer and wake V contours for $Ak = 0$

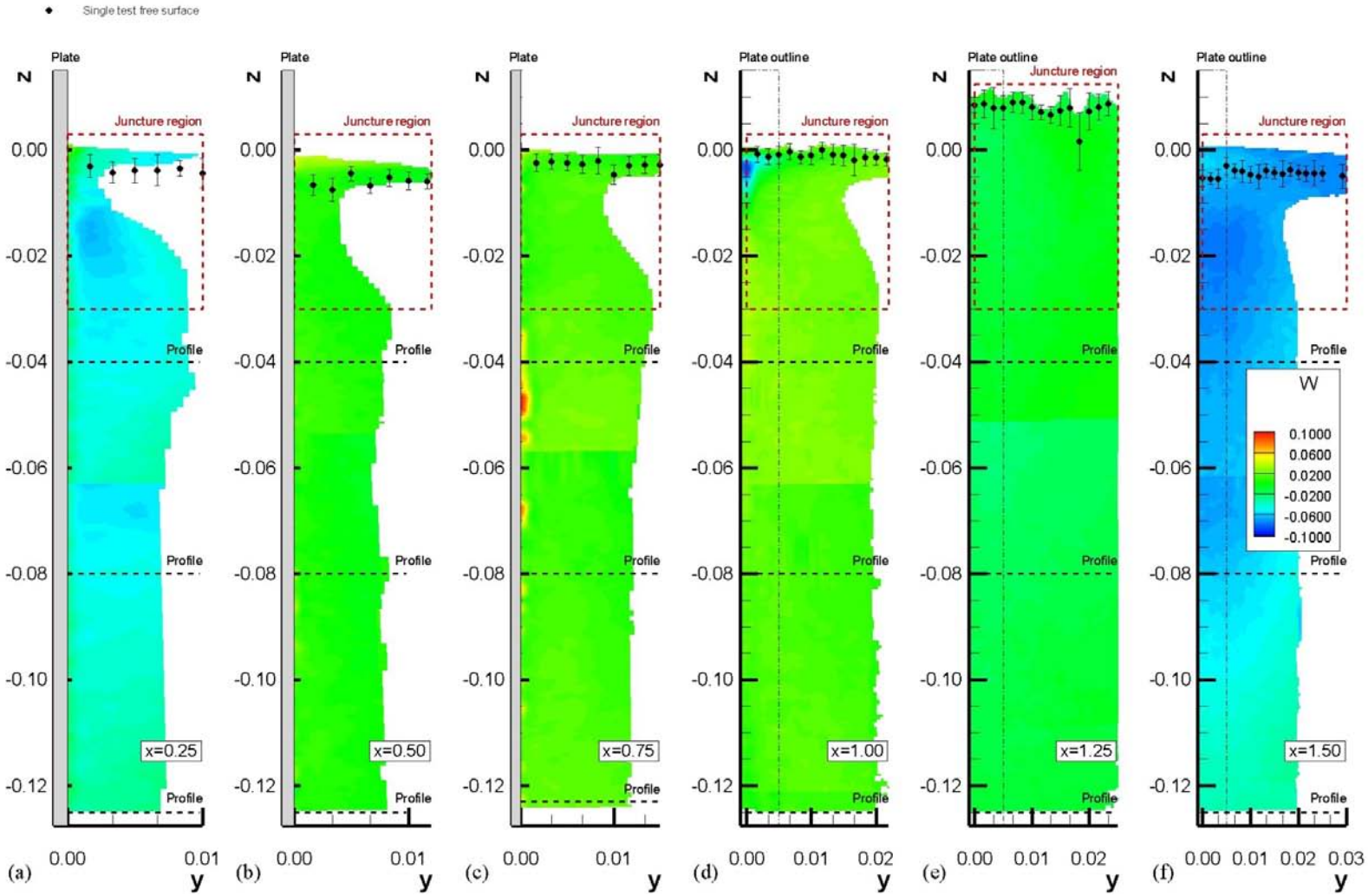

Figure 38: Boundary layer and wake W contours for $Ak = 0$

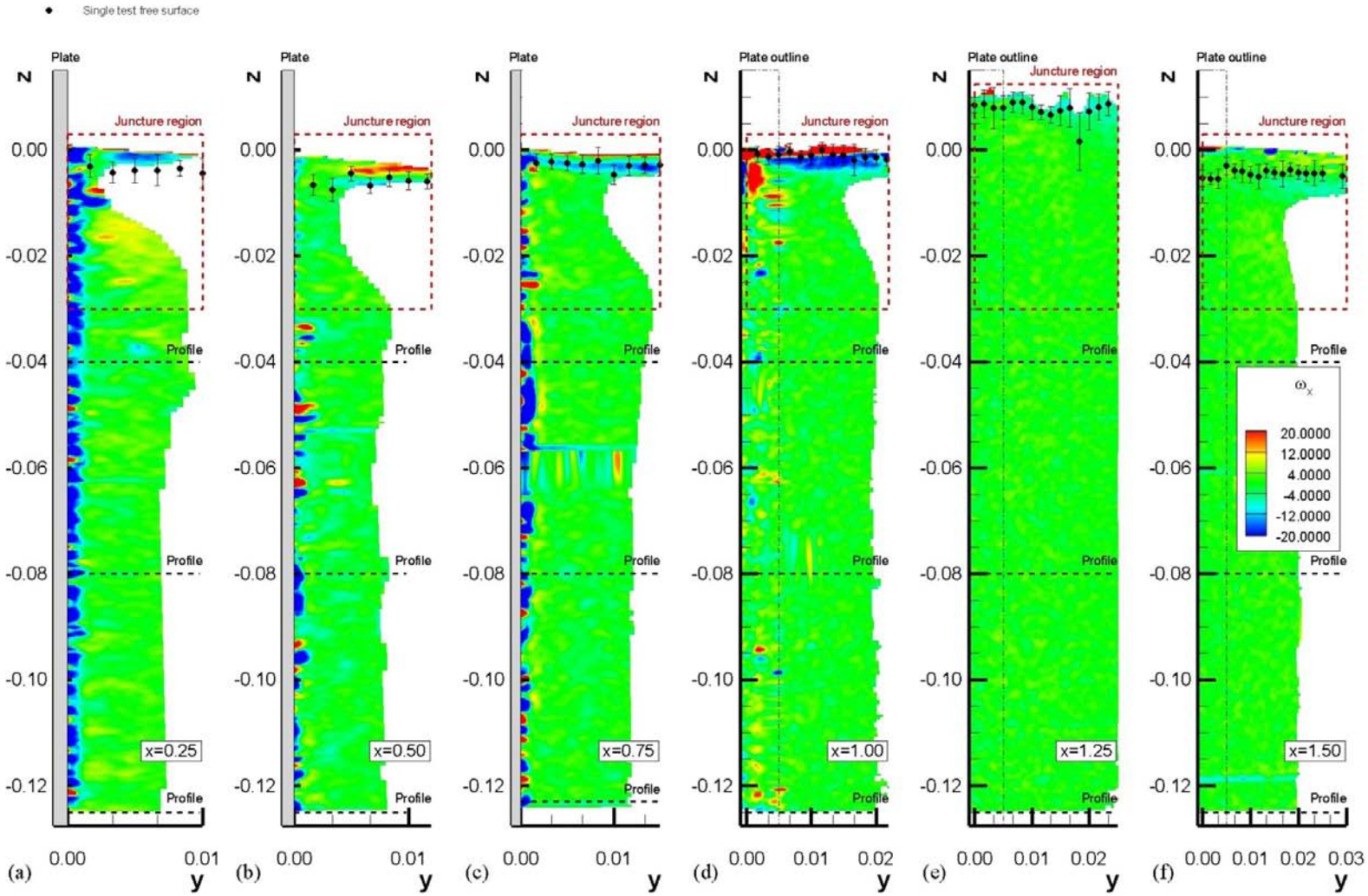

Figure 39: Boundary layer and wake ω_x contours for $Ak = 0$

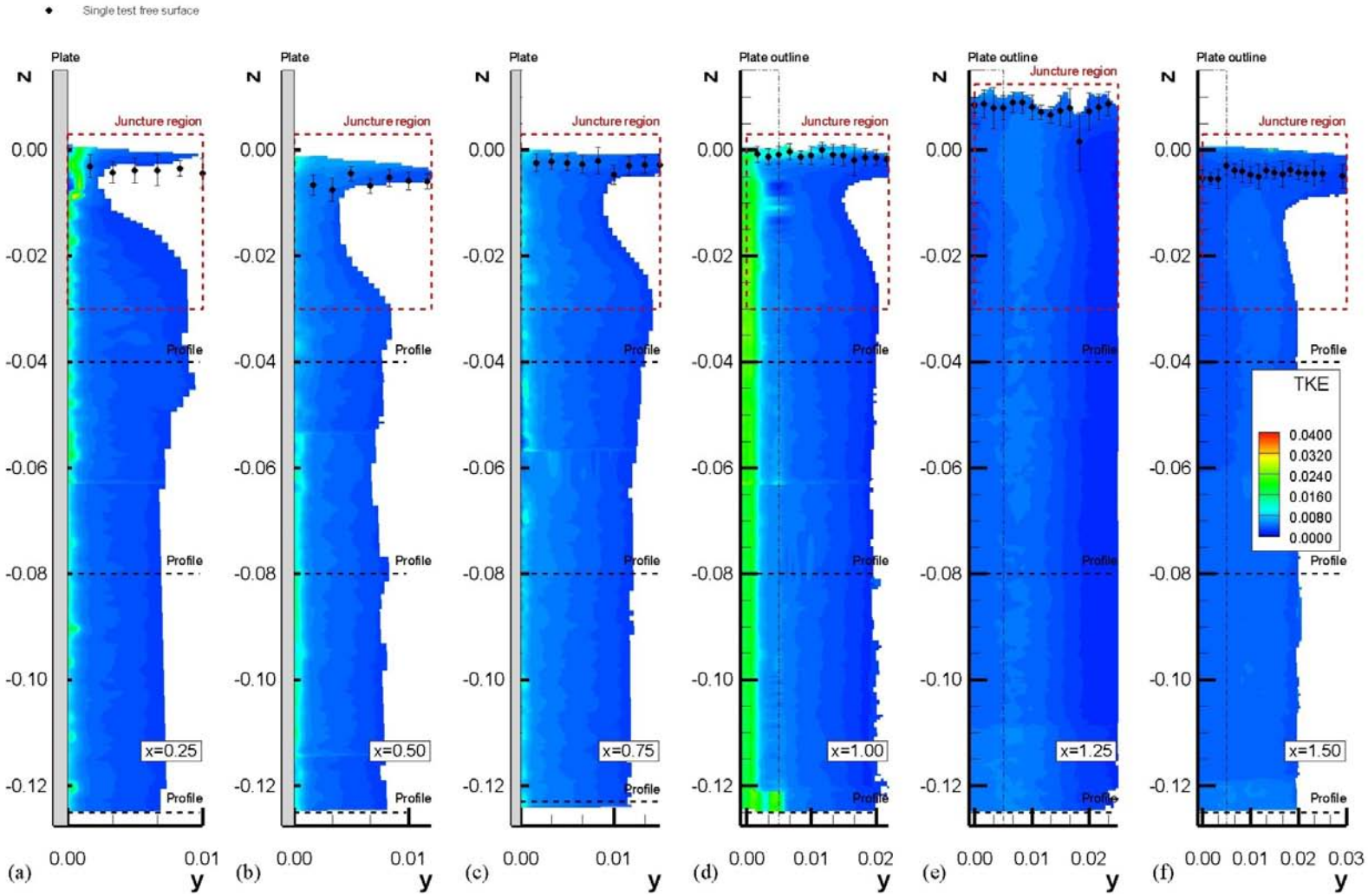

Figure 40: Boundary layer and wake *TKE* contours for $Ak = 0$

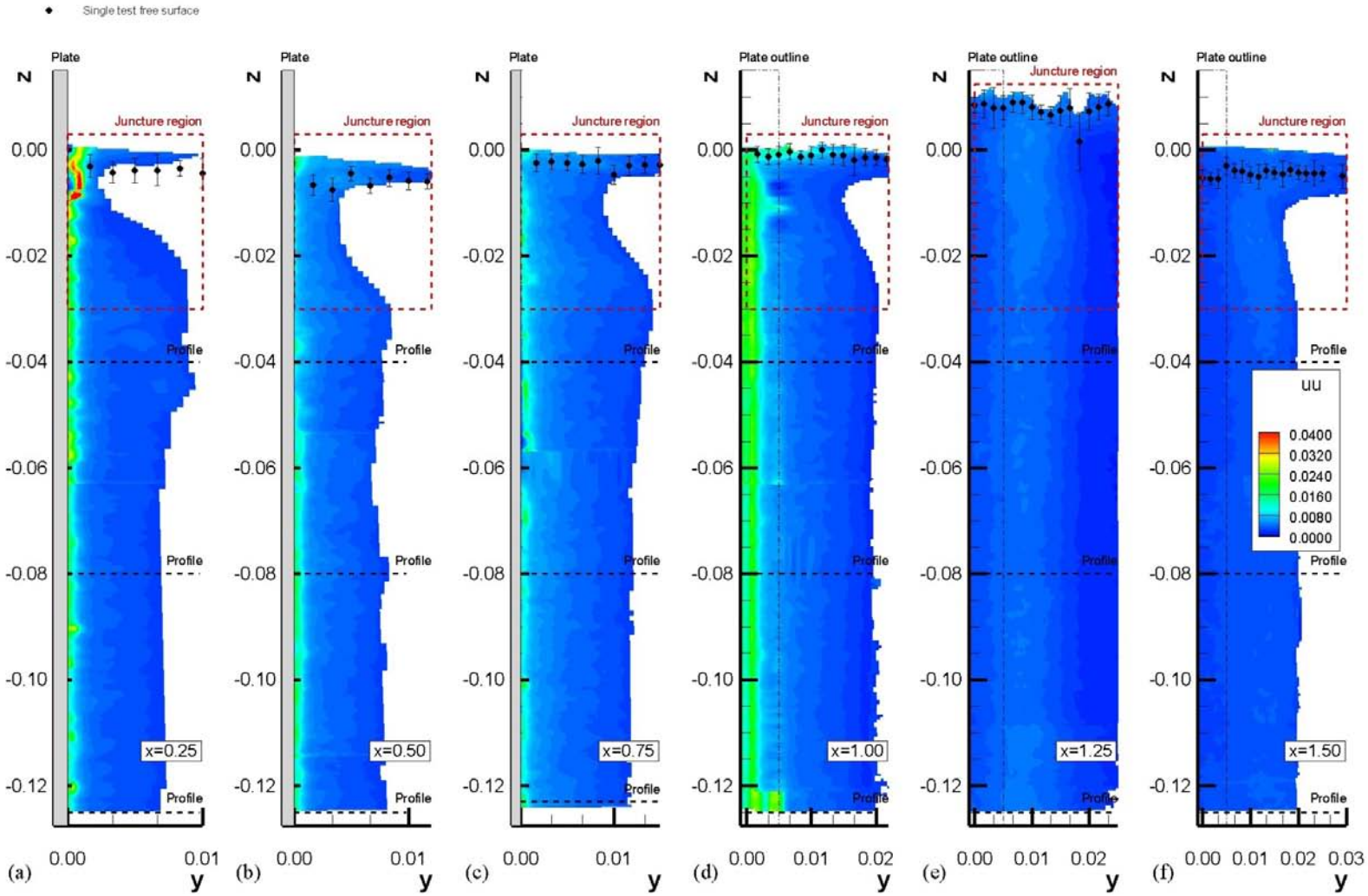

Figure 41: Boundary layer and wake *uu* contours for $Ak = 0$

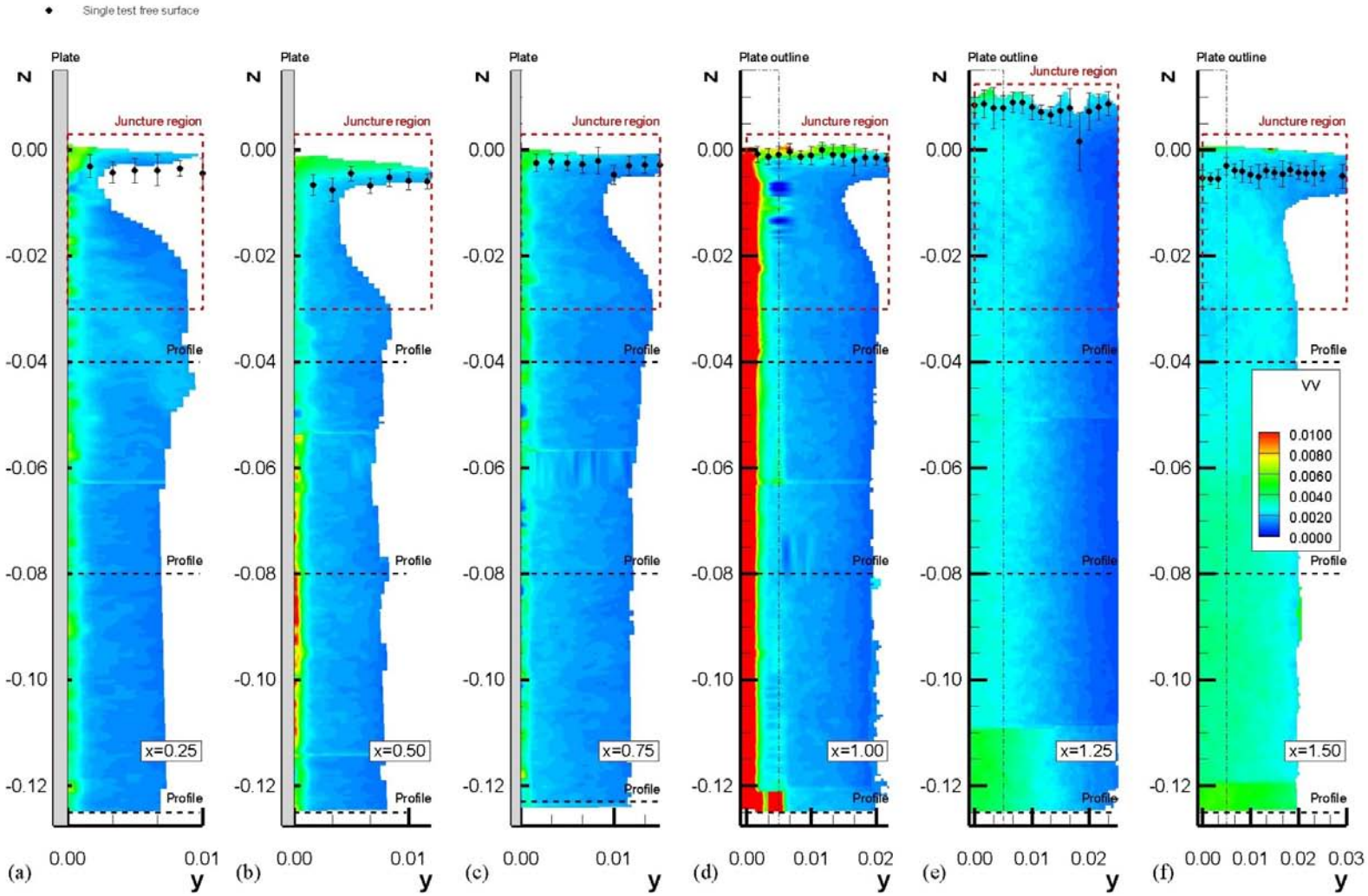

Figure 42: Boundary layer and wake *vv* contours for $Ak = 0$

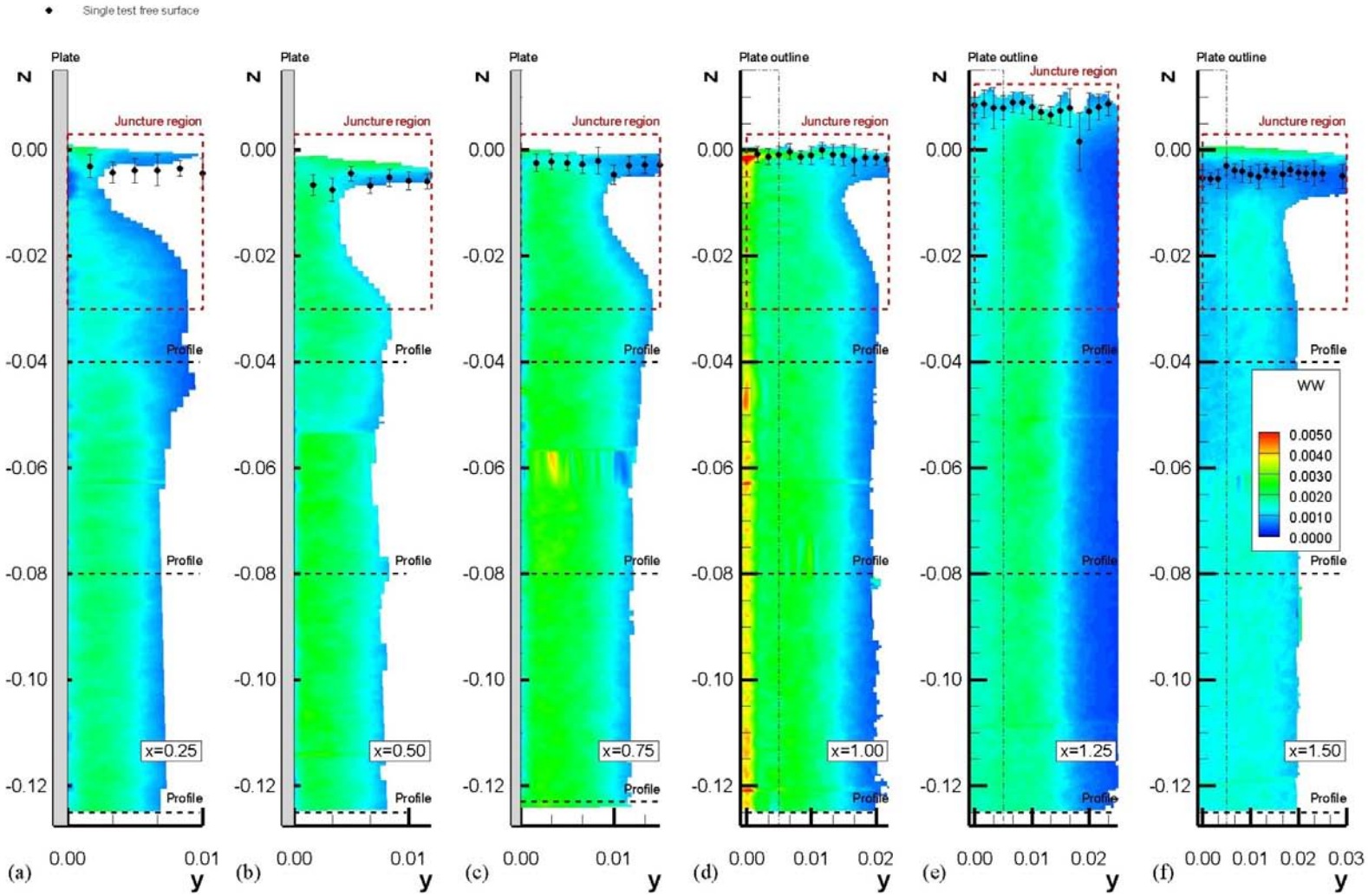

Figure 43: Boundary layer and wake *ww* contours for $Ak = 0$

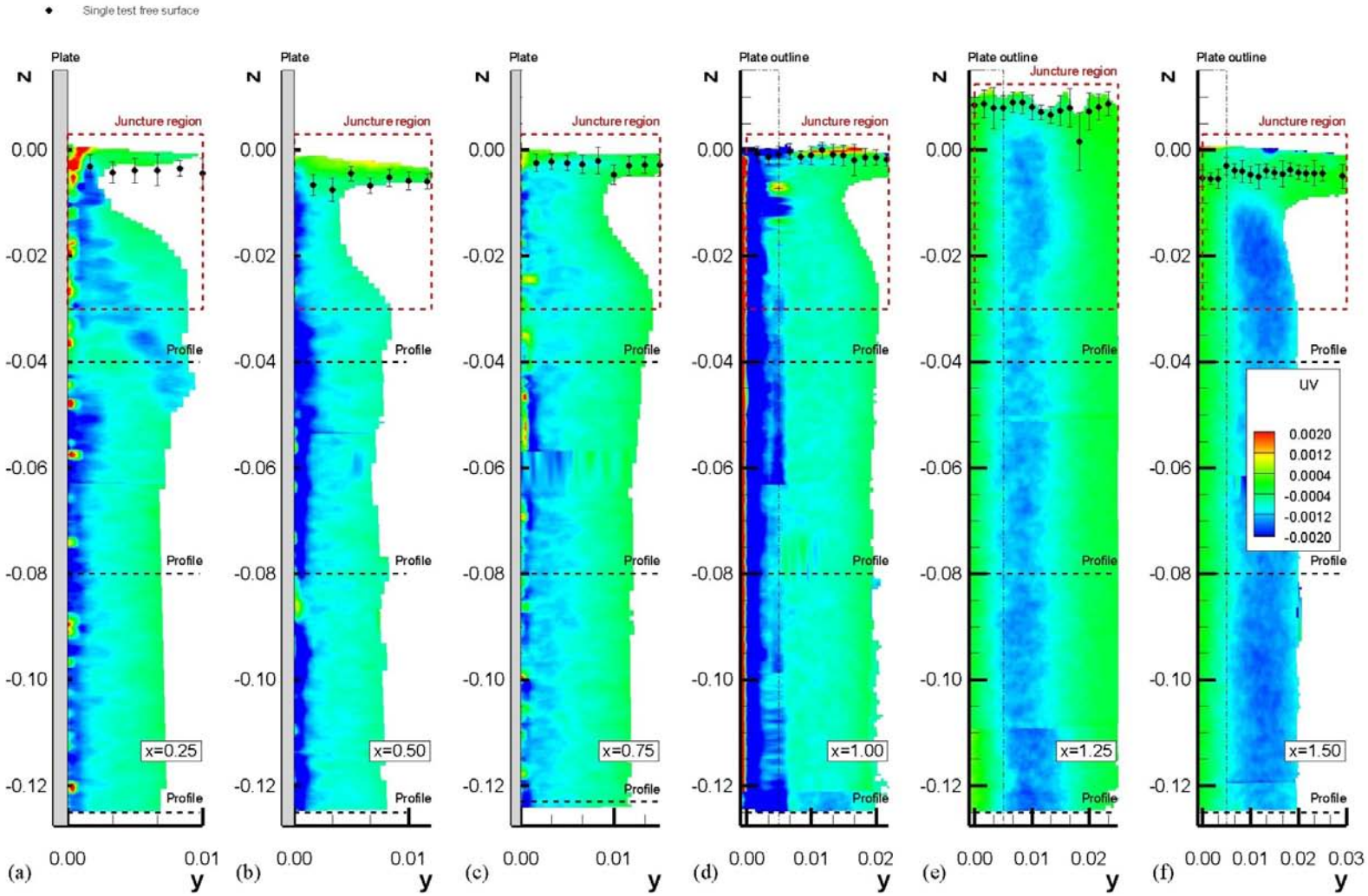

Figure 44: Boundary layer and wake *uv* contours for $Ak = 0$

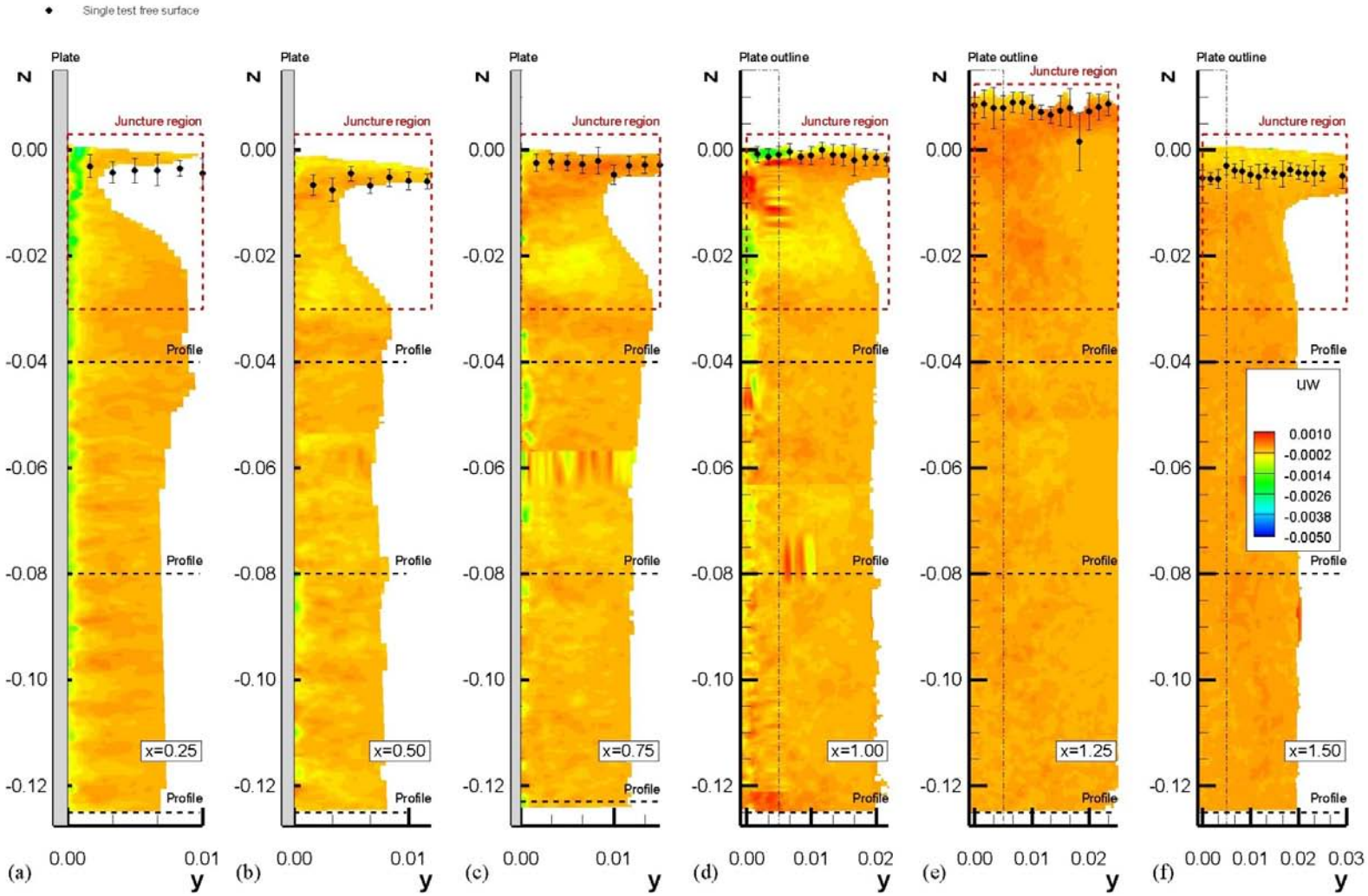

Figure 45: Boundary layer and wake *uw* contours for $Ak = 0$

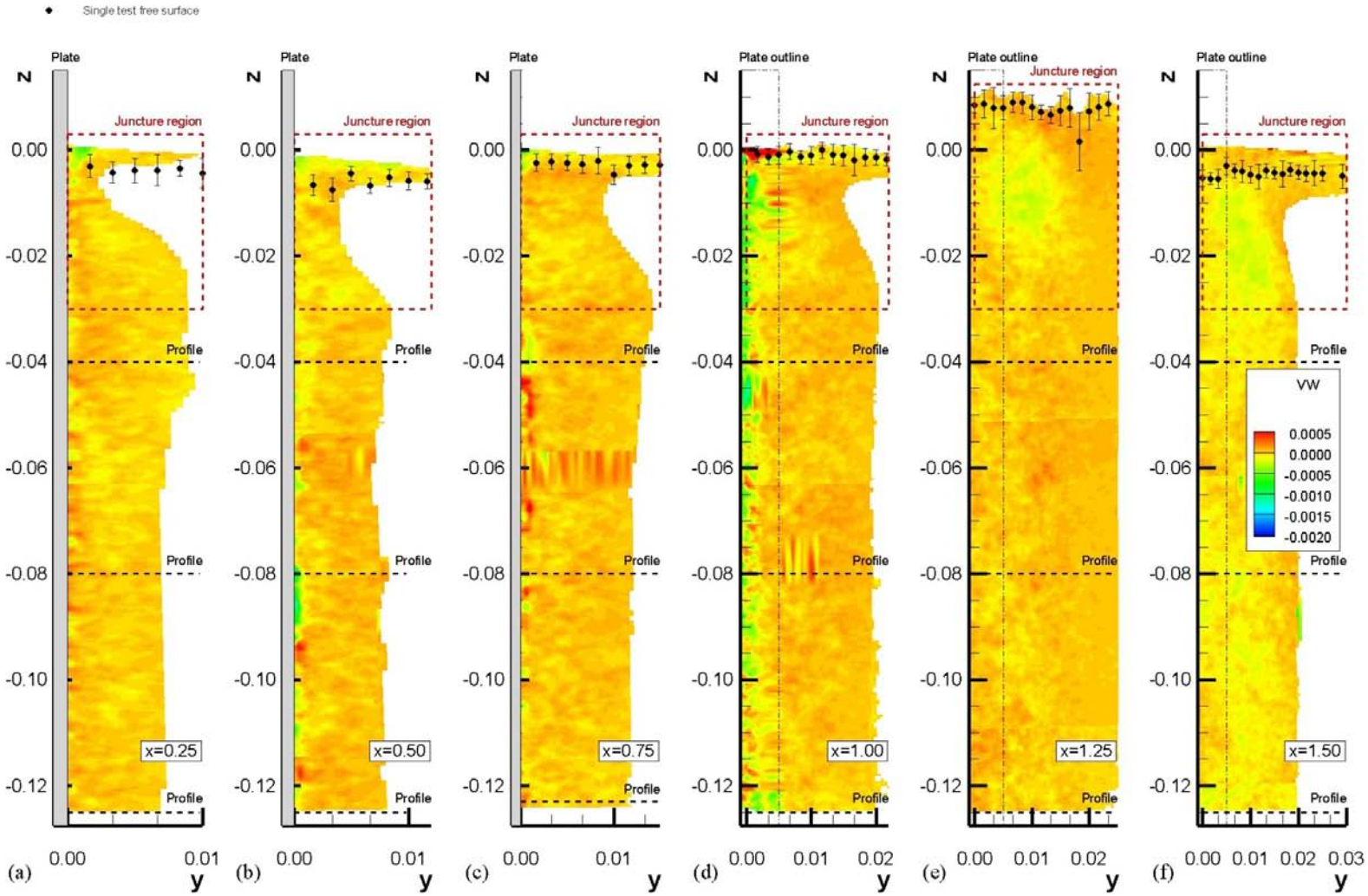

Figure 46: Boundary layer and wake *vw* contours for $Ak = 0$

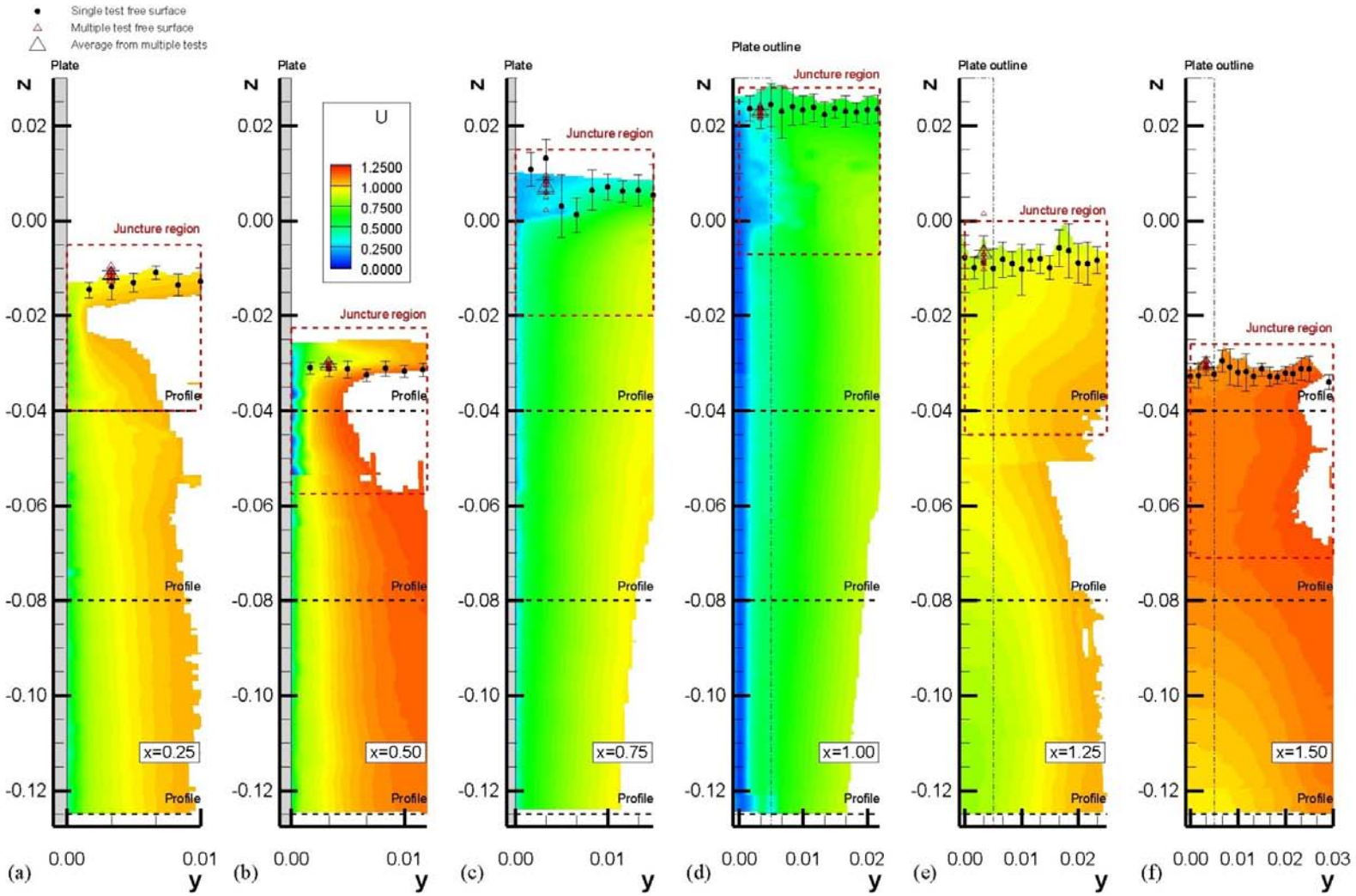

Figure 47: Boundary layer and wake U contours for $Ak = 0.21$

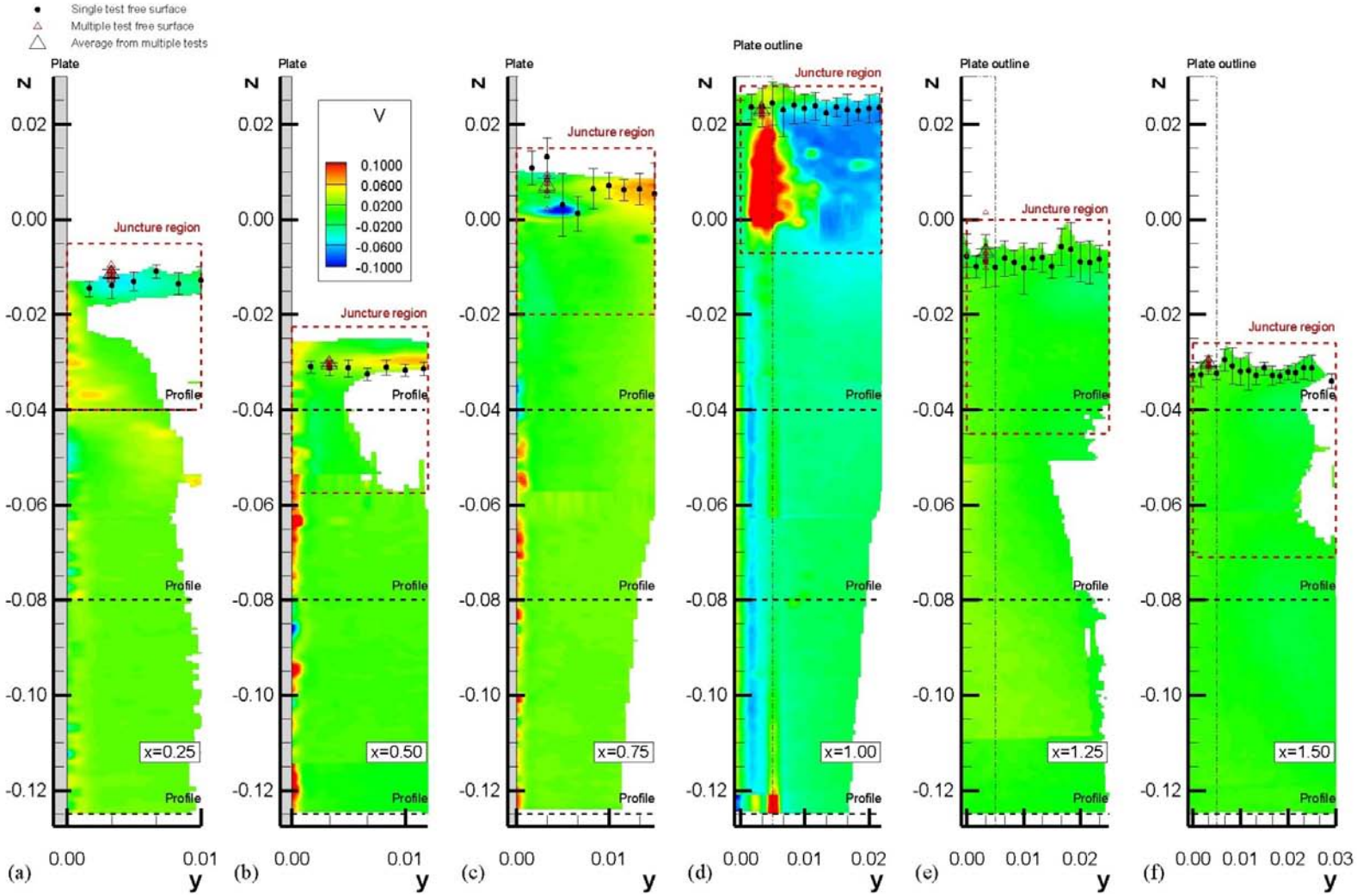

Figure 48: Boundary layer and wake V contours for $Ak = 0.21$

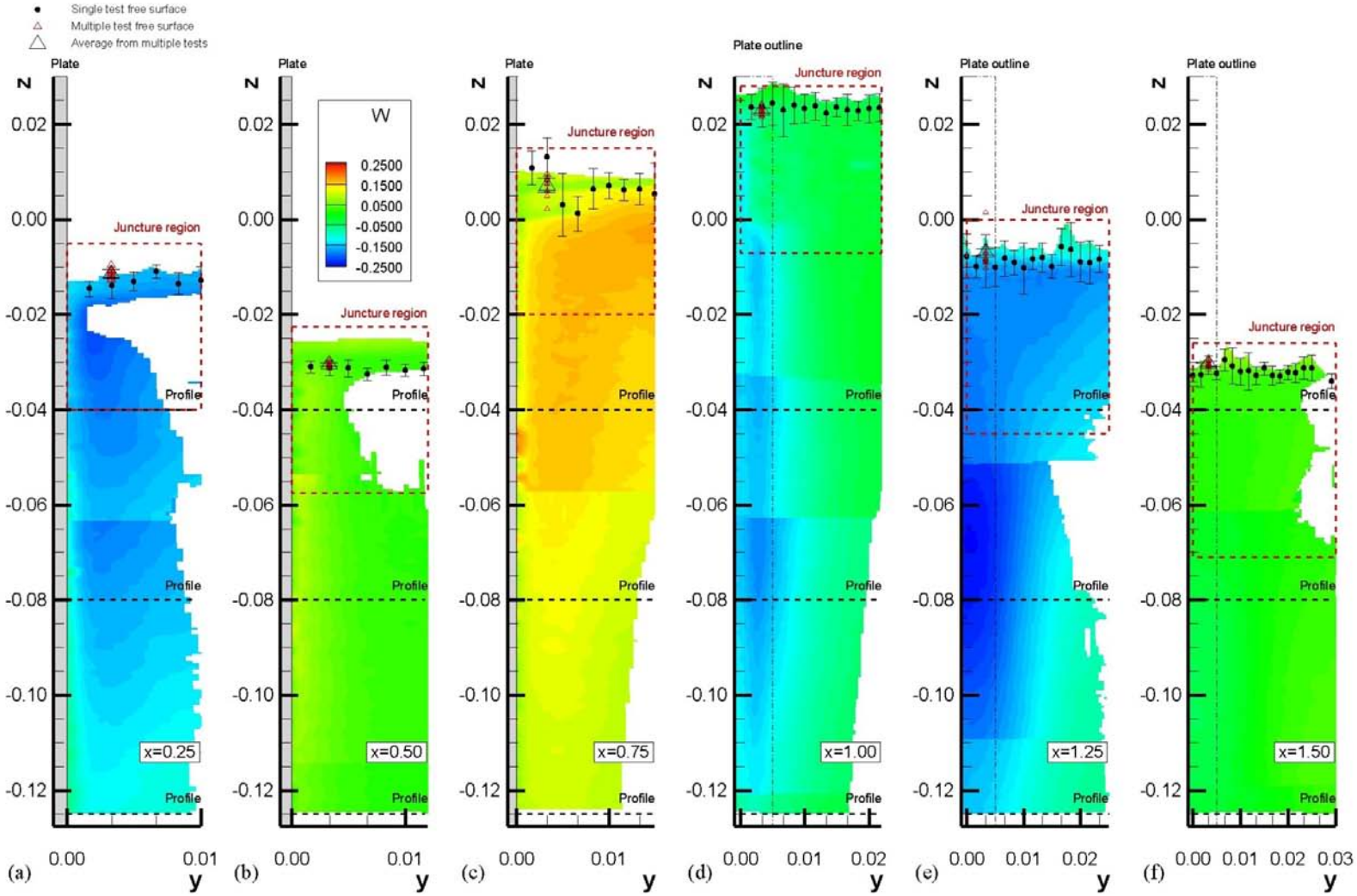

Figure 49: Boundary layer and wake W contours for $Ak = 0.21$

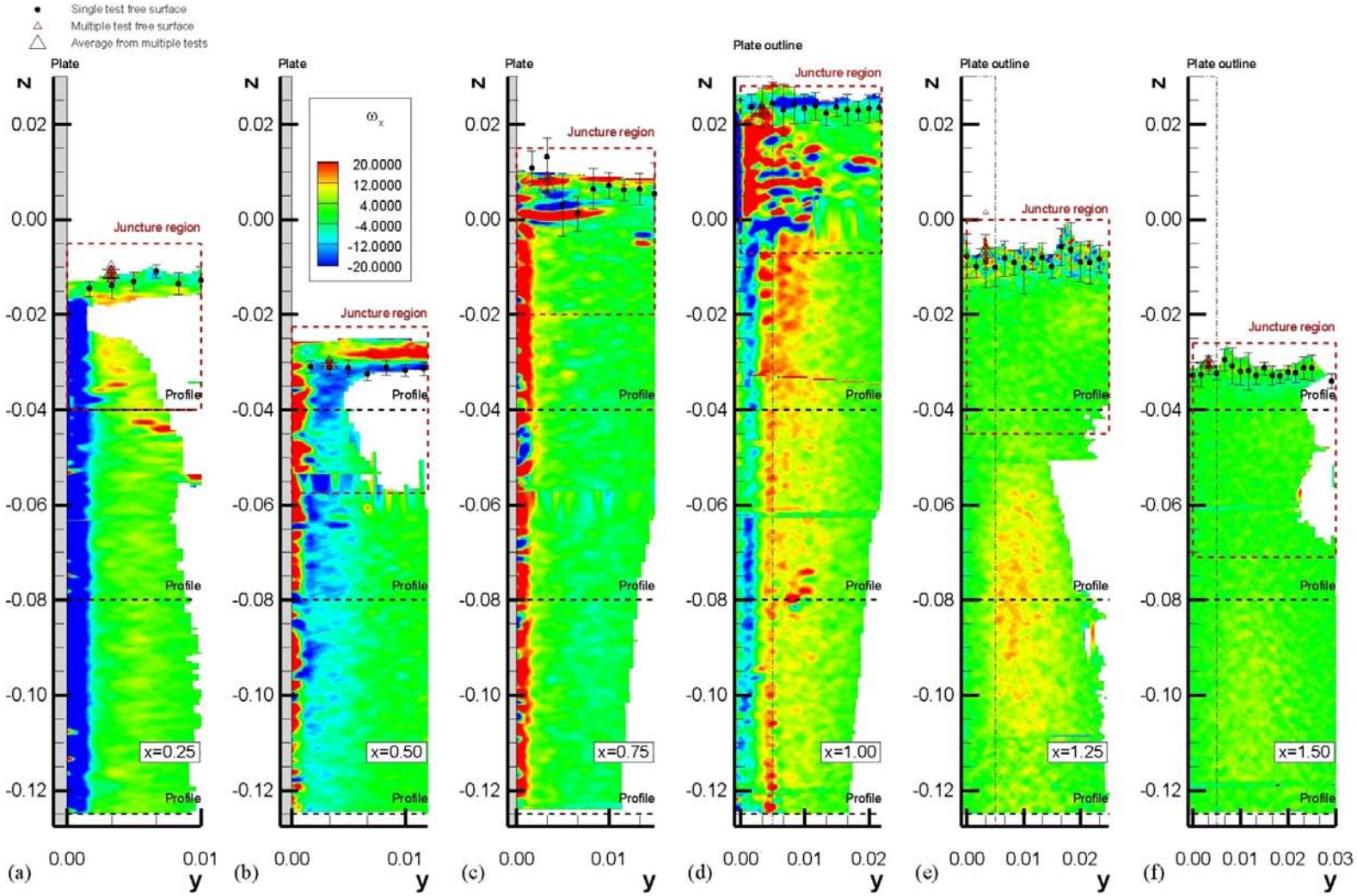

Figure 50: Boundary layer and wake ω_x contours for $Ak = 0.21$

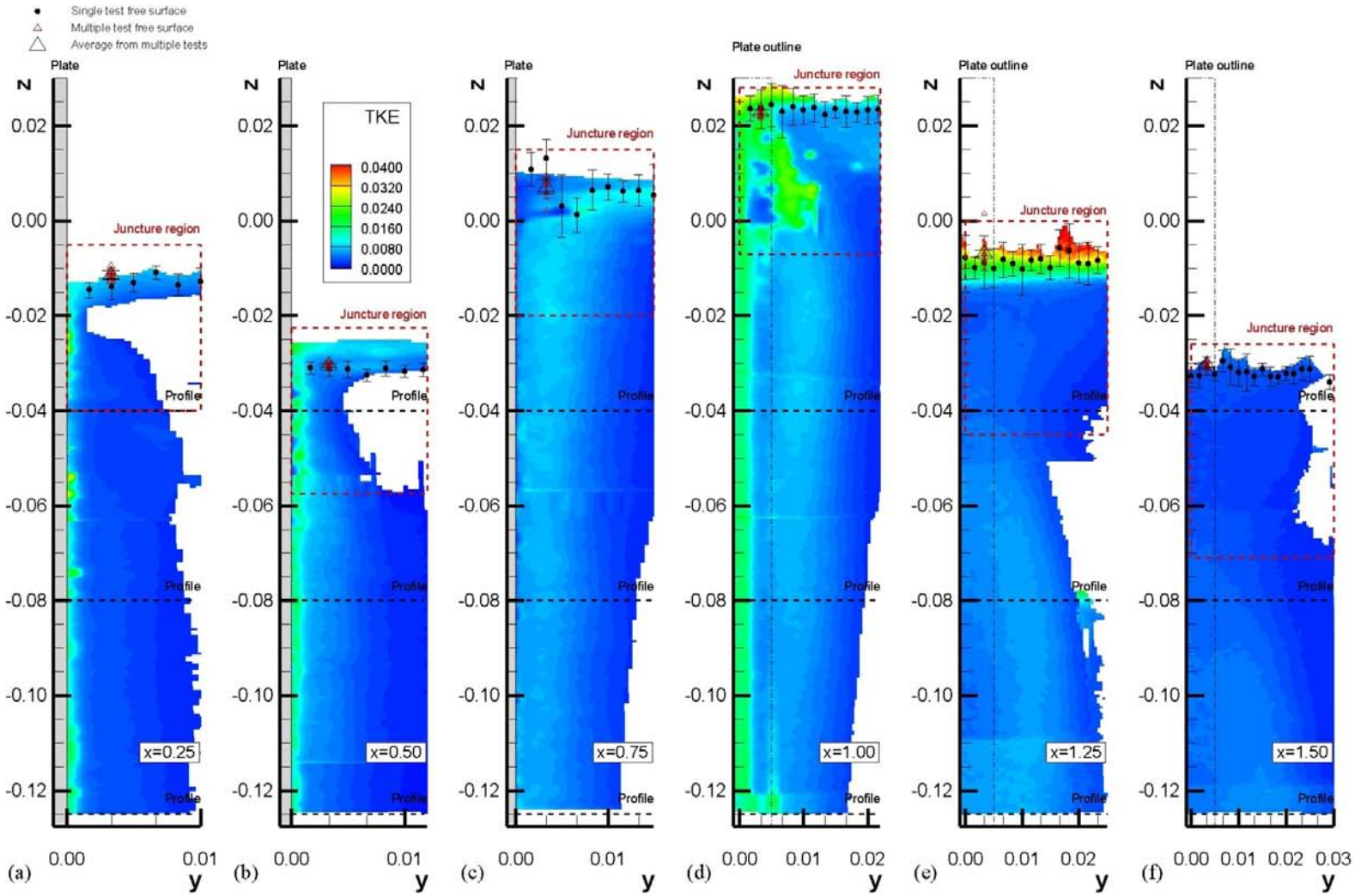

Figure 51: Boundary layer and wake *TKE* contours for $Ak = 0.21$

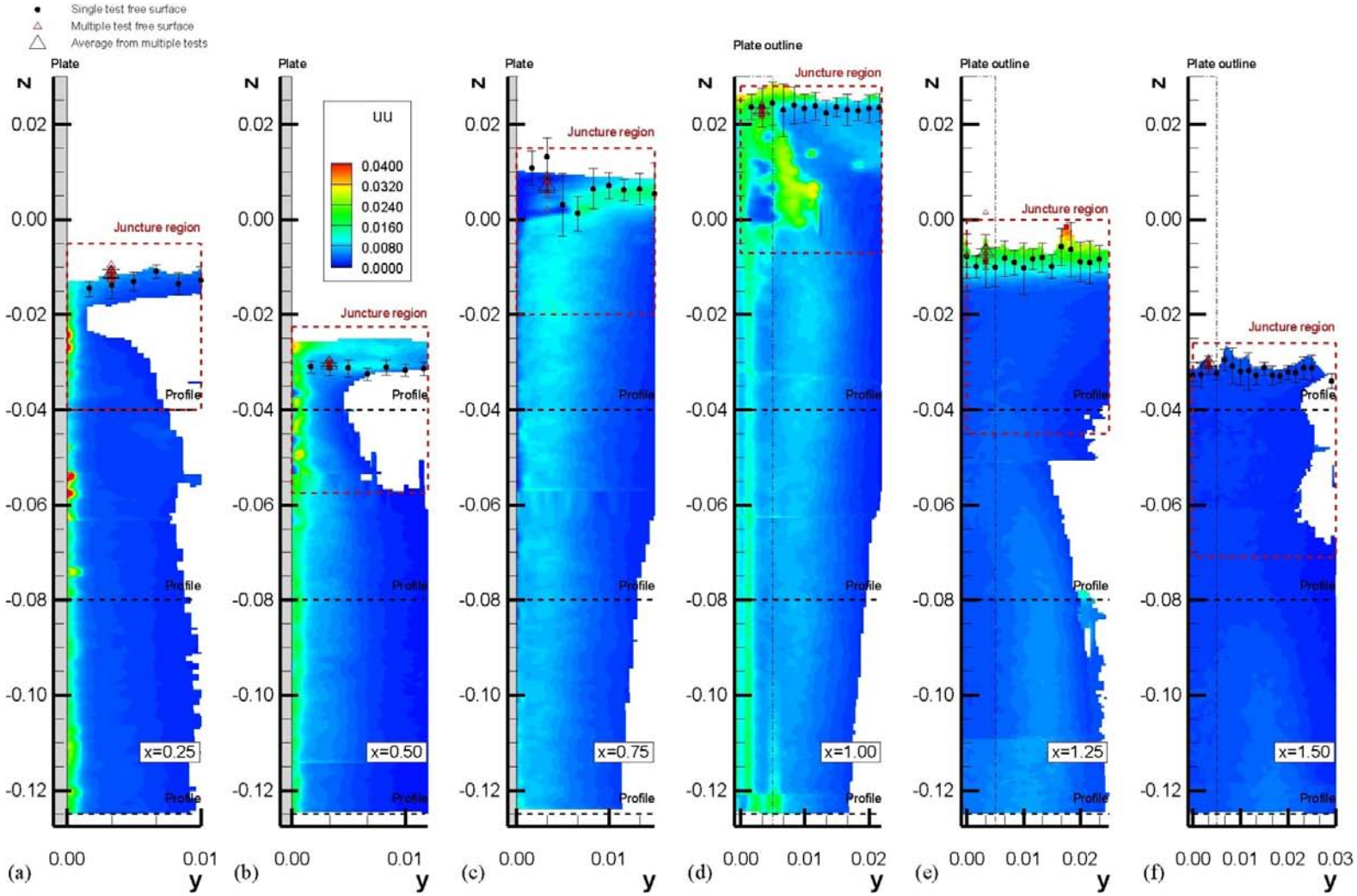

Figure 52: Boundary layer and wake *uu* contours for $Ak = 0.21$

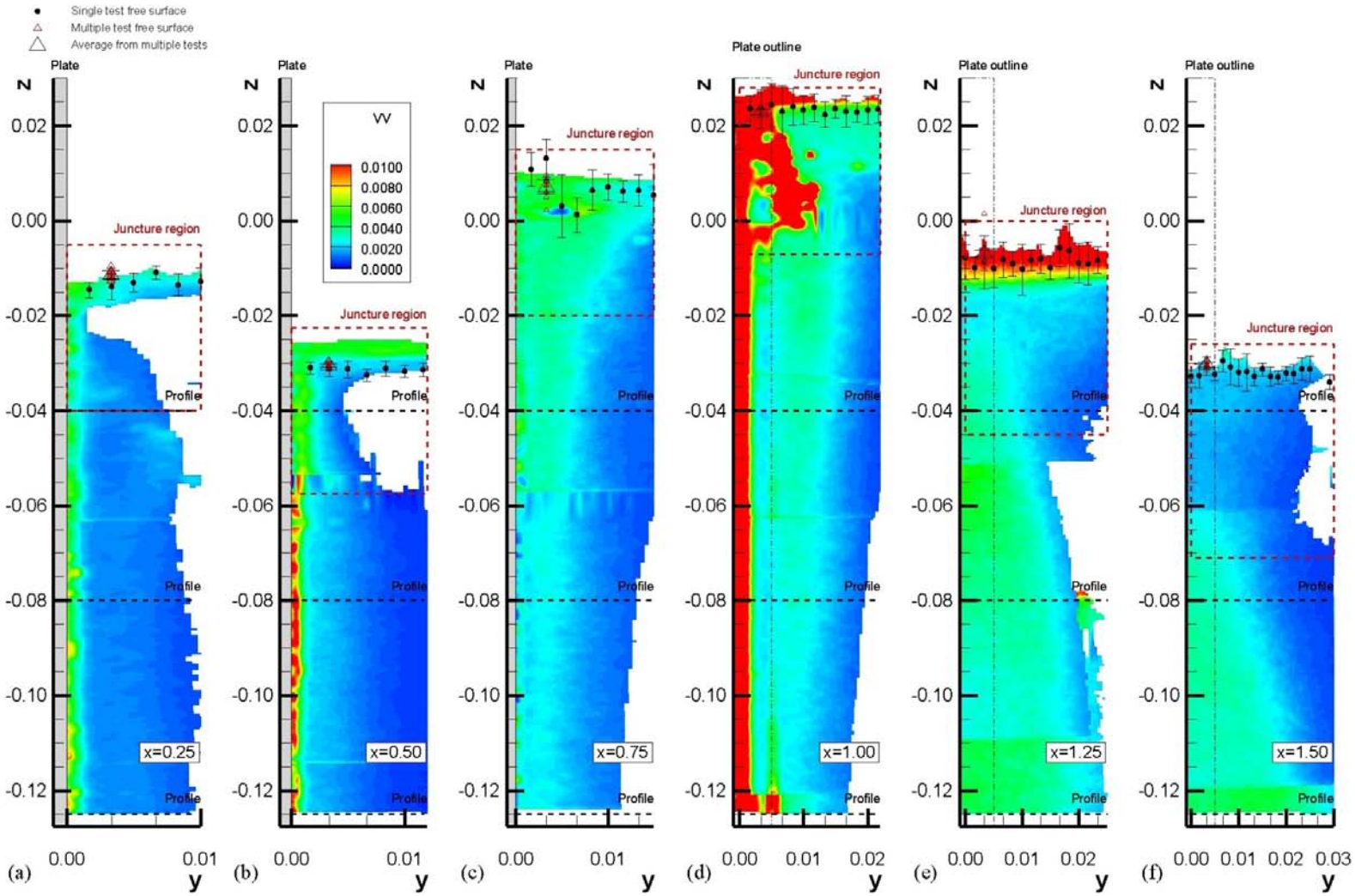

Figure 53: Boundary layer and wake *vv* contours for $Ak = 0.21$

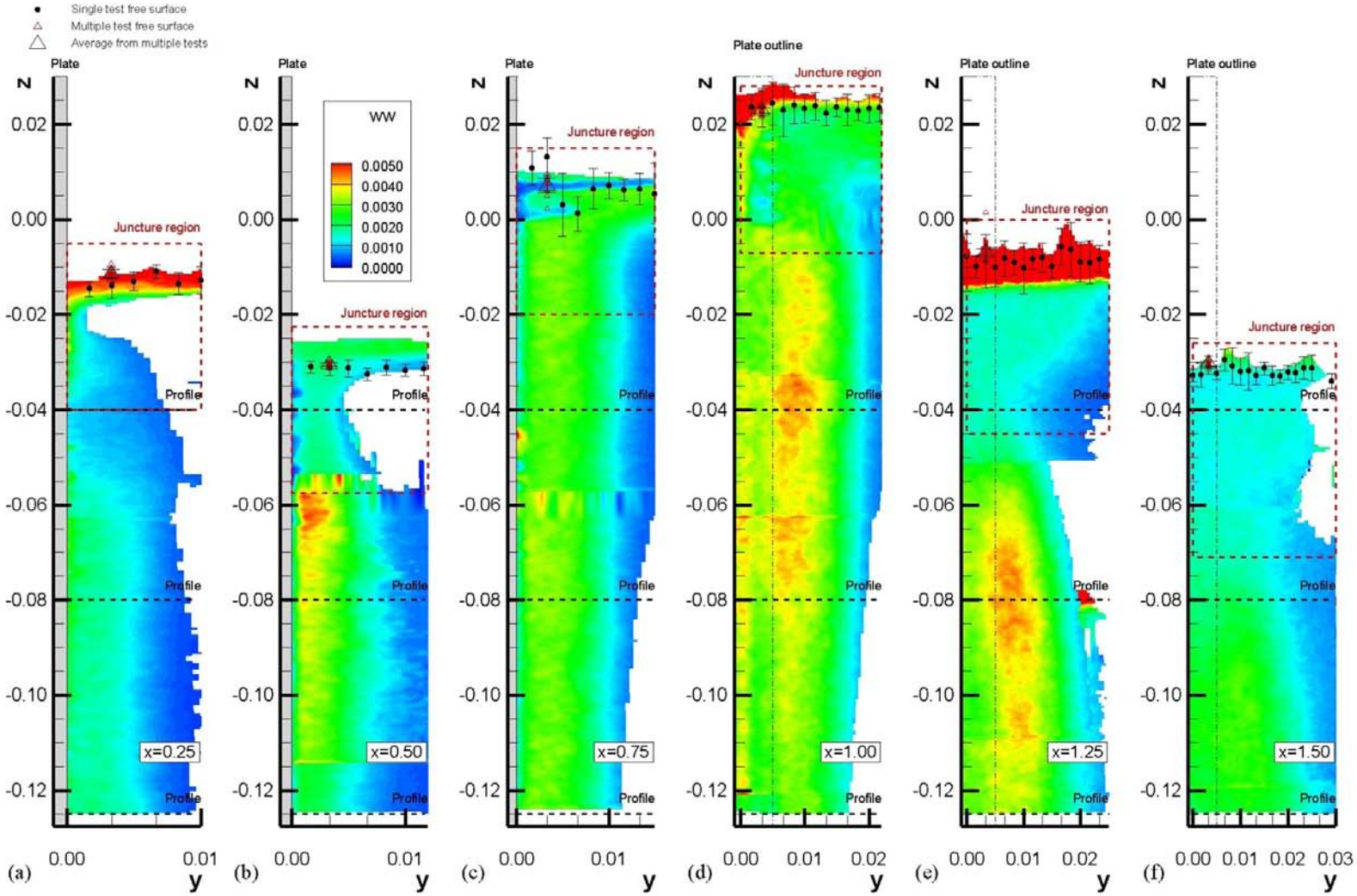

Figure 54: Boundary layer and wake *ww* contours for $Ak = 0.21$

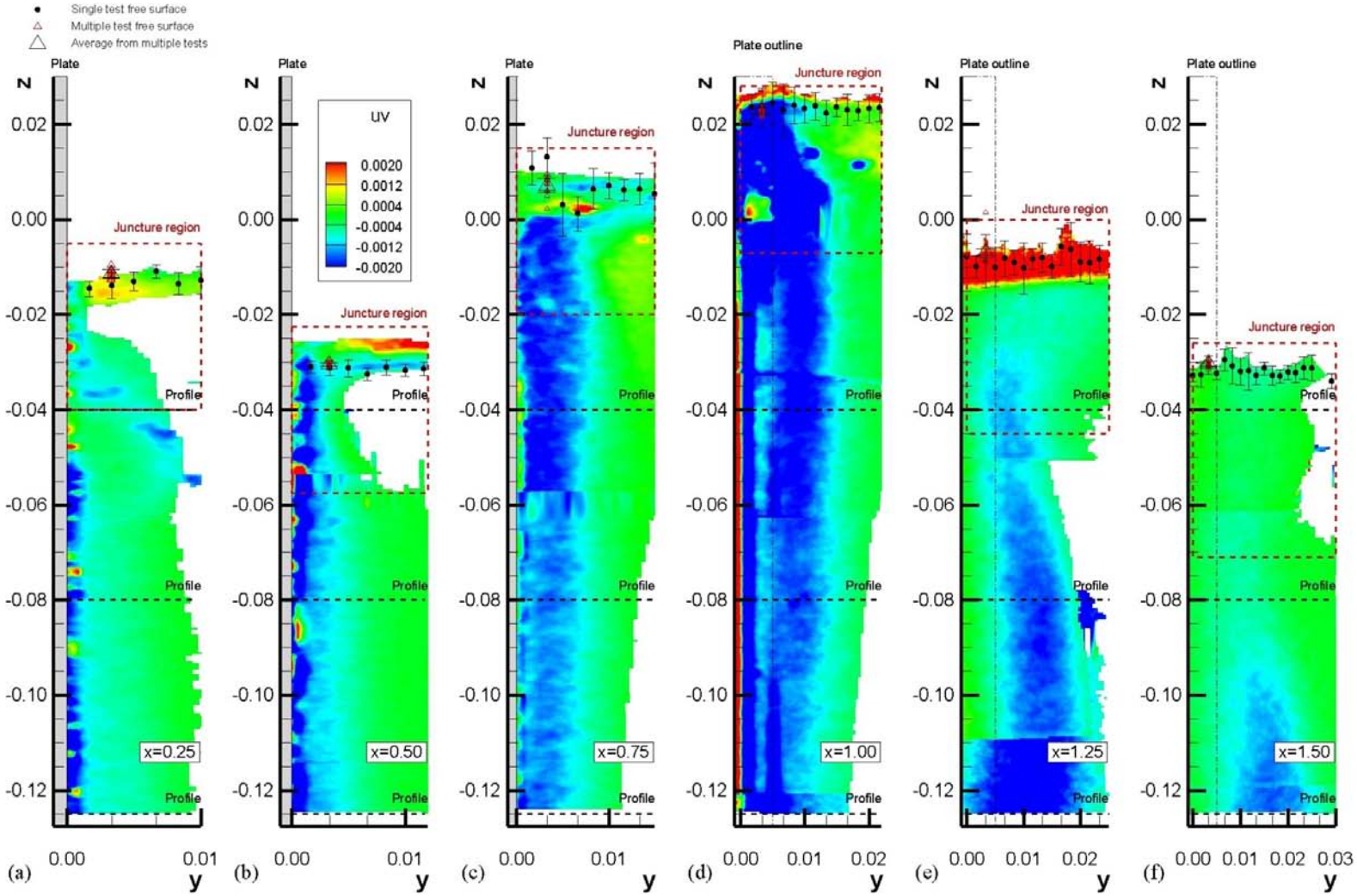

Figure 55: Boundary layer and wake *uv* contours for $Ak = 0.21$

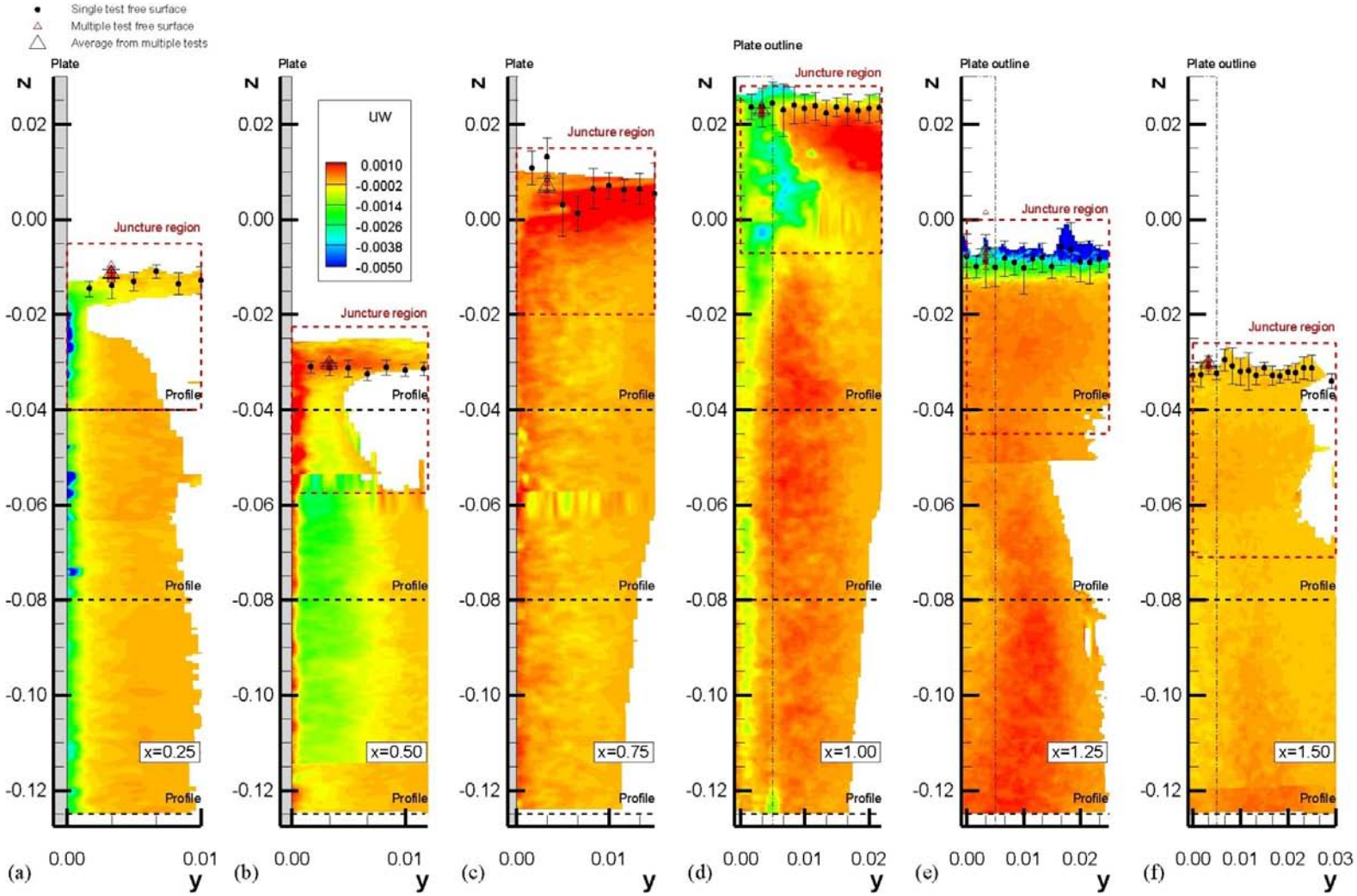

Figure 56: Boundary layer and wake *uw* contours for $Ak = 0.21$

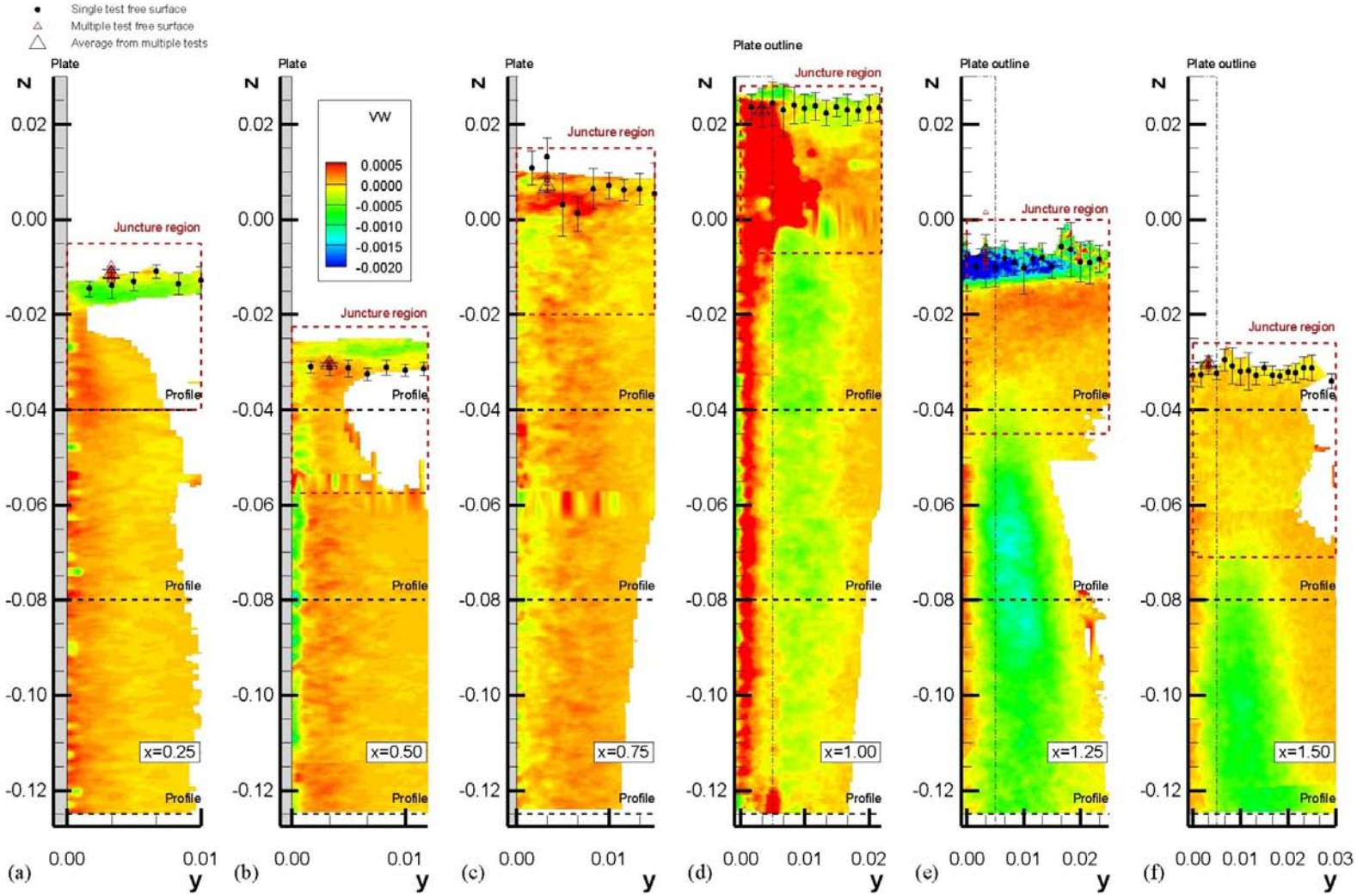

Figure 57: Boundary layer and wake *vw* contours for, $Ak = 0.21$

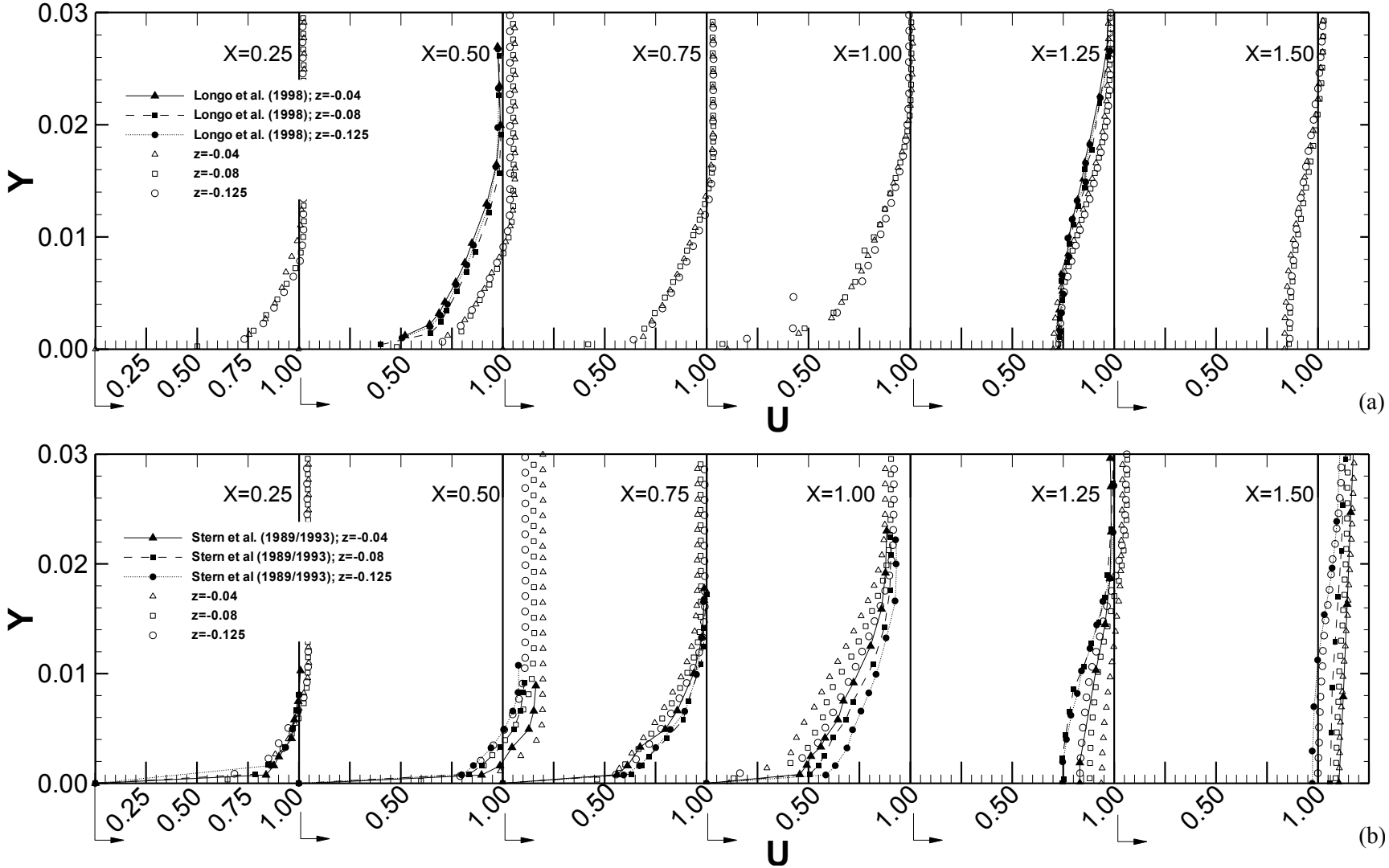

Figure 58: Detailed velocity profiles showing U for (a) $Ak = 0$ and (b) $Ak = 0.21$ (note shifted orgins)

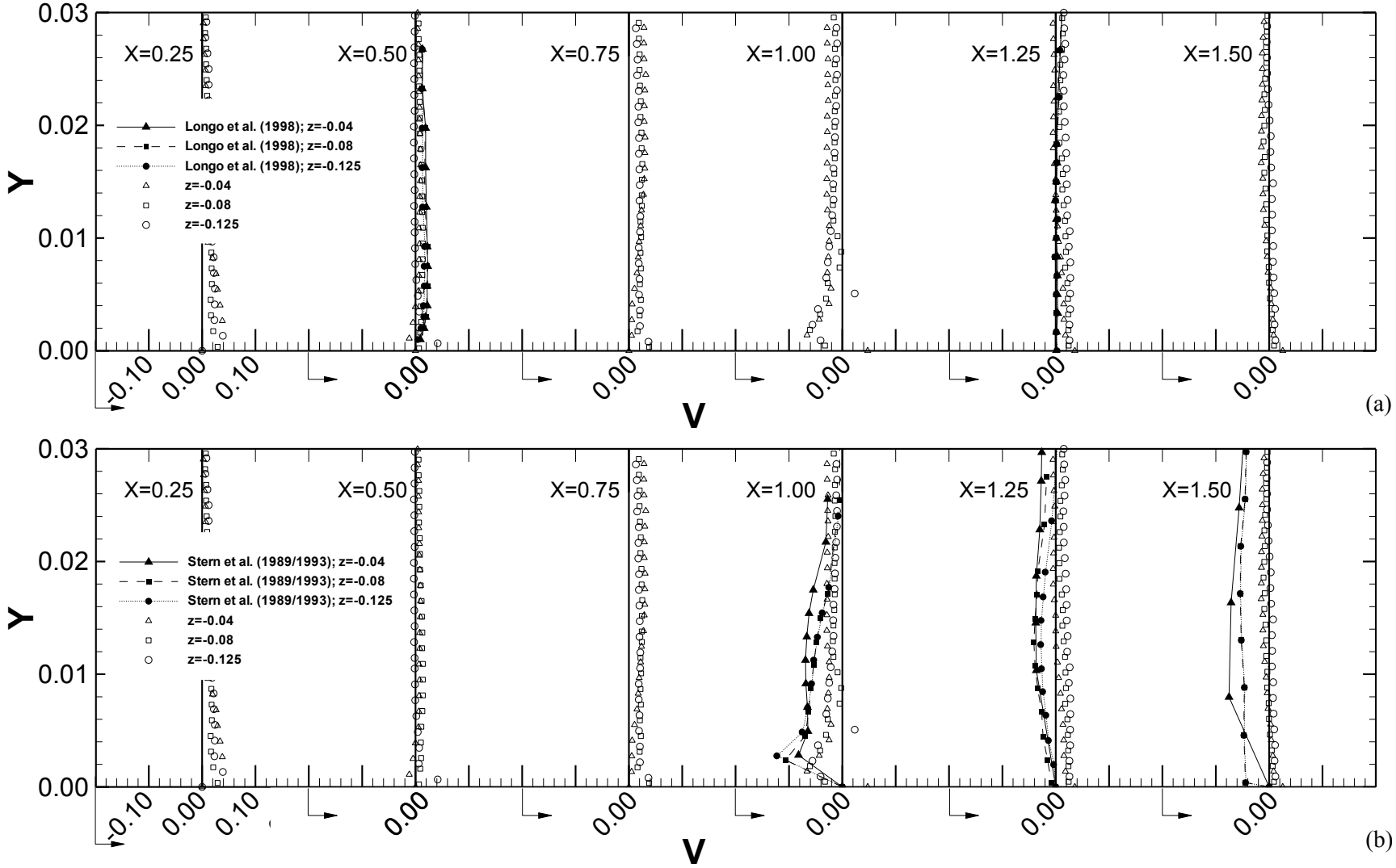

Figure 59: Detailed velocity profiles showing V for (a) $Ak = 0$ and (b) $Ak = 0.21$ (note shifted orgins)

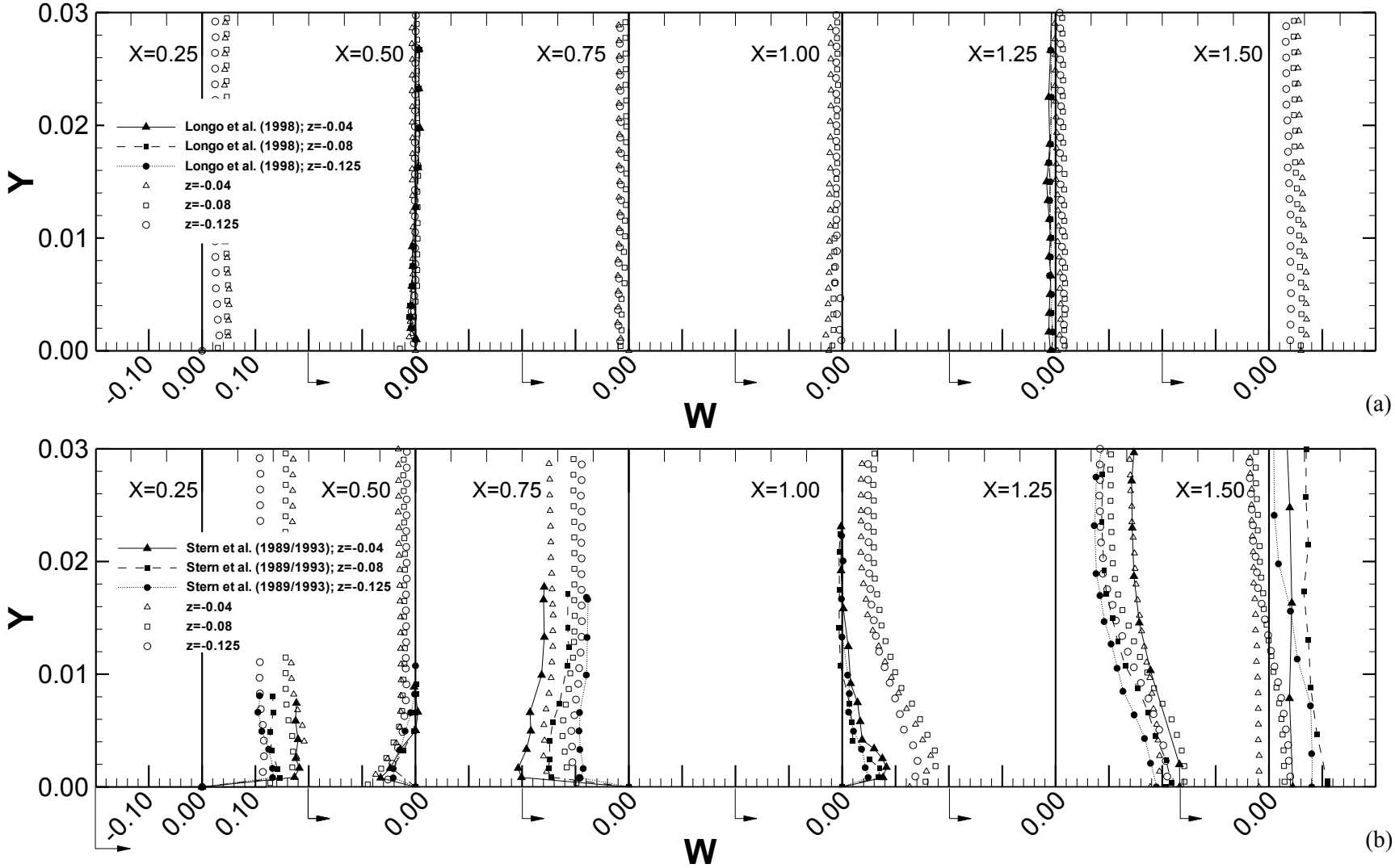

Figure 60: Detailed velocity profiles showing W for (a) $Ak = 0$ and (b) $Ak = 0.21$ (note shifted orgins)

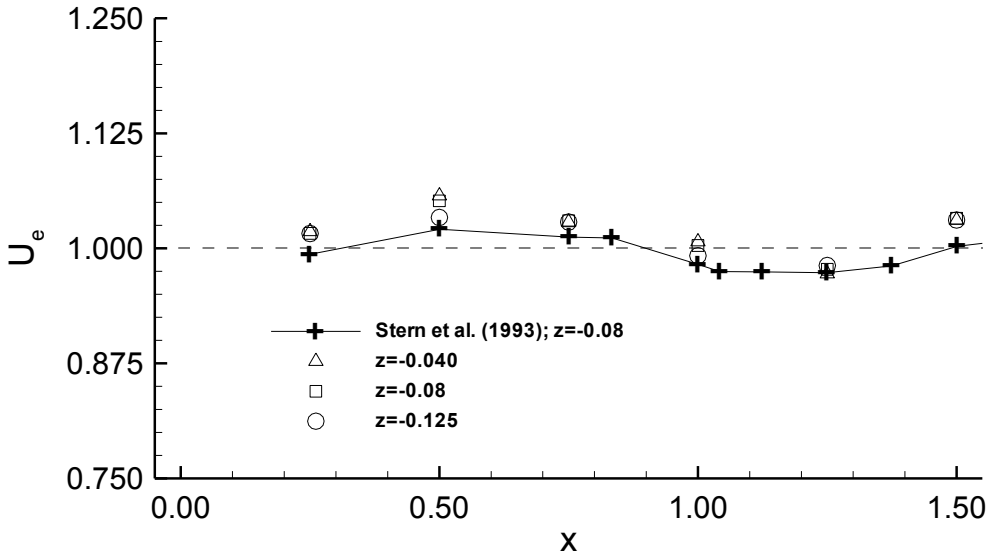

(a)

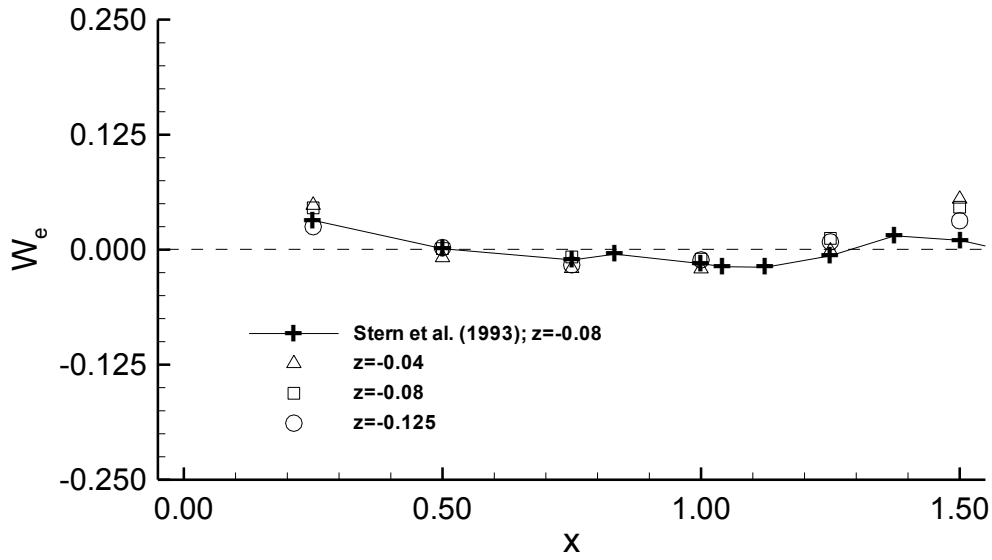

(b)

Figure 61: Edge velocities versus x for (a) U_e and (b) W_e, $Ak = 0$

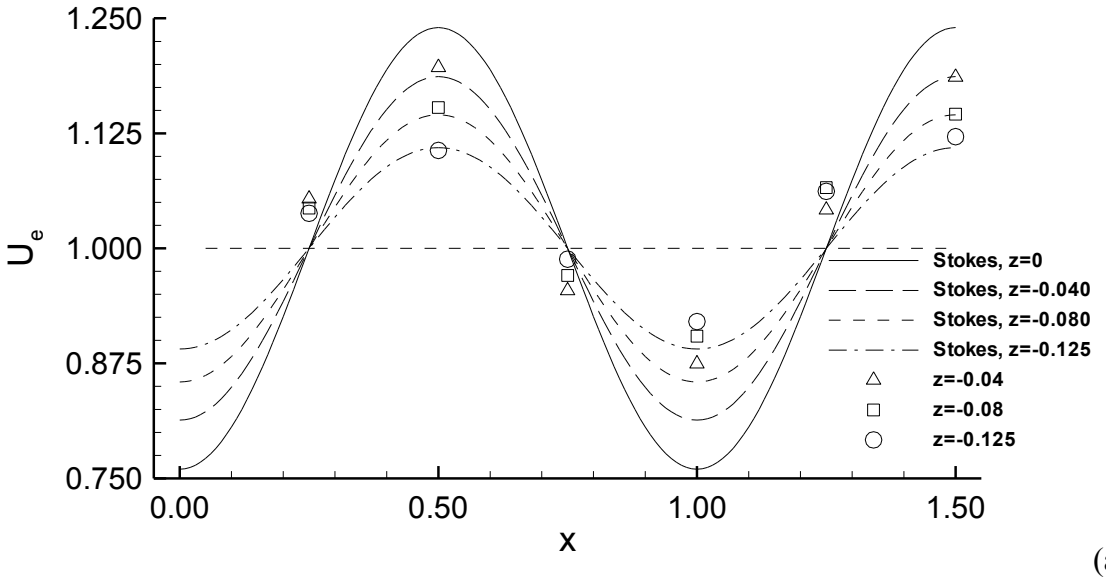

(a)

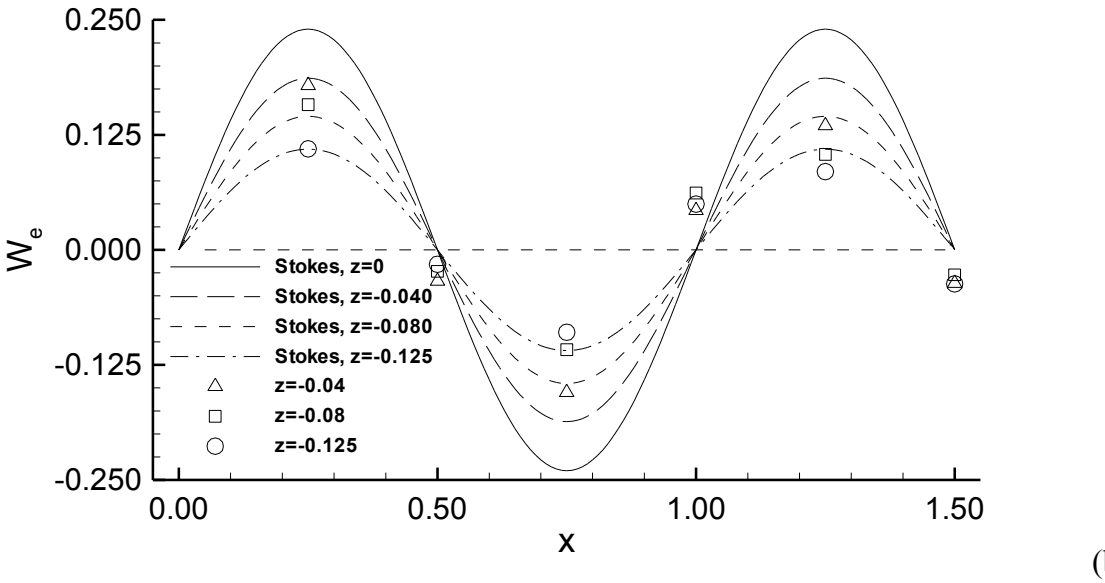

(b)

Figure 62: Edge velocities versus x for (a) U_e and (b) W_e, $Ak = 0.21$

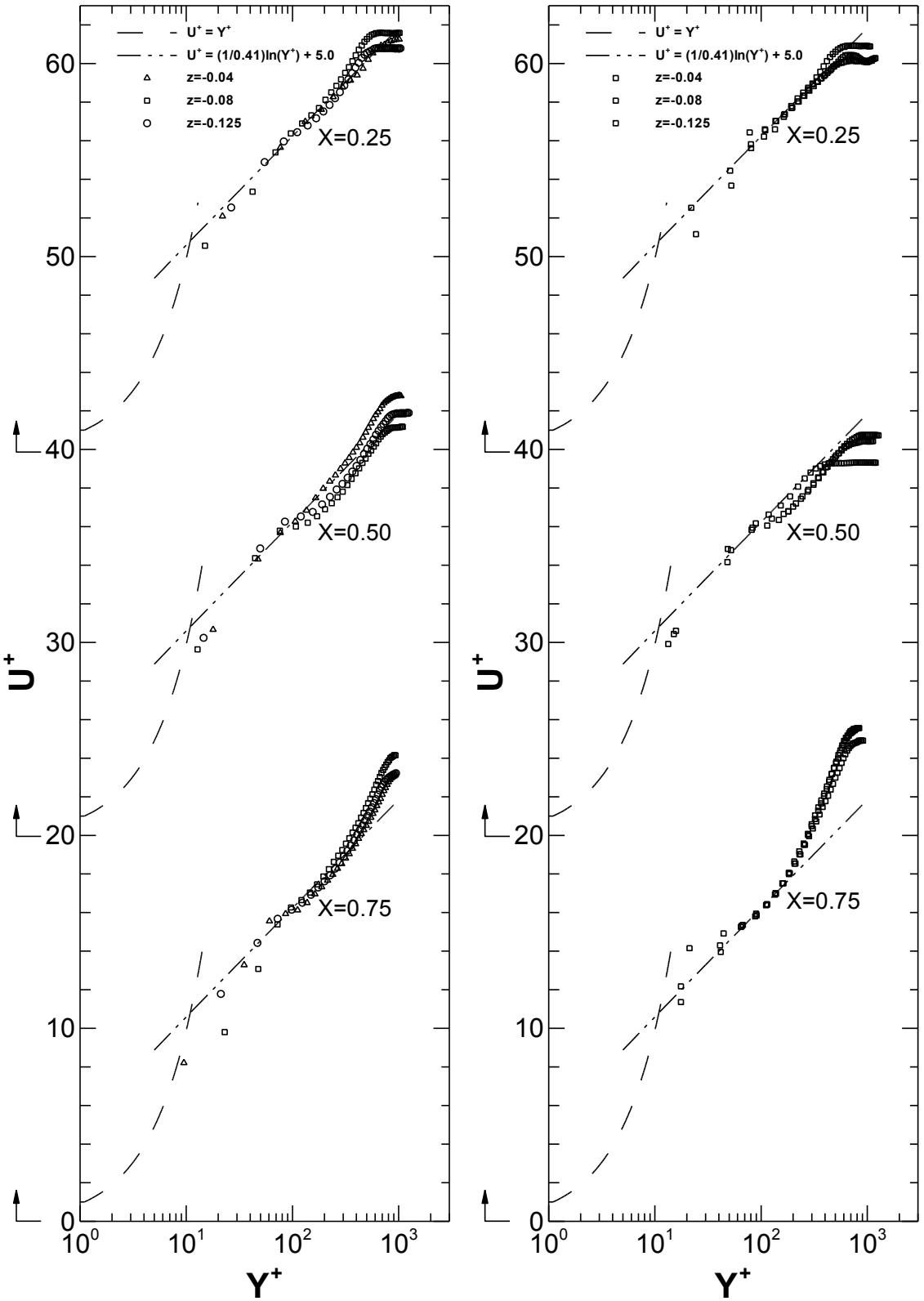

Figure 63: Profiles for u^+ and y^+ for $Ak = 0$ (left) and $Ak = 0.21$ (right) (note shifted orgins)

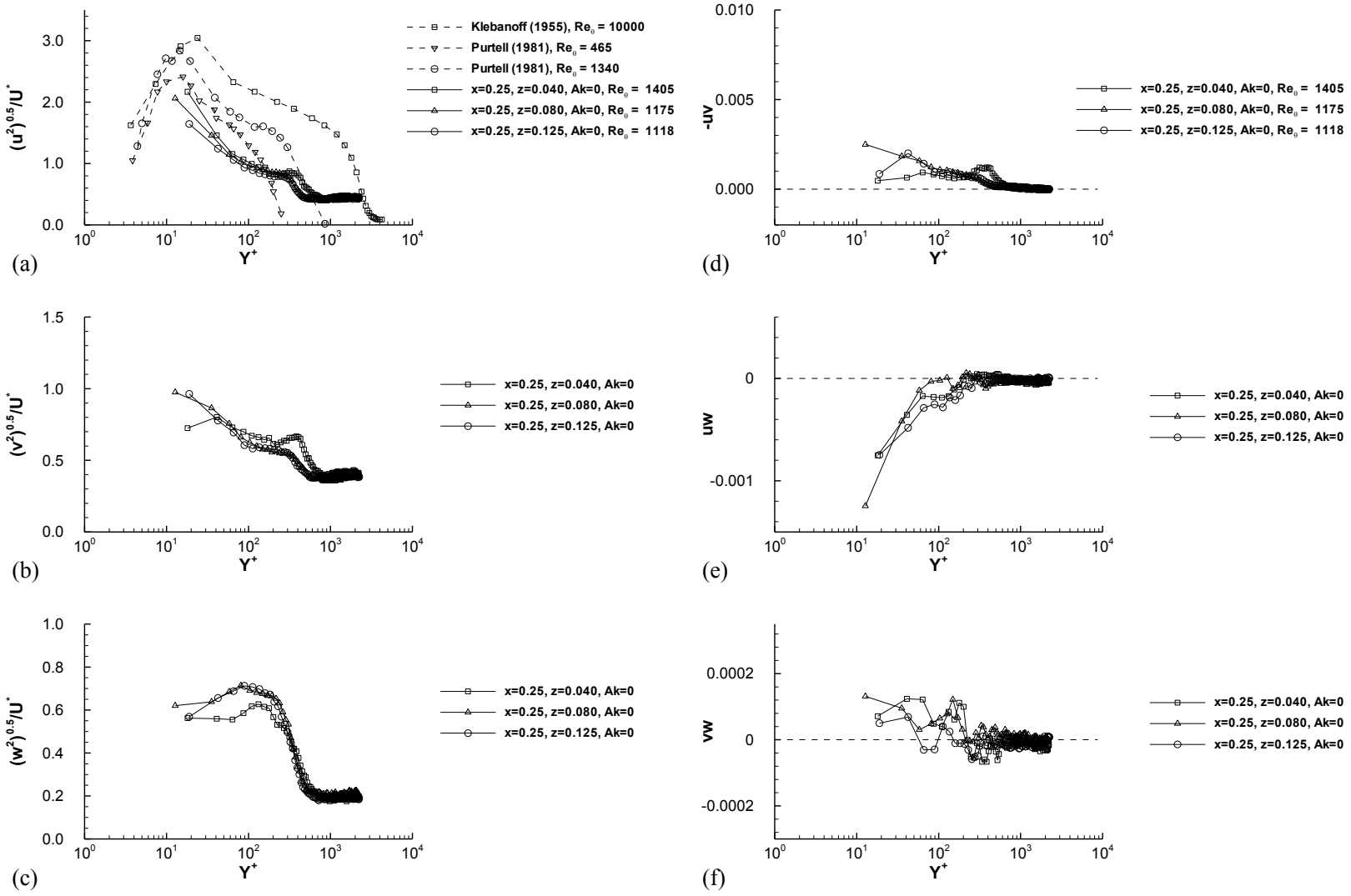

Figure 64: Underlying turbulent flow boundary layer data for $x = 0.25$, $Ak = 0$.

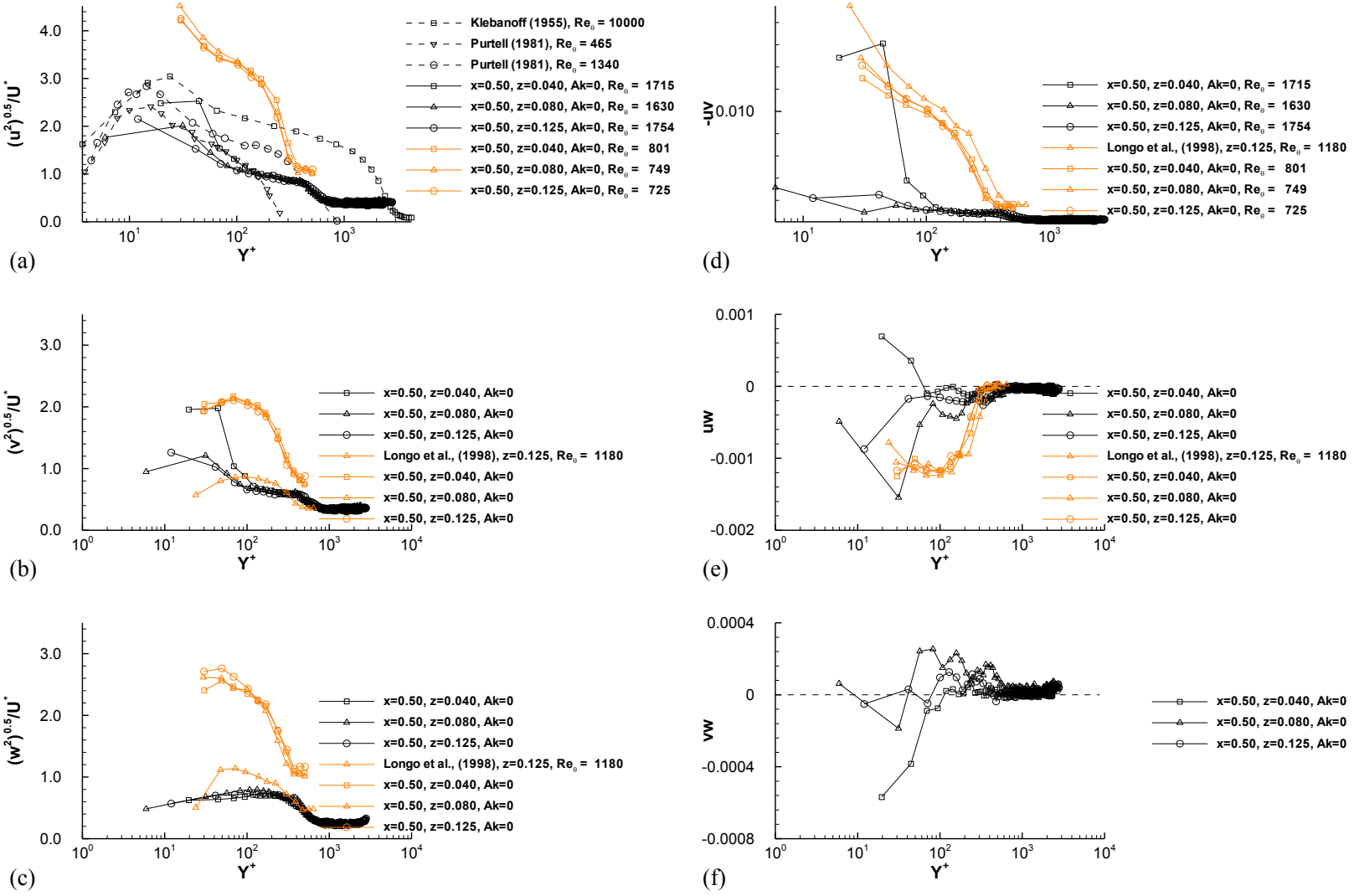

Figure 64 continued: Underlying turbulent flow boundary layer data for $x = 0.50$, $Ak = 0$.

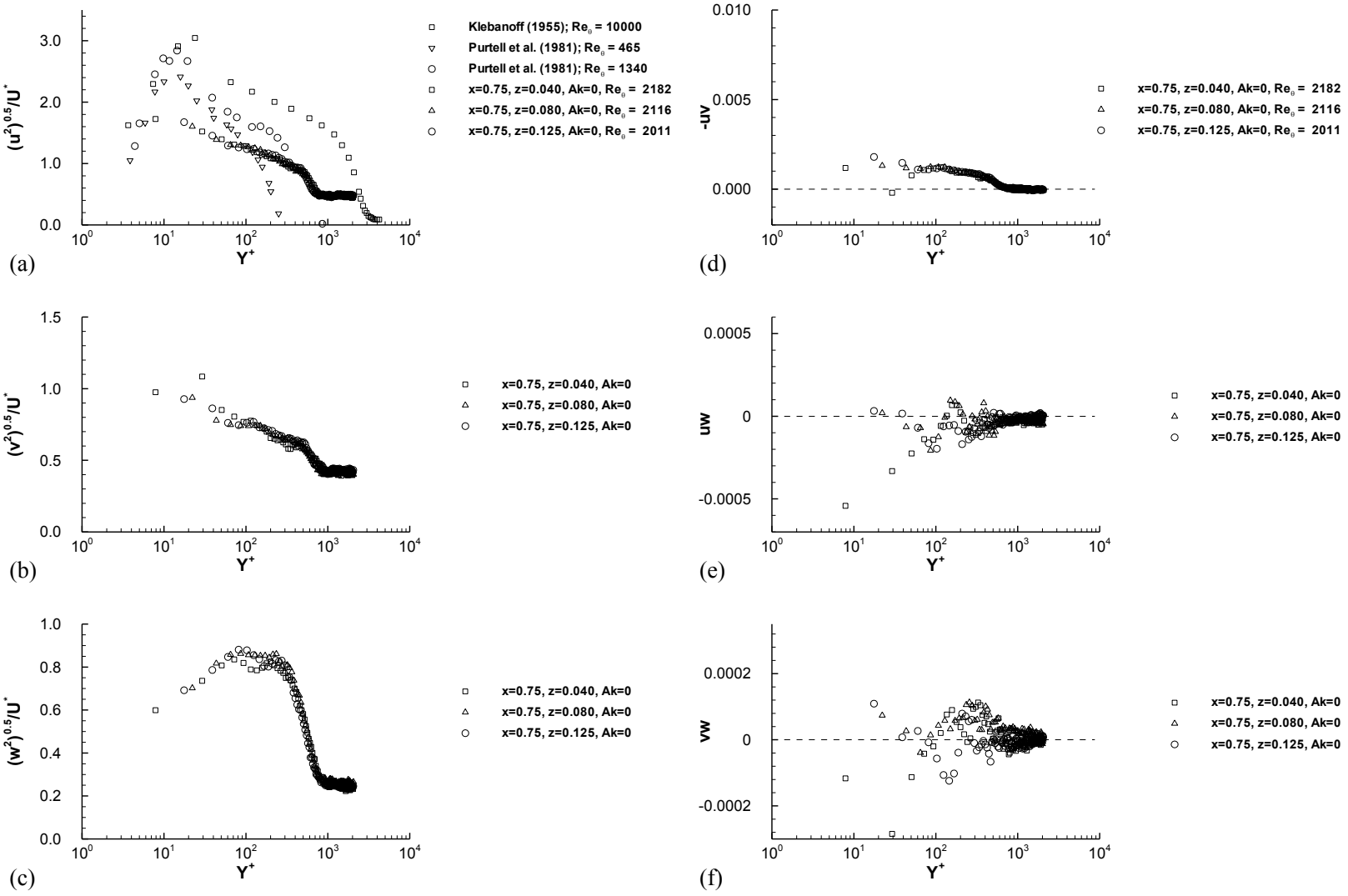

Figure 64 continued: Underlying turbulent flow boundary layer for $x = 0.75$, $Ak = 0$.

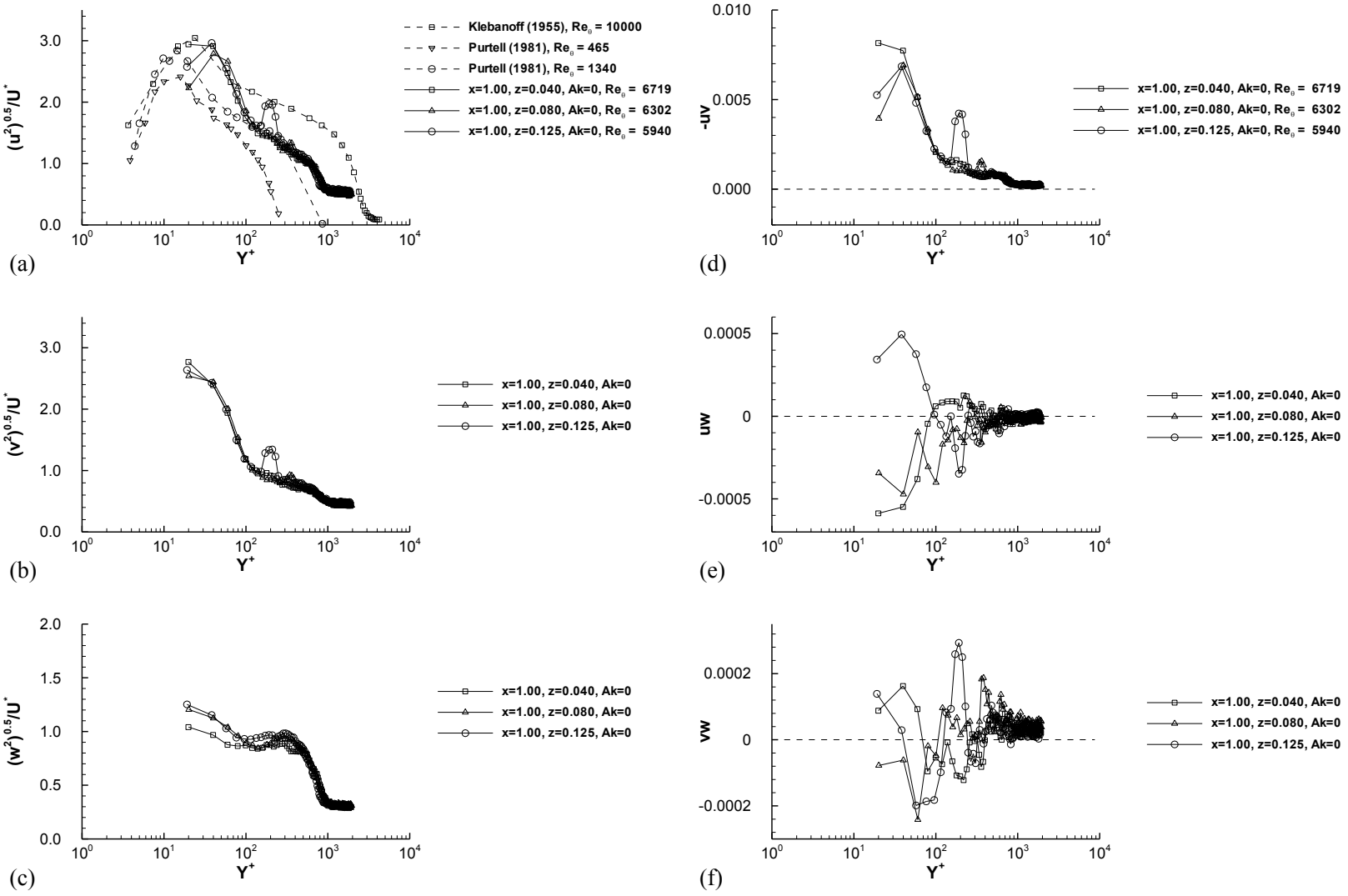

Figure 64 continued: Underlying turbulent flow boundary layer data for $x = 1.00$, $Ak = 0$

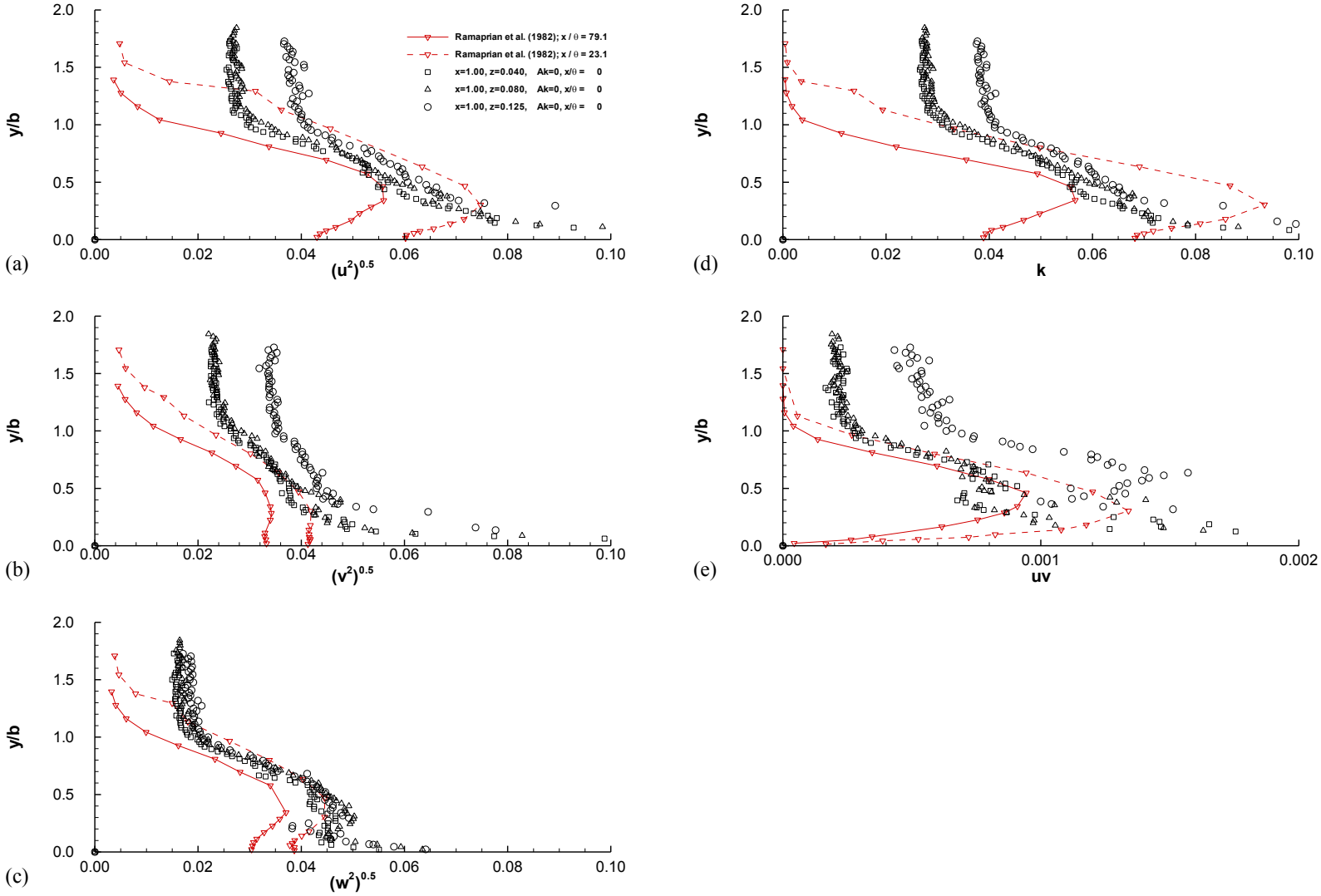

Figure 65: Underlying turbulent flow boundary layer data for $x = 1.00$, $Ak = 0$

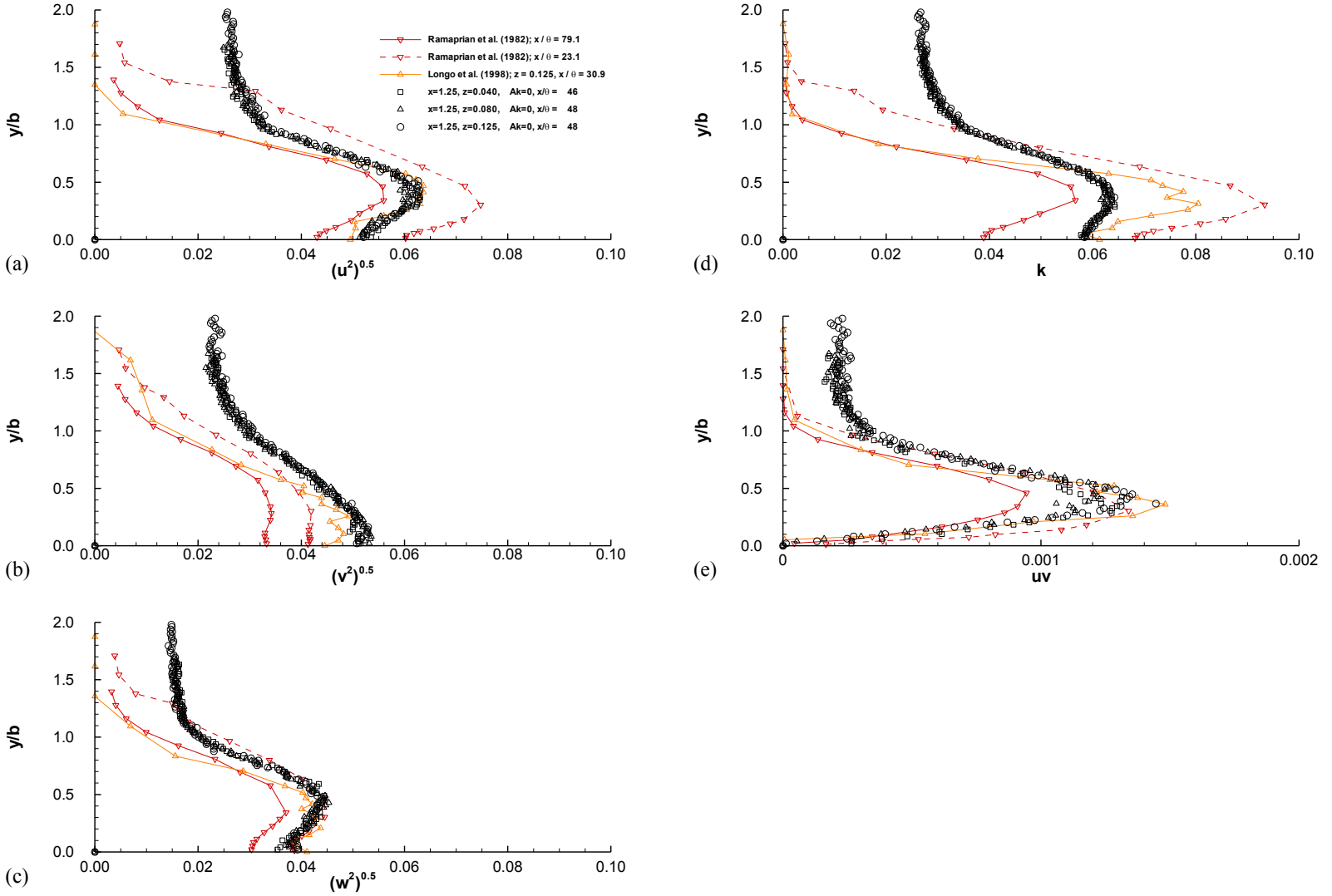

Figure 65 continued: Underlying turbulent flow boundary layer data for $x = 1.25$, $Ak = 0$

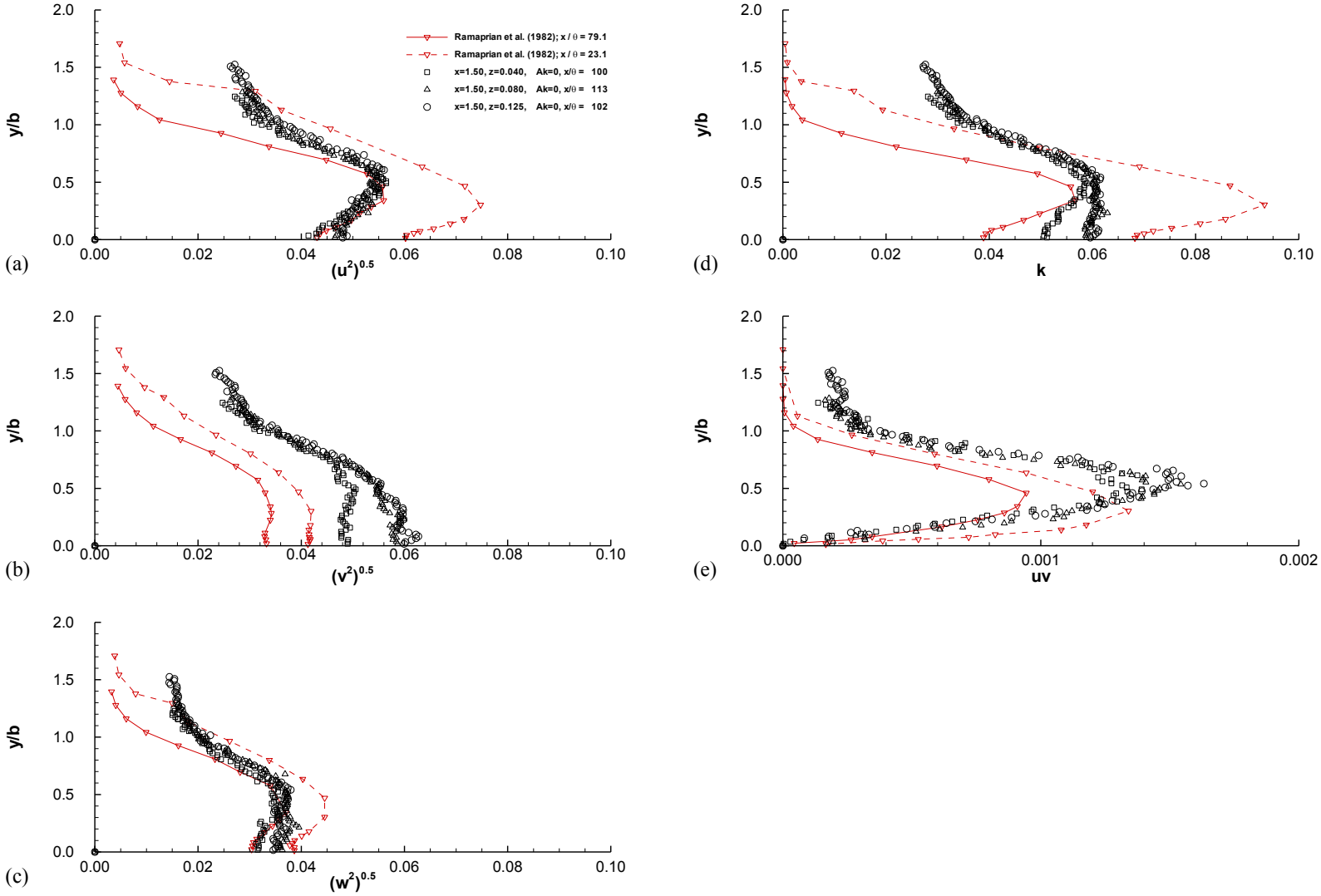

Figure 65 continued: Underlying turbulent flow boundary layer data for $x = 1.50$, $Ak = 0$

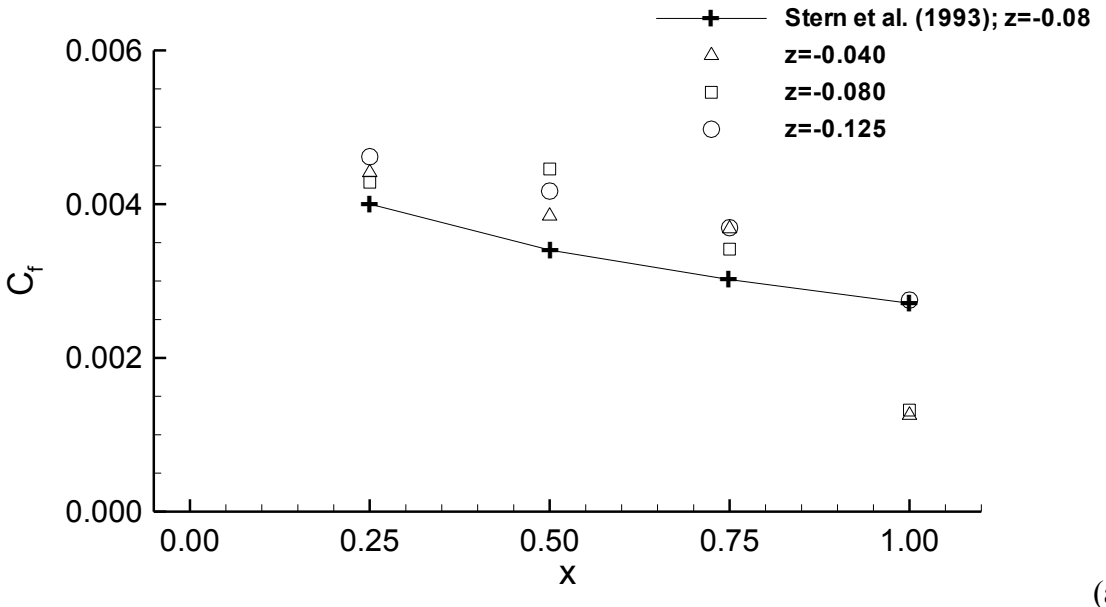

(a)

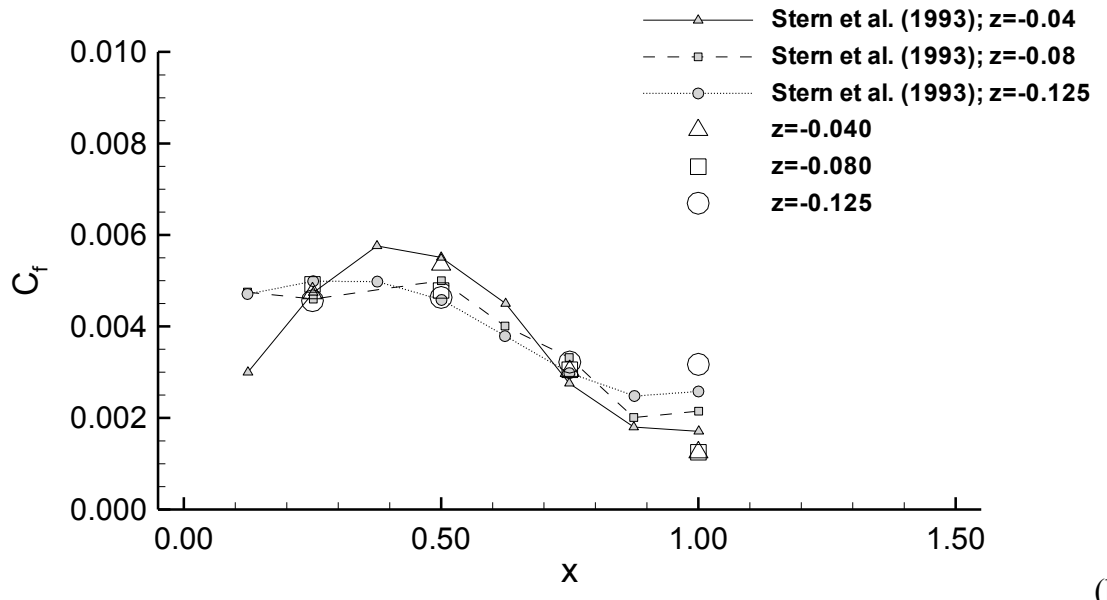

(b)

Figure 66: Wall-shear-stress magnitude, C_f versus x for (a) $Ak = 0$ and (b) $Ak = 0.21$

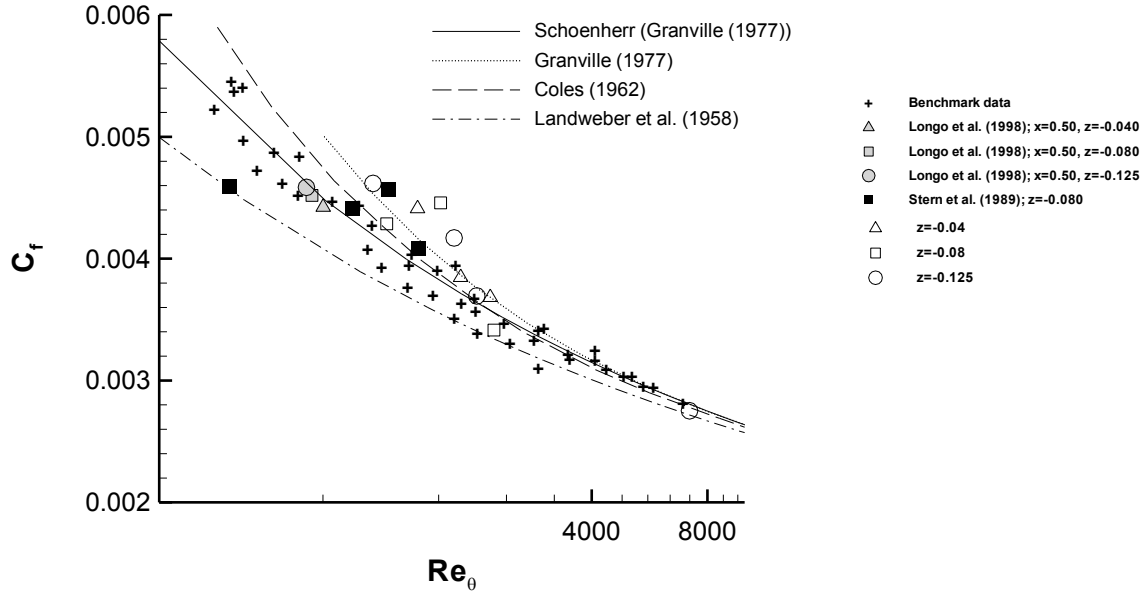

Figure 67: Wall-shear-stress magnitude, C_f versus Re_θ, $Ak = 0$

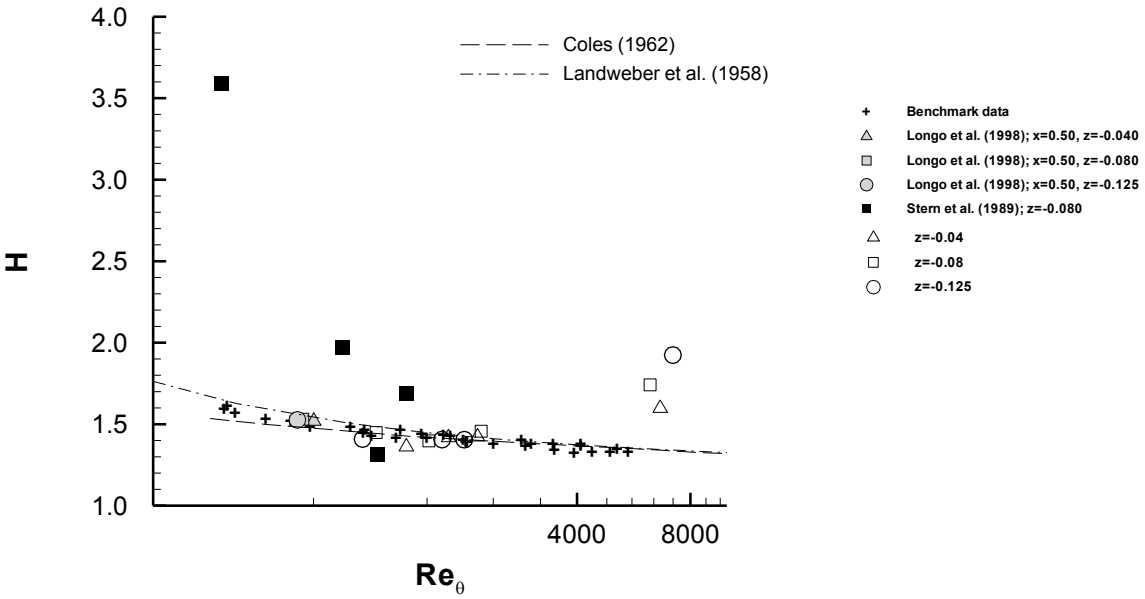

Figure 68: Shape parameter, H versus Re_θ, $Ak = 0$

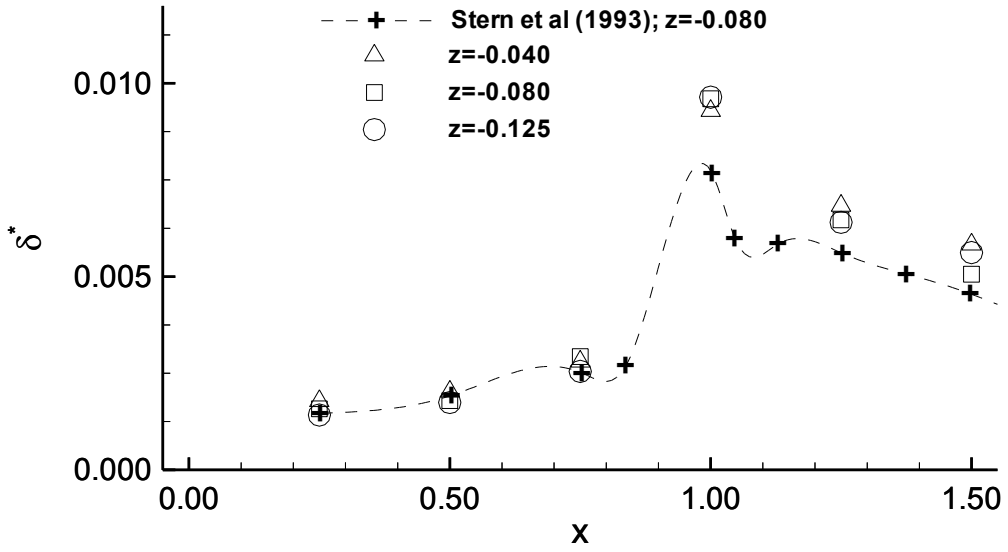

(a)

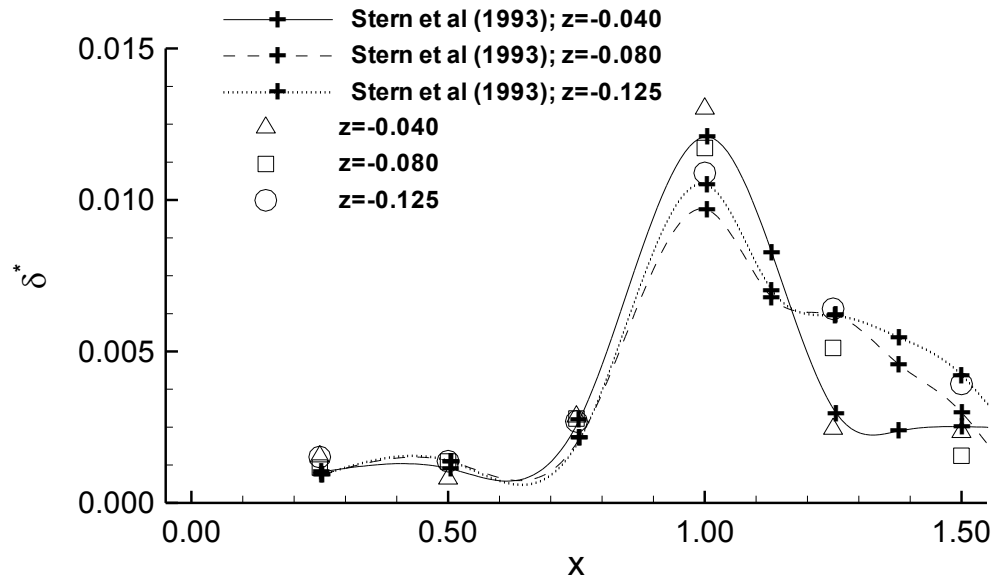

(b)

Figure 69: Displacement thickness, δ^* versus x for (a) $Ak = 0$ and (b) $Ak = 0.21$

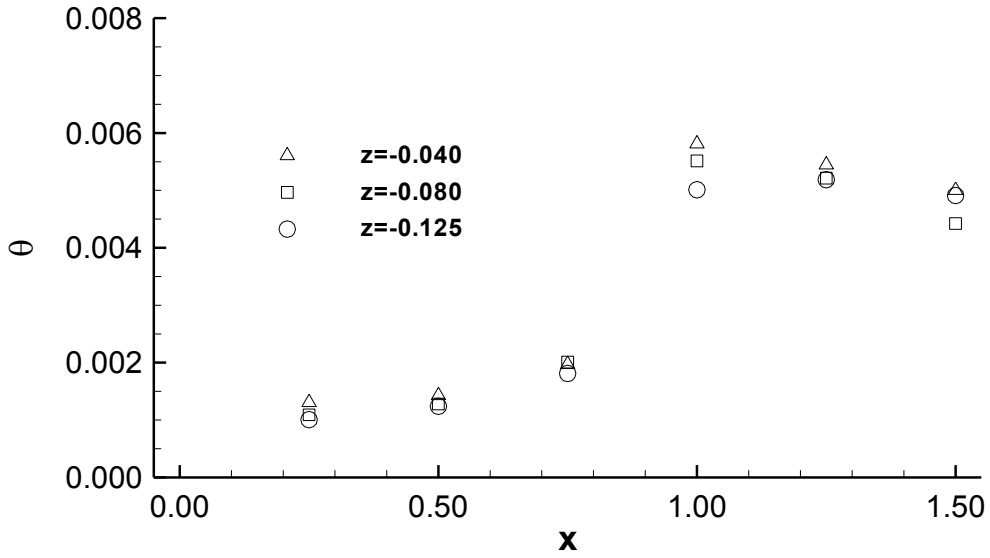

(a)

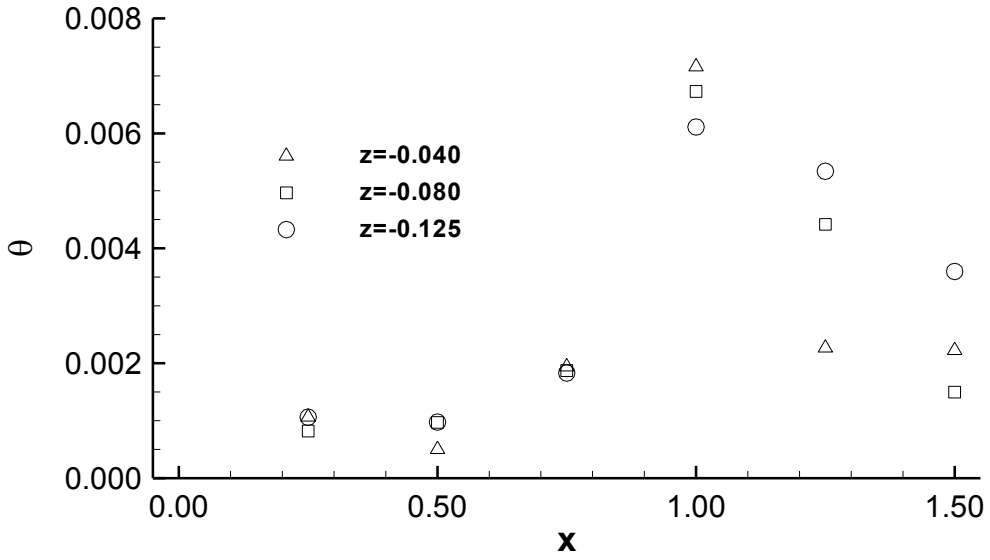

(b)

Figure 70: Momentum thickness, θ versus x for (a) $Ak = 0$ and (b) $Ak = 0.21$

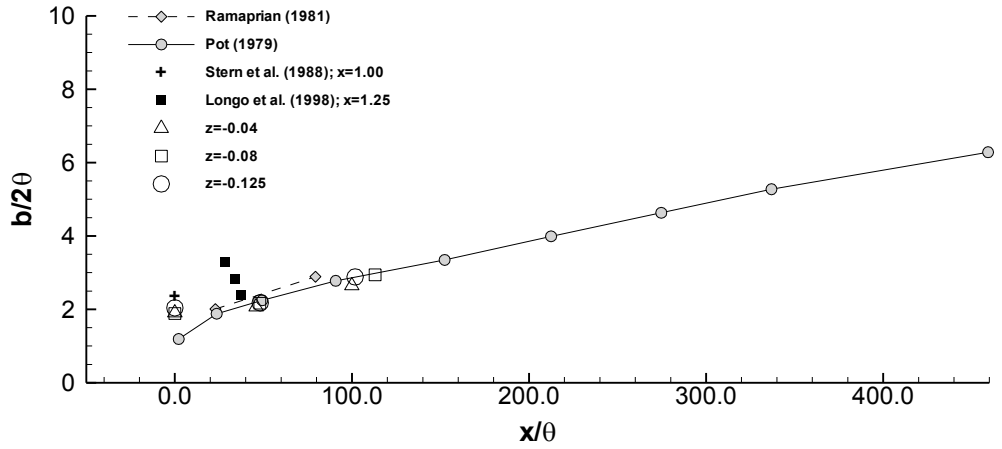

(a)

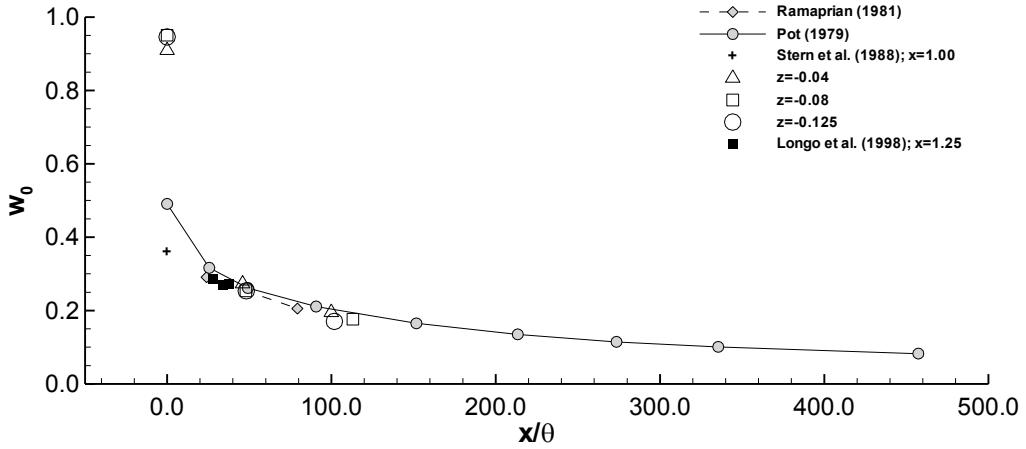

(b)

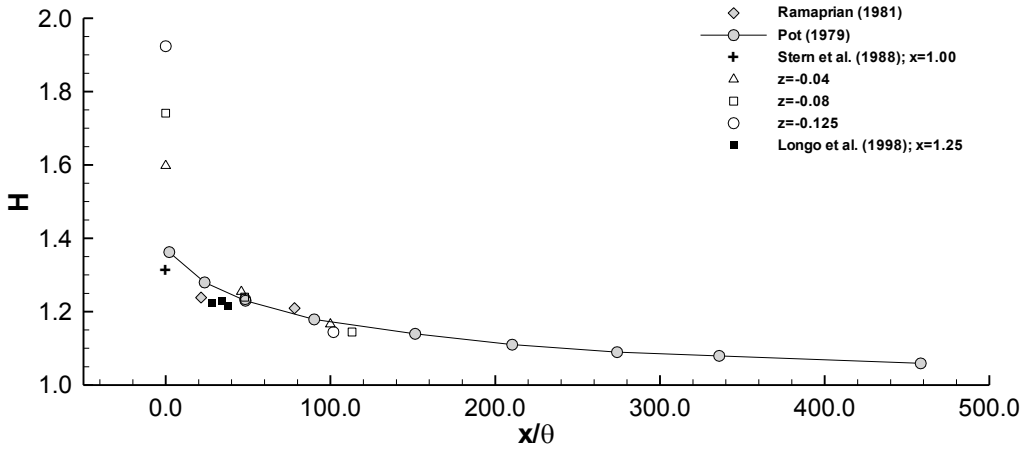

(c)

Figure 71: Wake parameters showing (a) half-width $^{b}/_{2\theta}$, (b) wake defect w_o, and (c) shape factor H, for $Ak = 0$

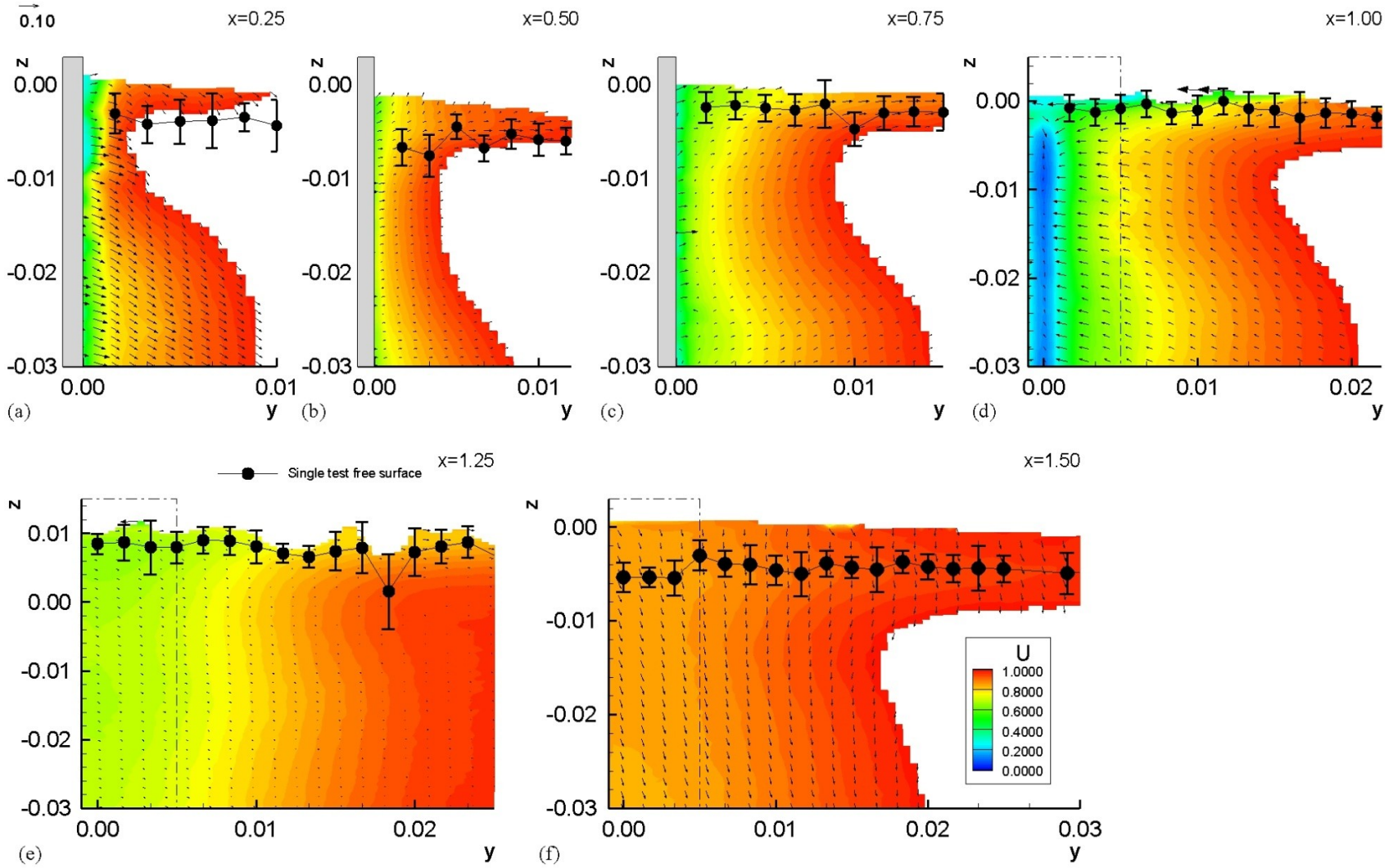

Figure 72: Juncture region U contours overlaid by V and W vectors, $Ak = 0$

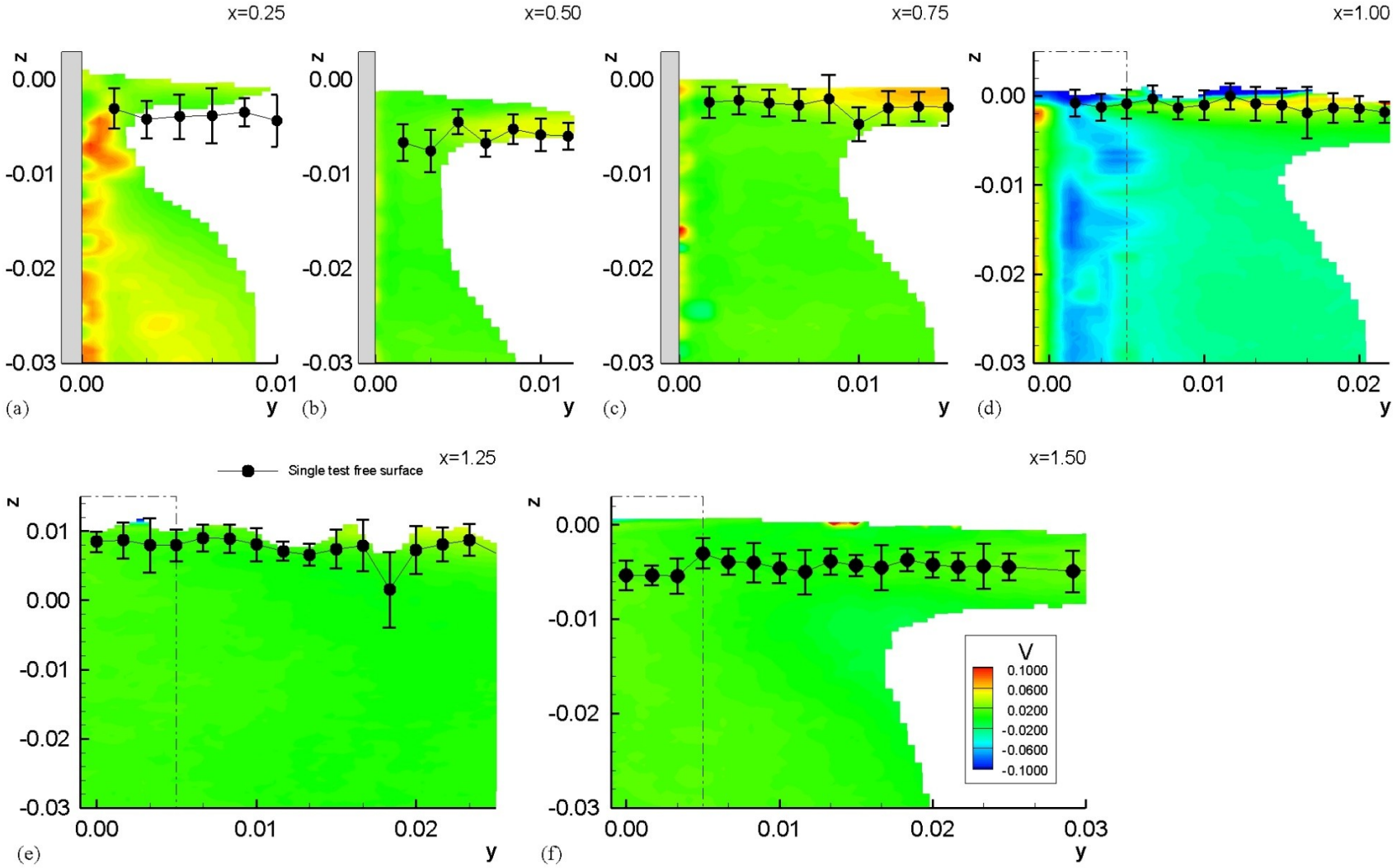

Figure 73: Juncture region V contours, $Ak = 0$

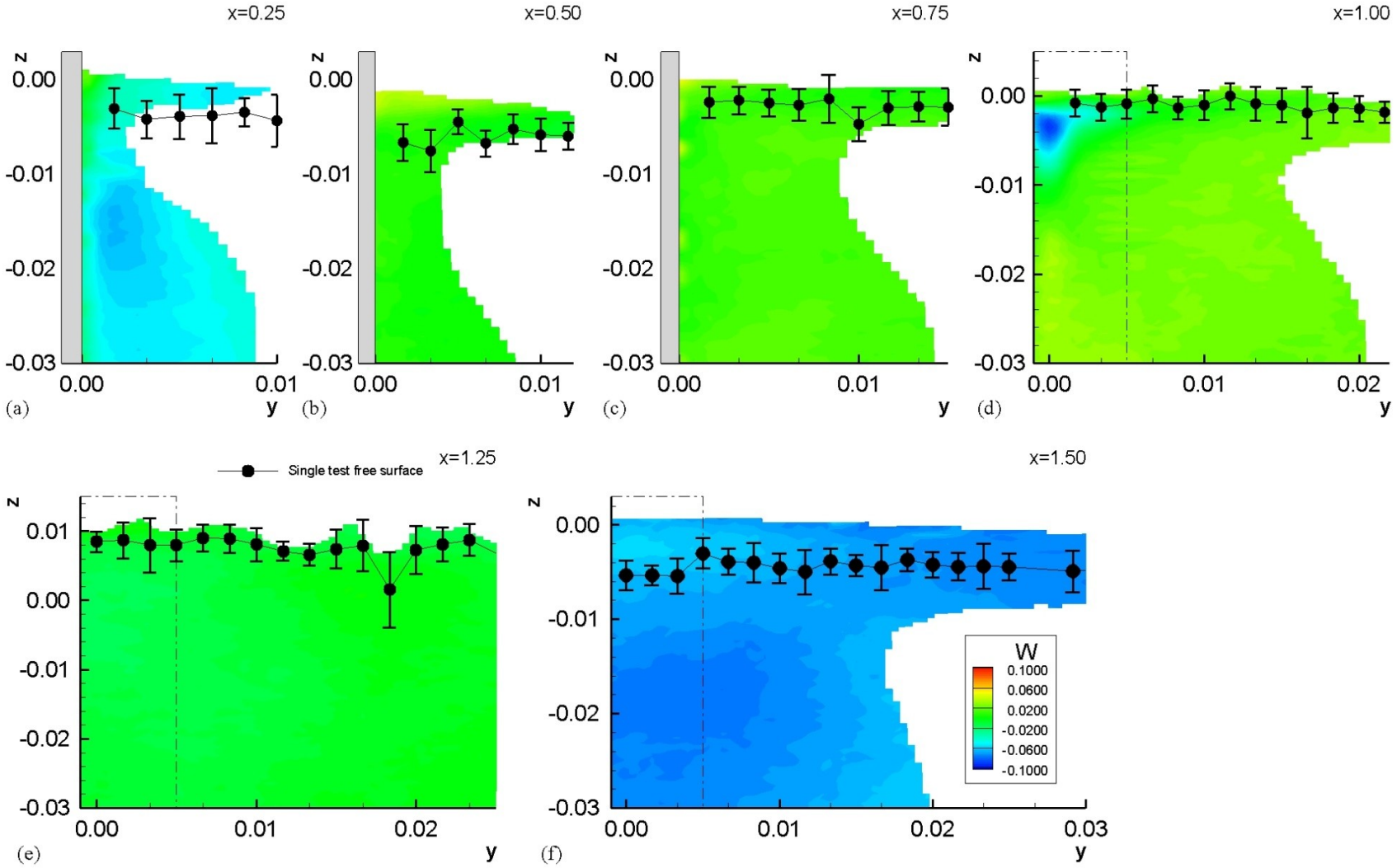

Figure 74: Juncture region W contours, $Ak = 0$

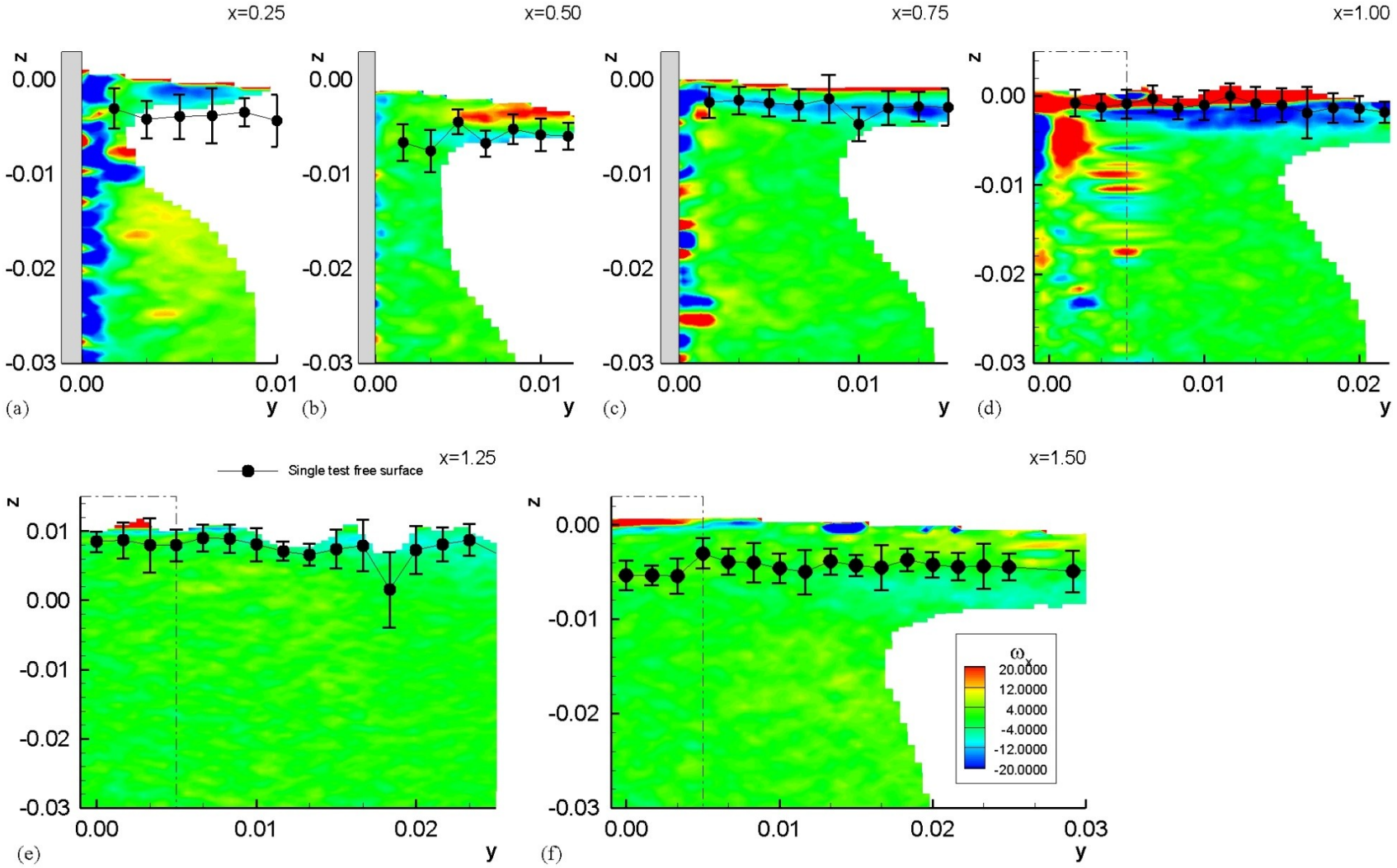

Figure 75: Juncture region ω_x contours, $Ak = 0$

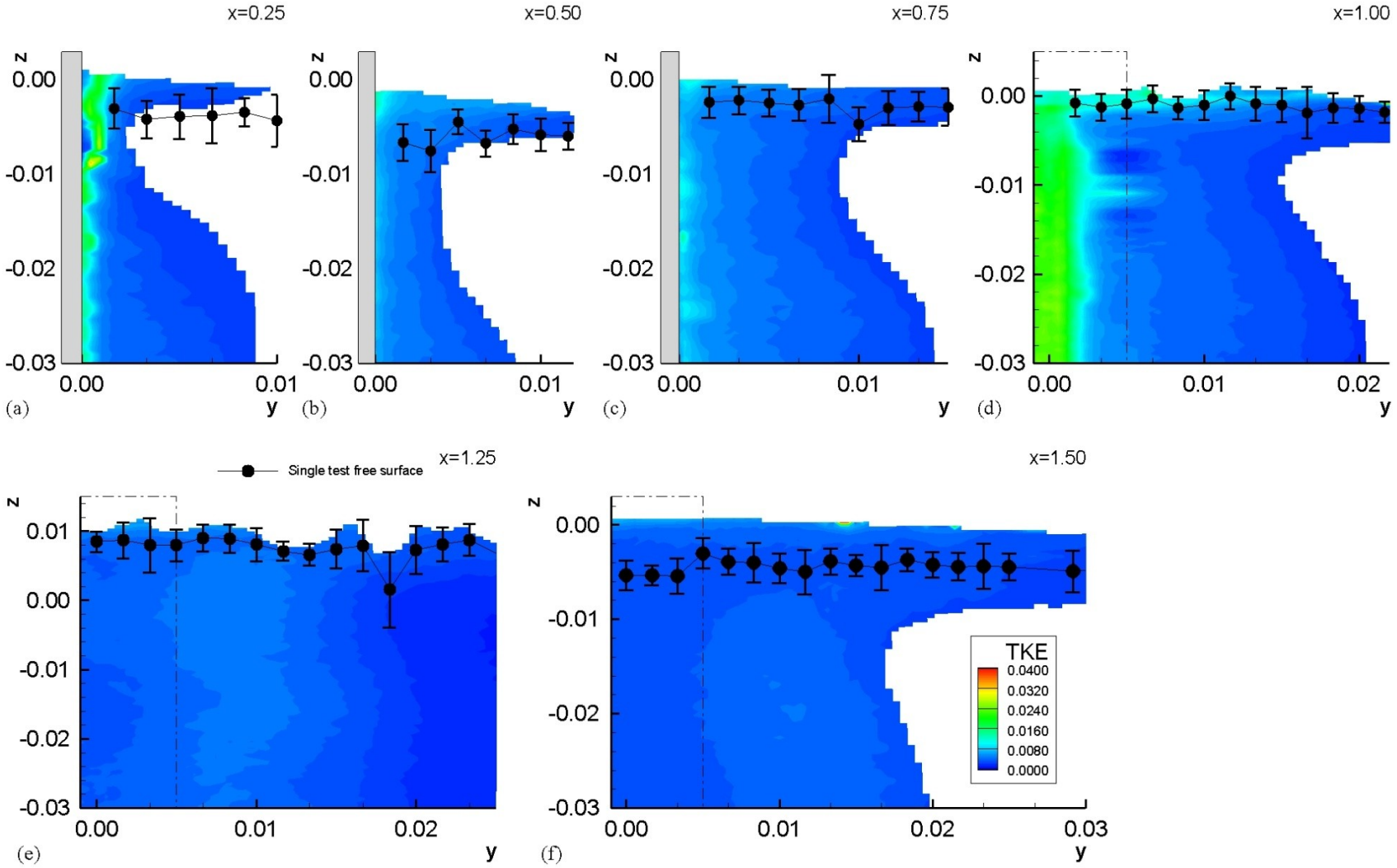

Figure 76: Juncture region *TKE* contours, $Ak = 0$

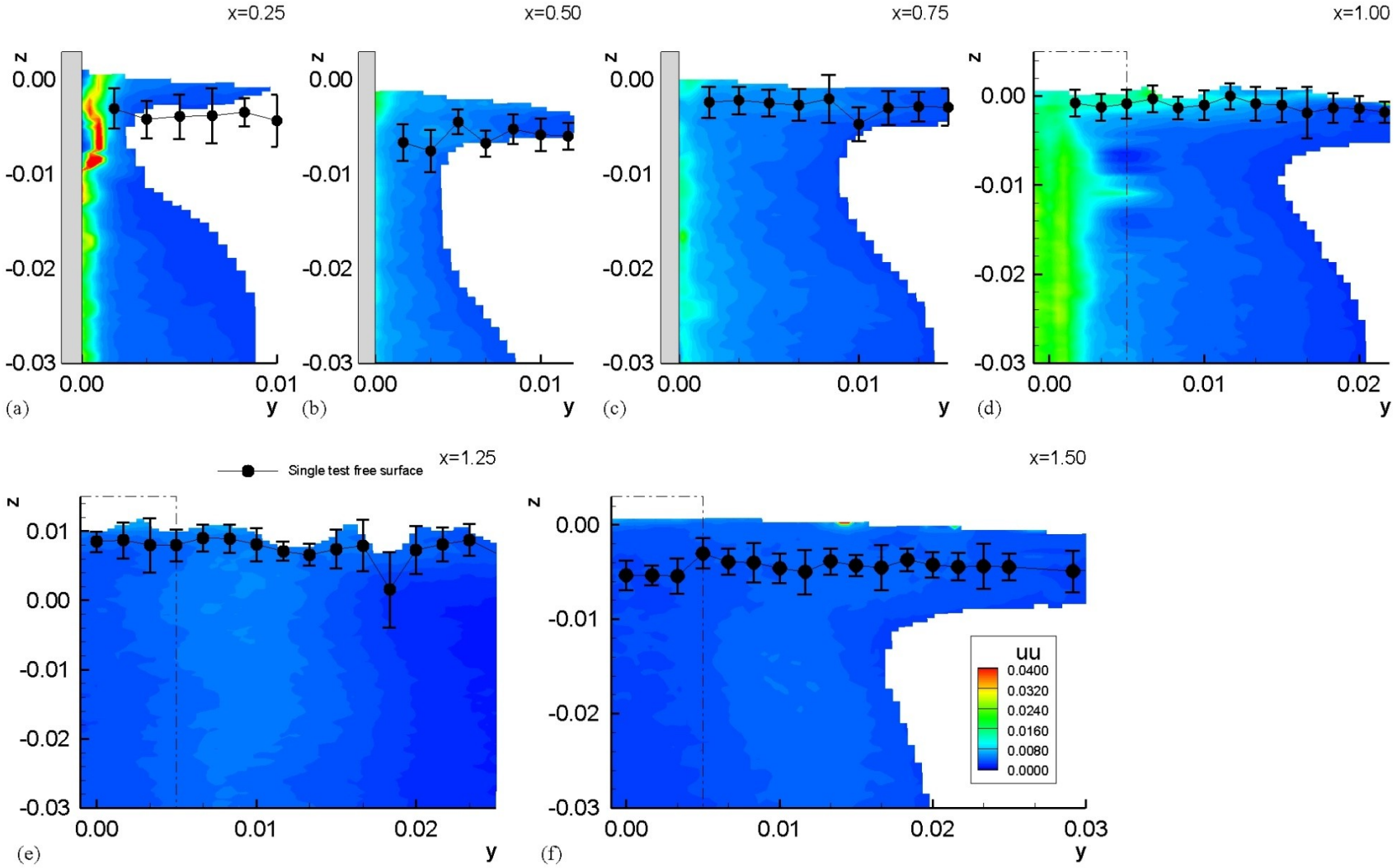

Figure 77: Juncture region *uu* contours, $Ak = 0$

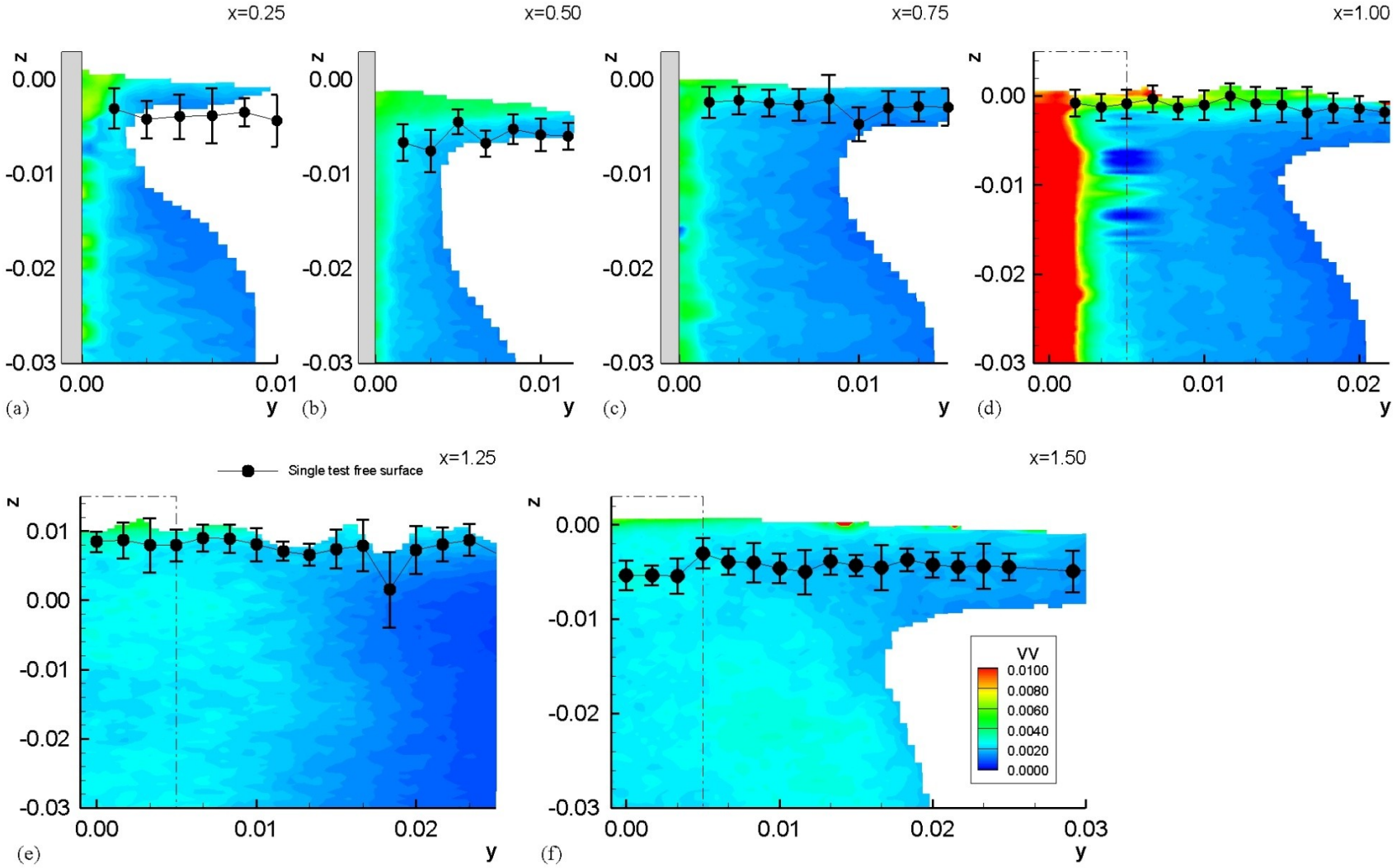

Figure 78: Juncture region *vv* contours, $Ak = 0$

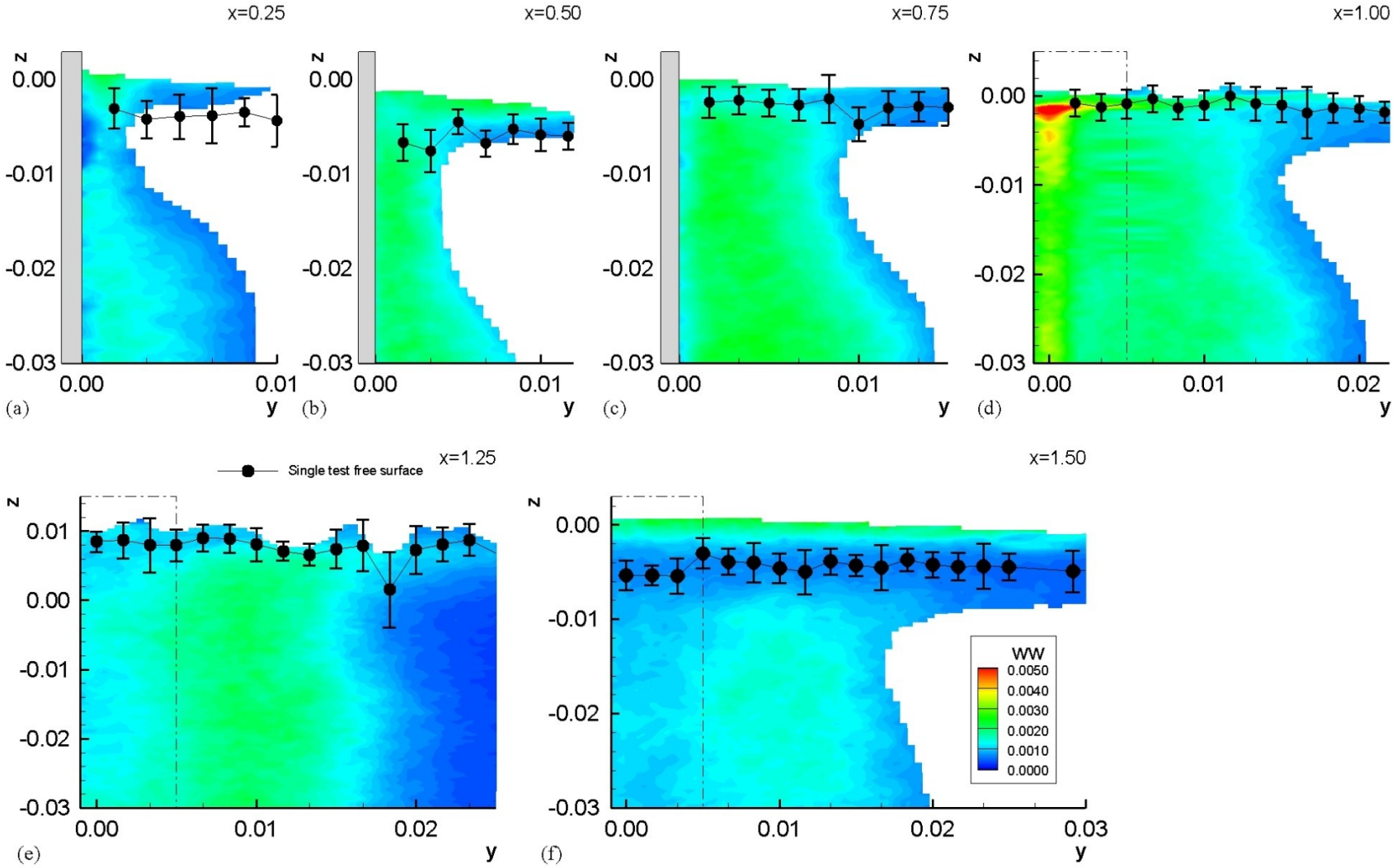

Figure 79: Juncture region *ww* contours, $Ak = 0$

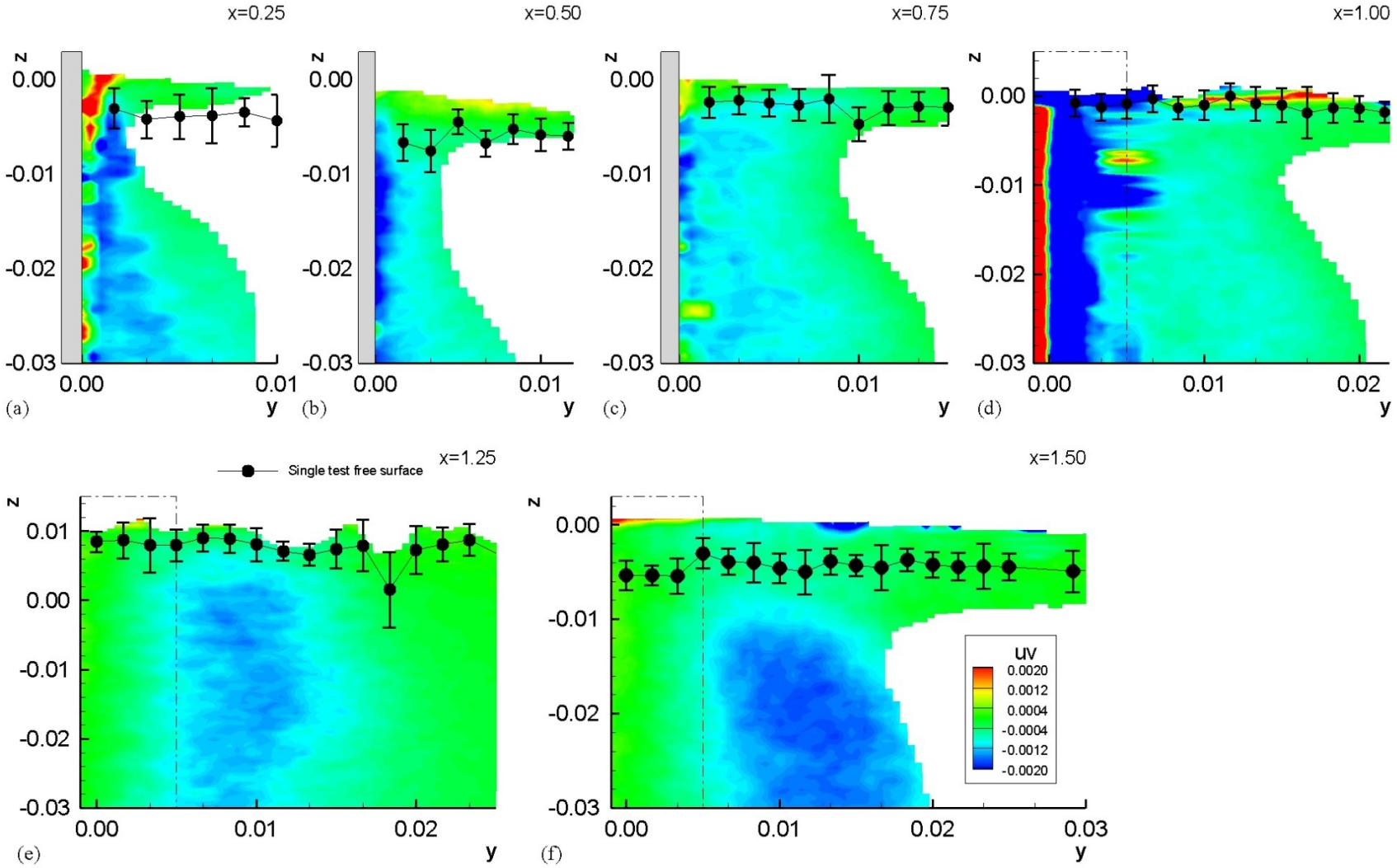

Figure 80: Juncture region *uv* contours, $Ak = 0$

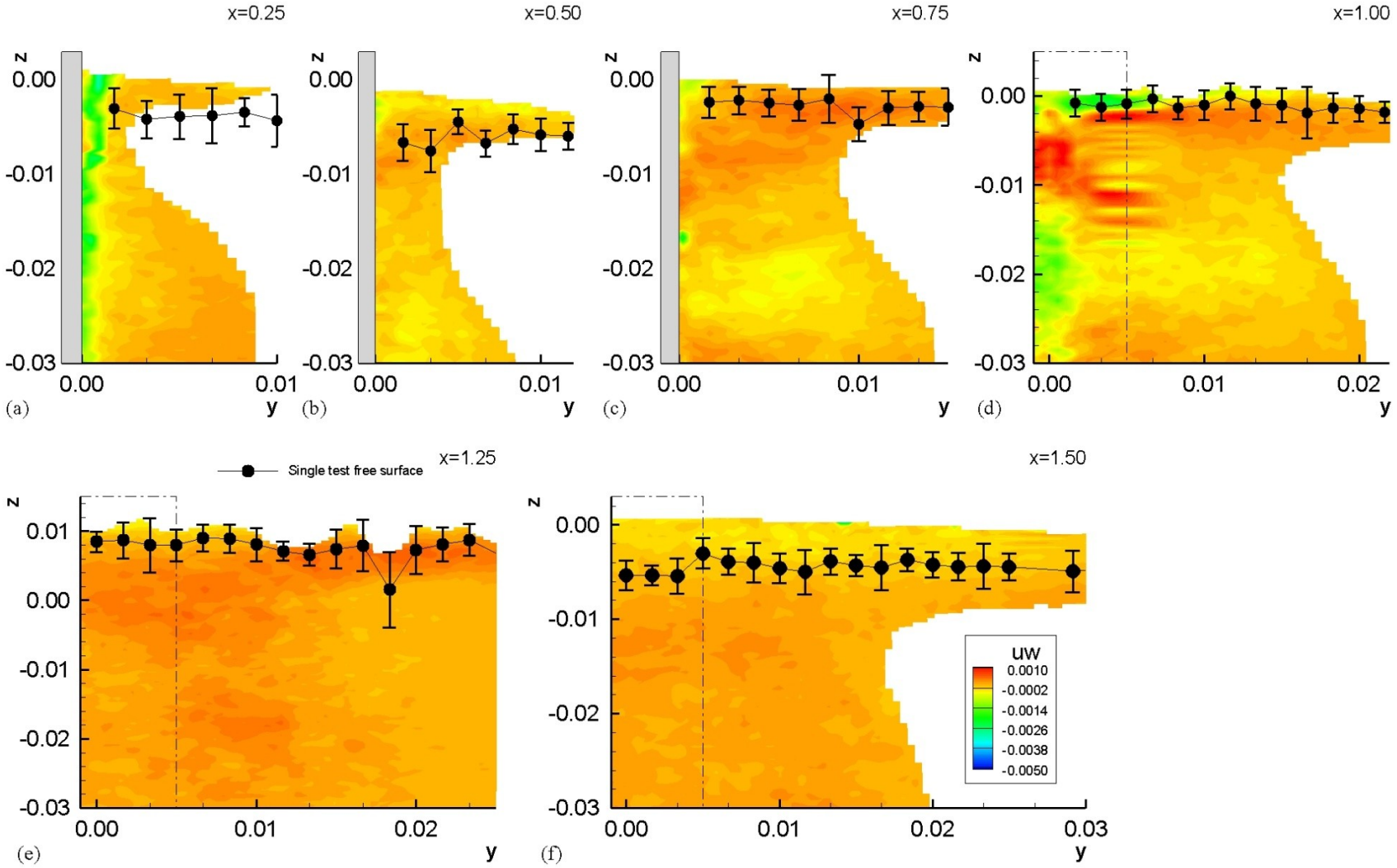

Figure 81: Juncture region *uw* contours, $Ak = 0$

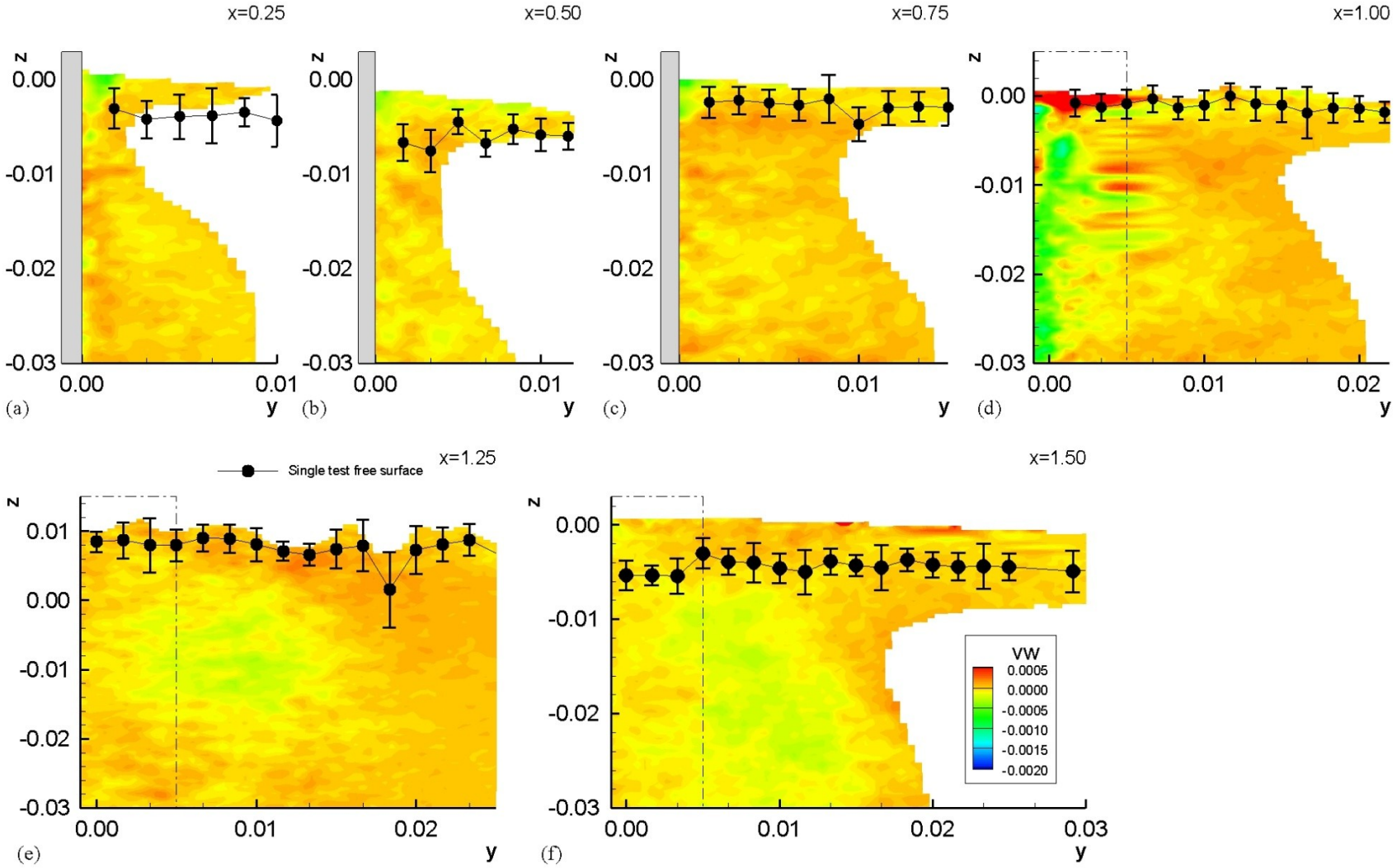

Figure 82: Juncture region *vw* contours, $Ak = 0$

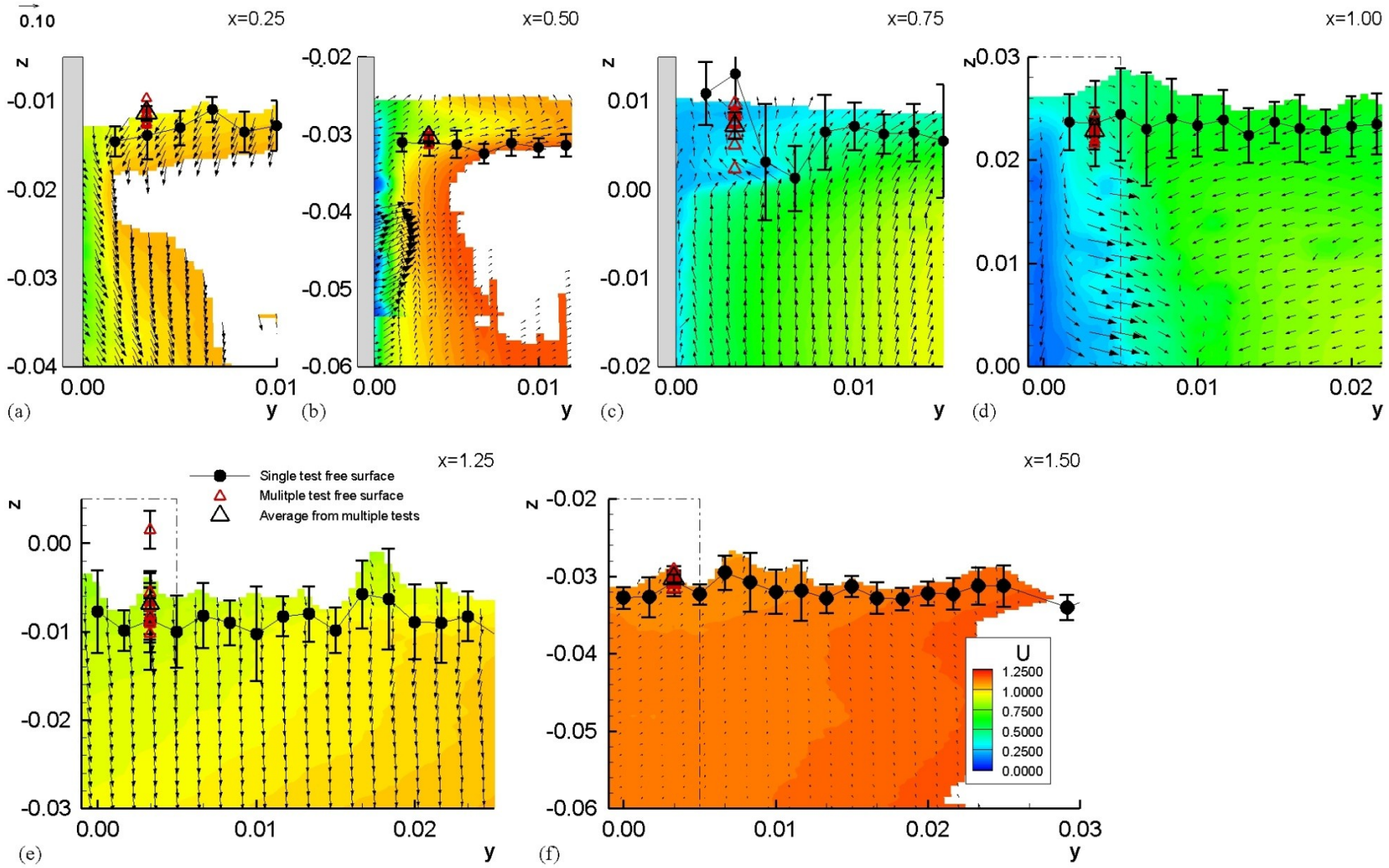

Figure 83: Juncture region U contours overlaid by V and W vectors, $Ak = 0.21$

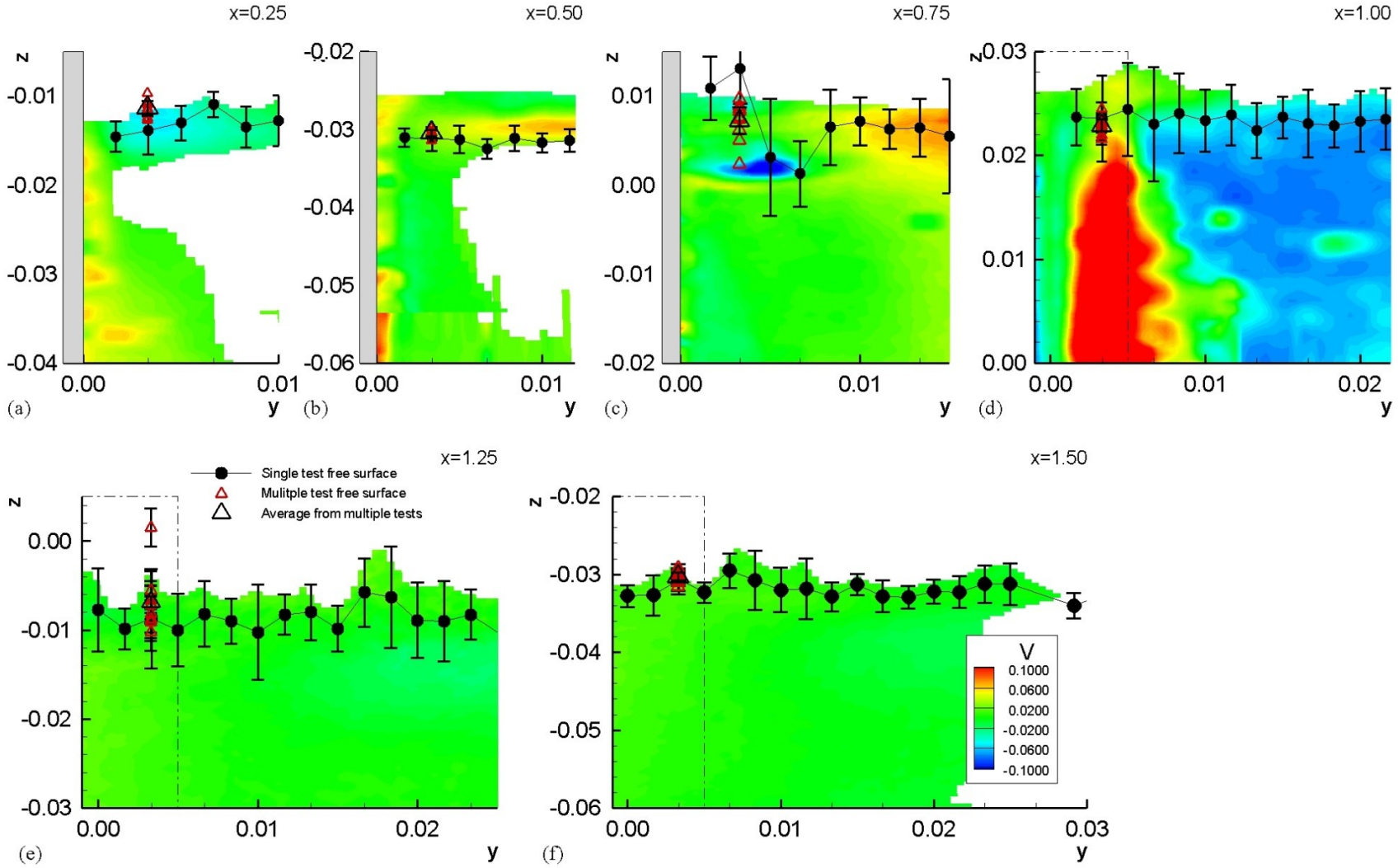

Figure 84: Juncture region V contours, $Ak = 0.21$

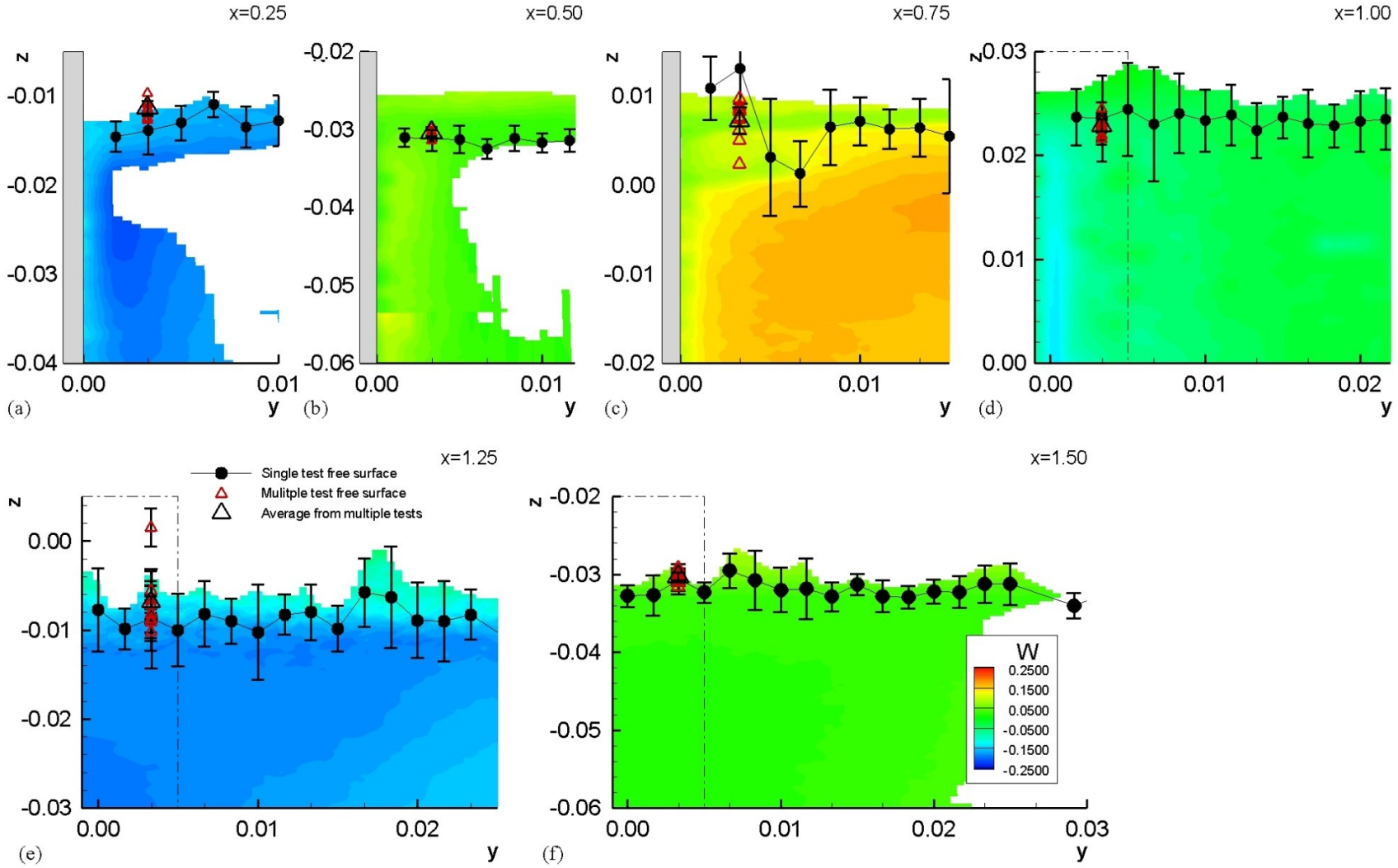

Figure 85: Juncture region W contours, $Ak = 0.21$

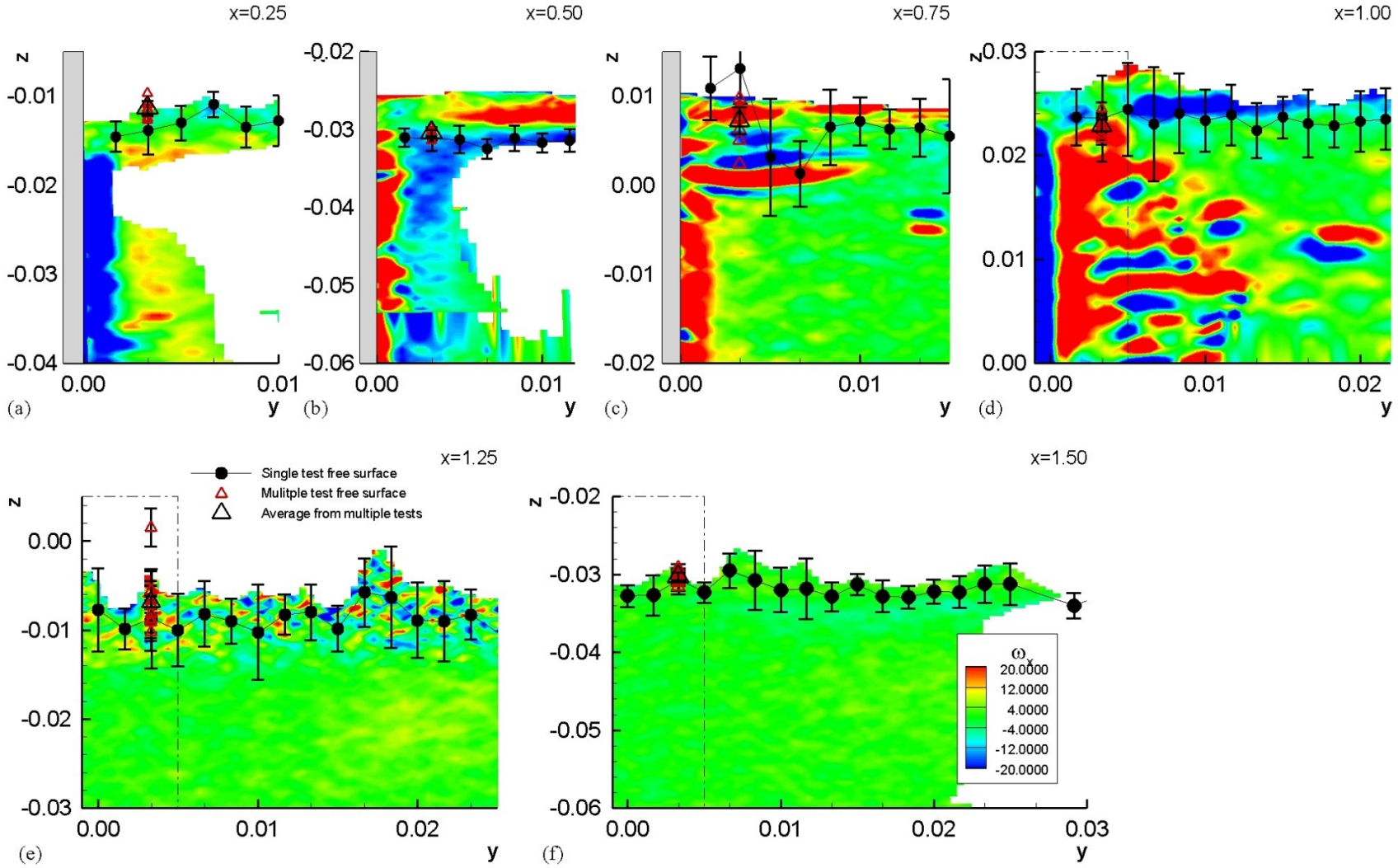

Figure 86: Juncture region ω_x contours, $Ak = 0.21$

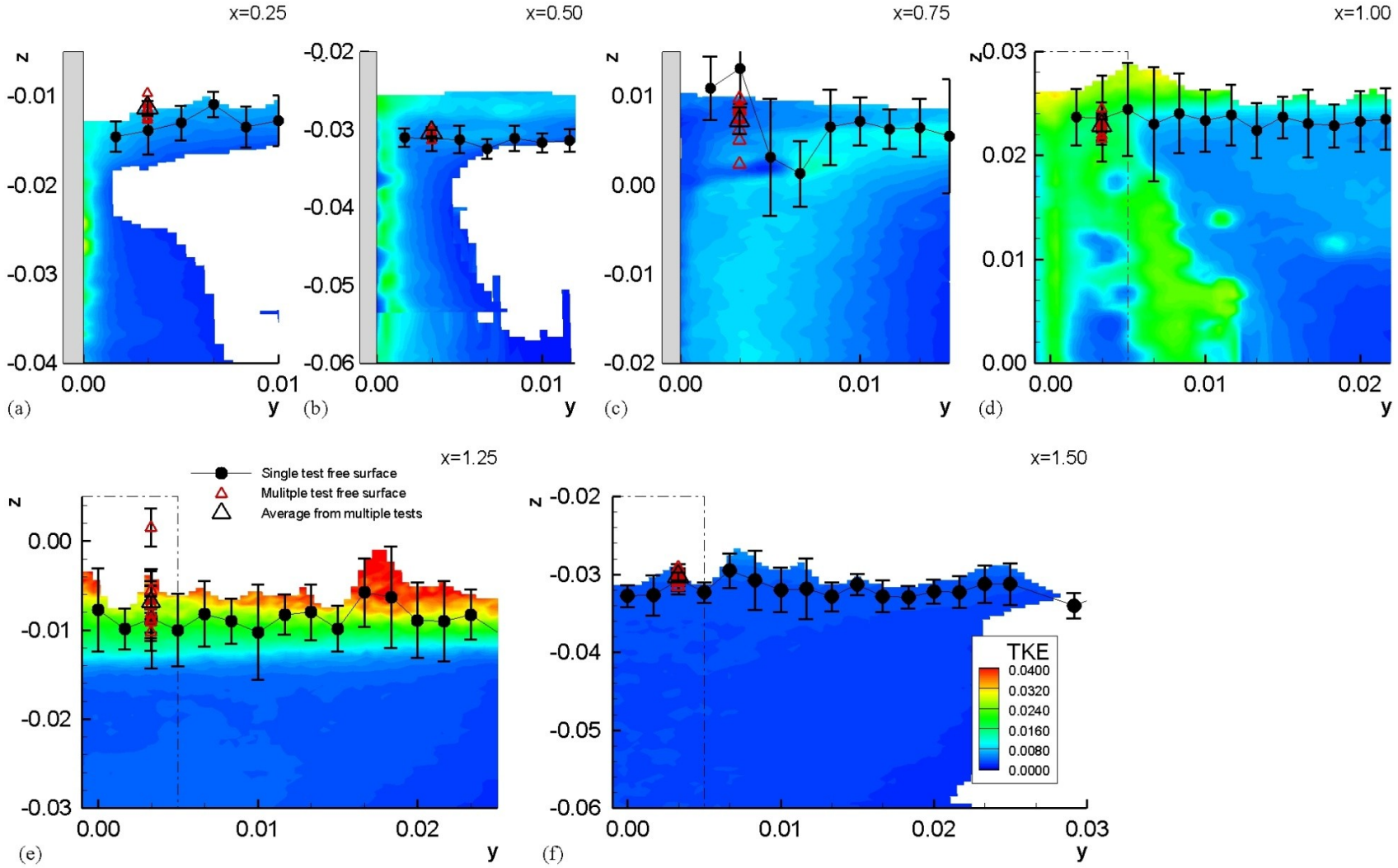

Figure 87: Juncture region *TKE* contours, $Ak = 0.21$

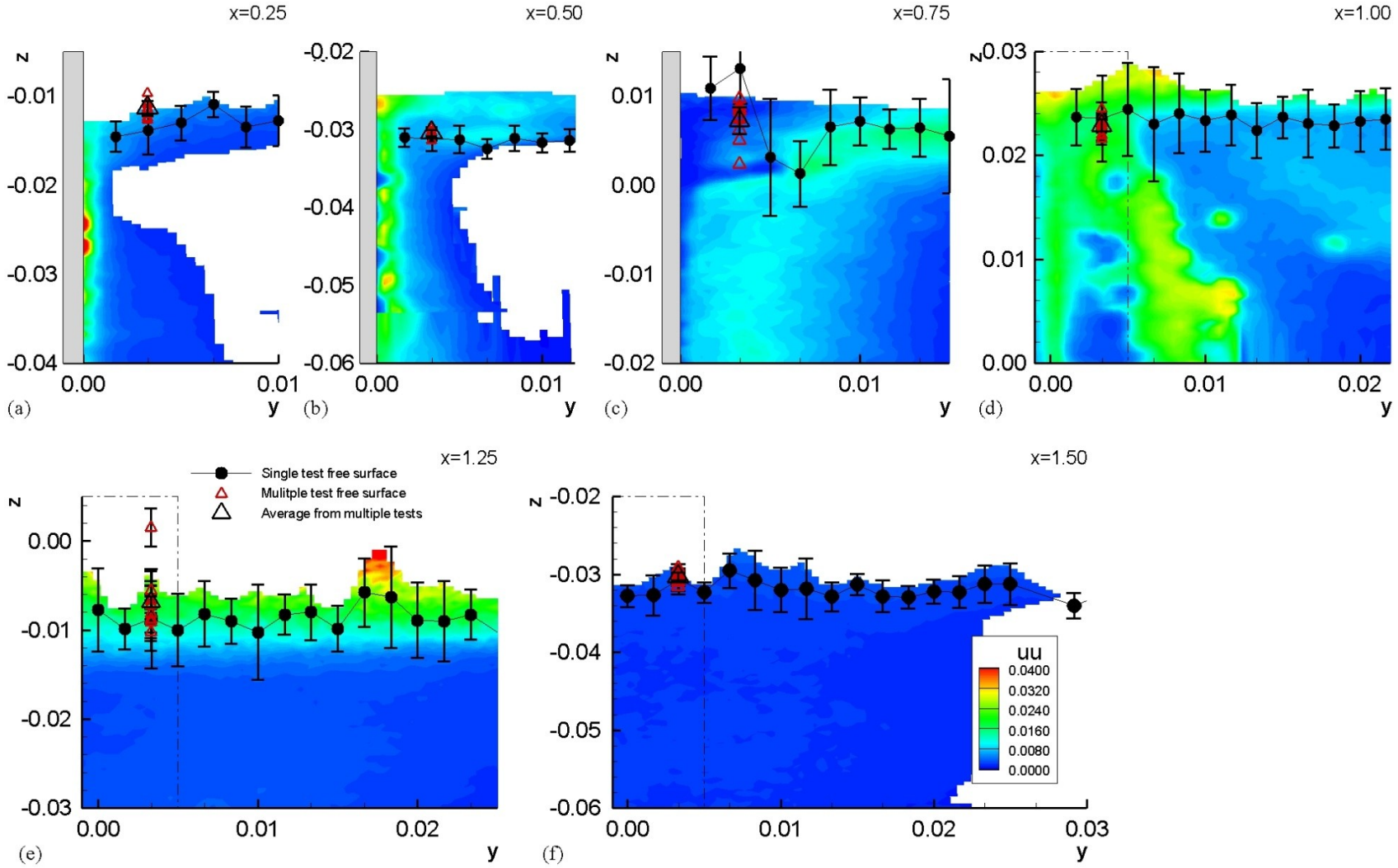

Figure 88: Juncture region *uu* contours, $Ak = 0.21$

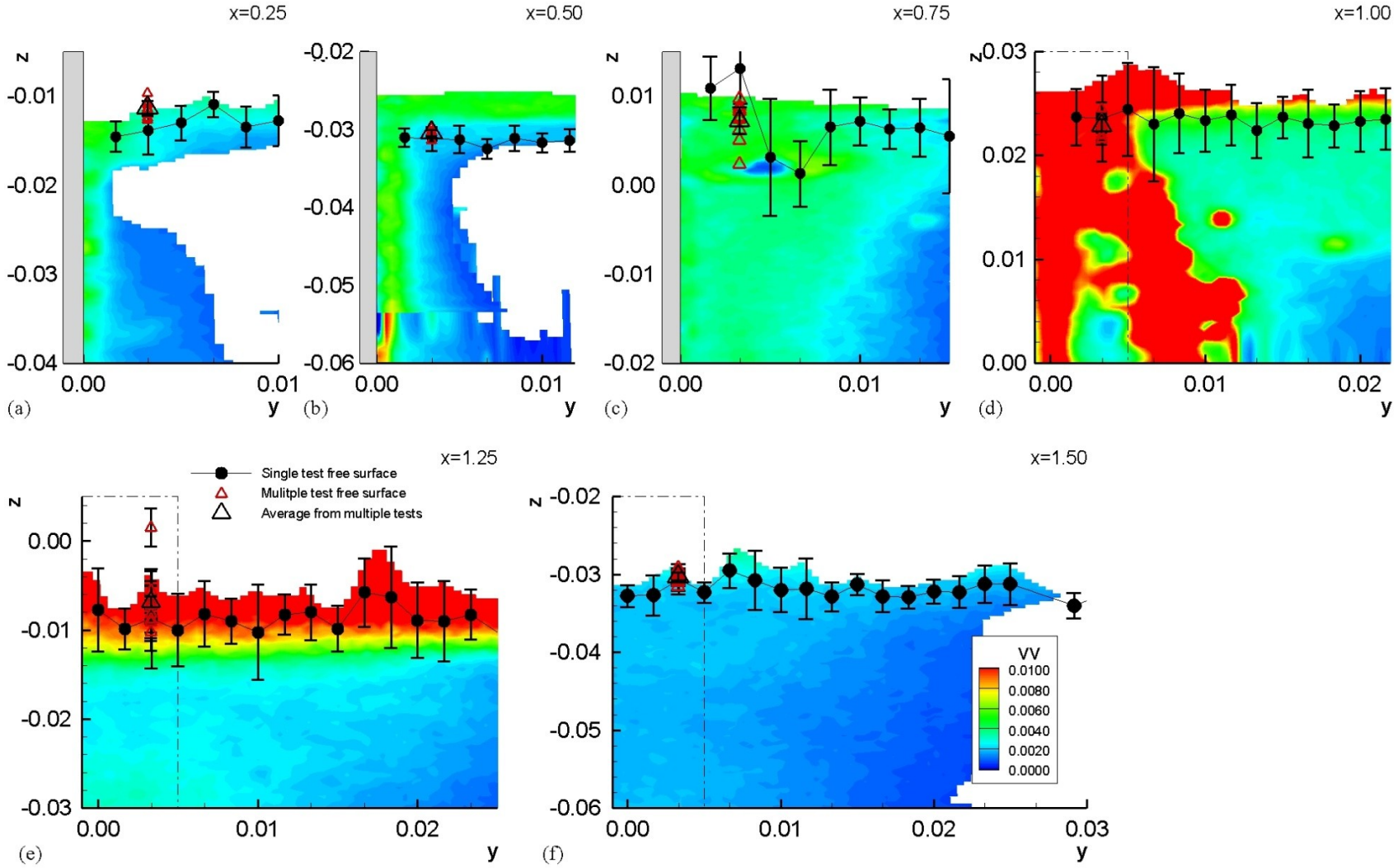

Figure 89: Juncture region *vv* contours, $Ak = 0.21$

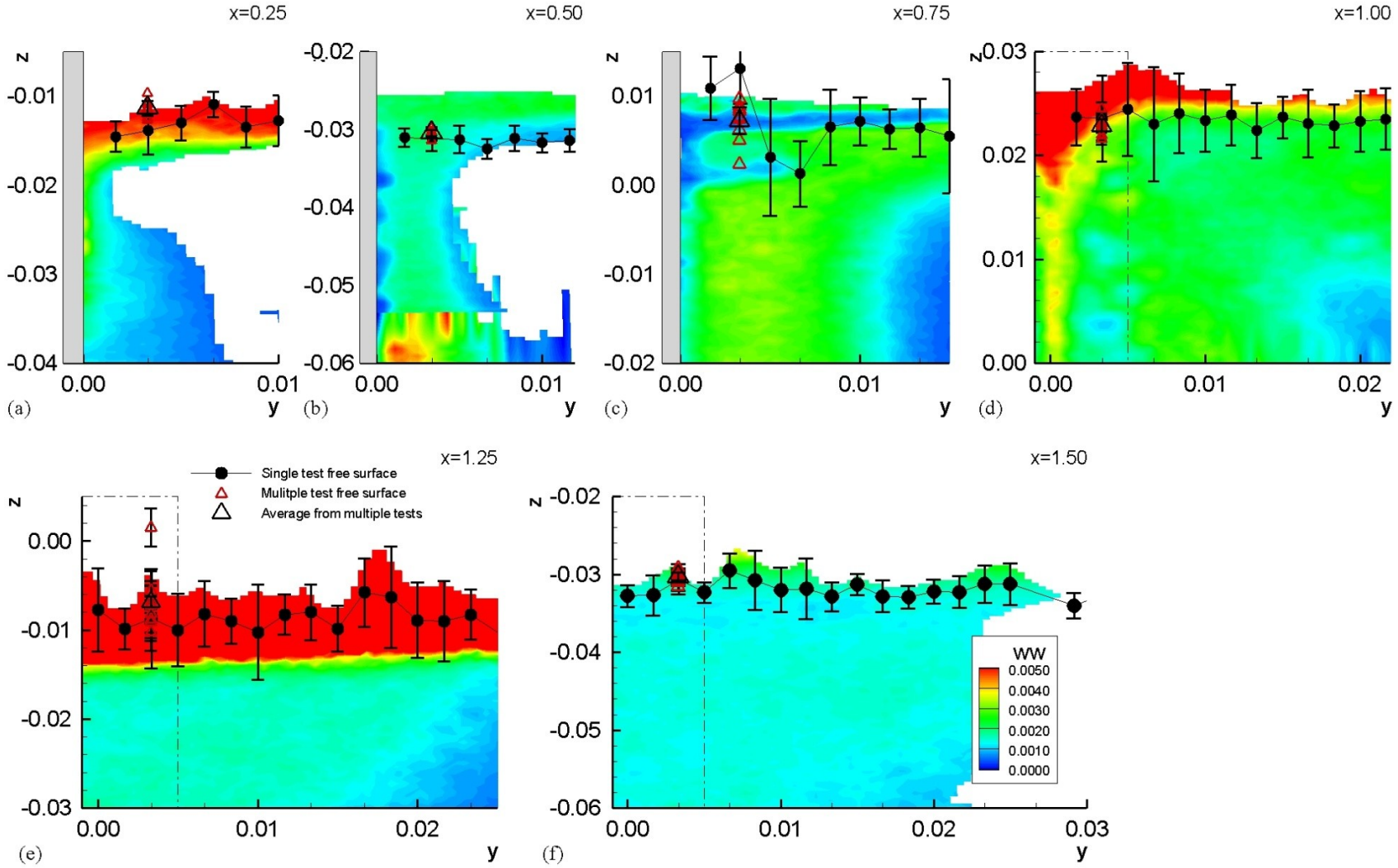

Figure 90: Juncture region *ww* contours, $Ak = 0.21$

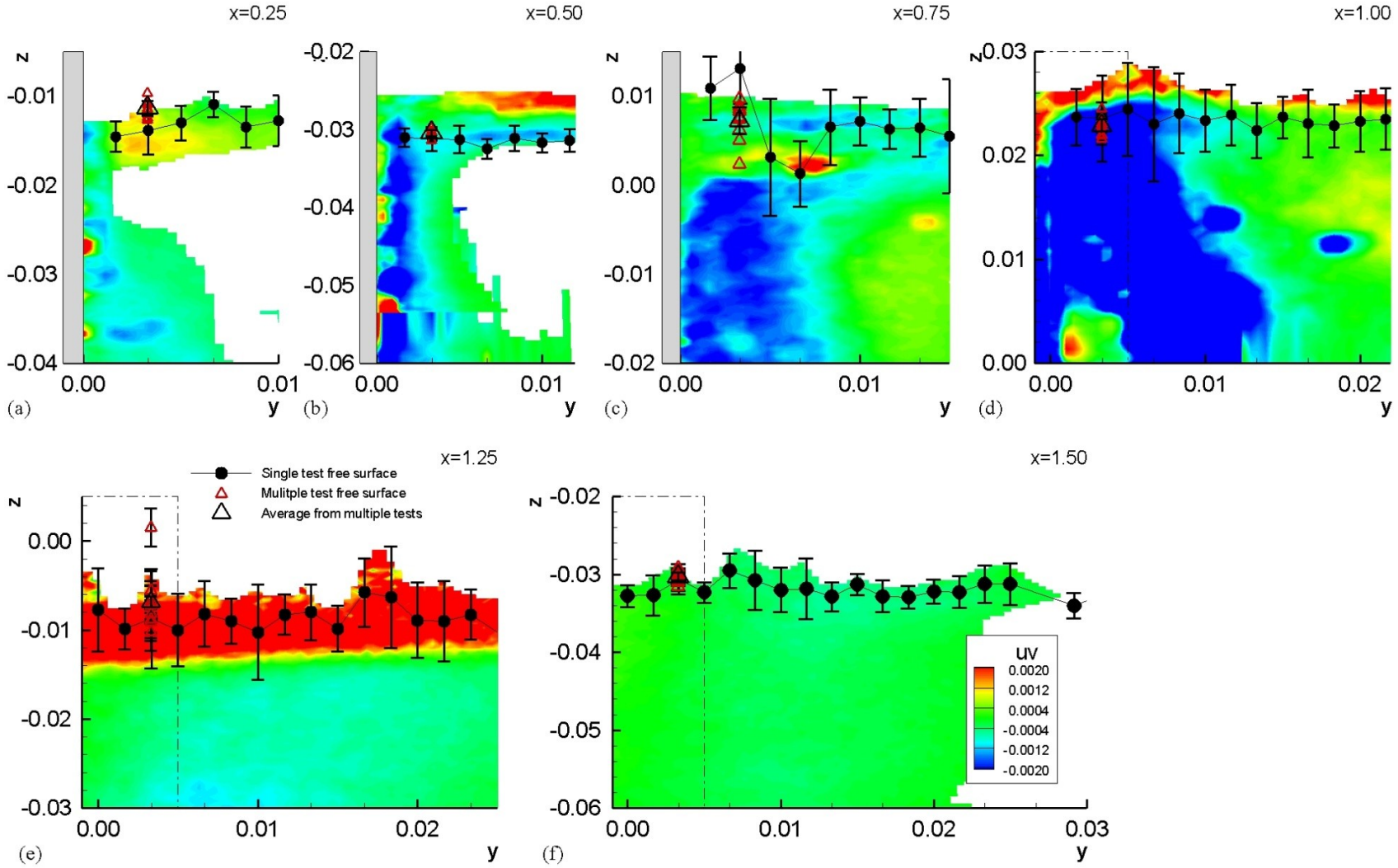

Figure 91: Juncture region *uv* contours, $Ak = 0.21$

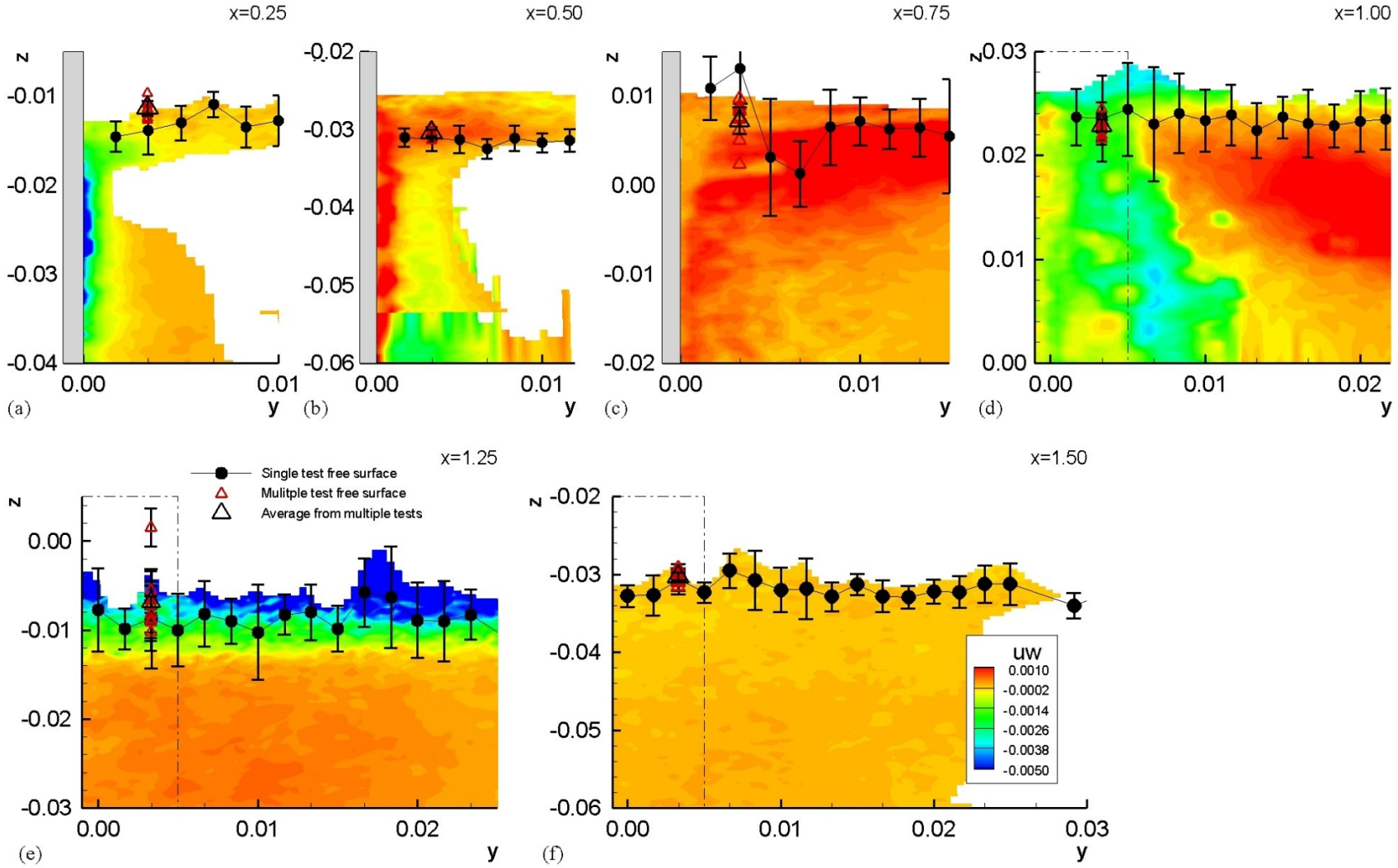

Figure 92: Juncture region *uw* contours, $Ak = 0.21$

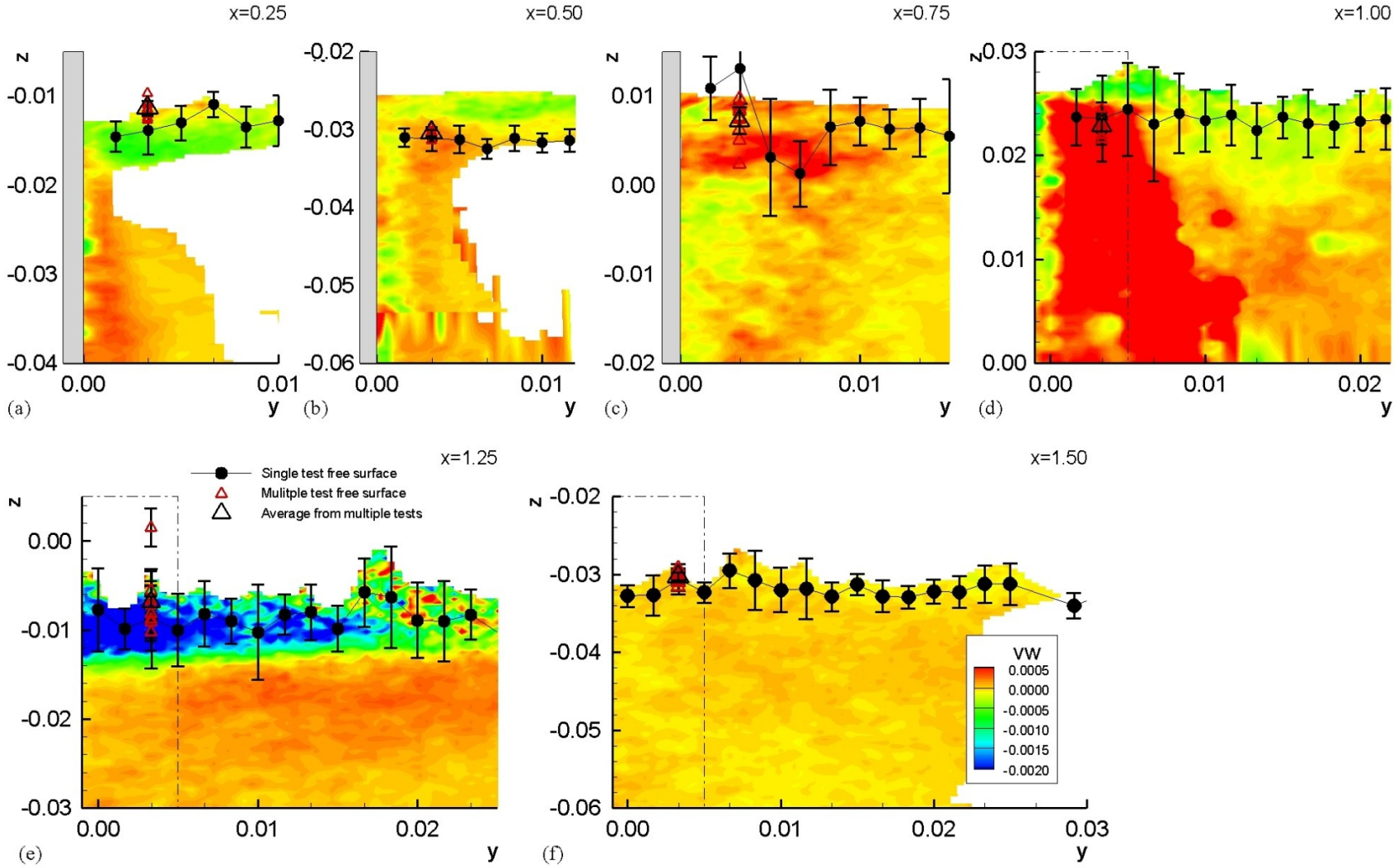

Figure 93: Juncture region *vw* contours, $Ak = 0.21$

REFERENCES

AIAA Standard, (1999), "Assessment of Experimental Uncertainty with Application to Wind Tunnel Testing," AIAA S-071A-1999, Washington, D.C., 84 pp.

ASME, (1998), "Test Uncertainty," ASME PTC 19.1-1998, The American Society of Mechanical Engineers, 112 pp.

ASME, (2005), "Test Uncertainty," ASME PTC 19.1-2005, The American Society of Mechanical Engineers, 102 pp.

Broglia, R., Pascarelli, A., and Piomelli, U., "Large-eddy simulations of ducts with a free surface," Journal of Fluid Mechanics, Vol. 484, 2003, pp. 223-253.

Coleman, H.W. and Steele, W.G., Experimentation and Uncertainty Analysis for Engineers, Wiley, New York, 1999, pp. 275.

Coles, D.E., "The Turbulent Boundary Layer in a Compressible Fluid," Rand Report R-403-PR, September 1962.

Gad-el-Hal, M. and Bandyopadhyay, P.R., "Reynolds Number Effects in Wall-Bounded Turbulent Flows," Applied Mechanics Review, Vol. 47, 1994, pp. 307-365.

Gibbings, J.C., Goksel, O.T., and Hall, D.J., "The Influence of Roughness Trips upon Boundary- Layer Transition, Part 2. Characteristics of Single Spherical Trips," Aeronautics Journal, Vol 38, No. 899, 1986, pp. 357-367.

Giesing, J.P., and Smith, A.M., "Potential Flow About Two-Dimensional Hyrdofoils," Journal of Fluid Mechanics, Vol. 28, Part 1, 1967, pp. 113-129.

Granville, P.S., "Drag and Turbulent Boundary Layers of Flat Plates at Low Reynolds Numbers," Journal of Ship Research, Vol. 21, No. 1, 1977, pp. 30-39.

Grega, L.M., Hsu, T.Y., and Wei, T., "Vorticity Transport in a Corner Formed by a Solid Wall and a Free Surface," Journal of Fluid Mechanics, Vol. 465, 2002, pp. 331-352.

Grega, L.M., Wei, T., Leighton, R.I., Neves, J. C., "Turbulent Mixed-Boundary Flow in a Corner Formed by a Solid Wall and a Free-Surface," Journal of Fluid Mechanics, Vol. 294, 1995, pp. 17-46.

Hama, F., "Boundary Layer Characteristics for Smooth and Rough Surfaces," Transactions of the Society of Naval Architects and Marine Engineers, Vol. 62, 1954, pp. 333-351

Head, M.R. and Bandyopadhyay, P., "New Aspects of Turbulent Boundary-Layer Structure," Journal of Fluid Mechanics, Vol. 107, 1981, 99. 297-338.

Hsu, T.Y., Grega, L.M., Leighton, R.I., and Wei, T., "Turbulent Kinetic Energy Transport in a Corner Formed by a Solid Wall and Free Surface," Journal of Fluid Mechanics, Vol. 410, 2000, pp. 343-366.

ITTC, Proceedings of the 23rd International Towing Tank Conference, Venice, Italy, 2002.

Landweber, L. and Siao, L., "Comparison of Two Analyses of Boundary-Layer Data on a Flat Plate," Journal of Ship Research, Vol. 1, No. 4, 1958, pp. 21-33.

Kang, D.H., Longo, L., Marquardt, M., and Stern, F., "Solid/Free-Surface Juncture Boundary Layer and Wake With Waves," 27th Symposium on Naval Hydrodynamics, Seoul, Korea, 2008.

Kendall, A. and Koochesfahni, M., "A Method for Estimating Wall Friction in Turbulent Wal-Bounded Flows," Experiments in Fluids, Vol 44, 2008, pp 773-780.

Longo, J., Huang, H.P., and Stern, F., "Solid-Fluid Juncture Boundary Layer and Wake," Experiments in Fluids, Vol. 25, No. 4, 1998, pp 283-297.

Murlis, J., "The Structure of Turbulent Boundary Layer at Low Reynolds Number," PhD thesis, Imperial College, London, 1975.

Musker, A.J., "Explicit Expression For the Smooth Wall Velocity Distribution in a TurbulentBoundary Layer," AIAA Journal, Vol. 17, 1979, pp. 655-657.

Patel, V.C., "Some aspects of Thick Three-Dimensional Boundary Layers" in *Proceedings*, 14th Office of Naval Research Symposium Naval Hydrodynamics, Ann Harbor, MI, 1982, pp. 999-1040.

Pot, P.J., "Measurement in a 2D Wake Merging into a Boundary Layer," NLR, Rept. TR 19063U, 1979, The Netherlands.

Purtell, L.P., Klebanoff, P.S., and Buckley, F.T., "Turbulent Boundary Layer at Low Reynolds Number," Physics of Fluids, Vol. 24, 1981, pp. 802–811.

Ramaprian, B.R., Patel, V.C., and Sastry, M.S., (1981), "Turbulent Wake Development behind Streamlined Bodies," Iowa Institute of Hydraulic Research, IIHR Report No.231, 1981, The University of Iowa, Iowa City, Iowa.

Ramaprian, B.R., Patel, V.C., and Sastry, M.S., "The Symmetric Turbulent Wake of a Flat Plate," AIAA Journal, Vol. 20, 1982, pp. 1228-1235.

Sachdeva, R.C., and Preston, J.H., "Three-Dimensional Boundary Layer on a Flat Plate," Indian Journal of Technology, Vol. 16, 1978, pp. 25-27.

Salvesen, N., "Second-Order Wave Theory for Submerged Two-Dimensional Bodies," Naval Hydrodynamics, Sixth Symposium, 1966. pp. 595-636.

Salvesen, N., "On Higher-Order Wave Theory for Submerged Two-Dimensional Bodies," Journal of Fluid Mechanics, Vol. 38, part 2, 1969, pp. 415-432.

Schlichting, K., Boundary Layer Theory, 6th ed., McGraw-Hill, New York, 1968.

Schultz-Grunow, F., "New Frictional Resistance Law for Smooth Plates," NACA, TM 986, 1941.

Sreedhar, M. and Stern, F., "Large Eddy Simulation of Temporally Developing Juncture Flows," International Journal of Numerical Methods in Fluids, Vol. 28, No. 1, 1998a, pp. 47-72.

Sreedhar, M. and Stern, F., "Prediction of Solid/Free-Surface Juncture Boundary Layer and Wake of a Surface-Piercing Flat Plate at Low Froude Number," ASME Journal of Fluids Engineering, Vol. 120, 1998b, pp. 354-362.

Stern, F., Choi, J.E., and Hwang, W.S., "Effects of Waves on the Wake of a Surface-Piercing Flat Plate: Experiment and Theory," Journal of Ship Research, Vol. 37, No. 2, 1993, pp. 102-118.

Stern, F., Hwang, W.S., and Jaw, S.Y., "Effects of Waves on the Wake of a Surface-Piercing Flat Plate: Experiment and Theory," IIHR Report No. 318, Iowa Institute of Hydraulic Research, University of Iowa, Iowa City, Iowa, 1987.

Stern, F., Hwang, W.S., and Jaw, S.Y., "Effects of Waves on the Boundary Layer of a Surface-Piercing Flat Plate: Experiment and Theory," Journal of Ship Research, Vol. 33, No. 1, 1989, pp. 63-80.

Stern, F., "Effects of Waves on the Boundary Layer of a Surface-Piercing Body," Journal of Ship Research, Vol. 30, No. 4, 1986, pp. 256-274.

Stokes, G.C., "On the Theory of Oscillatory Waves," Transactions of the Cambridge Philosophical Society. Vol 8, 1847, pp. 441-455.

White, F, Viscous Fluid Flows, 2nd ed., McGraw-Hill, New York, 1991.

White, F, Fluid Mechanics, 6th ed., McGraw-Hill, New York, 2008.

Wieghart, K. and Tillmann, W., "On the Turbulent Friction Layer for Rising Pressure," NACA TM 1314, 1951.

Wieneke, B., Anderson, S., (2009), IIHR Hydroscience & Engineering, Iowa City, IA., private communications.

Yoon, H.-S., Longo, J., Toda, Y., and Stern, F., "3D PIV Flow Map for Pure Sway and Pure Yaw PMM tests for Surface Combatant," IIHR Hydroscience & Engineering, IIHR Report, 2008, The University of Iowa, Iowa City, Iowa.

Yoon, H.-S., "Phase-Averaged Stereo-PIV Flow Field and Force/Moment/Motion Measurements for Surface Combatant in PMM Maneuvers," Ph.D. Thesis, The University of Iowa, 2008.